

Springer Aerospace Technology

Aniello Riccio *Editor*

Damage Growth in Aerospace Composites

 Springer

Springer Aerospace Technology

More information about this series at <http://www.springer.com/series/8613>

Aniello Riccio
Editor

Damage Growth in Aerospace Composites

 Springer

Editor
Aniello Riccio
Department of Industrial and Information
Engineering
Second University of Naples
Aversa
Italy

ISSN 1869-1730
Springer Aerospace Technology
ISBN 978-3-319-04003-5
DOI 10.1007/978-3-319-04004-2

ISSN 1869-1749 (electronic)
ISBN 978-3-319-04004-2 (eBook)

Library of Congress Control Number: 2014957962

Springer Cham Heidelberg New York Dordrecht London
© Springer International Publishing Switzerland 2015

This work is subject to copyright. All rights are reserved by the Publisher, whether the whole or part of the material is concerned, specifically the rights of translation, reprinting, reuse of illustrations, recitation, broadcasting, reproduction on microfilms or in any other physical way, and transmission or information storage and retrieval, electronic adaptation, computer software, or by similar or dissimilar methodology now known or hereafter developed.

The use of general descriptive names, registered names, trademarks, service marks, etc. in this publication does not imply, even in the absence of a specific statement, that such names are exempt from the relevant protective laws and regulations and therefore free for general use.

The publisher, the authors and the editors are safe to assume that the advice and information in this book are believed to be true and accurate at the date of publication. Neither the publisher nor the authors or the editors give a warranty, express or implied, with respect to the material contained herein or for any errors or omissions that may have been made.

Printed on acid-free paper

Springer International Publishing AG Switzerland is part of Springer Science+Business Media (www.springer.com)

Contents

1	Introduction	1
	Aniello Riccio and Tomas Ireman	
 Part I Detailed Methodologies for Damage Growth in Aerospace Composites		
2	Detailed Methodologies for Integrated Delamination Growth and Fiber-Matrix Damage Progression Simulation	9
	Aniello Riccio, Elisa Pietropaoli and Antonio Raimondo	
3	Delamination and Debonding Growth in Composite Structures	63
	Javier San Millán and Iñaki Armendáriz	
4	Delamination Growth in Composite Plates Under Fatigue Loading Conditions	89
	Aniello Riccio, Andrea Sellitto and Rocco Ricchiuto	
5	Influence of Intralaminar Damage on the Delamination Crack Evolution	107
	Cédric Huchette, Thomas Vandellos and Frédéric Laurin	
6	Microdamage Modeling in Laminates	141
	Janis Varna	
 Part II Fast Methodologies for Damage Growth in Aerospace Composites		
7	Finite Element Study of Delaminations in Notched Composites	177
	Sören Nilsson, Alann André and Anders Bredberg	

8	Effect of the Damage Extension Through the Thickness on the Calculation of the Residual Strength of Impacted Composite Laminates	187
	Sören Nilsson, Anders Bredberg and Tonny Nyman	
9	A Fast Numerical Methodology for Delamination Growth Initiation Simulation	199
	Aniello Riccio and Michele Damiano	
 Part III Manufacturing and Testing		
10	An Experimental Study on the Strength of Out of Plane Loaded Composite Structures	223
	Sören Nilsson, Alann André and Anders Bredberg	
11	Buckling and Collapse Tests Using Advanced Measurement Systems	231
	Richard Degenhardt	
12	Vacuum Infusion Manufacturing of CFRP Panels with Induced Delamination	249
	Vincenza Antonucci and Mauro Zarrelli	
13	Lock-in Thermography to Detect Delamination in Carbon Fibres Reinforced Polymers	263
	Carosena Meola and Giovanni Maria Carlomagno	

Chapter 1

Introduction

Aniello Riccio and Tomas Ireman

1.1 State of the Art of European Projects on Composites Damage Management

The high specific strength and stiffness of composite materials make them suitable for use in aerospace structures. However, the high sensitivity of these materials to the presence of damage, arising after impact with foreign objects or caused by manufacturing defects and stress concentrators, makes designing with composites a very challenging task.

The damage mechanisms in composites are very complex and can involve one or more constituents at a time. Delaminations, fibre breakage and matrix cracking can strongly reduce the load carrying capability of composite structures leading, in general, to a premature failure. Moreover, depending on the composite internal layout and on the adopted manufacturing technique, the damage mechanisms may interact with each other, making it difficult to predict the residual properties of composite components.

In recent years, the inability in predicting the damage onset and its evolution in composite structures, has led to over-conservative designs, not fully realising the composites promised economic benefits. Hence, in order to make the composites affordable in aerospace design, many research projects have been started in the last

A. Riccio (✉)

Department of Industrial and Information Engineering, Second University of Naples,
via Roma n 29, 81031 Aversa, Italy
e-mail: aniello.riccio@unina2.it

T. Ireman

Saab, Business Area Aeronautics, SE 581 88 Linköping, Sweden

decade aimed to investigate the composites' damage mechanisms and to promote damage tolerant design approaches.

A number of GARTEUR action groups have been started on damage management in composite structures:

GARTEUR AG 09 "Damage mechanics of composites" (1986–1994) had the focal point on the buckling and growth of delaminated areas to gain a substantial degree of understanding of delamination growth mechanism.

GARTEUR AG 14 "Fractography of composites" (1991–1995) wanted to establish a series of standards to follow in the field of non-destructive tests.

GARTEUR AG 16 "Damage propagation in Composites" (1994–1997) was focused on the delaminations in composites. Most of the work done was addressed to the development and validation of basic methods for the delamination growth simulation.

GARTEUR AG 20 "Fractographic aspects of fatigue failure in composites" (1994–2001) had the objective to develop analysis methods contributing to the failure prediction of composite wing panel and to validate them with experimental data.

GARTEUR AG 22 "Design Methodology for Damage Tolerant Composite Wing Panels" (1998–2000) was aimed to the development of methodologies for the failure prediction of composite wing panels.

GARTEUR AG 28 "Impact Damage and Repair of Composites" (2002–2006) was addressed to the development of methodologies for the prediction and characterisation of the impact damage. Relevant effort was also put on the analysis of impacted post-buckling designed composite structures.

Additionally, several EU funded projects have been carried out to improve the knowledge about composites fracture mechanisms:

EDAVCOS "Efficient Design and Verification of Composite Structures" (1998–2001) was addressed to the development of methods for design of composite structures with damage tolerance constraints.

BOJCAS "Bolted Joint in Composite Aircraft Structures" (2000–2003) was focused on the development of methodologies for the prediction of final failure of composite joints. Delamination, fibre breakage and matrix cracking have been taken into account.

FALCOM "Failure, Performance and Processing Prediction for Enhanced Design with Non-crimp-Fabric Composites" (2001–2004) aimed to the development of methodologies for predicting the mechanical behaviour including failure of non-crimp fabric composites.

Finally, being composites widely adopted for military scopes, their structural behaviour including damage evolution has been studied under MoD funded projects:

DAMOCLES "Damage Management of Composite Structures for Cost Effective Life Extensive Service" (1999–2005). DAMOCLES programmes were finalised to the development of design numerical tools able to perform a cost oriented

optimisation taking into account damage resistance and damage tolerance constraints. Applications to composite stiffened panels and composite wing-box proved the validity of the developed approaches.

All these projects have contributed to increasing the knowledge of the composites structural response and failure mechanisms. However, since GARTEUR AG 16, which represented the first attempt to analyse the composites damage evolution, in the last fifteen years, big steps forward have been made in the field of computational technologies and new “composites oriented” non-destructive inspection tools have been introduced. These innovative numerical/experimental features can be considered as relevant driving factors for the development of newer effective numerical approaches oriented to the prediction of damage on-set and growth in composites.

Furthermore, fifteen years of research and growing applications in industries have brought to life new needs, to be addressed by Research and Development, for example related to the presence of new composites typologies (textile composites) and new manufacturing techniques (RFI, RTM, fibres placement).

The lesson learned from the majority of the mentioned research projects also suggests trying to introduce more general approaches able to deal with different failure mechanisms (delamination, fibres breakage, matrix cracking, etc.) at a time and to take into account their interaction, independently from the damage causes (impact, manufacturing defect etc.).

Finally the emerging tendency to adopt composite materials for primary structures opens new scenarios involving new safety issues which imply considering damage tolerance design approaches from the earlier phases of the design process (including optimisation) rather than limiting the use of damage on-set and growth numerical techniques to complex/expensive non-linear verification analyses.

From the above considerations, the GARTEUR Action Group AG 32:

C.I.R.A. (Centro Italiano Ricerche Aerospaziali)—Italy (Chairman)

QinetiQ—United Kingdom

DLR (The German Aerospace Center)—Germany

INTA (Instituto Nacional de Tecnica Aeroespacial)—Spain

SWEREA-SICOMP—Sweden

EADS-M—Germany

ALENIA—Italy

Imperial College of London—United Kingdom

CNR (Centro Nazionale Ricerche)—Italy

Lulea University of Technology—Sweden

SAAB—Sweden

ONERA (The French Aerospace Lab)

University of Nantes—France

University of Naples “Federico II”—Italy

carried out between year 2006 and year 2011 a joint research work focused on “DAMAGE GROWTH IN COMPOSITES”.

1.2 AG-32 Objectives and Relationships with Previous Projects

The main objective of the Action Group AG-32, based on of the emerging needs related to the composites usage in aerospace applications, can be summarized in:

To develop integrated numerical/experimental methodologies capable to take into account the presence of damage and its evolution in composite structures from the early phases of the design (conceptual design) up to the detailed FEM analysis and verification phases

This objective addresses the following issues:

- Integration between numerical and experimental methodologies (oriented to the validation and to the interpretation of the most significant physical phenomena governing the damage mechanisms in composites)
- Investigation of generalised composite structures (laminated, textiles, etc.)
- Prediction of generalised composite damage (delamination, fibre breakage, matrix cracking, etc.), onset and evolution
- Development of numerical methodologies oriented to the different design phases (fast methodologies for conceptual/preliminary design and detailed methodologies for analysis and verification)

The new methodologies developed in the frame of AG-32, able to support the composites design process and able to drive it towards a damage tolerant philosophy, can surely imply strong changes in the way composite structures are adopted in aerospace industry leading to:

- the reduction of the overall composite design time and costs by improving the efficiency of simulation tools and by reducing the number of experimental validation tests;
- the improvement of composite components performances by optimising the weight according to damage tolerant design philosophies;
- the reduction of certification costs by adopting numerical procedures able to strengthen the certification approach based on the no-growth philosophy and, at the same time, able to promote a future growth certification approach;
- the reduction of the in-service costs by increasing the inspections intervals.

The Action Group AG-32 is strongly connected, in terms of topics and objectives, with other past and coexisting projects. The connections are summarized in Fig. 1.1.

Indeed, in the frame of the AG-32 activities, coupons and benchmarks tests performed under several past projects (GARTEUR AG 22, EDVAVCOS, BOJCAS, FALCOM and DAMOCLES) have been used for the validation of novel numerical methodologies. At the same time, the novel methodologies developed within the AG-32 project have been used as input for coexisting projects (GARTEUR AG-31, GARTEUR AG-32, MAAXIMUS, etc.) dealing with damage development in composite structures.

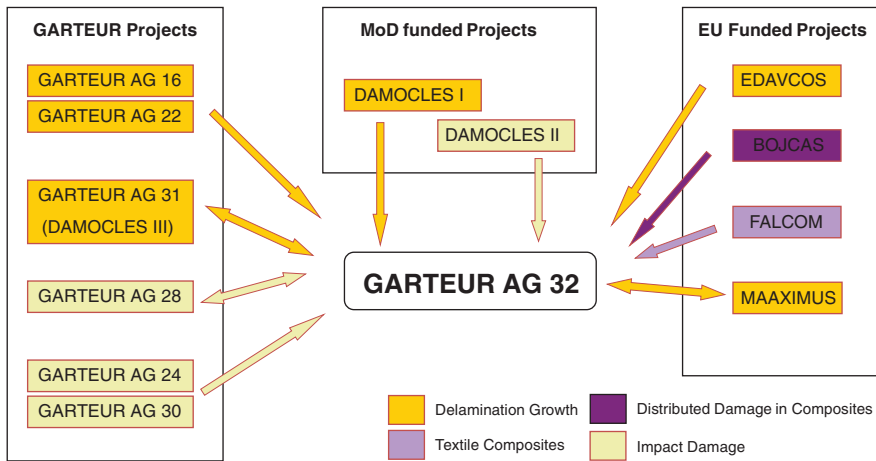


Fig. 1.1 Relationships between GARTEUR AG-32 (former EG-31) and past and existing projects

1.3 AG-32 Work Breakdown Structure and Presentation of Results

The activities have been grouped into Work Elements based on proper classifications of the developed methods and activity typology.

A first classification in “fast” and “detailed” methods has been considered based on the method positioning within the design process: “fast” procedures are naturally oriented to a preliminary design phase where the computational time is of main concern, while “detailed” approaches suit for analysis and verification phases where the accuracy of the prediction of the mechanical behaviour of composite structures is the main focus. A further classification of the methods has been considered based on the typology of the predicted damage mechanism: “inter-laminar damage growth oriented” and “intra-laminar damage growth oriented” methods.

According to the assumed methods’ classifications, the project activities have been grouped into four Work Elements (WE). WE 1 and WE 2, focused on the numerical development activities, bring together respectively the activities related to “detailed” and “fast” numerical methods. WE 3 is dedicated to the experimental activities consisting in experimental methods development or experimental campaigns for the validation of numerical tools. WE 4 ensembles activities oriented to the validation of the developed methodologies.

In Table 1.1, a schematic representation of the Work Elements is given with information on the partners’ involvement.

The main results from the AG-32 project, in terms of methodologies developments, experimental methods developments and validation experimental activities

Table 1.1 WE partners' involvement

	WE1: Detailed Methodologies		WE2: Fast Methodologies		WE3: Manufacturing and tests		WE4: Validation	
	WE 1.1: Inter-laminar damage growth	WE 1.2: Intra-laminar damage growth	WE 2.1: Inter-laminar damage Growth	WE 2.2: Intra-laminar damage growth	WE 3.1: Coupons	WE 3.2: Benchmark	WE 4.1: Detailed methods	WE 4.2: Fast methods.
CIRA								
INTA								
SICOMP								
Imperial College								
ALENIA								
QINETIQ								
EADS-M								
CNR								
SAAB								
ONERA								
University of Nantes								
University of Naples								
Lulea University								
DLR								

are summarised in this book. Regardless of the AG-32 Work Elements subdivision, the results are presented in chapters grouped in three main sections.

Part 1 is focused on the development and validation of “detailed” methodologies able to accurately predict the damage evolution in composites while Part 2 brings together the main activities oriented to the development and validation of affordable “fast” numerical tools able to efficiently predict the damage evolution in composites. Finally, in Part 3, the main results from the experimental test campaigns needed for the validation of the developed numerical tools are presented. In this last section, however, also a description of the developed effective procedures, to monitor the damage evolution during mechanical tests, and the results from the experimental investigation of new effective degradation laws for composites have been included.

Part I
Detailed Methodologies for Damage
Growth in Aerospace Composites

Chapter 2

Detailed Methodologies for Integrated Delamination Growth and Fiber-Matrix Damage Progression Simulation

Aniello Riccio, Elisa Pietropaoli and Antonio Raimondo

2.1 Introduction

In previous years significant progresses have been made in understanding failure mechanisms of composite materials such as delamination and fiber-matrix breakage. Delaminations, which can arise during the manufacturing process or as a consequence of impacts from foreign objects, are probably the most investigated mode of failure in composite laminates. However, others damages such as matrix cracks, fiber-matrix debonding, fiber fractures can also appear in composite structures under service conditions.

These different damage mechanisms are able to interact with each other and lead to a considerable reduction in stiffness and strength of local critical areas and consequently to the reduction of the load-carrying capability of the entire composite structure.

Studies on delaminations and on other damage mechanisms have been conducted separately. Indeed, in literature, several works deal distinctly with delamination and intralaminar damages; actually these phenomena are seldom analyzed together in order to assess how the interferences between the different damages mechanisms can influence their evolution under various loading conditions.

The delaminations have been extensively investigated both numerically and experimentally and, whenever possible, analytical models have been developed.

A. Riccio (✉) · A. Raimondo
Department of Industrial and Information Engineering, Second University of Naples,
via Roma n 29, 81031 Aversa, Italy
e-mail: aniello.riccio@unina2.it

E. Pietropaoli
Centro Italiano Ricerche Aerospaziali (CIRA), via Maiorise snc, 81043 Capua, Italy

A first analytical model has been developed in [1] where, based on the “thin film” approximation, a prediction of the strain needed to cause delamination buckling is given together with an approximate evaluation of the energy release rate for the delamination growth initiation in a composite laminate under compressive load. Further analytical research works have been performed by Kardomates and Schmueser who investigated the buckling and the post buckling behaviour of homogeneous orthotropic linear elastic laminates with a through the width delamination [2, 3] taking into account also transverse shear effects.

Experimental campaigns on delaminations have been conducted by several authors [4–9] in order to improve the knowledge on the physical phenomena governing this damage mechanism and to provide substantial data for validation of analytical and numerical models.

Earlier numerical studies have been carried out in [10–12] where 2-dimensional models have been proposed. 3-dimensional numerical approaches are presented in [13–16] focusing on the buckling and post buckling behaviour of embedded delaminations. Especially in the post buckling regime, it was found that the contacts between sub-laminates affect mostly the Energy Release Rate distribution along the delamination front [17, 18].

All the cited models, even if capable to provide a realistic stress distribution in the delaminated area, are not able to simulate the growth of delaminations.

In Refs. [19–27], respectively, 2D and 3D models are presented. These ones are able to take into account the delamination growth by adopting the Virtual Crack Closure Technique to evaluate the Energy Release Rate.

In particular in [23, 24] an interface element able to cope with the delamination initiation and growth which is based on the Modified Virtual Crack Closure Technique for the Energy Release Rate distribution evaluation is proposed.

Considerable studies have been devoted also to the understanding of the damage onset and progression in composite structures in terms of matrix and fiber breakage both experimentally and numerically.

Experimental activities aimed to characterize the damage in terms of matrix and fibers breakage in laminated composites are presented in [28, 29]. Often, from an experimental point of view, fiber and matrix cracking in composites have been found strongly related to the delamination onset and growth events.

The progression of damage in composites in term of matrix and fiber failure is the subject of several papers. In [30, 31] the failure criteria and the material properties degradation rules are identified as the basic steps for a progressive damage approach in composite structures.

Among the others, the failure criteria proposed in [32, 33] by Hashin and Rotem have been found extremely effective for their capability to identify the different failure modes being based on a strong physical interpretation of the failure mechanisms.

In order to take into account the degradation of the material properties, on failure occurrence, several material degradation models are available in literature. Three categories for the material degradation models can be identified: instantaneous unloading [34], gradual unloading [35–37] and constant stress at ply failure [38].

Examples of numerical procedures for damage propagation taking into account the non-linear stress evaluation, failure criteria and properties degradation are

provided in [39–41]. However none of the previously cited research works deals with the interactions between delamination and matrix-fiber damage mechanism in laminated composites under any loading conditions.

These interactions can have a relevant role in particular for delaminated composite plates under compression. Hence, for the simulation of the complex physical phenomena behind the compressive behaviour of composite plates with a delamination, the development of integrated numerical methodologies considering simultaneously the presence of different damage mechanisms in composites becomes mandatory.

The activities performed in the frame of the GARTEUR AG-32 Research Project by CIRA are the result of an extensive development of numerical methodologies for delamination growth and matrix-fiber damage progression simulation. This development started with the simulation of 2D-3D buckling and post-buckling behaviour of delaminated composite plates taking into account contact phenomena and delamination growth by means of an incremental procedure based on interface fracture and contact elements [22–24]. On a parallel path, a progressive damage procedure was developed, for the matrix-fiber damage progression simulation, based on Hashin's failure criteria and instantaneous material properties degradation rules, with a first application to composite joints [39, 40].

In Sect. 2.2 the objectives of the CIRA activity within the work Element 1, related to detailed tools for damage growth simulation in composites, are illustrated while in Sect. 2.3 the background theory and the numerical implementation in the B2000 research FEM code are described. In Sect. 2.4 a first validation of the developed B2000 numerical modules is provided.

Finally, in order to emphasize the need, when designing with composites, for improved novel numerical approaches taking into account inter-laminar and intra-laminar damage interaction (as the ones described in Sect. 2.3), some applications on stiffened composite panels with the ABAQUS FEM code are presented in Sect. 2.5. Indeed, even if ABAQUS uses standard numerical tools for damage evolution such as the VCCT and PDA approaches on solid shell elements (not able to reproduce the real three-dimensional stress state), these applications allow to roughly quantify the influence of the damages evolution and their mutual interaction on the loading carrying capability of real composite structures (such as stiffened panels with delaminations and skin-stringer debonding). These ABAQUS applications have been presented at the end of this chapter also to give an idea of the promising added value of the proposed novel numerical approaches (validated only for very simple composite specimens) if extended to the prediction of the evolution of delamination and skin-stringer debonding in complex composite structures.

2.2 Objectives

The mechanical behaviour of post-buckled composite structures is governed by the onset, evolution and interaction of inter-laminar (delaminations) and intra-laminar (fiber/matrix failures) damages. Thus, an accurate prediction of the residual

stiffness and strength of delaminated structures under compressive load requires that intra-laminar/inter-laminar damage interaction be taken into account.

Although delamination buckling and growth have been widely studied in literature, the effect of fiber-matrix failure on the buckling behaviour of a delaminated structure up to final failure hasn't been adequately analysed yet.

The work performed under the Work Element 1 of the GARTEUR AG-32 Research Project has been aimed at developing a numerical procedure able to simulate this kind of interaction, thus leading to a deeper understanding of its effects on the response of a composite laminate structure subjected to compressive load.

2.3 Description of the Method

Starting from the observation of the physical phenomenology of the damage for composite plates under compressive load, a numerical methodology has been developed based on failure criteria and material propagation rules for intra-laminar damage and on fracture mechanics concepts for inter-laminar damage.

2.3.1 Phenomenology

The stiffness and strength reduction associated to the presence of a delamination in a composite laminate plates can be very relevant especially in compression.

The experimental measure of residual properties in compression of structures with impact induced damages usually foresees the presence of an artificial delamination obtained by placing a very thin film of Teflon between two adjacent layer of a composite laminate. The laminate is thus subdivided into a thin sub-laminate and a thick sublaminar (or base sublaminar).

Two parallel edges of the plate are then clamped in a test machine and a compressive displacement is gradually applied. The behaviour of the damaged plates can be defined by monitoring the out of plane displacements of the two sublaminates.

In Fig. 2.1 a schematic representation of the out of plane displacements of two characteristic control points U and L (placed respectively on the top of the thin sublaminar and on the bottom of the thick sublaminar) is shown together with qualitative deformed shapes for a delaminated composite plate under compression at different loading stages.

In Fig. 2.1 it is possible to distinguish three characteristic values for the applied load: F_B is the local delamination buckling load, F_C represents the load at which the maximum out of plane displacement for the thinnest sub-laminar is attained (usually close to the delamination growth load) and F_D is the global buckling load.

The two sub-laminates remain in contact in the unbuckled condition until the load reaches the first critical value F_B (see configuration A–B in Fig. 2.1).

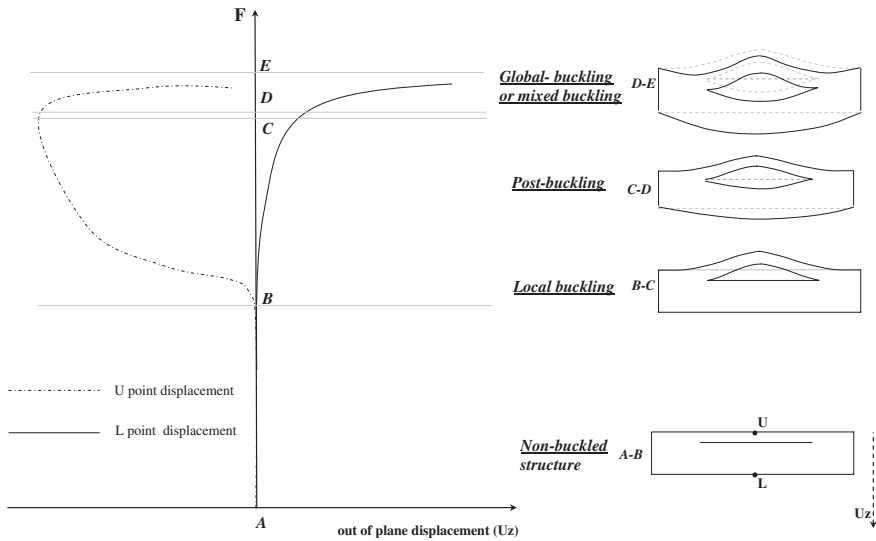


Fig. 2.1 Load-displacement behaviour (*left*) and characteristic deformed shapes (*right*)

At the load F_B the thinnest sub-laminate starts to buckle and the distance between the two characteristic points U and L increases: as a matter of fact the point L doesn't change its position while U moves away from L (see configuration B–C in Fig. 2.1). The maximum out of plane displacement for the thinnest sub-laminate is reached at F_C when the thickest sub-laminate starts to buckle. From F_C to F_D the composite panel undergoes the post-buckling regime: when load exceeds the F_C value, the global buckling of the plate takes place and the point L moves in the opposite direction with respect to the point U.

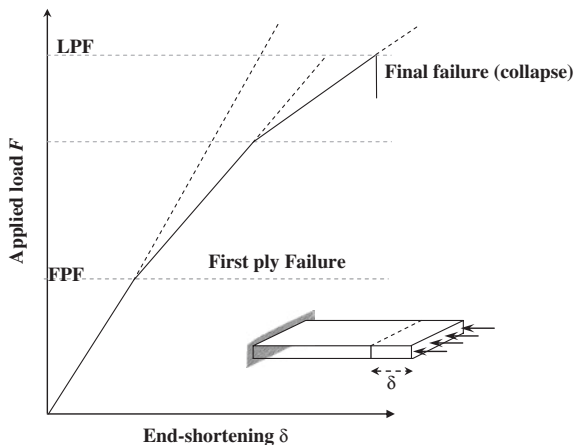
For loads beyond F_D , the thinner sub-laminate is dragged by the thicker one and the two points U and L generally move in the same direction (see configuration D–E in Fig. 2.1).

However during this compression process, intra-laminar damage may onset and propagate. Indeed, the failure in composite laminates, can initiate at local level (first ply failure) in an individual ply or in the interface between plies but ultimate failure in multi-directional laminates may not occur until the failure has propagated to several plies [42].

The compressive behaviour of a composite laminate is sketched in Fig. 2.2 where the reduction in stiffness due to the onset of intra-laminar failure is clearly associated to a slope variation of the applied load versus end-shortening curve.

Thus the prediction of the ultimate failure requires to follow the progression of failure within the laminate in order to take into account the stiffness reduction associated to the presence of damaged areas within the structure (Progressive Damage Analysis—PDA).

Fig. 2.2 Progressive damage of a composite laminate



2.3.2 Theoretical Background

In order to be able to develop numerical tools for the analysis of the damage phenomenology in compression after impact tests on composites (intra-laminar damage onset and evolution/inter-laminar damage growth), progressive damage procedures must be used in conjunction with fracture mechanics techniques.

2.3.2.1 Intra-laminar Damage: A Progressive Damage Procedure

According to progressive damage procedures, the load is gradually applied to the structure and failure criteria are used at each load step to establish the damage onset. At failure detection, the stiffness of the failed ply is reduced to a percentage of its undamaged value and the laminate is re-analysed to check whether the remaining plies are capable to sustain the load or not. The load is increased gradually until ultimate failure of the structure has occurred.

Thus, the basic steps of progressive damage procedures may be itemized as:

- determination of the stresses distribution on a ply by ply basis
- application of failure criteria for each ply
- degradation of the material properties to take into account the typical post-damage stiffness reduction of the material

2.3.2.2 Stress Evaluation

The deformation and, consequently, the state of stress and strain within a body can be expressed with reference both to the initial (or un-deformed configuration) or to the actual configuration of the structure: the first case leads to the Total Lagrangian formulation while the second to the Updated Lagrangian formulation.

Defined \mathbf{X} and \mathbf{x} as the position vectors of a point P with reference, respectively, to the initial configuration and to the deformed configuration, the displacement of the point P from a position P_0 to P_1 can be defined by means of the vector \mathbf{u} where:

$$\mathbf{x} = \mathbf{X} + \mathbf{u} \quad (2.1)$$

The evaluation of the total differential of \mathbf{x} allows to define the deformation gradient \mathbf{F} :

$$d\mathbf{x} = \frac{\partial \mathbf{x}}{\partial \mathbf{X}} d\mathbf{X} = \frac{\partial (\mathbf{X} + \mathbf{u})}{\partial \mathbf{X}} d\mathbf{X} = \mathbf{F} d\mathbf{X} \quad (2.2)$$

According to the Total and the Updated Lagrangian formulations, the second Piola-Kirchhoff and the Cauchy tensor are, respectively, adopted for stress evaluation. The second Piola-Kirchhoff stress tensor (\mathbf{S}) is defined as the force on the undeformed reference area while the Cauchy stress tensor ($\boldsymbol{\sigma}$) is a representation of the stress evaluated with respect to the deformed or actual configuration.

The relation between the second Piola-Kirchhoff stress tensor and the Cauchy stress tensor is given by the Eq. (2.3) [43]:

$$\mathbf{S} = \det(\mathbf{F}) \mathbf{F}^{-1} \boldsymbol{\sigma} (\mathbf{F}^T)^{-1} \quad (2.3)$$

2.3.2.3 Failure Criteria and Material Properties Degradation Rules

Composite materials behave differently under tension and compression loads, therefore it is necessary to define five dissimilar strength parameters: X_t and X_c longitudinal strength in tension and in compression, Y_t and Y_c transversal strength in tension and in compression, S in plane strength. Thus, with respect to common criteria for isotropic material, the strength of composite materials is strongly dependent on the direction of the applied load.

Failure criteria for composite laminates are mainly analytical approximations or curve fitting of experimental results. Lamina failure criteria [44] can be categorised as:

Limit criteria: each lamina stress is compared with the corresponding strength separately. Interaction among the stresses (or strains) is not considered (Maximum stress, maximum strain)

Interactive criteria: it is assumed that all the stress components contribute simultaneously to the failure of the composite (Tsai-Hill, Tsai-Wu)

Separate mode criteria: different criteria are used to distinguish between failure modes. Each criterion may involve more than one stress components (Hashin-Rotem).

In particular, Hashin's failure criteria allow the distinction among several characteristic modes of failure of laminated composites (such as fiber breakage and the matrix cracking under tension and compression loading conditions) to be obtained by adopting separated polynomial expressions for each failure mode of each composite constituent [see Eq. (2.4)].

$$\text{Hashin criterion} \left\{ \begin{array}{ll} \frac{\sigma_{11}}{X_C} = 1 & \text{Fiber failure (compression)} \\ \left(\frac{\sigma_{11}}{X_T}\right)^2 + \left(\frac{\tau_{12}}{S}\right)^2 = 1 & \text{Fiber failure (tension)} \\ \left(\frac{\sigma_{22}}{Y_T}\right)^2 + \left(\frac{\tau_{12}}{S}\right)^2 = 1 & \text{Matrix failure (tension)} \\ \left(\frac{\sigma_{22}}{2S}\right)^2 + \left[\left(\frac{X_T}{2S}\right)^2 - 1\right] \frac{\sigma_{22}}{Y_C} + \left(\frac{\tau_{12}}{S}\right)^2 = 1 & \text{Matrix failure (compression)} \end{array} \right. \quad (2.4)$$

When the application of failure criteria leads to the prediction of a failure in one of the laminae that constitute the laminate, the FPF has been reached (see Fig. 2.2).

As already remarked, the laminate can undergo additional load beyond the first ply failure (FPF): however once the FPF is reached, one or more plies become degraded by the formation of matrix cracks or by fiber break or fiber buckling.

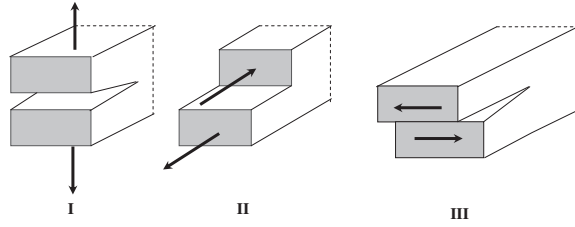
Degradation of plies that have partially or completely failed is a critical phase for the prediction of the ultimate failure. As plies fail progressively, strain energy of all plies must be redistributed. In homogeneous stress conditions, the intact plies absorb the energy from the degraded plies. The redistribution is more complex in case of non-homogeneous stress conditions.

Degradation rules, such as those proposed in Eq. (2.5), can be used to reduce stiffness of damaged plies in order to account for the presence of matrix cracks, fiber failure and of other intra-laminar damage mechanisms.

Failure mode		Material properties degradation rules
Matrix failure (tension)	$\sigma_{yy} > 0$	$\bar{E}_y = kE_y; \bar{E}_z = kE_z; \bar{G}_{yz} = kG_{yz}$
Matrix failure (compression)	$\sigma_{yy} < 0$	
Fiber failure (tension)	$\sigma_{xx} > 0$	$\bar{E}_x = kE_x; \bar{G}_{xy} = kG_{yz}; \bar{G}_{xz} = kG_{yz}$
Fiber failure (compression)	$\sigma_{xx} < 0$	
Fiber matrix failure (shear-out)	$\sigma_{xx} > 0$	$\bar{G}_{xy} = G_{yz}; \bar{G}_{xz} = G_{yz}$
Fiber failure (Kinking)	$\sigma_{xx} < 0$	$\bar{E}_x = kE_x; \bar{E}_y = kE_y; \bar{E}_z = kE_z$ $\bar{G}_{xy} = kG_{yz}; \bar{G}_{xz} = kG_{yz}; \bar{G}_{yz} = kG_{yz}$

(2.5)

Fig. 2.3 Fracture modes



2.3.2.4 Inter-laminar Damage: Energy Release Rate and Crack Growth Criteria

Delamination is usually treated as a fracture process between anisotropic layers. Thus, fracture mechanics principles are used to characterise the delamination growth phenomenon.

In fracture mechanics the most important parameter to be evaluated and verified is the strain energy release rate G which is defined as the energy dissipated during the creation of a fracture surface of unit area.

Actually, when the computed energy release rate reaches a critical value characteristic of the material, G_c (material fracture toughness), the crack is assumed to start to grow.

Thus, the evaluation of the Energy Release Rate allows to characterize the delamination's initiation and growth. Three different fracture modes can be defined associated to the three orthogonal modes of loading (see Fig. 2.3), namely mode I (opening), mode II (sliding shear) and mode III (tearing shear or scissoring).

Indeed, a delamination may be loaded in one of these modes or rather in some combination of them [45].

Experimental tests (DCB, ENF, MMB, ECT) are used to measure the critical fracture toughness, mixed-mode combinations can be taken into account choosing specific specimen and loading conditions configurations [42].

Delamination growth criteria may be viewed as a curve fitting of fracture test data. One of the most known criteria is the Power law:

$$\text{Power law criterion} \left| \left(\frac{G_I^m}{G_{IC}} \right)^\alpha + \left(\frac{G_{II}^m}{G_{IIC}} \right)^\beta + \left(\frac{G_{III}^m}{G_{IIIC}} \right)^\chi = 1 \quad (2.6) \right.$$

which states that delamination will start to propagate as soon as Eq. (2.6) is satisfied.

Different techniques can be used to compute the Energy Release Rate distribution at the delamination front such as the Virtual Crack Closure Technique (VCCT) and the Modified Virtual Crack Closure Technique (MVCCT).

The VCCT is based on the consideration that the strain energy released by a crack growing is equal to the amount of work required to close the same crack. This technique involves two analyses, one on the current crack front (a) and the other on the crack front appropriately extended (b) [46–55].

$$W = \frac{1}{2} \left(\int_0^{\Delta a} \sigma_{yy}^{(a)}(x) \delta u_y^{(b)}(x) dx + \int_0^{\Delta a} \sigma_{yx}^{(a)}(x) \delta u_x^{(b)}(x) dx + \int_0^{\Delta a} \sigma_{yz}^{(a)}(x) \delta u_z^{(b)}(x) dx \right) \quad (2.7)$$

Simplified approaches can be adopted for the calculation of the ERR. In particular, the Modified Virtual Crack Closure Technique (MVCCT) assumes that the crack front does not undergo substantial changes in a small crack opening Δa and that, therefore, it is possible to compute the energy release rate (ERR) contributions in one step, using nodal forces and displacements estimated at the actual crack front (a):

$$W = \frac{1}{2} \left(\int_0^{\Delta a} \sigma_{yy}^{(a)}(x) \delta u_y^{(a)}(x - \Delta a) dx + \int_0^{\Delta a} \sigma_{yx}^{(a)}(x) \delta u_x^{(a)}(x - \Delta a) dx + \int_0^{\Delta a} \sigma_{yz}^{(a)}(x) \delta u_z^{(a)}(x - \Delta a) dx \right) \quad (2.8)$$

And the Energy Release Rate becomes:

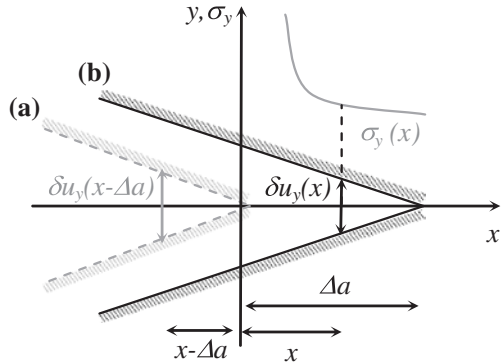
$$G = \lim_{\Delta a \rightarrow 0} \frac{W}{\Delta a} = \frac{1}{2\Delta a} \left(\int_0^{\Delta a} \sigma_{yy}^{(a)}(x) \delta u_y^{(a)}(x - \Delta a) dx + \int_0^{\Delta a} \sigma_{yx}^{(a)}(x) \delta u_x^{(a)}(x - \Delta a) dx + \int_0^{\Delta a} \sigma_{yz}^{(a)}(x) \delta u_z^{(a)}(x - \Delta a) dx \right) \quad (2.9)$$

where each integral corresponds to the Energy Release Rate for a basic fracture mode (G_I , G_{II} and G_{III}) (Fig. 2.4).

2.3.3 Numerical Implementations in B2000

Progressive damage procedures and crack growth criteria can be used in conjunction with the finite element method in order to be applicable to real structures. In this section the numerical implementations, performed in B2000 to evaluate the interaction between the intra-laminar and inter-laminar damages, are presented.

Fig. 2.4 Schematization of the two configurations before (a) and after the crack extension (b)



2.3.3.1 Progressive Damage Brick Element

A brick layered finite element with progressive damage capabilities has been implemented in the B2000 finite element open code by following the steps outlined before.

Failure criteria [see Eq. (2.4)] require stresses to be computed with respect to the structural deformed configuration. Being the B2000 based on the Total Lagrangian formulation, the transformation of stresses from the second Piola-Kirchhoff to Cauchy tensorial form must be carried out using the Eq. (2.3) in order to be capable to use these failure criteria.

Thus, the failure is checked for each ply of each element, at each load step by using Eq. (2.4); at the failure detection, the material properties of the failed ply are reduced according to suitable material properties degradation rules [Eq. (2.5)].

It is worth noting that the degradation factor (k) gives only a rough estimation of the stiffness loss. However, a too small value of (k) may lead to problems in numerical stability.

A more sophisticated and realistic choice for the selection of the degradation factor should consider the physical mechanism behind the matrix and fiber degradation. As a matter of facts, a constant value for k , reasonably small, has been demonstrated [39, 40] to be sufficient to ensure the desired material property degradation without affecting the numerical convergence.

As said above, the application of the progressive failure procedure requires the knowledge of the Cauchy stress field in each layer of the layered brick element. The following steps in the B2000 implementation have been followed in order to evaluate the stresses layer by layer:

1. 27 “virtual” integration points, where the 20 element shape functions h are evaluated, have been placed in each layer as shown in Fig. 2.5. Starting from the element Green-Strain nodal values (according to the Total Lagrangian formulation adopted by B2000), the strains in each virtual integration point are

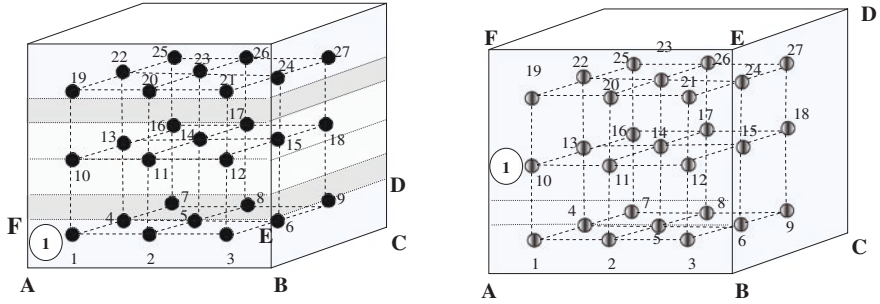


Fig. 2.5 “Virtual” integration points positions in each layer of the 20 nodes brick element

computed [see Eq. (2.10)] by using the shape functions derived directly from the isoparametric formulation of the element.

$$Strain_{VIP}(j) = \sum_{k=1}^{20} h(k)|_{VIP} Strain_{NODAL}(j, k) \quad (2.10)$$

In Eq. (2.10) $j = 1, \dots, 6$ is the index associated to the number of the independent components of the Green-Strain tensor.

The information about the position of a layer through the thickness is introduced by the definition of the coordinates of the “virtual” integration points with reference to the natural coordinate system of the element.

2. The material matrix in global coordinates is computed for each layer by taking into account the layer orientation.
3. The Piola-Kirchhoff stresses in global coordinates are obtained by multiplying the material stiffness matrix by the strains in the 27 “virtual” integration points.

Once evaluated the Piola-Kirchhoff stress tensor layer by layer it is possible to obtain the Cauchy Stress by using Eq. (2.3). It should be noted that the deformation gradient is evaluated by taking into account the updated nodal coordinates (i.e. coordinates of the nodes in the deformed configuration).

The maximum stress values within each layer are then used to perform the failure check, therefore a ply is considered to be failed if the failure criteria are satisfied in at least one of its virtual integration points. It is a natural consequence of the algorithm itself that the number of information to be stored for each element is huge, although conservative results will be obtained in terms of failure.

2.3.3.2 Interface Fracture Element for Delamination Growth

The calculation of the energy release rates G_I , G_{II} , G_{III} can be performed by using nodal forces and nodal displacements at the delamination front.

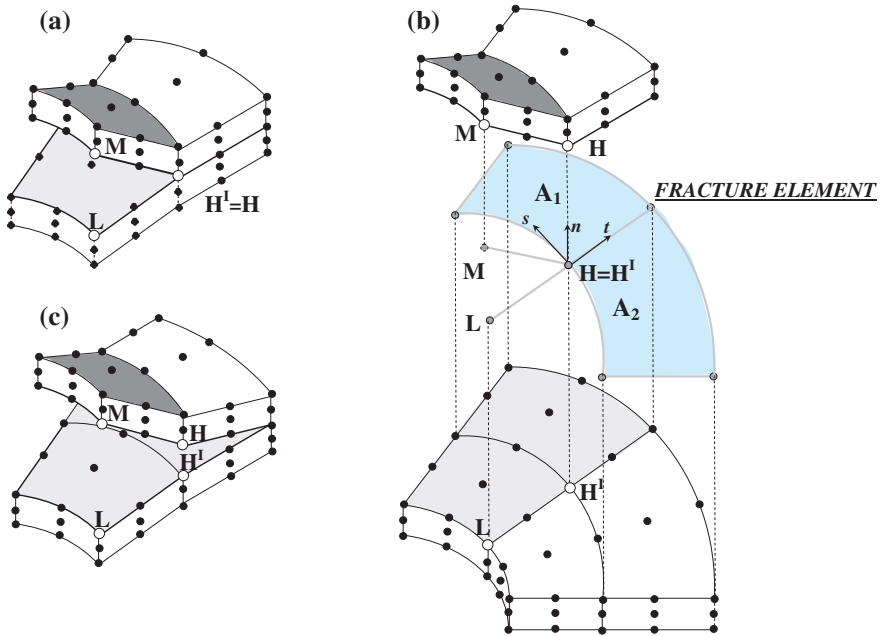


Fig. 2.6 Interface fracture element placed between adjacent sublaminates

In order to perform this kind of evaluation, an interface fracture element has been implemented in B2000 which formulation has been based on the Modified Virtual Crack Closure Technique.

The effectiveness of this interface element has been already proved in Refs. [23, 24] where the growth of circular embedded delaminations and through the width delaminations is simulated. The interface fracture elements are placed between two adjacent blocks of brick elements with their nodes rigidly connected to those of the brick elements.

The energy release rate G associated to the interface elements (see Fig. 2.6) for each failure mode can be computed as:

$$\begin{aligned}
 G_I^H &= \frac{1}{2} \frac{1}{(A_1 + A_2)/2} F_n^H (u_n^M - u_n^L) \\
 G_{II}^H &= \frac{1}{2} \frac{1}{(A_1 + A_2)/2} F_t^H (u_t^M - u_t^L) \\
 G_{III}^H &= \frac{1}{2} \frac{1}{(A_1 + A_2)/2} F_s^H (u_s^M - u_s^L)
 \end{aligned}
 \tag{2.11}$$

where (t, s, n) is the interface element local coordinate system, H is the node where forces (F) are computed, M-L are the nodes where displacements u are calculated, A1 and A2 are the surfaces surrounding the interface fracture elements.

The two nodes H and H' of the fracture element belong to the adjacent free surfaces induced by the delamination into a composite laminate. Thus, even if placed in the same location, these nodes are not merged and, within the fracture element, they are connected to each other by using high stiffness springs. If the criterion in Eq. (2.4) is satisfied, the propagation of the delamination front, simulated by reducing the stiffness of the spring between H and H' , will cause the debonding of adjacent elements and the consequent modification in the delaminated area.

2.3.3.3 Contact Element

Contact phenomena can become relevant especially in delaminated region in post-buckling regime: 3D node to node contact elements have been introduced [23, 24] in the B2000 FEM code in order to avoid overlaps between two contacting surfaces.

The implemented contact elements are based on the penalty method: the penalty formulation assumes that the contact force between the nodes placed on two contacting surfaces is a linear function of their interference (or GAP). This linear proportionality is expressed by means of the penalty constant α [see Eq. (2.12)]:

$$|F_C| = \alpha |GAP| \quad (2.12)$$

Adopting such a formulation, given a contact force F_C , obtained from the equilibrium equation, it is possible to obtain a small interference between the two contact surfaces by introducing relatively high values of the penalty constant α . A small interference between contacting surfaces is suitable in order to correctly represent the contact phenomena.

When considering node to node contact elements, the linear relation (2.12) involves separated couples of nodes where each node represents a contact interface. Hence, there's no need to interpolate between nodes to find the contacting surface, heading to a considerably reduction of computational cost. However this approach leads to reduced accuracy in simulating contact phenomena when contact surfaces undergo relevant sliding during the analyses.

As well as the selection of the degradation factor in the matrix-fiber damage propagation, the choice of the penalty constant α is the major weak point of the penalty method: big overlapping and convergence problems can derive from an inaccurate selection of the α value.

It is important to emphasize that contact capabilities are also implemented in the interface fracture element in order to prevent structural overlaps between delaminated region.

2.3.4 Numerical Tool for Intra-laminar Damage and Delamination Growth

Based on the numerical implementations described in the previous section a progressive damage/delamination growth procedure has been developed. The flowchart of this procedure is shown in Fig. 2.7.

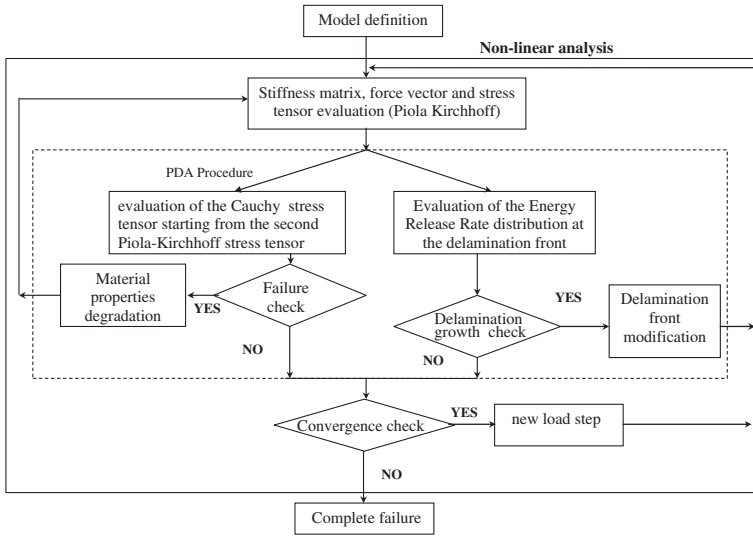


Fig. 2.7 Flowchart of the numerical procedure

According to the flowchart of Fig. 2.7, following the model definition (geometry, mesh, boundary conditions, material properties, loads), the element matrices are computed. Then two parallel branches are respectively defined for the progressive damage and the delamination growth.

The onset of intra-laminar damage is detected using failure criteria (Hashin). These require the determination of stresses (Cauchy stress) and strains for each ply. If the failure is detected, the stiffness of the failed ply is reduced to a percentage of its undamaged value by means of suitable material properties degradation rules and the laminate re-analysed to check whether the remaining plies may still withstand the load. Then the load is incremented until the next ply fails. When the load cannot be carried anymore ultimate failure occurs (structural collapse).

At the same time, in the other branch of the flowchart the algorithm for the analysis of the delamination growth is shown: the energy release rate of the undamaged/damaged structure at the delamination front is computed, later the linear criterion in Eq. (2.6) checks the delamination growth and the delamination front is eventually modified by releasing nodes as shown in Figs. 2.6 and 2.8.

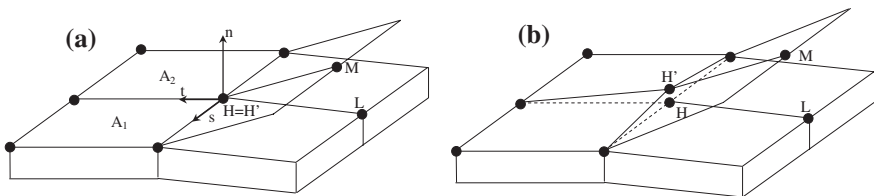


Fig. 2.8 Interface fracture element

Three models with different degree of complexity have been used for the numerical validation of simulations presented in Sect. 2.4.

1. *Delamination growth not allowed.* This FE model, which does not comprise interface fracture elements and matrix-fiber damage propagation capabilities, will be identified with the acronym B2000-DEL-NO-GROWTH.
2. *Delamination growth allowed.* This FE model includes interface fracture elements but does not take into account matrix-fiber damage propagation capabilities. The acronym that will be used for this model is B2000-DEL-GROWTH.
3. *Delamination growth allowed plus progressive damage.* Interface fracture elements and layered brick elements with matrix-fiber damage propagation capabilities are used in this FE model which will be named B2000-DEL-GROWTH-PDA.

By comparing results obtained by means of these approaches, the effects of intra-laminar damage on inter-laminar damage have been evaluated.

2.3.5 Benefits and Limitations of the Method and Added Value with Respect to the State of the Art

The added value of the proposed methodology with respect to state of the art numerical models is the opportunity to analyse the effects of intra-laminar and inter-laminar damage interactions, by adopting brick (allowing the correct computation of the three dimensional stress within the material) layered elements (with PDA capabilities) and interface fracture elements simultaneously. Furthermore, the implementation of the numerical tool in the B2000 code has made possible to simulate the post buckling behaviour of damaged structure by using the continuation method developed by Riks [56] for non-linear analyses. An high accuracy in the stresses evaluation is essential both for the intra-laminar damage (failure check and stress redistribution caused by failed elements) and for the inter-laminar damage (for the evaluation of the stress state at the delamination front and therefore for the Energy Release Rate distribution) simulation. Unfortunately an high computational cost is associated to each analysis when using brick elements.

The proposed approach still relies on simplified material properties instantaneous degradation rules which are not based on the physics of damage. Furthermore, even if very effective for undamaged structure, the continuation method still doesn't take into account the progressive damage of the material for the determination of the time step size of the non-linear analysis.

Even in presence of these limitations (in terms of simplified assumption on the behaviour of the material and time step size) a very good agreement has been found between literature data and numerical results obtained thanks to the proposed methodology (see Sect. 2.4).

2.4 Validation of the Developed Numerical Tools: B2000 Applications

For the validation of the developed approaches presented in Sect. 2.3, two benchmarks have been chosen: A tension loaded laminate with hole for the validation of the PDA approach and a composite panel with a circular embedded delamination under compression to study the interaction between intra-laminar and inter-laminar damage.

2.4.1 Tension-Loaded Laminate with Hole

A 20-ply tensile specimen containing a circular hole has been considered to validate the intra-laminar Progressive Damage Approach proposed in this chapter. The stacking sequence is $[0/(\pm 45)_3/90_3]_S$. The specimen is clamped at one edge and loaded in tension on the other one. Material properties and geometric characteristics are shown in Table 2.1 and Fig. 2.9.

As schematically shown in Fig. 2.10, the PDA elements have been used for discretization of the area with stress concentration (region near the hole). The rest of the specimen has been meshed with standard non-linear hexahedral 20 node elements (based on the Bathe’s theory) and available in the standard B2000 version: this meshing strategy has been adopted in order to reduce the computational time needed for the simulations (Fig. 2.10).

Table 2.1 Material properties

T300/1034-C graphite/epoxy			
E_{11}	$1.4690 \text{ e} + 05 \text{ N/mm}^2$	X_T	$1.731 \text{ e} + 03 \text{ N/mm}^2$
E_{22}	$1.12790 \text{ e} + 04 \text{ N/mm}^2$	X_C	$1.379 \text{ e} + 03 \text{ N/mm}^2$
ν_{12}	0.3	Y_T	$6.655 \text{ e} + 01 \text{ N/mm}^2$
G_{12}	$6.186 \text{ e} + 03 \text{ N/mm}^2$	Y_C	$2.683 \text{ e} + 02 \text{ N/mm}^2$
		S	$1.338 \text{ e} + 02 \text{ N/mm}^2$

Fig. 2.9 Geometry, boundary condition and loads description—tension-loaded laminate with hole

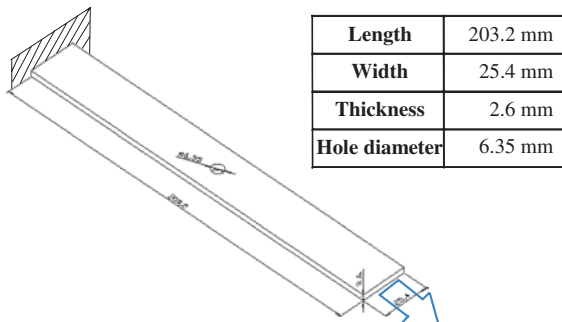
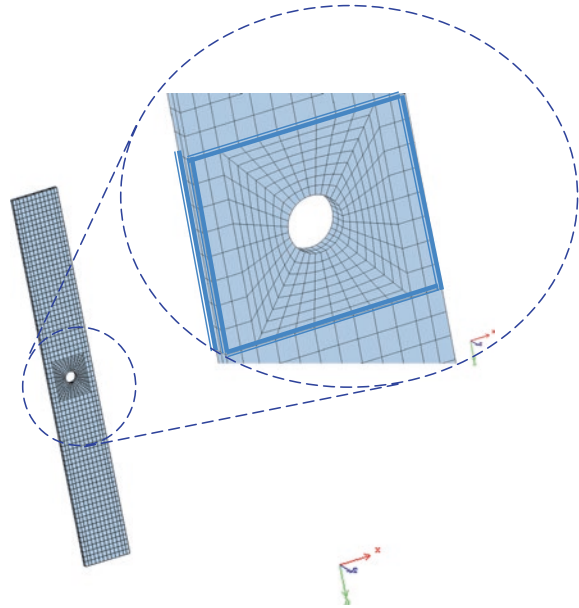


Fig. 2.10 Mesh description—tension-loaded laminate with hole



Literature results for this test case are available in [57–59] and employed to perform appropriate comparisons. The result of the B2000/PDA tool in terms of final failure load is in excellent agreement with the numerical results of Ref. [57] obtained by using the Hashin criterion and the Christensen’s criteria and with the experimental data. In the following table the first ply failure and the final failure load levels evaluated by means of the above mentioned procedures are shown in Table 2.2.

The first ply failure has been detected at 5,711 N within the 90° plies while the others plies remain undamaged until they reach the 6,394 N load level.

The final failure load has been predicted with a 3 % error level with respect to the experimental one. Experimental results are available only for the final failure load.

Data sets have been created in order to monitor the progressive failure in each ply of each element during the loading process: the matrix cracking, the

Table 2.2 First-ply and final failure load—tension-loaded laminate with hole

	Final failure		First ply failure
	Final failure load (N)	Error evaluation (with respect to experimental results) (%)	First ply failure load (N)
Numerical result [57] Hashin’s criterion	14,293.4	8.83	6,764
Numerical result [57] Christensen’s criterion	14,511.45	7.44	6,764
PDA/B2000	16,147.52	3	5,711
Experimental results [57–59]	15,677.37		N.A.

fiber breakage and the cracking of both fiber and matrix have been stored. Representative values for the BASPL ++(that is the B2000 postprocessor) visualization are shown in Table 2.3.

The damage distribution in each ply at final failure is shown in Fig. 2.11

Table 2.3 Representative values for the damage visualization in B2000/BASPL++

Failure mode	BASPL ++ representative number
Undamaged ply	2
Matrix failure	5
Fiber failure	6
Shear-out + fiber + matrix failure	7
Kinking failure	8
Shear-out + matrix failure	9
Matrix + fiber failure	10
Completely failed ply	11

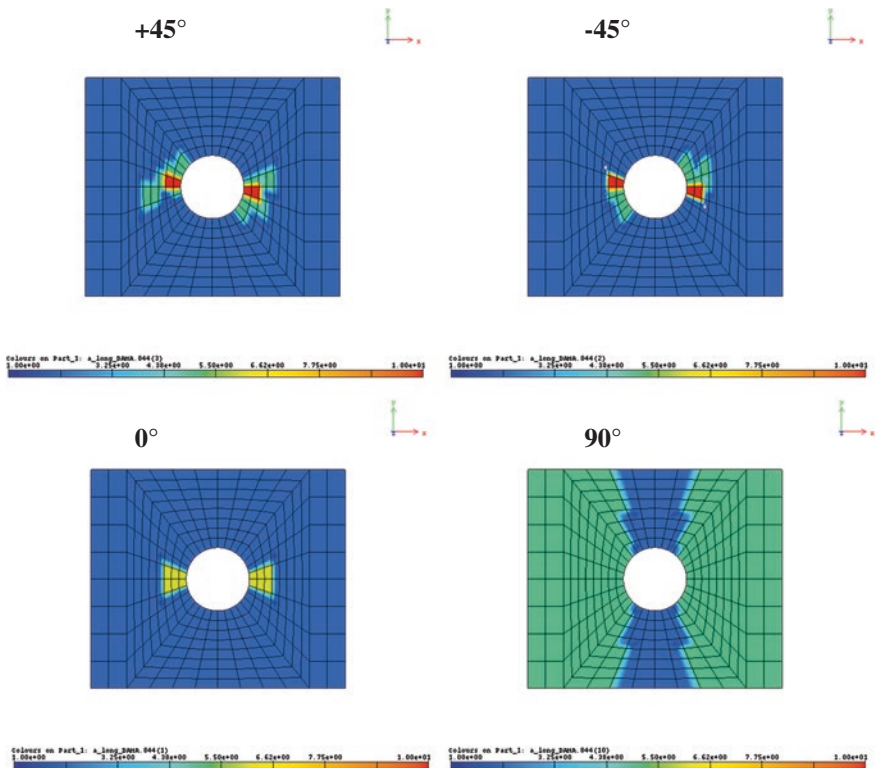


Fig. 2.11 Damage of each ply—tension-loaded laminate with hole

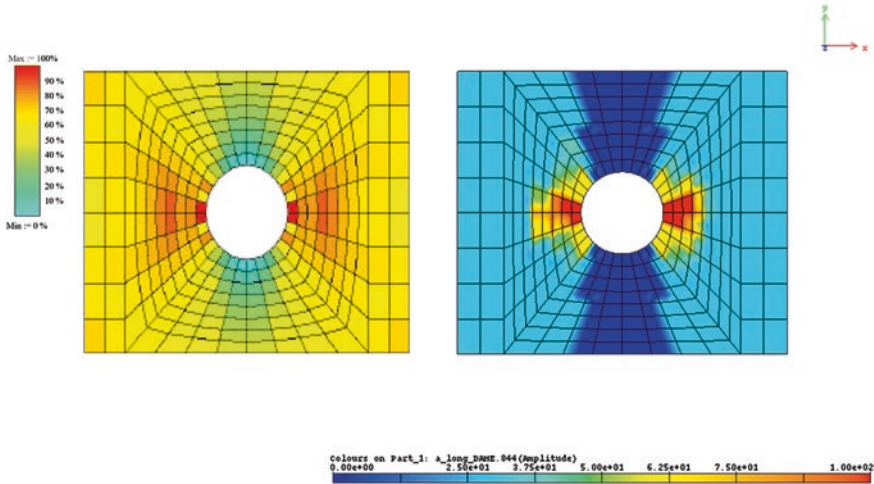


Fig. 2.12 Damage detected at failure load: percentage of damaged plies along the thickness. Comparisons between B2000/PDA and literature results—tension-loaded laminate with hole

A comparisons between B2000/PDA and literature results, in term of damaged plies percentage along the thickness, is shown in Fig. 2.12.

In Fig. 2.13 is possible to follow the damage evolution starting from the first failure detection up to the final failure (in this case the value scale is starting from 10 up to 100 %).

2.4.2 Composite Delaminated Panels Loaded in Compression

The composite panels geometrical and material configurations, used for the validation of the developed numerical tools, have been taken from [9] where the experimental results for cross-ply carbon fiber/epoxy laminated panels with an implanted artificial delamination are reported. A schematic representation of the analysed panels geometry is given in Fig. 2.14.

Only one quarter of the structure (shown in Fig. 2.14 as A, B, C, D) has been considered for the numerical simulations thanks to the conditions of symmetry with respect to the x and y axes of geometry, boundary conditions and applied loads. The stacking sequence of the laminate is $[(90^\circ/0^\circ)_{17}/90^\circ]$ and the ply material properties are shown in Table 2.4.

A delamination, with a radius of 30 mm, is placed in three different positions through the thickness. The three panel configurations, identified by #SS3, #SS4 and #SS5 are detailed in Table 2.5.

The compression load has been simulated by applying a displacement along the x-axis (see Fig. 2.14). The panels have been modeled by using the 20-nodes layered brick elements: this element type has 3 degrees of freedom at each node

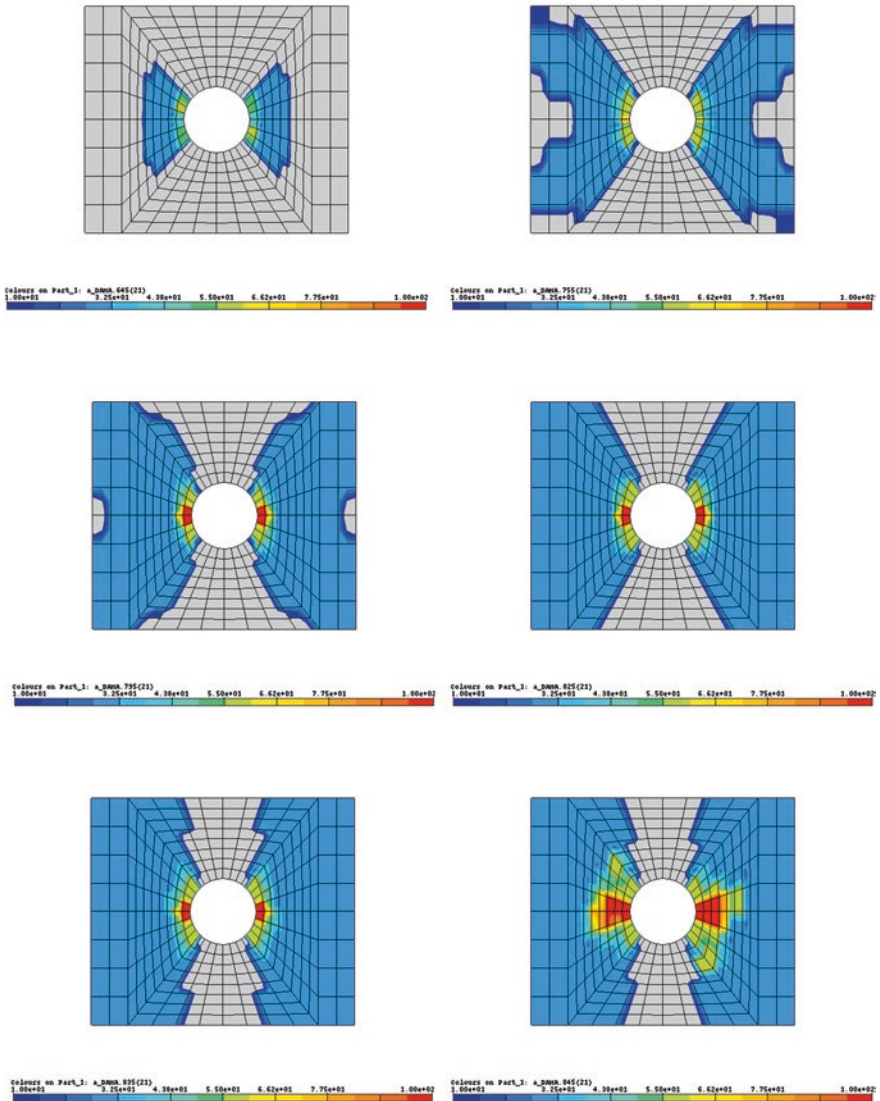


Fig. 2.13 Damage evolution—tension-loaded laminate with hole

therefore the boundary conditions applied to the quarter of structure represented in Fig. 2.15 are the ones shown in Table 2.6.

It should be noted that the out of plane displacement of all the nodes in the FEBC volume has been constrained in order to simulate the clamping of the specimen's tabs to the test machine [9].

Fig. 2.14 Panels geometry, dimensions (mm) and direction of the applied load—composite delaminated panels loaded in compression

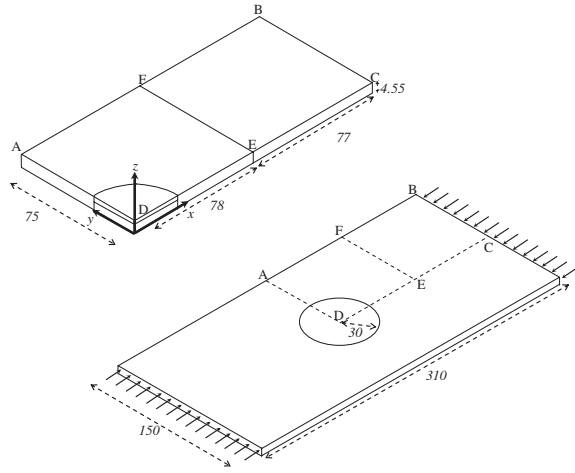


Table 2.4 Material properties

Material ply thickness	t	0.13 mm
Longitudinal young's modulus	E_{11}	146 GPa
Transverse young's modulus	E_{22}	10.5 GPa
Shear modulus	$G_{12} = G_{13}$	5.25 GPa
	G_{23}	3.48 GPa
Poisson's ratio	$\nu_{12} = \nu_{13}$	0.3
	ν_{23}	0.51
Longitudinal tensile strength	X_T	1730 MPa
Transverse tensile strength	Y_T	66.54 MPa
Longitudinal compression strength	X_C	1379 MPa
Transverse compression strength	Y_C	268.21 MPa
In-plane shear strength	S	133.763 MPa
Critical strain energy release rate for mode I	G_{IC}	200 J/m ²
Critical strain energy release rate for mode II	G_{IIC}	570 J/m ²

Table 2.5 Delamination position through the thickness—composite delaminated panels loaded in compression

Specimen ID	Stacking sequence (// indicates the delamination position)	Distance of delamination from panel bottom surface (mm)	Delamination radius (mm)
SS#3	[90°/0°/90°//((0°/90°) ₁₆]	4.16	30
SS#4	[90°/(0°/90°) ₂ //((0°/90°) ₁₅]	3.9	30
SS#5	[90°/(0°/90°) ₃ //((0°/90°) ₁₄]	3.64	30

Fig. 2.15 Adopted finite element discretization. Delamination area (zone I) and growth area (zone II)—composite delaminated panels loaded in compression

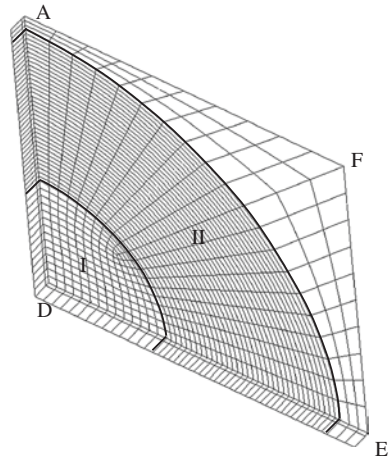


Table 2.6 Boundary conditions—composite delaminated panels loaded in compression

Lateral surface (with ref. to Fig. 2.14)	Condition
AD	$U_x = 0$ (symmetry b.c.)
AF and FB	Free
DE and EC	$U_y = 0$ (symmetry b.c.)
BC	Applied displacement U_x
FEBC	$U_z = 0$

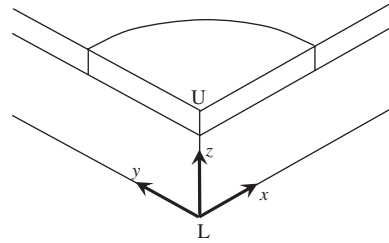
Two layered brick element types have been adopted:

- standard 20-noded layered brick element
- 20-noded layered brick element with matrix-fiber damage propagation capabilities

In order to reduce the computational cost associated with the analyses, the adoption of the modified 20-noded layered brick element has been limited to the area surrounding the delamination. Hence, the volume AFED (Fig. 2.14) has been meshed with 20 nodes brick elements with matrix-fiber damage propagation capabilities, while the volume named FBCE has been meshed with standard elements.

The interface fracture elements, introduced and described in detail in the previous section, have been positioned in the ring area (Fig. 2.15—Zone II) around the delamination to simulate the delamination growth phenomena. The dimensions of this area have been appropriately chosen to allow the delamination growth simulation until the structural collapse. Node to node contact elements, based on the previously introduced theory, have been placed in the delaminated area (Fig. 2.15—Zone I) and in the ring area (Fig. 2.15—Zone II) to avoid inter-penetrations between adjacent elements. In Fig. 2.15 the adopted finite element discretization is presented. The dependence of the Energy Release Rate evaluation from the size of the interface fracture elements decreases as the size of interface element

Fig. 2.16 Control points position—composite delaminated panels loaded in compression



decreases choosing an appropriately small time-step. A suitable value for the size of interface elements associated to a proper load-step has been chosen according to the convergence study performed in Ref. [60]. Detailed information on the influence of mesh size and time-step on the evaluation of the Energy release Rate with the Virtual crack Closure Technique approach can be found in [61–65].

In Ref. [9] the experimental data concerning the benchmarks under investigation are presented in terms of out of plane displacement of two corner points (named U and L in Fig. 2.16) placed respectively at the top and at the bottom of the two sub-laminates.

2.4.3 Specimen Configuration #SS3

The B2000-DEL-NO-GROWTH, the B2000-DEL-GROWTH and the B2000-DEL-GROWTH-PDA models have been used for the simulation of the compressive behaviour of the specimen configuration #SS3 (the configuration with the thinnest delamination). The numerical results have been compared with experimental data on the configuration available in [9].

Comparisons in terms of load displacement curves between the numerical results, obtained by means of the different models and the experimental data available in Ref. [9], are shown in Fig. 2.17.

It should be noted that the scatter in experimental data is not reported here since detailed information are provided in Ref. [9]. The overall agreement between numerical and experimental results can be evaluated from Fig. 2.17. The numerical delamination buckling load (10 kN), which is the same for all the three models, slightly overestimates the experimental value 7.26 kN.

The maximum out of plane displacement of the thin sub-laminate found by numerical analyses (1.02 mm) is also slightly over the experimental one 0.89 mm.

In Fig. 2.17, differences among the adopted numerical models appear from the delamination growth initiation up to the global buckling. These differences are presented model by model providing comparisons with the experimental results.

- *B2000-DEL-NO-GROWTH (Delamination growth not allowed—Composite delaminated panels loaded in compression).*

This model does not allow delamination growth and matrix-fiber failure under compressive load. Therefore the carrying-load capability of the structure, evaluated numerically overestimates the one obtained experimentally.

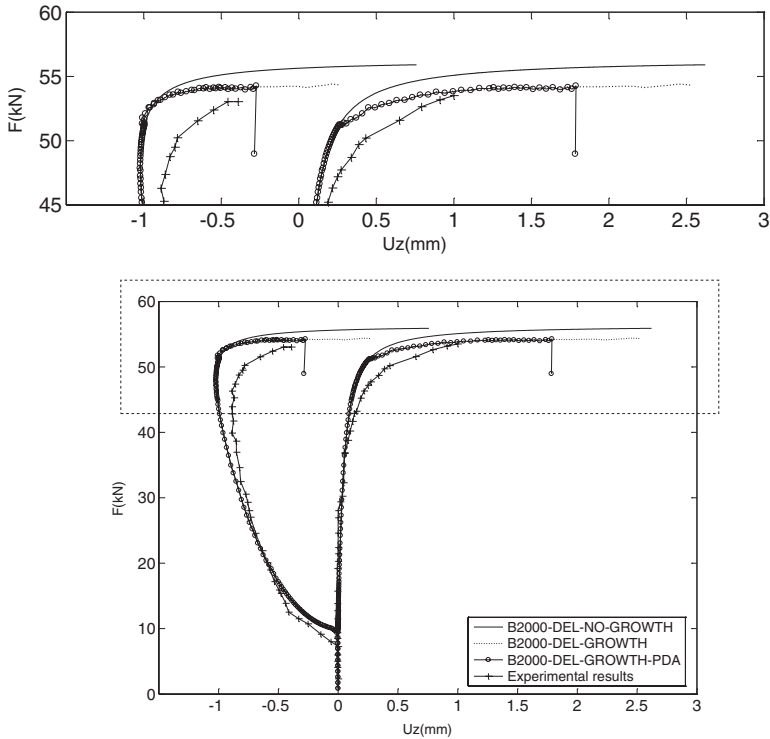


Fig. 2.17 Load displacement graph. Comparison between numerical model and experimental curve—specimen #SS3 [67]—composite delaminated panels loaded in compression

As expected, the global-buckling load predicted by this model (55 kN) overestimates the experimental one (53 kN) due to the lack of both structural stiffness degradation related to delamination propagation and material properties degradation associated to matrix-fiber failure.

The failure of the specimen cannot be simulated with the B2000-DEL-NO-GROWTH model because no failure conditions have been implemented in it.

- *B2000-DEL-GROWTH (Delamination growth allowed—Composite delaminated panels loaded in compression)*

In order to better mimic the physical phenomenology, interface fracture elements, able to simulate the delamination growth, have been introduced in this model. According to this model, when the condition in Eq. (2.6) is satisfied the delamination will start to grow.

The increase in delaminated area, due to compression load, involves a reduction of the structural stiffness and the post buckling regime is quite different from the one obtained with the B2000-DEL-NO-GROWTH model.

In Fig. 2.17, for this model, the load displacement curve shown a clear slope variation at the global-buckling leading to a more accurate prediction of the global buckling load (53.86 kN) which is closer to the experimental one.

Even if the prediction is more accurate with respect to the B2000-DEL-NO-GROWTH model, the specimen failure cannot be correctly predicted by the B2000-DEL-GROWTH model due to the lack of material properties degradation associated to fiber-matrix failure. Indeed the numerical out of plane displacement of the thick sub-laminate at failure (2.5 mm) substantially overestimates the experimental one (1 mm).

- *B2000-DEL-GROWTH-PDA* (*Delamination growth allowed—fiber/matrix progressive damage allowed*)

This last and more refined model is the one allowing delamination growth and matrix-fiber failure. In this case numerical results closest to experimental data have been obtained. The global buckling load (53.70 kN) is the same found with the previous model without matrix and fiber failure. This demonstrates that the matrix-fiber failure phenomenon becomes critical only after the global buckling phenomenon and close to the structural collapse. The out of plane displacements obtained with this last model are the ones that best fit the experimental values.

Indeed this last model provides the best prediction in terms of failure of the specimen: the out of plane displacement of the thick sub-laminate at failure is 1.75 mm. At the structural collapse, the relevant degradation of material properties due to matrix-fiber failure leads to a sudden decrease in the load carry capability of the panel.

For the more refined model (B2000-DEL-GROWTH-PDA), including the delamination growth and matrix-fiber progressive failure, additional numerical results are presented showing the buckling and post-buckling behaviour of the composite panel and the damage propagation during the entire loading process.

The deformed shapes corresponding to the delamination buckling and global buckling load are shown in Fig. 2.18.

This figure highlights the transition from the local delamination buckling to the global buckling of the panel caused by the increase of compressive load. The two conditions shown in Fig. 2.18 can be easily recognized from the schematic description given in Fig. 2.1.

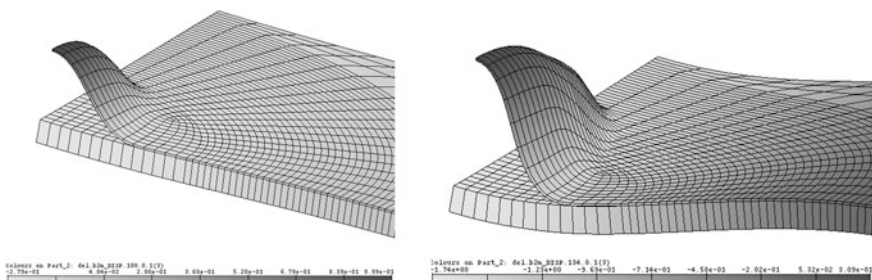


Fig. 2.18 Deformed shape at local delamination and global buckling regime for specimen #SS3. An amplification factor equal to 10 has been used. ($F = 10$ kN and $F = 54$ kN respectively)—composite delaminated panels loaded in compression

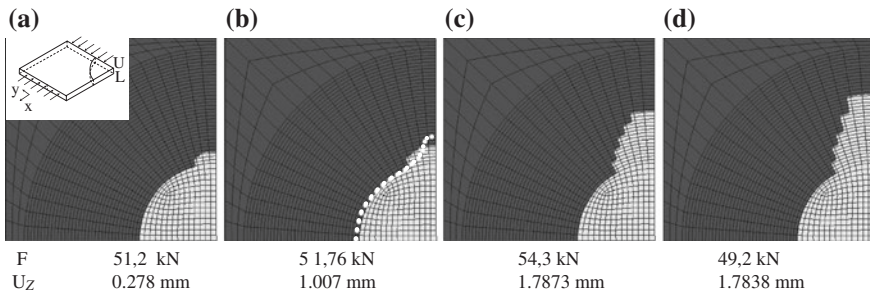


Fig. 2.19 Delaminated area (with zones) starting from delamination growth initiation up to final failure for specimen #SS3. The load and the out of plane displacement of the L point are indicated for each configuration—composite delaminated panels loaded in compression

The delamination propagates perpendicularly to the load direction and the high distortion of the elements near the propagating delamination front is substantial in the global buckling regime. The negligible sliding in the wide contact area near the delamination front along the load direction, pointed out in Fig. 2.18, justifies the adoption of node to node contact elements in the model.

The progressive growth of the delamination can be clearly appreciated in Fig. 2.19.

For the specimen #SS3 the delamination growth initiation has been found at 51.2 kN, very close to the global buckling. The delamination growth initiates along the (y) direction perpendicularly to the applied load direction. As the load increases the portion of the delamination front involved in the growth phenomenon increases.

As already mentioned, the matrix-fiber failure becomes relevant for specimen #SS3 in the final stages of the loading process. In particular, the curve discontinuity of Fig. 2.17 is caused by the sudden failure of a relevant amount of elements that determines the immediate reduction of the structural stiffness due to the instantaneous material properties degradation rules adopted in the progressive damage formulation.

The monitoring of the progressive failure in each ply of each element during the loading process has been carried out. In order to provide a clear representation of the damage status in term of matrix-fiber failure during the loading process, in the next figures, numerical values are associated to a particular failure mode according to Table 2.3.

The failed elements for each ply at load drop (see curve of Fig. 2.17) and at final failure, are shown in Fig. 2.20a, b, respectively. For both the load steps only the damage in upper sub-laminate is shown.

The damage (fiber + matrix failure) onset in the upper sub-laminate takes place close to the delamination front in 90° oriented plies while the 0° plies experience prevalently matrix failures (see Fig. 2.20a). This behaviour can be associated to the high compressive stresses perpendicularly to the load direction at the delamination front.

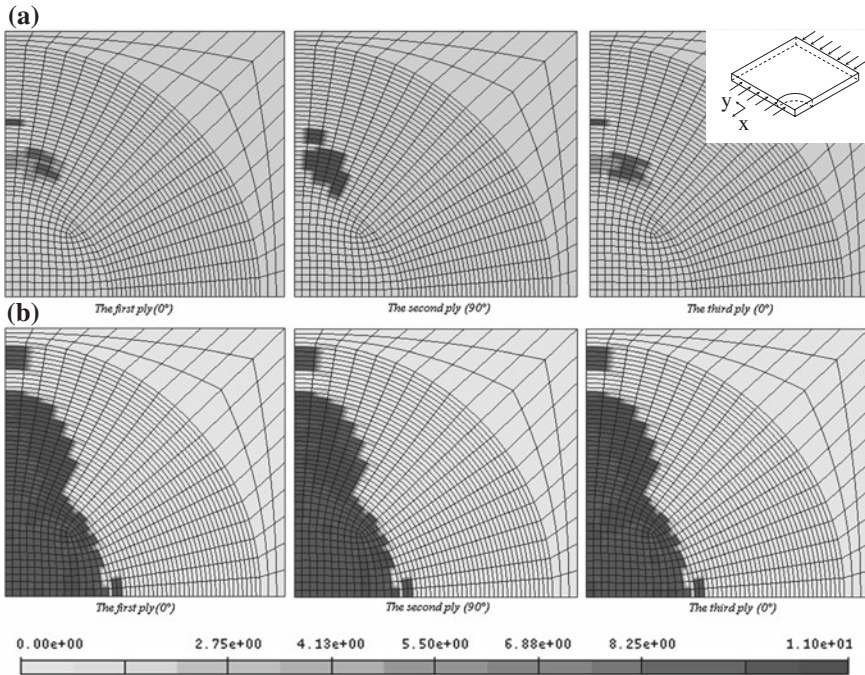


Fig. 2.20 #SS3 failure maps: failure modes for each ply of the upper sub-laminate **a** 54.3 kN, **b** final failure $F = 49.2$ kN—composite delaminated panels loaded in compression

At final failure, the most of elements (see Fig. 2.20b) in the delaminated area are failed (fiber + matrix failure mode) due to the increase of compressive stress at the growing delamination front and due to the tensile stress at the center of the panel.

According to Fig. 2.20b, broken elements can be also found near the edge of the specimen perpendicularly to the load direction. The failure of these elements is caused by the tensile stresses arising as a consequence of the global buckling phenomenon. Therefore the discontinuity in the load displacement curve at failure can be associated to the sudden failure of a relevant number of elements when passing from the failure map of Fig. 2.20a with a few failed elements to the one shown in Fig. 2.20b.

2.4.4 Specimen Configuration #SS4

The B2000-DEL-GROWTH-PDA model has been adopted to simulate the compressive behaviour of the specimen #SS4 (the panel with delamination positioned between the 5th and the 6th ply). The load displacement graph for this specimen is shown in Fig. 2.21.

Except for the local delamination buckling phenomenon, which, probably, has not been adequately detected during the experimental tests, the agreement between

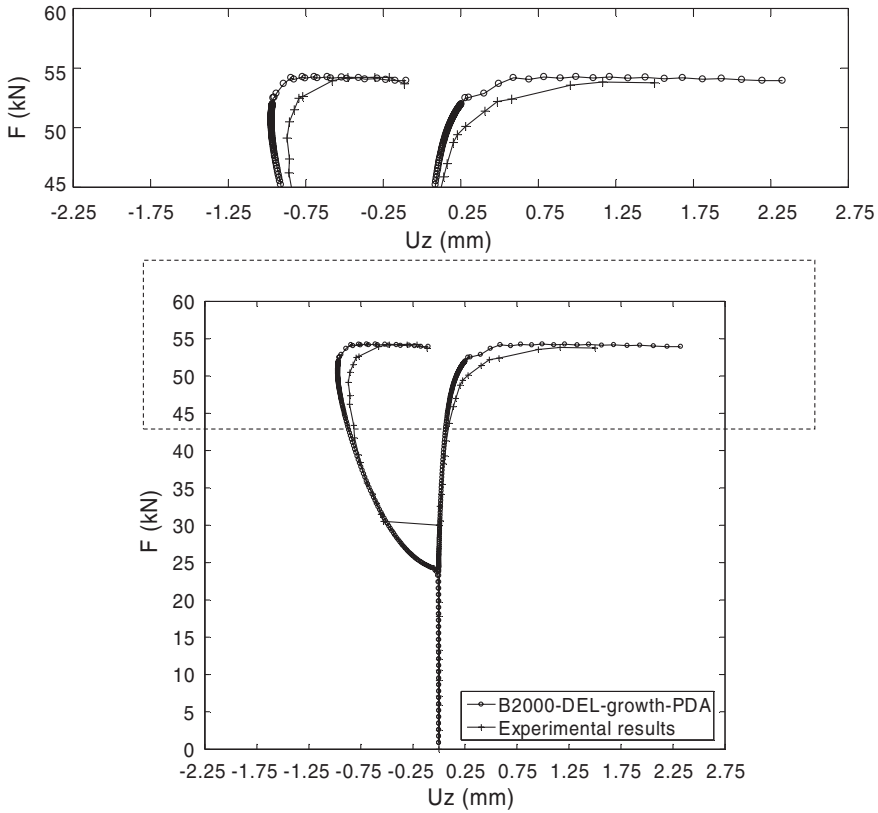


Fig. 2.21 Specimen#SS4 load displacement curve: comparison between numerical model and experimental data—composite delaminated panels loaded in compression

numerical results and experimental data is excellent. The numerical global buckling load (54 kN) matches very well the experimental one (53.9 kN). The numerical failure load (54.9 kN) is also in excellent agreement with the experimental one (53.7 kN). The delamination growth initiates at 52.48 kN very close to the global buckling (see Figs. 2.21 and 2.22).

The propagation of delamination front for specimen #SS4 is very similar to the one observed from specimen #SS3; however the growth is much more pronounced along the applied load direction. Hence, the shape of the growing delamination area is wider than the one observed for the specimen #SS3. This is due to the higher applied load reached at propagation initiation causing higher stress concentrations and a more extended delamination growth front.

As expected, the most of the damage in terms of fibre and matrix breakage, at final failure, was found in the plies oriented at 90° with respect to the direction of the applied load. The damage status in 0° and 90° plies at final failure, for the specimen configuration #SS4, are shown in Fig. 2.23 together with the last computed delamination front.

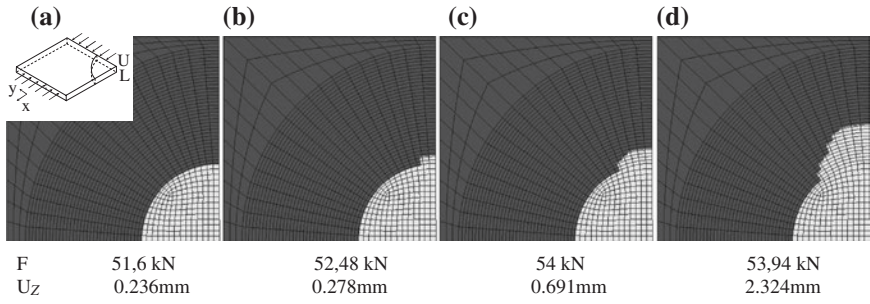


Fig. 2.22 Delamination area (*light zones*) starting from the delamination growth initiation up to the final failure for specimen #SS4—composite delaminated panels loaded in compression

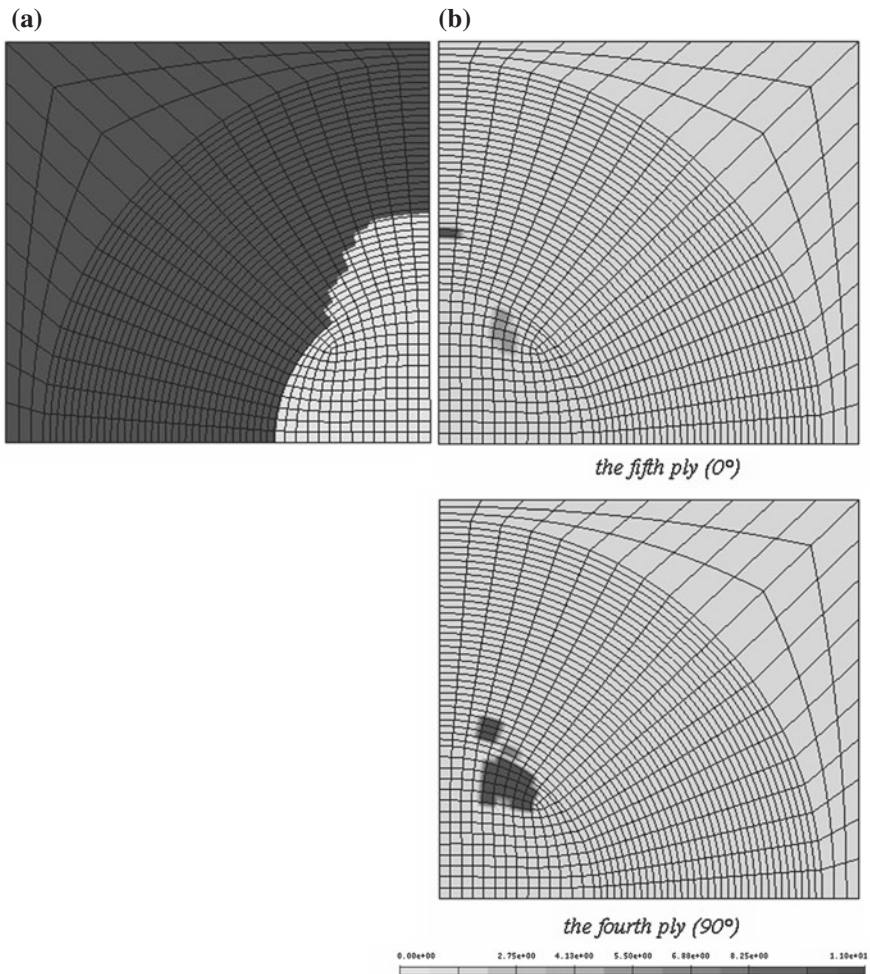


Fig. 2.23 #SS4 Damage visualization in the 0 and 90 ply (b) and the delamination area (a)—composite delaminated panels loaded in compression

2.4.5 Specimen Configuration #SS5

The compressive behaviour of the specimen configuration #SS5 (with delamination positioned between the 7th and the 8th ply) has been simulated by adopting the most refined model allowing growth and matrix-fiber failure propagation (B2000-DEL-GROWTH-PDA). In this case the experimental data do not seem to be completely reliable, as it can be seen in Fig. 2.24 where the load-displacement curve is presented.

The experimental load-displacement curve for the #SS5 specimen is characterized by a negative slope before the local buckling load. This, as specified in [9], is probably due to the adhesion between the delaminated area and the rest of the panel (Teflon insert) and it can be an indication of an imperfect execution of the experimental tests. Even if the structural collapse load is predicted quite well by the numerical simulation, the load-displacement curve is very different from the experimental one (see Fig. 2.24).

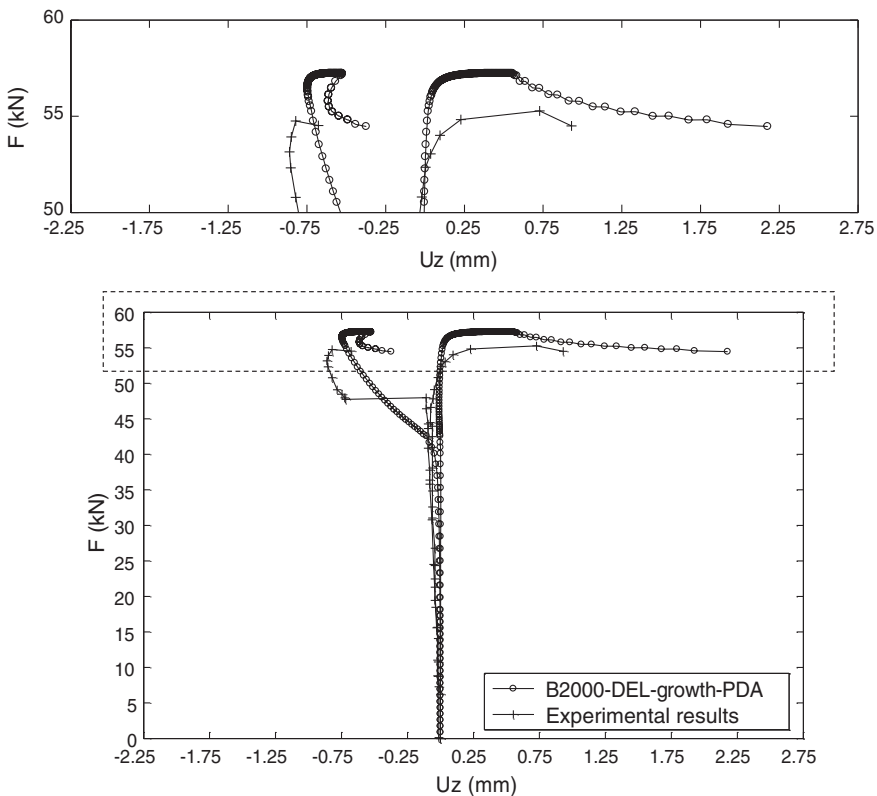


Fig. 2.24 Specimen #SS5: comparison between numerical and experimental curves—composite delaminated panels loaded in compression

The post-buckling behaviour of the #SS5 specimen configuration differs from the others because the load-displacement graph in correspondence of a certain load level (57 kN) shows an inversion in the U point displacement direction.

The apparently strange post-buckling behaviour could be explained as follows: at the global-buckling load the two points U and L are both dragged downwards, this condition is characterized by a significant reduction of the out of plane displacement of the point U caused by a little variation of the applied load.

On the other hand, when the delamination starts to grow, the U point has a displacement upwards while L continues to move downward. Therefore U changes its displacement direction generating a cusp in the graph while the load displacement curve for the L point has no inversion (as shown in Fig. 2.24). The effect of the delamination growth at global buckling for the specimen configuration #SS5 is schematized in Fig. 2.25 where the two conditions before and after the growth are shown.

The variation of delaminated area during the load application is shown (see Fig. 2.26) starting from the incipient global buckling condition (57.216 kN) up to the structural collapse (54.42 kN). Once again, the delamination front moves perpendicularly to the load direction. However for this specimen the propagation involves a more consistent portion of delamination front with respect to the specimen configurations #SS3 and #SS4.

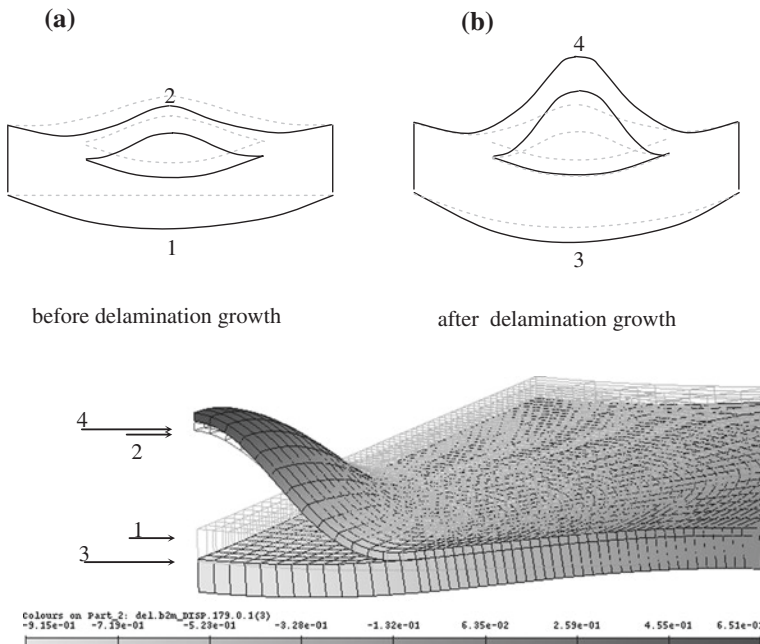


Fig. 2.25 Schematic representation of the load-displacement behaviour for the #SS5 specimen and comparison with the out of plane displacement obtained for configuration (a) and (b)—Composite delaminated panels loaded in compression

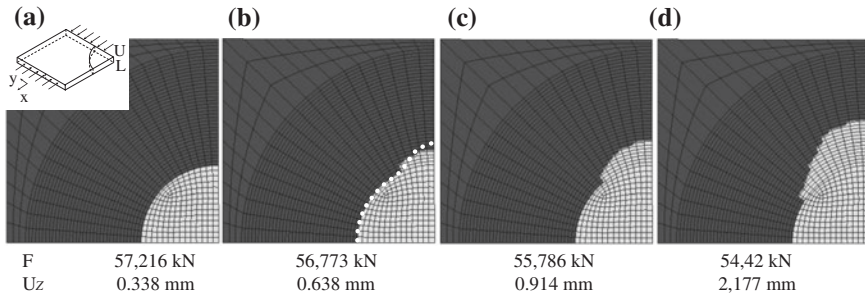


Fig. 2.26 Delamination area (*light zones*) starting from delamination growth initiation up to the final failure for specimen #SS5 (for configuration (b) also the experimental delamination shape is shown)—Composite delaminated panels loaded in compression

Only four plies over seven in the upper sub-laminate have been found damaged. It can be emphasized that the damaged plies are those on the outer parts of the upper sub-laminate.

For this specimen configuration the number of damaged elements is lower than in the other analyzed cases. The damage map obtained for the seventh ply shows failed elements on the portion of delamination front where the upper sub-laminate returns in contact with the lower sub-laminate (due to the orthotropy of composite plies): the same condition has been already found for the specimen configuration #SS4 and shown in Fig. 2.23.

2.5 ABAQUS™ Exploratory Applications: Stiffened Panels with Embedded Delaminations and a Skin-Stringer Debonding

In this section, in order to emphasize the need, when designing with composites, for improved novel numerical approaches taking into account inter-laminar and intra-laminar damage interaction (as the ones described in Sect. 2.3), some exploratory applications on stiffened composite panels with the ABAQUS FEM code are introduced.

Two different configurations of stiffened composite panels have been considered. The first configuration is characterized by a delamination located in the middle of the bay while the second one has an artificial skin-stringer debonding positioned in the center of the first stiffener. The local buckling, the global panel buckling and the inter-laminar and intra-laminar defects growth have been investigated. The standard ABAQUS™ VCCT approach and a progressive damage approach in solid shell elements (not able to fully reproduce the three-dimensional stress state) have been used to perform the numerical analyses. However these ABAQUS exploratory applications, can give a roughly idea of the influence of the

damages evolution and their mutual interaction on the loading carrying capability of real composite structures allowing at the same time to assess the promising added value of the proposed novel numerical approaches (validated only for very simple composite specimens) if extended to the prediction of the evolution of delamination and skin-stringer debonding in complex composite structures.

2.5.1 Simulating the Damage Onset and Evolution in ABAQUS

In this sub-section, a brief description of the models adopted in ABAQUS™, respectively, for the inter-laminar and intra-laminar damage onset and evolution will be provided.

2.5.1.1 Inter-laminar Damage

In ABAQUS™, the inter-laminar damages can be modeled using contact surfaces. The Virtual Crack Closure Technique (VCCT) equations can be adopted to calculate the Energy Release Rate (ERR) along the delamination front for each pair of nodes. In general case the fracture criterion is defined as:

$$f = \frac{G_{equiv}}{G_{equivC}} \geq 1.0 \quad (2.13)$$

where G_{equiv} is the equivalent strain energy release rate calculated at a node, and G_{equivC} is the critical equivalent strain energy release rate calculated based on the user-specified mode-mix criterion and the strength of the interface. The software provides several growth criteria, one of the most used is the Power Law:

$$\frac{G_{equiv}}{G_{equivC}} = \left(\frac{G_I}{G_{IC}} \right)^{a_m} + \left(\frac{G_{II}}{G_{IIC}} \right)^{a_n} + \left(\frac{G_{III}}{G_{IIIC}} \right)^{a_0} \quad (2.14)$$

where G_j is the Energy Release Rate associated to the fracture mode j and G_{jc} is the critical value of the Energy Release Rate associated to the fracture mode j . Indeed three main fracture modes can be defined: opening mode I, forward shear mode II and parallel shear mode III. In case of 4-noded solid element the VCCT equations for the calculation of the Energy Release Rate can be written as follows:

$$G_j = \frac{F_j \Delta u_j}{2 \Delta A} \text{ with } j = I, II, III \quad (2.15)$$

In Eq. (2.15) F_j is the force at delamination tip for the fracture mode j , Δu_j is the opening displacement for the fracture mode j and ΔA is the crack surface created by the delamination opening. The critical energy release rate values (G_{IC} , G_{IIC} and G_{IIIC}) can be evaluated from standard experimental procedures.

In this work the Power Law criterion is used in the linear form with $a_m = a_n = a_0 = 1$. The crack-tip pair of nodes are separated when the fracture criterion, f , reaches the value 1.0 within a given tolerance:

$$1 \leq f \leq 1.0 + f_{tol} \quad (2.16)$$

If $f \geq 1.0 + f_{tol}$ the time increment is reduced such that the crack propagation criterion (2.14) is satisfied. For the analyses presented in this work the default value ($f_{tol} = 0.1$) has been used.

2.5.1.2 Intra-Laminar Damage

In ABAQUSTM the onset of intra-laminar damage is determined by the initiation criteria proposed by Hashin and Rotem [32, 33]. Four different damage mechanisms are considered: fiber tension, fiber compression, matrix tension and matrix compression [see Eq. (2.17)].

$$\begin{aligned} \left(\frac{\sigma_{11}}{X_C}\right)^2 &= 1 && \text{Fiber failure (compression)} \\ \left(\frac{\sigma_{11}}{X_T}\right)^2 + \alpha \left(\frac{\tau_{12}}{S^L}\right)^2 &= 1 && \text{Fiber failure (tension)} \\ \left(\frac{\sigma_{22}}{Y_T}\right)^2 + \left(\frac{\tau_{12}}{S^L}\right)^2 &= 1 && \text{Matrix failure (tension)} \\ \left(\frac{\sigma_{22}}{2S^T}\right)^2 + \left[\left(\frac{Y_C}{2S^T}\right)^2 - 1\right] \frac{\sigma_{22}}{Y_C} + \left(\frac{\tau_{12}}{S^L}\right)^2 &= 1 && \text{Matrix failure (compression)} \end{aligned} \quad (2.17)$$

In Eq. (2.17) the presence of the parameter α allows to take into account the contribution of the shear stress to the fiber tensile initiation criterion. A characteristic length is defined in ABAQUS, in order to reduce the mesh dependency during damage evolution, hence the constitutive law can be expressed in terms of stress-displacement relation. When a damage initiation criterion is satisfied the behavior of the element evolves according to the stress-displacement curve shown in Fig. 2.27.

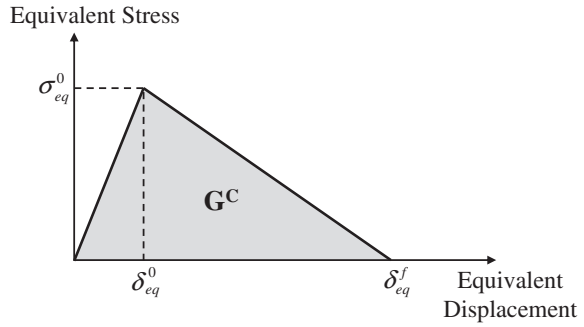
In Fig. 2.27, σ_{eq} and δ_{eq} denote respectively the equivalent stress and the equivalent displacement computed for each of the four damage modes.

The first part of the stress-displacement curve, prior to the damage initiation, is representative of the linear elastic material behavior; the second part with negative slope, after the damage initiation, is associated to the damage evolution. The value of failure displacement (δ_{eq}^f) can be computed using the Eq. (2.18).

$$\delta_{eq}^f = \varepsilon^f L^C = \frac{2G_C}{\sigma_{eq}^0} \quad (2.18)$$

where G_C represents the intra-laminar fracture energy and L^C the characteristic length of the element.

Fig. 2.27 Intra-laminar damage evolution



2.5.2 Stiffened Panel with an Embedded Bay Delamination

In this sub-section, a detailed description of the FEM model of the stiffened composite panel with an embedded delamination will be provided together with all the numerical results of the non-linear analysis.

The geometrical features of the test-case are given in Fig. 2.28; while the material properties of the adopted composite system (HTA-6376C) are summarized in Table 2.7. The stacking sequence of the panel’s skin is $[+45^\circ/-45^\circ/0^\circ/90^\circ]_{3S}$, while the stringers, according to Fig. 2.28, consist of three laminates, each with the following lay-up $[+45^\circ/-45^\circ/0^\circ_3/90^\circ/0^\circ_3/-45^\circ/+45^\circ]$. In this figure, the angle θ adopted to univocally identify a location along the delamination front, is also defined.

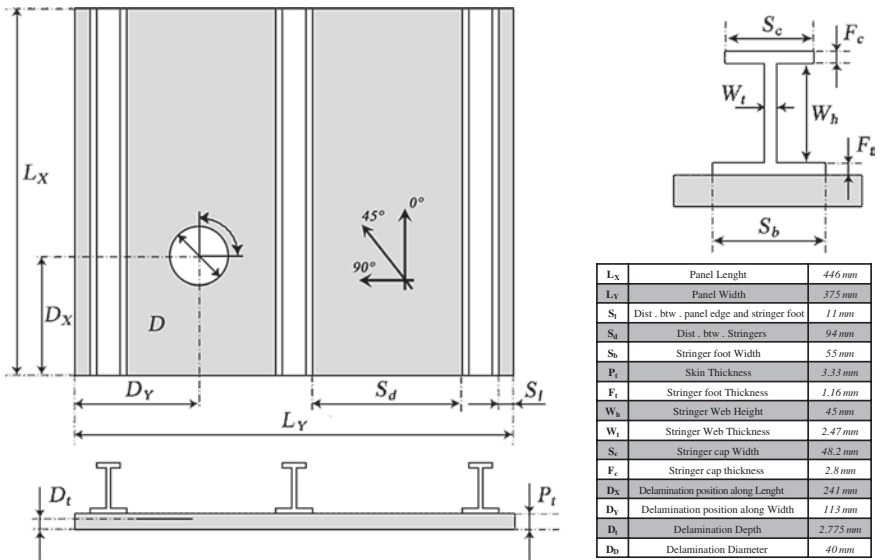


Fig. 2.28 Geometrical description of the delaminated stiffened panel configuration

Table 2.7 Material properties of the composite lamina used for the delaminated stiffened composite panel

HTA—6376C		
E_{11}	140 GPa	Longitudinal young's modulus
E_{22}	10.5 GPa	Transverse young's modulus
$G_{12} = G_{13}$	5.2 GPa	Shear modulus
G_{23}	3.48 GPa	
$\nu_{12} = \nu_{13}$	0.3	Poisson's ratio
ν_{23}	0.51	
X_T	2,100 MPa	Longitudinal tensile strength
Y_T	70 MPa	Transverse tensile strength
X_C	1,650 MPa	Longitudinal compressive strength
Y_C	240 MPa	Transverse compressive strength
S	105 MPa	In plane shear strength
G_{Ic}	260 J/m ²	Critical ERR for mode I
G_{IIc}	950 J/m ²	Critical ERR for mode II
G_{IIIc}	1,200 J/m ²	Critical ERR for mode III
t_1	0.13875 mm	Ply thickness (skin)
t_2	0.112 mm	Ply thickness (web)
t_3	0.127 mm	Ply thickness (cap)
t_4	0.105 mm	Ply thickness (foot)

In Fig. 2.29 the loading and boundary conditions applied to the structure are introduced. The stiffened panel is considered compressed by means of applied displacements allowing the realistic simulation of the displacement controlled experiments. One edge of the panel is clamped while the opposite one is subjected to an applied uniform displacement, maintaining the rotations and the out of plane displacements blocked.

In the specimen under consideration, a circular delamination which diameter is equal to 40 mm, is located in the bay between the fourth and the fifth ply.

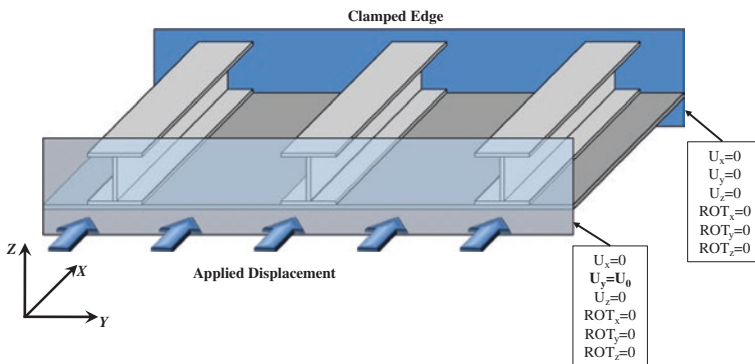


Fig. 2.29 Applied load and boundary conditions—delaminated stiffened composite panel

Fig. 2.30 Solid model representing the delaminated stiffened panel defined in ABAQUS

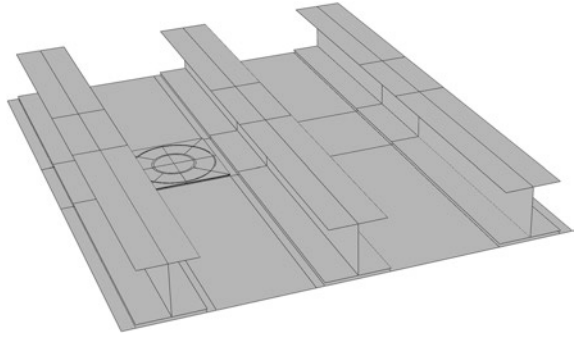


Fig. 2.31 Solid model representing the delaminated region

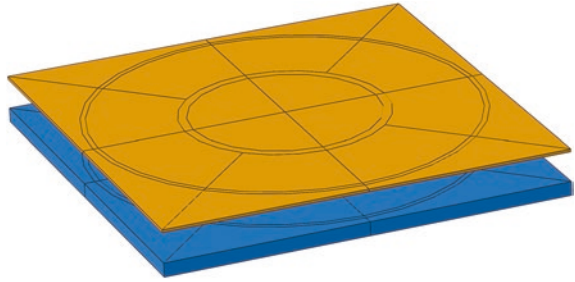
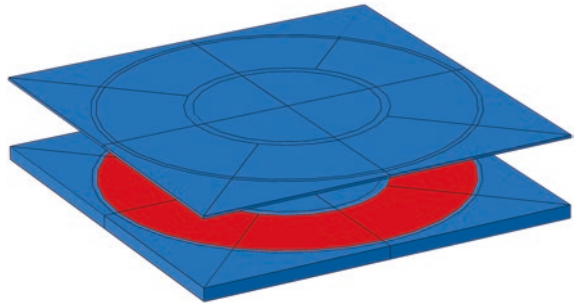


Fig. 2.32 Node-to-surface interaction zone with the option VCCT



The FEM model of the stiffened panel has been created by adopting the commercial FEM software ABAQUSTM, by using a combination of solid and shell elements. The complete geometrical model of the panel is shown Fig. 2.30.

The stringers and the skin have been connected each other by means of the surface to surface constraints “tie” available in ABAQUS [66]. The delaminated region has been modeled by brick volumes aimed to represent the delamination and the surrounding area of the thinner and the thicker sub-laminates (Fig. 2.31).

The sub-laminates have been connected in the region potentially interested by the propagation by node to surface interactions with the option “Virtual Crack Closure Technique”. The surfaces effectively connected are the contacting surfaces between the two parts except the surfaces of the initially delaminated area; as shown in Fig. 2.32.

The delaminated area solid model has been connected to the shell model of the rest of the panel by means of the “solid-shell” coupling. The solid model of the delaminated region has been filled with continuum shell elements SC8R (Continuum shell element with 8 nodes) while the shell element S4R (Shell element with 4 nodes and Reduced integration scheme) has been used for the rest of the model. A representation of the Finite element discretization is shown in Fig. 2.33.

The applied strains as a function of the applied compressive loads is plotted in Fig. 2.34.

In Fig. 2.34 the non-linearity of the global compressive behavior of the stiffened panel is highlighted by comparison with linear analysis. As it can be seen, close to the skin buckling load the non-linear results deviated from the linear trend and the stiffness starts to decrease.

In Fig. 2.35 the global stiffness of the panel as a function of the applied strain is presented. Here the phenomenon of the global buckling is clearly visible and the method adopted for the calculation of the global buckling applied strain is schematically shown.

In Table 2.8, the delamination buckling, the growth initiation load and applied strain, for non-linear analysis are shown.

Fig. 2.33 Abaqus FE model—delaminated stiffened composite panel

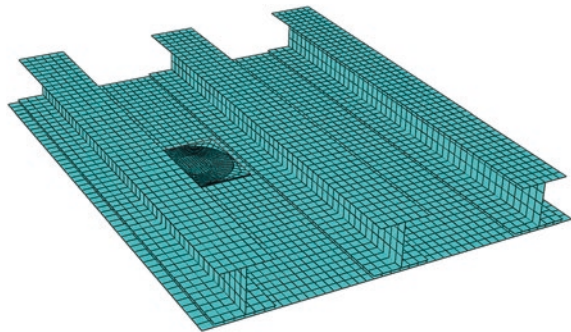


Fig. 2.34 Applied load versus applied strains—delaminated stiffened composite panel

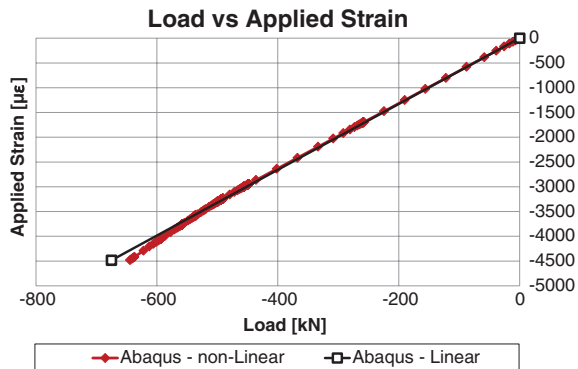


Fig. 2.35 Global panel stiffness versus applied strains—delaminated stiffened composite panel

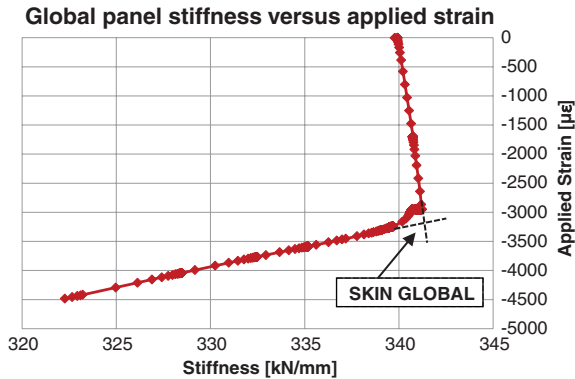


Table 2.8 Results from non-linear analysis with progressive damage—delaminate stiffened composite panel

	Delamination buckling strain ($\mu\epsilon$)	Delamination growth strain ($\mu\epsilon$)	Global buckling strain ($\mu\epsilon$)
Abaqus non-linear	1,700.6	2,952.9	3,242.1

The non-linear buckling analysis has been performed on the selected stiffened panel configuration in order to investigate the structural response of the panel itself when subjected to an incremental compressive load up to the global buckling event. The panel, loaded by means of applied displacements, experiences the delamination buckling, the delamination growth and the buckling of the skin. In Fig. 2.36 the non-linear deformed shapes with out-of-plane displacements contour plot for the analysed stiffened panel obtained at delamination buckling, delamination growth initiation and global skin buckling are presented.

In Fig. 2.37, the non-linear numerical out of plane displacements distributions within the delaminated area, at delamination buckling and growth initiation, are shown for the specimen under consideration.

As expected, due to the very thin delamination, the non-linear delamination buckling contour is identical to the shape of the non-linear buckled sub-laminate contour at the delamination growth initiation. This is an evident proof that the out of plane displacements distribution does not undergo changes from the delamination buckling to the growth initiation event.

The location of maximum Energy Release Rate on the delamination front, predicted by the non-linear approach, is characterised by an inclination (Θ) of about -9° with respect to the global X-axis.

The out-of-plane displacements in the delaminated area are reported in Fig. 2.38.

The delamination buckling phenomenon corresponds to the load step where the front displacement consistently and suddenly increases and it is clearly visible from Fig. 2.38. The delamination growth initiation event with the ABAQUS

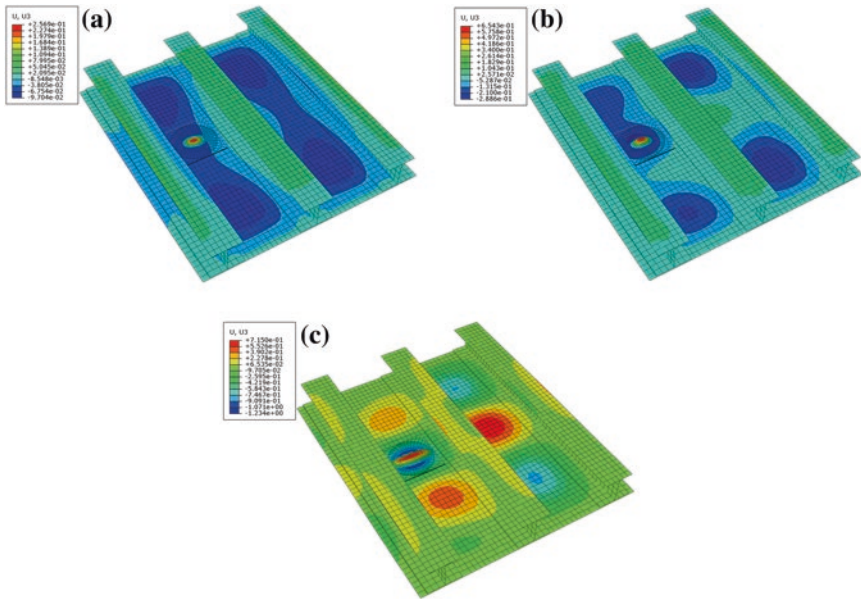


Fig. 2.36 Non-linear deformed shapes at: **a** delamination buckling; **b** delamination growth initiation; **c** global buckling of the skin—delaminated stiffened composite panel

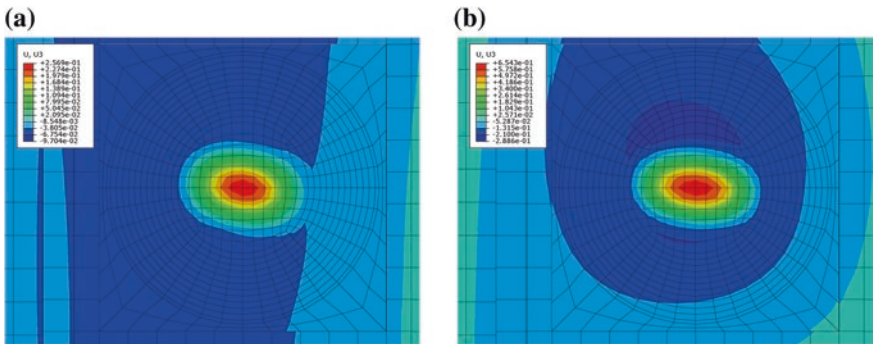
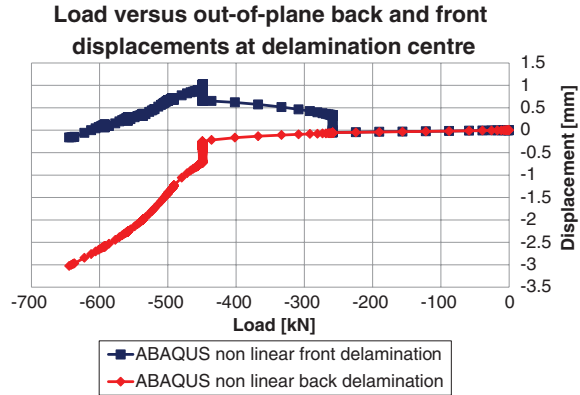


Fig. 2.37 Applied contour plots of the out-of-plane displacements distributions in the delaminated area at: **a** delamination buckling; **b** growth initiation—delaminated stiffened composite panel

non-linear model is located at 2,952 $\mu\epsilon$. The predominant fracture mode, as expected, is the *Mode I*; hence the delamination growth initiation is a consequence of the delamination buckling event. The growth reaches the boundary of the delaminated region at 3,600 $\mu\epsilon$. Beyond this point, the growth results and the results of the analysis in general are no more reliable. This is a limit of this model where the delaminated region (modeled by brick elements) cannot change

Fig. 2.38 Out-of-plane displacement versus applied strain at delamination centre—delaminated stiffened composite panel



size during the analysis. In Fig. 2.39 the delamination growth shapes are shown at delamination growth initiation ($2,952 \mu\epsilon$), at intermediate delamination growth state ($3,200 \mu\epsilon$) and at delamination growth reaching boundaries of the delaminated region ($3,600 \mu\epsilon$).

The distribution of the *ERR* at growth initiation is very useful to understand the location of growth and the contribution of each fracture modes to the growth initiation. The distribution of the *ERR* along the delamination front for the three fracture modes at growth initiation for the ABAQUS non-linear analysis is shown in Fig. 2.40.

Figure 2.41 shows the contour plots, on the thinner sub-laminate of the delamination, of Hashin damage initiation criteria for the four damage mechanisms under consideration: fiber compression, fiber tension, matrix compression and matrix tension. At each integration point of each element, the maximum value reached in the four plies of the thinner sub-laminate has been plotted. A unit value for the Hashin damage initiation criterion means that the criterion is fully met.

As can be appreciated in Fig. 2.41, around the delaminated area only the matrix tension criterion is completely satisfied.

2.5.3 Stiffened Panel with an Skin-Stringer Debonding

In this sub-section, a detailed description of the FEM model of the stiffened composite panel with a skin-stringer debonding will be provided together with all the numerical results of the non-linear analysis.

The geometrical features of the test-case are given in Fig. 2.42 while the material properties of the adopted composites system are given in Table 2.9.

The stacking sequence of the panel's skin is $[0/+45^\circ/-45^\circ/90^\circ]_{2S}$, the stringers foot stacking sequence is $[0/+45^\circ/-45^\circ/90^\circ/90^\circ/-45^\circ/+45^\circ/0]_S$, while the web stringer stacking sequence is $[0/+45^\circ/-45^\circ/90^\circ/90^\circ/-45^\circ/+45^\circ/0]_{2S}$.

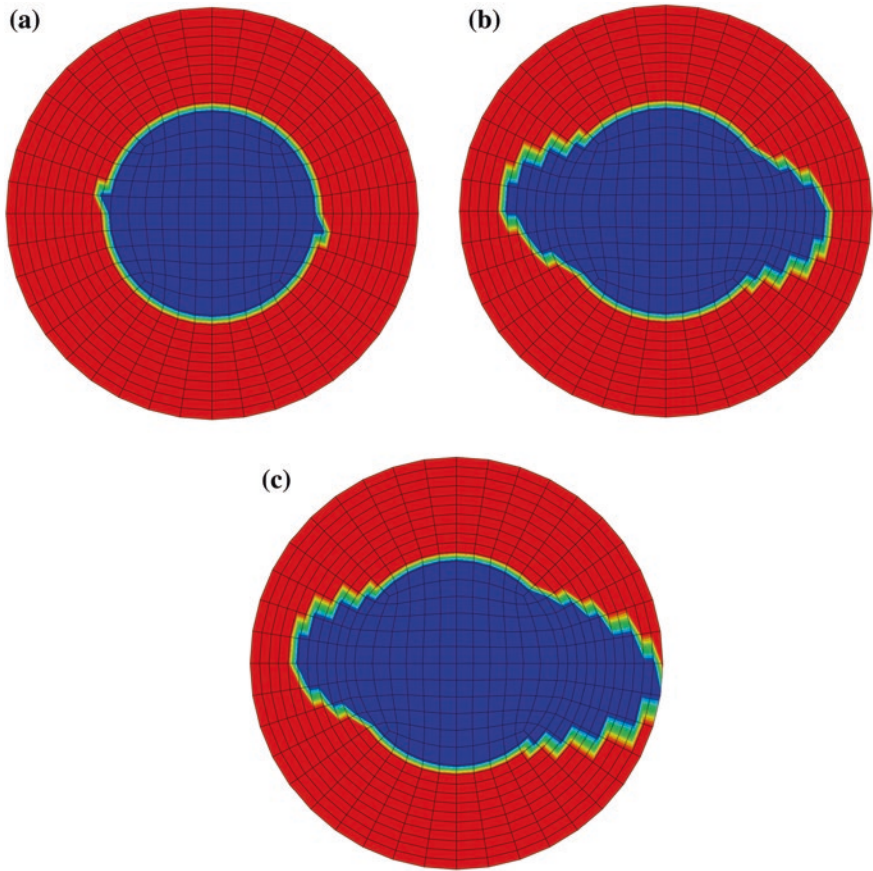
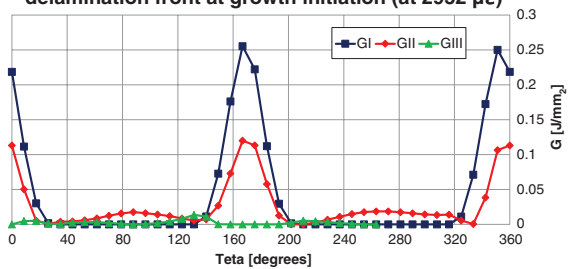


Fig. 2.39 Delamination growth shapes at: **a** delamination growth initiation (2,952 $\mu\epsilon$); **b** intermediate delamination growth state (3,200 $\mu\epsilon$); **c** delamination growth reaching boundaries of the delaminated region (3,600 $\mu\epsilon$)—delaminated stiffened composite panel

Fig. 2.40 ERR distributions for the three fracture modes at growth initiation (2,952 $\mu\epsilon$)—ABAQUS non-linear model—delaminated stiffened composite panel

G mode I, II and III contributions -distribution along the delamination front at growth initiation (at 2952 $\mu\epsilon$)



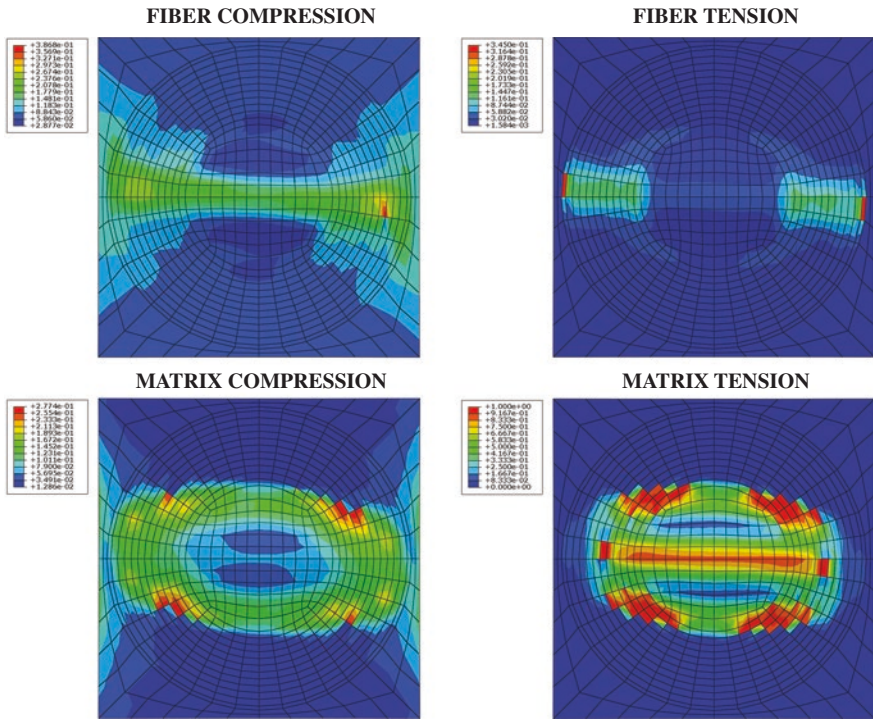


Fig. 2.41 Maximum value of Hashin damage initiation criteria in the thinner sub-laminate—delaminated stiffened composite panel

The boundary conditions of Fig. 2.29 have been applied. In the specimen under consideration, a debonded zone of 250 mm is located at the interface between the first stringer and the skin.

A solid model has been created in ABAQUS with all the surfaced and volumes needed to define the geometry. A picture of the solid model is shown in Fig. 2.43.

The stringers and the skin have been modeled by brick volumes and connected by “tie” surface to surface constraints available in ABAQUS [66]. The debonded zone is shown in Fig. 2.44.

The debonded interfaces have been connected by node to surface interaction with the option “Virtual Crack Closure Technique”. The surfaces effectively connected are the contacting surfaces between the two parts except the surfaces of the initially debonded area; as shown in Fig. 2.45 in red.

The whole solid model of the debonded stiffened panel has been filled with continuum shell elements SC8R (Continuum shell element with 8-nodes).

A representation of the Finite element discretization is shown in Fig. 2.46.

A non-linear buckling analysis has been performed on the selected stiffened panel configuration in order to investigate its structural response under an incremental compressive load up to the global bucking event. The panel, loaded by

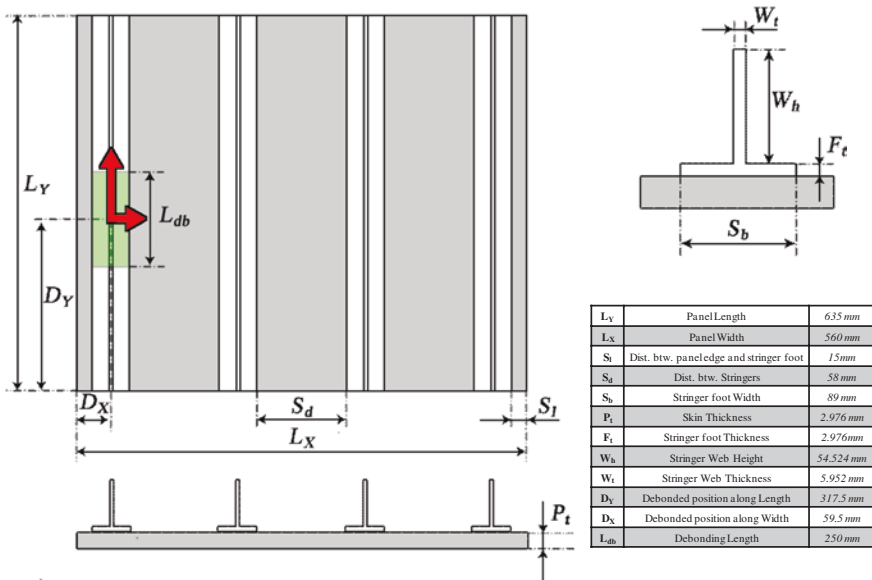


Fig. 2.42 Geometrical parameters of the stiffened panel with debonded stringer—stiffened composite panel with skin-stringer debonding

Table 2.9 Material properties of the composite lamina used in stiffened composite panels

Composite material system		
E_{11}	156 GPa	Longitudinal young's modulus
E_{22}	8.35 GPa	Transverse young's modulus
$G_{12} = G_{13}$	4.2 GPa	Shear modulus
G_{23}	2.52 GPa	
$\nu_{12} = \nu_{13}$	0.33	Poisson's ratio
ν_{23}	0.55	
G_{Ic}	288 J/m ²	Critical ERR for mode I
G_{IIc}	610 J/m ²	Critical ERR for mode II
G_{IIIc}	610 J/m ²	Critical ERR for mode III
t	0.186 mm	Ply thickness

means of applied displacements, experienced the skin local buckling in debonded zone, the debonding growth and the panel global buckling.

In Fig. 2.47 the ABAQUS non-linear deformed shapes at debonding buckling, at debonding growth initiation and at advanced growth state are presented. Unfortunately, the global buckling event cannot be shown because it is significantly delayed with respect to the complete debonding of the stringer.

Fig. 2.43 Solid model representing the stiffened panel defined in ABAQUS—stiffened composite panel with skin-stringer debonding

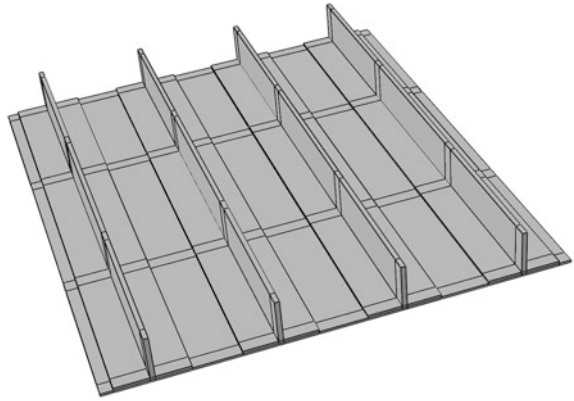


Fig. 2.44 Solid model representing the debonded region—stiffened composite panel with skin-stringer debonding

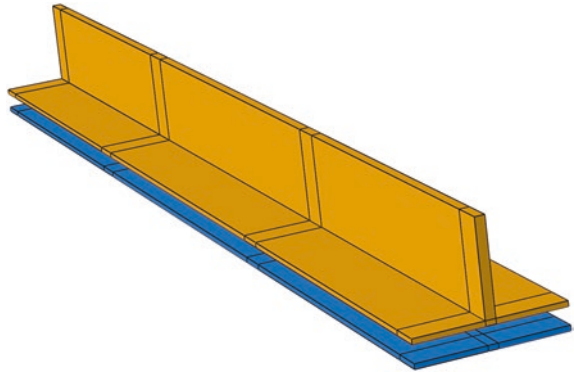
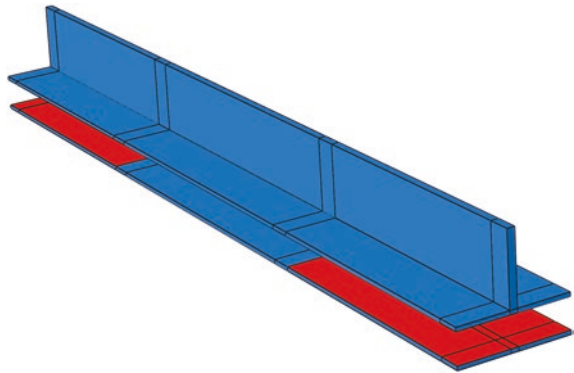


Fig. 2.45 Node-to-surface interaction zone with the VCCT option—stiffened composite panel with skin-stringer debonding



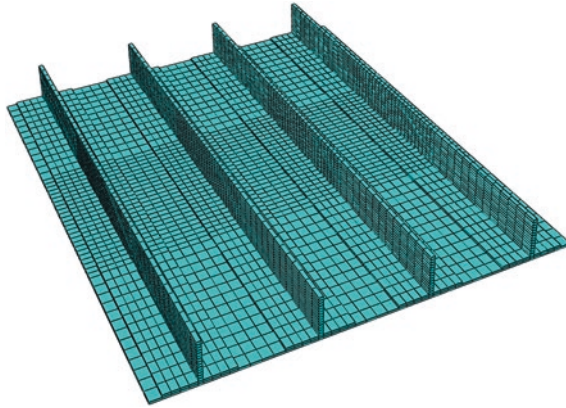


Fig. 2.46 Abaqus FE model—debonded stiffened panel

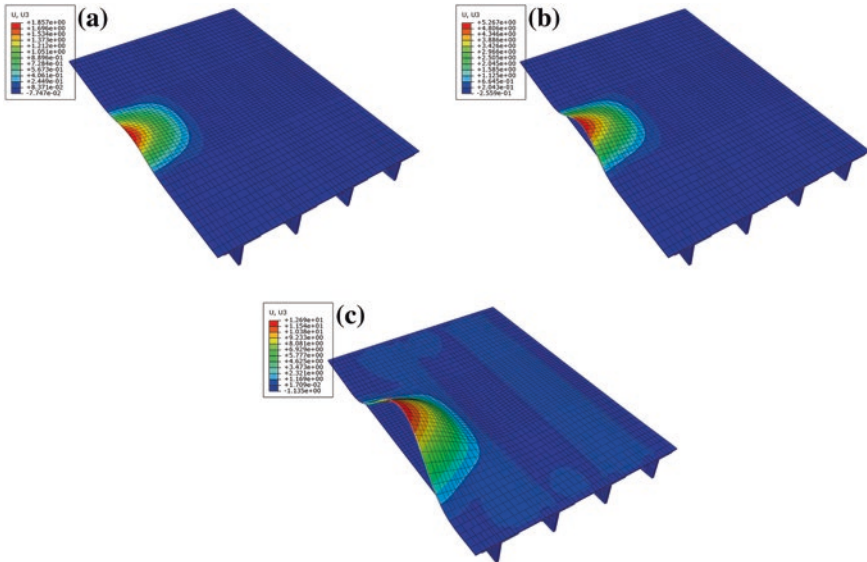
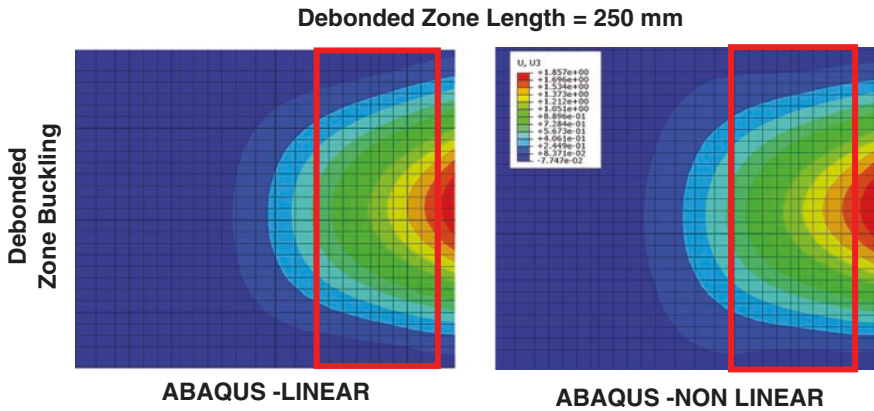


Fig. 2.47 Non-linear deformed shapes at **a** debonded zone buckling; **b** debonding growth initiation; **c** advanced debonding growth state—stiffened composite panel with skin-stringer debonding

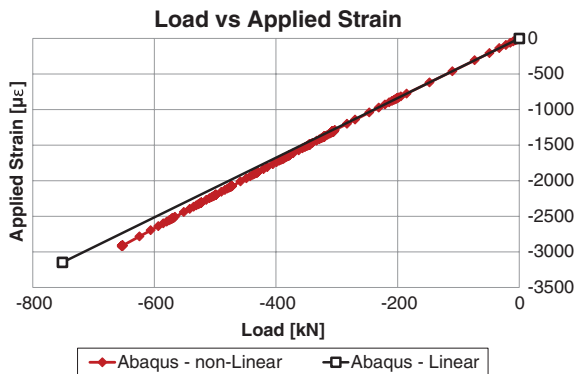
In Fig. 2.48, the excellent agreement between the linear and non-linear results, in terms of global longitudinal stiffness, confirms the linearity of the global compressive behavior of the stiffened panel, up to the debonding growth initiation load.



In Fig. 2.49 the debonding growth shapes are shown at debonding growth initiation (1,286 $\mu\epsilon$), at an intermediate state (1,310 $\mu\epsilon$) and when the debonding extend to the complete stringer foot surface (2,198 $\mu\epsilon$).

In Figs. 2.50 and 2.51 it is possible to appreciate both the distributions of ERR and location of growth initiation at upper and lower delamination fronts. As it can be seen from both the figures, delamination growth takes place in both cases on the external edge of the stringer as a consequence of the skin buckling.

Fig. 2.48 Applied load versus applied strains. ABAQUS non-linear results—stiffened composite panel with skin-stringer debonding



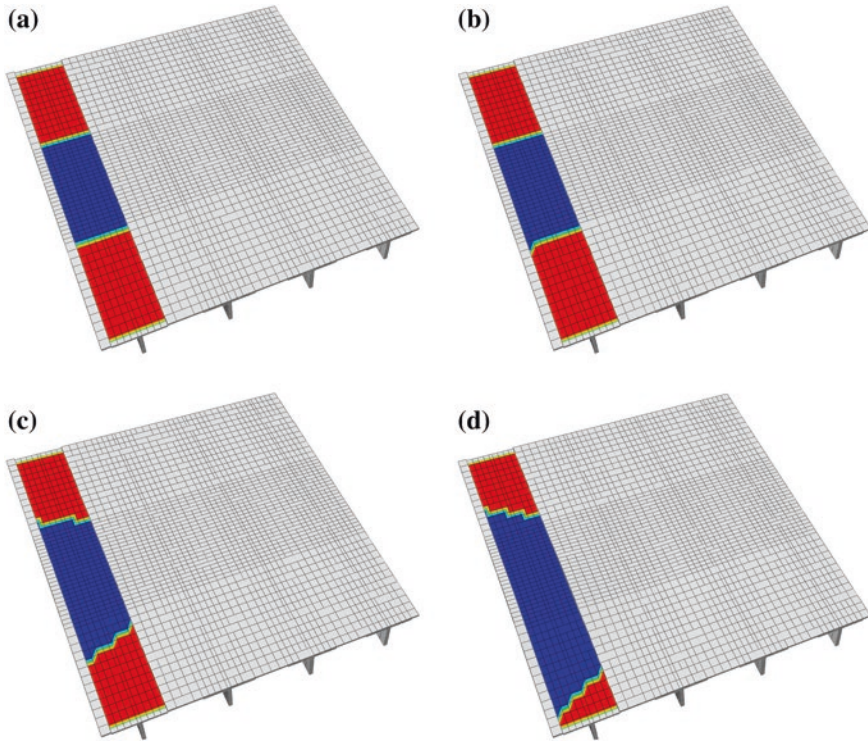


Fig. 2.49 Debonding growth shapes at: **a** no growth; **b** debonding growth initiation (1,286 $\mu\epsilon$); **c** Intermediate debonding growth state (1,310 $\mu\epsilon$); **d** debonding growth reaching the boundaries of the stringer foot (2,198 $\mu\epsilon$)

Fig. 2.50 ERR distributions at growth initiation for the ABAQUS non-linear model upper side—Stiffened composite panel with skin-stringer debonding

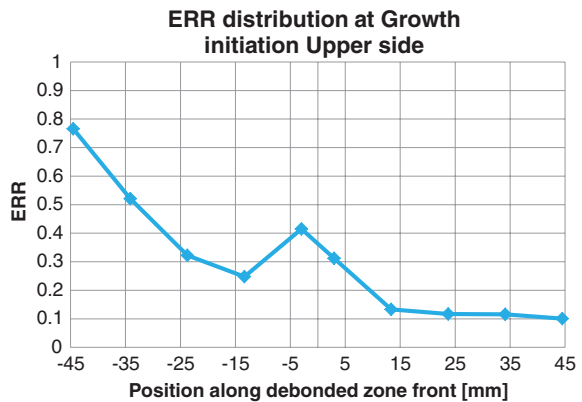
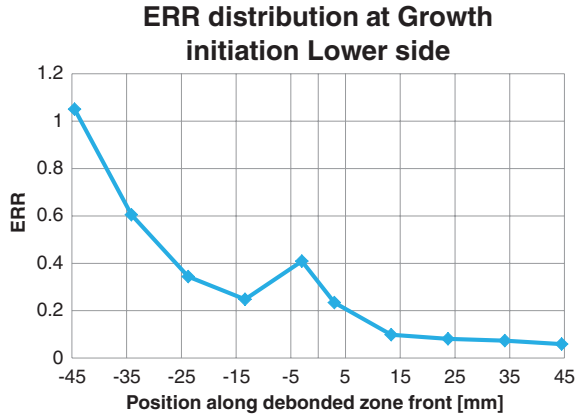


Fig. 2.51 ERR distributions at growth initiation for the ABAQUS non-linear model—lower side—stiffened composite panel with skin-stringer debonding



References

1. Chai, H., Babcock, C.D., Knauss, W.G.: One dimensional modelling of failure in laminated plates by delamination buckling. *Int. J. Solids Struct.* **17**, 1069–1083 (1981)
2. Kardomates, G.A.: Large deformation effects in the postbuckling behaviour of composites with thin delaminations. *AIAA J.* **27**, 624–631 (1987)
3. Kardomates, G.A., Schmueser, D.W.: Buckling and post-buckling of delaminated composites under compressive loads including transverse shear effects. *AIAA J.* **27**, 337–343 (1988)
4. Ashizawa, M., Fast M.: Interlaminar fracture of a compressively loaded composite containing a defect. Paper presented to the fifth DoD/NASA conference on fibrous composites in structural design, New Orleans, LA, 27–29 Jan 1981
5. Ramkumar, R.L.: Fatigue degradation in compressively loaded composite laminates. NASA CR-16568 (1981)
6. Ramkumar, R.L.: Performance of a quantitative study of instability-related delamination growth. NASA CR-166046 (1983)
7. Byers, B.A.: Behaviour of damaged graphite/epoxy laminates under compression loading. NASA CR-159293 (1980)
8. Chai, H., Knauss, W.G., Babcock, C.D.: Observation of damage growth in compressively loaded laminates. *J. Exp. Mech.* **23**(3), 329–337 (1983)
9. Nilsson, K.-F., Asp, L.E., Alpmann, J.E., Nystedt, L.: Delamination buckling and growth for delaminations at different depths in a slender composite panel. *Int. J. Solids Struct.* **38**(17), 3039–3071 (2001)
10. Whitcomb, J.D.: Approximate analysis of Postbuckled through-the-width delaminations. *Compos. Technol. Rev.* **4**(3), 71–77 (1982)
11. Whitcomb, J.D.: Parametric analytical study of instability-related delamination growth. *Compos. Sci. Technol.* **25**(1), 18–48 (1986)
12. Chai, H., Babcock, C.D., Knauss, W.G.: One delamination modelling of failure in laminated plates by delamination buckling. *Int. J. Solids Struct.* **17**(1), 1069–1083 (1981)
13. Fei, Z., Yin, W.L.: Postbuckling growth of a circular delamination in a laminate under compression and bending. In: *Proceedings of the Twelfth South-eastern Conference on Theoretical and Applied Mechanics*. Georgia Institute of Technology, Pine Mountain, Georgia (1984)
14. Shivakumar, K.N., Whitcomb, J.D.: Buckling of a sublaminates in a quasi-isotropic composite laminate. *Int. J. Compos. Mater.* **19**, 2–18 (1985)

15. Whitcomb, J.D., Shivakumar, K.N.: Strain-energy release rate analysis of a laminate with a postbuckled delamination. *Numerical Methods in Fracture Mechanics*. NASA TM-89091 (1987)
16. Kim, H.J., Hong, C.S.: Buckling and postbuckling behaviour of composite laminates with an embedded delamination. In: *Proceedings of ICCM-10, Whistler* (1995)
17. Whitcomb, J.D.: Analysis of a laminate with a postbuckled embedded delamination, including contact effects. *Int. J. Compos. Mater.* **26**(10), 1523–1535 (1992)
18. Whitcomb, J.D.: Three dimensional analysis of a postbuckled embedded delamination. *Int. J. Compos. Mater.* **23**, 862–889 (1989)
19. Perugini, P., Riccio, A., Scaramuzzino, F.: Influence of delamination growth and contact phenomena on the compressive behaviour of composite panels. *Int. J. Compos. Mater.* **33**(15), 1433–1456 (1999)
20. Riccio, A., Perugini, P., Scaramuzzino, F.: Modelling compression behaviour of delaminated composite panels. *Comput. Struct.* **78**, 73–81 (2000)
21. Nilsson, K.-F., Thesken, J.C., Sindelar, P., Giannakopoulos, A.E., Storakers, B.: A theoretical and experimental investigation of buckling induced delamination growth. *J. Mech. Phys. Solids.* **41**(4), 749–782 (1993)
22. Gaudenzi, P., Perugini, P., Riccio, A.: Post-buckling behaviour of composite panels in the presence of unstable delaminations. *Compos. Struct.* **51**(3), 301–309 (2001)
23. Riccio, A., Perugini, P., Scaramuzzino, F.: Embedded delamination growth in composite panels under compressive load. *Compos. B Eng.* **32**(3), 209–218 (2001)
24. Riccio, A., Scaramuzzino, F., Perugini, P.: Influence of contact phenomena on embedded delamination growth in composites. *AIAA J.* **41**(5), 933–940 (2003)
25. Davies, G.A.O., Hitchings, D., Ankersen, J.: Predicting delamination and debonding in modern aerospace composite structures. *Compos. Sci. Technol.* **66**, 846–854 (2006)
26. De Borst, R., Remmers, J.J.C.: *Comput. Model. Delamination*. *Compos. Sci. Technol.* **66**, 713–722 (2006)
27. Allix, O., Blanchard, L.: Mesomodelling of delamination: towards industrial applications. *Compos. Sci. Technol.* **66**, 731–744 (2006)
28. Backlund, J., Aronsson, C.: Tensile fracture of laminates with holes. *J. Compos. Mater.* **20**, 259–286 (1986)
29. Ireman, T., Ranvik, T., Eriksson, I.: On damage development in mechanically fastened composite laminates. *Compos. Struct.* **49**, 151–171 (2000)
30. Ochoa, O.O., Reddy, J.N.: *Finite Element Analysis of Composite Laminates*. Kluwer Academic Publishers, Dordrecht (1992)
31. Sleight, D.W., Knight, N.F., Wang, J.T.: Evaluation of a progressive failure analysis methodology for laminated composite structures. *AIAA paper*, pp. 97–1187 (1997)
32. Hashin, Z., Rotem, A.: A fatigue failure criterion for fiber reinforced materials. *J. Compos. Mater.* **7**, 448–474 (1973)
33. Hashin, Z.: Failure criteria for unidirectional fiber composites. *J. Appl. Mech.* **47**, 329–334 (1980)
34. Murray, Y., Schwer, L.: Implementation and verification of fiber-composite damage models. failure criteria and analysis in dynamic response. *ASME AMD* **107**, 21–30 (1990)
35. Petit, P.H., Waddoups, M.E.: A method of predicting the non-linear behaviour of laminated composites. *J. Compos. Mater.* **3**, 2–19 (1969)
36. Sandhu, R.S.: Non-linear behaviour of unidirectional and angle ply laminates. *AIAA J. Aircraft* **13**, 104–111 (1974)
37. Nahas, M.N.: Survey of failure and post-failure theories of laminated fiber-reinforced composites. *J. Compos. Tech. Res.* **8**, 138–153 (1986)
38. Hahn, H.T., Tsai, S.W.: On the behaviour of composite laminates after initial failures. *Astronaut. Aeronaut.* **21**, 58–62 (1983)
39. Perugini, P., Riccio, A., Scaramuzzino, F.: Three-dimensional progressive damage analysis in composite joints. In: *Proceedings of the Eighth International Conference on Civil and Structural Engineering Computing*, Civil-Comp Press, Stirling, (2001)

40. Riccio, A.: Effects of geometrical and material features on damage onset and propagation in single-lap bolted composite joints under tensile load: Part II—numerical studies. *Int. J. Compos. Mater.* **39**(23), 2091–2112 (2005)
41. Sun, H.T., Chang, F.K., Qing, X.: The response of composite joints with bolt-clamping loads. Part I: model development. *J. Compos. Mater.* **36**(1), 47–67 (2002)
42. Baker, A.A., Dutton, S., Kelly, D.: *Composite Materials for Aircraft Structures*, 2nd edn. (AIAA Educational Series, 2004)
43. Crisfield, M.A.: *Non-Linear Finite Element Analysis of Solids and Structures*. Wiley, New York (1996)
44. Sun, C.T.: Strength Analysis of unidirectional composites and laminates. *Compr. Compos. Mater.* **1**, 641–666 (2008)
45. Reeder, J.R., Crews, J.H.: Mixed-mode bending method for delamination testing. *AIAA J.* **28**(7), 1270–1276 (1990)
46. Wang, J.T., Raju, I.S.: Strain energy release rate formulae for skin-stiffener debond modeled with plate elements. *Eng. Fract. Mech.* **54**, 211–228 (1996)
47. Glaessgen, E.H., Riddell, W.T., Raju, I.S.: Nodal constraint, shear deformation and continuity effects related to the modeling of debonding of laminates, using plate elements. *CMES* **3**, 103–116 (2002)
48. Glaessgen, E.H., Riddell, W.T., Raju, I.S.: Effect of shear deformation and continuity on delamination modeling with plate elements, in the 39rd AIAA/ASME/ASCE/AHS/ASC Structures, Structural Dynamics and Materials. Conference, Long Beach, CA, USA, (1998)
49. Krueger, R., O'Brien, T.K.: A shell/3D modeling technique for the analysis of delaminated composite laminates. *Compos. A Appl. Sci. Manuf.* **32**, 25–44 (2001)
50. Shivakumar, K.N., Tan, P.W., Newman, J.C.: A Virtual crack closure technique for calculating stress intensity factors for cracked three dimensional bodies. *Int. J. Fracture.* **36**, R43–R50 (1988)
51. Krueger, R.: The virtual crack closure technique: history, Approach and Applications. NASA/CR-2002-211628 (2002)
52. Riccio, A.: Sviluppo di procedure numeriche non lineari agli elementi finite orientate allo studio di strutture in materiale composito danneggiate. Tesi di Dottorato, Seconda Università degli Studi di Napoli, Tutor. Prof. F. Scaramuzzino, A.A. (1998–99)
53. Hwu, C., Hu, J.: Stress intensity factors and energy release rates for of delaminations in composite laminates. *Eng. Fract. Mech.* **42**, 988–997 (1992)
54. Liu, S., Chang, F.K.: Matrix cracking effect on delamination growth in composite laminates induced by a spherical indenter. *J. Compos. Mater.* **28**, 940–977 (1994)
55. Mukherjee, Y.X., Gulrajani, S.N., Mukherjee, S., Netravali, A.N.: A numerical and experimental study of delaminated layered composites. *J. Compos. Mater.* **28**, 837–870 (1994)
56. Riks, E.: Progress in collapse analysis. Presented at the 1984 ASME Pressure Vessel and Piping Conference (Session on Collapse Analysis of Structures-I), San Antonio (1984)
57. Sleight, D.W.: Progressive failure analysis methodology for laminated composite structures. NASA/TP-1999-209107
58. Chang, F.K., Chang, K.Y.: A progressive damage model for laminated composites containing stress concentrations. *J. Compos. Mater.* **21** (1987)
59. Tan, S.C.: A Progressive Failure Model for composite laminates containing openings. *J. Compos. Mater.* **25**, 556 (1991)
60. Riccio, A., Gigliotti, M.: A Novel numerical delamination growth approach for the preliminary design of damage tolerant composite structures. *J. Compos. Mater.* **41**(16), 1939–1960 (2007)
61. Pietropaoli, E., Riccio, A.: On the robustness of finite element procedures based on virtual crack closure technique and fail release approach for delamination growth phenomena. Definition and assessment of a novel methodology. *Compos. Sci. Technol.* **70**(8), 1288–1300 (2010)
62. Pietropaoli, E., Riccio, A.: Formulation and assessment of an enhanced finite element procedure for the analysis of delamination growth phenomena in composite structures. *Compos. Sci. Technol.* **71**(6), 836–846 (2011)

63. Riccio, A., Raimondo, A., Scaramuzzino, F.: A study on skin delaminations growth in stiffened composite panels by a novel numerical approach. *Appl. Compos. Mater.* **20**(4), 465–488 (2013)
64. Riccio, A., Raimondo, A., Di Caprio F., Scaramuzzino, F.: Delaminations buckling and growth phenomena in stiffened composite panels under compression. Part II: a numerical study. *J. Compos. Mater.* (2013), doi: [10.1177/0021998313502742](https://doi.org/10.1177/0021998313502742)
65. Riccio, A., Raimondo, A., Fragale, S., Camerlingo, F., Gambino, B., Toscano, C., Tescione, D.: Delaminations buckling and growth phenomena in stiffened composite panels under compression. Part I: an Experimental Study. *J. Compos. Mater.* doi: [10.1177/0021998313502741](https://doi.org/10.1177/0021998313502741). (2013)
66. ABAQUS MANUAL (revision 6.5-1): theory
67. Riccio, A., Pietropaoli, E.: Modeling damage propagation in composite plates with embedded delamination under compressive load. *J. Compos. Mater.* **42**(13), 1309–1335 (2008)

Chapter 3

Delamination and Debonding Growth in Composite Structures

Javier San Millán and Iñaki Armendáriz

3.1 Introduction

The general trend in modern aircraft structures is the progressive replacement of metallic materials with composites. Composites exhibit superior structural properties, such as higher stress allowables, better behaviour in fatigue and damage tolerance, less sensitivity to corrosion phenomena, etc. Airbus new A350 or Boeing B787, both characterised by a massive use of composite materials for structural components (about 50 % of the total structural weight), are perfect examples of this tendency. The attractive levels of fuel consumption reduction (around 20 %), and economization achieved with this new designs, are some of the reasons that justify composites utilization.

One of the typical failure modes of composite materials is inter-laminar delamination, which consists in a lack of cohesion between adjacent plies in the laminate. Delaminations can be originated by design features prone to develop interlaminar stresses (curved sections, drop-offs, free edges, etc.), manufacturing defects (shrinkage of the matrix during curing, formation of resin-rich areas, etc.), or accidental causes such as tool impacts. Fatigue loading may create inside the material fibre-matrix debonding (interfacial failure) or matrix damage at micro-scale, which eventually leads to inter-laminar delaminations.

Delaminations degrade material structural properties and reduce the structural load capacity. Moreover they are prone to grow when compression and out of plane loads (static or fatigue) are applied to the structure. Currently aircraft developers

J.S. Millán (✉) · I. Armendáriz

Materials and Structures Department, Instituto Nacional de Técnica Aeroespacial (INTA),
Carretera de Ajalvir Km. 4, 28850 Torrejón de Ardoz (Madrid), Spain
e-mail: sanmillan@inta.es

use a strain design approach to cover impact damage and to avoid delamination growth, for monolithic laminates this limit is typically 3,500–4,000 $\mu\epsilon$, for other applications such as honeycomb panels, lower limits are quoted.

Bonded joints in composites are often used in many aircraft structures such as stiffened panels (joint skin—stiffener), or in general joints such as skin—ribs, skin—spar, and so on. This kind of joints is quite complicated to analyze even for a simple strength prediction, because the stress distribution at the joints is rather complex showing high stress concentrations at its edges. Progressive debonding is particularly complicated to simulate.

The lack of accurate and reliable simulation methodologies for both problems, and the partial knowledge of the real damage mechanics in composites, usually lead to conservative designs. Additionally, when developing a new aircraft model, an extensive test campaign at various levels (coupons, details, stiffened panels, components, etc.) is required. Finally, airworthiness certification requirements are usually more restrictive for composite materials than for metallic ones.

Substantial Research has been carried out during last decades to find accurate and reliable simulation methodologies for damaged composite structures, in static or fatigue load environments. When dealing with complex structures, Finite Element (FE) techniques are often used. In particular two theories are among the most commonly used to simulate delamination and debonding damage with Finite Elements: Virtual crack closure technique (VCCT) [1–9], and Cohesive Zone (CZ) [10–15].

The VCCT is derived from the *linear fracture mechanics*, and requires the calculation of the Strain Energy Release Rates (SERR) to predict delaminations or debonding *growth*. The SERRs are calculated according to the pure modes of fracture (mode *I*, *II* and *III*). The VCCT requires a *pre-damaged* structure, therefore damage onset cannot be predicted with this theory. The Modified Crack Closure Technique (MVCCT) is a variation of the general VCCT allowing to estimate the SERR by using only one FEM analysis.

The Cohesive zone (CZ) model is derived from *damage mechanics*, and it does not require a pre-damage structure to predict delamination and debonding growth, allowing to evaluate also the damage onset.

Both simulation methodologies require a pre-defined damage growth path that has to be introduced into the FEM. Additionally the techniques are highly non-linear leading to high computation times, often unsuitable for complex structures.

Instituto Nacional de Técnica Aeroespacial (INTA), the Spanish research centre for aerospace, is currently involved in developing reliable simulation techniques for composites structural behaviour in the presence of damages such as inter-laminar delaminations and debondings. In the next chapters two methodologies are introduced in detail, respectively, aimed to simulate the debonding growth and the inter-laminar delamination growth in composites. Both the methodologies allow to perform Progressive Failure Analysis (PFA) for static load conditions.

Besides accuracy, INTA focuses on developing efficient techniques from a computational point of view (reasonable computation times), and also to properly

understand and correct *mesh size* effects (FE results dependency on the mesh size). This is a typical inconvenient of both theories VCCT and CZ.

3.2 Delamination Growth

As above mentioned INTA has been involved in R+D projects focused in finding robust and reliable FEM simulation methodologies for damage growth in composite structures. The idea is to investigate the residual strength of an aeronautic structure with the presence of damages, either produced by manufacturing defects, fatigue, ambient conditions, or accidental causes. This concept is often referred as Damage Tolerance, and a structure safe in the presence of damages is called Fail safe. Structures designed with such philosophy are inspected according to the maintenance procedures to check damage progression, and to assure that the residual strength of the structure is still above the structure ultimate load (damage size lower than allowable one).

In the case of inter-laminar delaminations, there is an additional inconvenient: this type of internal damages requires complicated and expensive inspections.

Many authors have characterized both the onset and growth of delaminations proposing a variety of numerical tools to predict the composite behaviour. One of these tools, based on linear Fracture Mechanics, is the Virtual Crack Closure Technique (VCCT) based on the computation of the Strain Energy Release Rates (SERR). VCCT technique fundamentals are explained in the next section [1–9].

In the aerospace industry, MSC. Nastran is largely accepted as a valid Finite Element (FE) simulation tool which allow to save time and costs by reducing the amount of tests needed for certification of metallic and composite structures [16, 17]. INTA has developed an in-house delamination growth tool, that uses as inputs the Nastran input file (*.bdf file) and the Nastran results file (*.f06 file, in text format). The tool post-processes the displacements and force results, calculates the SERR based on the VCCT, and it is also able to simulate the progressive growth of the delamination. The main characteristics of the developed tool can be summarised as follows:

- The source code of the application is written in C++ language.
- It allows the choice of different options for delamination growth criteria: linear, K criterion, power law, Hackle Exponential.
- It is completely automatized, almost no user involvement is required.
- It has shown a robust behaviour, low processing time, and good convergence, (at least for the analysed benchmark: a composite stiffened panel).

In the next sections the VCCT theory fundamentals, the experimental benchmark and test data (used to validate the simulation tool), the developed FEMs, the scheme and fundamentals of the Delamination growth tool, and finally a detailed correlation of Simulation and Tests results are introduced. Different FEM models,

(with different mesh sizes to investigate the mesh size effects), and different failure criteria have been used. Finally, the conclusions and further work are presented.

3.2.1 Virtual Crack Closure Technique Fundamentals

The Virtual Crack Closure Technique was originally published in 1977 [18], although even lately more articles have been published showing some applications of this technique. There are also articles which assess the implementation of this technique on the commercial software [19, 20].

In order to compute the total SERR, three components need to be calculated: mode I component (G_I) due to inter-laminar tension, mode II component (G_{II}) due to inter-laminar sliding shear, and mode III component (G_{III}) due to inter-laminar scissoring shear:

$$\begin{aligned} G_I &= \frac{\Delta U_I}{\Delta A} = \frac{1}{2} \frac{F_Z |u_Z^{upper} - u_Z^{lower}|}{\Delta A} \\ G_{II} &= \frac{\Delta U_{II}}{\Delta A} = \frac{1}{2} \frac{F_r |u_r^{upper} - u_r^{lower}|}{\Delta A} \\ G_{III} &= \frac{\Delta U_{III}}{\Delta A} = \frac{1}{2} \frac{F_\theta |u_\theta^{upper} - u_\theta^{lower}|}{\Delta A} \end{aligned} \quad (3.1)$$

In the equations, ΔU_i is the energy increment released consistently with the mode i due to the progress of the delamination front (delamination area grows ΔA). F_i are the forces (along i direction) at the delamination front before delamination growth, and u_i are the displacements of the delamination front along i direction in the grown configuration (upper or lower sub-laminate). Therefore the VCCT requires 2 different FEM analyses for the calculations involving two different FE models with slight variations in the delamination sizes.

In order to simplify the FE simulations, the Modified Virtual Crack Closure Technique (MVCCT) was introduced. Its simplification speeds up the analyses, being necessary only one FE model (and one analysis) to estimate the SERR. The hypothesis underlying this technique is that the displacement shape of the delamination front, once the growth has taken place, is, in fact, similar to the delamination front displacement shape before the growth. In this way the SERR may be easily obtained with a unique FE analysis.

Usually, the G_{III} contribution to the failure is much lower than the contribution associated to modes I and II , so, as a further hypothesis, this contribution can be neglected. Thus the applied formula for the Failure index (linear failure criterion) becomes

$$F = \frac{G_I}{G_{Ic}} + \frac{G_{II}}{G_{IIc}} + \frac{G_{III}}{G_{IIIc}} \approx \frac{G_I}{G_{Ic}} + \frac{G_{II}}{G_{IIc}} \geq \quad \text{Linear Criterion} \quad (3.2)$$

being G_{Ic} and G_{IIc} the composite material inter-laminar fracture toughness for modes I and II respectively. Delamination growth takes place when Eq. (3.2) is satisfied.

The test methods to derive these critical values are:

- Mode *I*: Double Cantilever Beam DCB [21].
- Mode *II*: End Notched Flexure (ENF), for which standardized test method is not available yet.
- Mixed Mode *I* and *II*: Mixed Mode Bending MMB [22].

Besides Linear criterion, other delamination growth criteria, typically used for composites, are introduced hereafter:

$$F = \frac{G_I + G_{II}}{(G_{Ic} - G_{IIc})e^{\gamma \left(1 - \sqrt{1 + \frac{G_{II}}{G_I} \sqrt{\frac{E_{11}}{E_{22}}}}\right)} + G_{IIc}} \quad \text{Exponential Hackle} \quad (3.3)$$

where E_{11} E_{22} are the young modulus of the material and $\gamma = 1/4$ [23, 24].

$$F = \frac{G_I + G_{II}}{G_{IIc} - (G_{IIc} - G_{Ic})\sqrt{\frac{G_I}{G_{Ic}}}} \quad \text{K Criterion} \quad (3.4)$$

$$F = \sqrt{\left(\frac{G_I}{G_{Ic}}\right)^2 + \left(\frac{G_{II}}{G_{IIc}}\right)^2} \quad \text{Quadratic Criterion} \quad (3.5)$$

3.2.2 Validation Benchmark Definition

The benchmark selected for validation of the developed tool is a typical structural subcomponent: it is a three bonded stringers panel fabricated from Fibredux HTA/6376C, with a single embedded delamination (circular shape, $\Phi = 40$ mm) in one of the bays (between 4th and 5th plies). This stiffened panel is representative of a typical semi-monocoque aircraft structure in the wing or the fuselage.

The panel was tested at QinetiQ (Farnborough, UK) at compression static load until final failure [25]. In the test campaign several configurations of the stiffened panels were tested: undamaged panels, panels with impact damage, panels with artificial damages. Only one configurations is of interest for the validation activity presented in this chapter: the panel with a single embedded delamination (artificial defect) at the centre of one of the bays.

3.2.3 FE Model Definition and Buckling Simulations

The FE model have been created by using MSC. Nastran, the standard solver in aeronautic industry [16, 17]. The panel has been modelled by using composite plate elements (QUAD4) for skin and stiffeners, rigid elements (Multipoint constraints or MPC) for the adhesive, and contact elements between the delaminated sub-laminates.

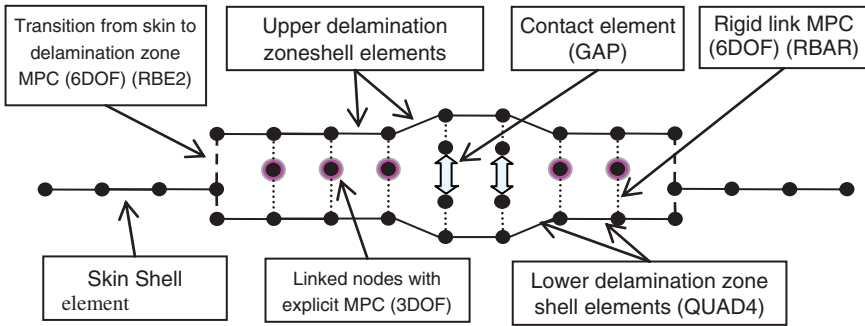


Fig. 3.1 FEM scheme at delamination zone

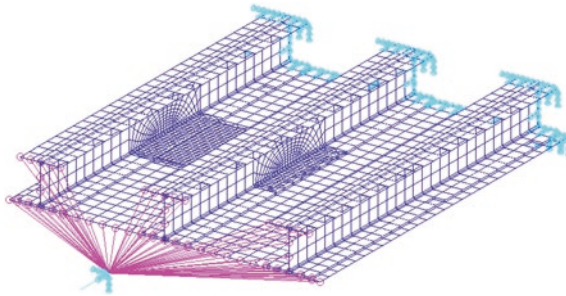


Fig. 3.2 Stiffened panel FEM showing boundary conditions

A part of the panel FEM has been prepared for possible delamination growth, in this part the skin is divided in two sub-laminates: upper and lower, the nodes are linked by MPCs and contact elements. All these FEM features are shown in Fig. 3.1.

The lamina properties and the lay-up have been given in input to the FEM, by the constitutive model of the plate composite material option in MSC. Nastran.

The FEM boundary conditions (see Fig. 3.2) try to reproduce the actual test conditions:

- One node (in the left in the figure) is linked by means of a rigid MPC to a panel border. In this node all Degrees of Freedom (DOFs) are constrained except the one along the applied load direction.
- The other panel edge is clamped in all DOFs.

To verify the mesh size dependency, a typical drawback of the VCCT, 3 different FE models of the panel were defined, each one using a different mesh size at the pre-defined delamination area (see Fig. 3.3).

Since the delamination area in models 2 and 3 reach the stringers (see Fig. 3.3), the delamination zone modelling is slightly more complex in these FE models, as it is shown in Fig. 3.4.

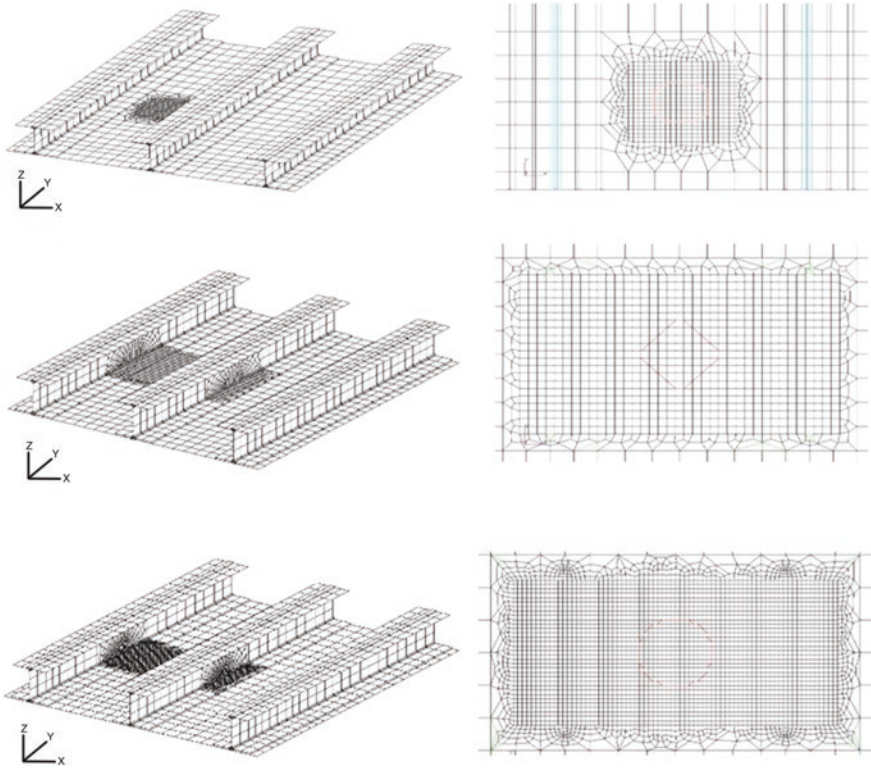


Fig. 3.3 FEM models (1 *top*, 2 *middle*, 3 *bottom*) showing details of the delamination zone

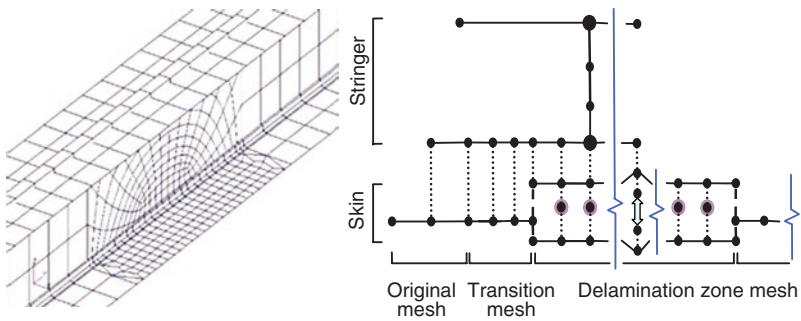


Fig. 3.4 Delamination zone detail

To compare the 3 FE models, buckling analyses (linear and non-linear) have been performed for all of them. The FE models buckling loads have been compared each other and with the available experimental data in terms of delamination buckling load (first buckling mode) and skin buckling load (fourth buckling

Table 3.1 Local and global buckling loads—FEMs and tests

Buckling mode	Test (KN)	FEM 1 (KN)	FEM 2 (KN)	FEM 3 (KN)
1st (delamination buckling)	211	215	213	206
2nd	–	223	273	229
3rd	–	373	–	381
4th (skin buckling)	437	456	445	457
5th	–	470	460	471

mode). This last buckling mode is local, the stringers are still able to carry the load, and just the skin in the bay between the stringers is buckled.

In Table 3.1 a comparison between the FE models and tests buckling loads is shown; more details can be found in [3, 6]. It can be seen that buckling loads are quite similar for all the FE models, and that the correlation between the FE models and the tests buckling loads is adequate.

3.2.4 Delamination Growth Algorithm

As previously explained, the delamination growth tool developed at INTA uses MSC. Nastran as base solver. The tool uses the nodal release technique to simulate the growth of the delamination at a given position (X, Y coordinates) by eliminating the MPC (in pink colour in Fig. 3.2) connecting the two nodes, at that position, belonging respectively to the upper and lower sub-laminate.

The stiffened panel FE models have been arranged by defining a plane along which delamination can progressively grow, the reasonable assumption made is that the delamination grows remaining in the initial delaminated plane (between 4th and 5th plies of the skin) without migrating to other interfaces.

The delamination growth tool was written in C++ language, it is completely automatized (almost no user involvement is required), and uses the original Nastran FEM. The overall scheme of the tool and its interaction with MSC. Nastran is shown in Fig. 3.5.

The process begins with an initial Nastran non-linear analysis of the FE model requesting results for different percentages (load steps) of the applied load.

Then, the delamination growth tool asks the user for G_{Ic} and G_{IIc} values of the used composite material, and reads the results file (*.f06) generated by Nastran for the different applied load steps. The tool computes the value of the Failure Index F above mentioned for the selected failure criteria.

This Failure index F is calculated for every node of the delamination front (the edge of the delamination), and for all load steps. If F is greater than 1.0 for one or more nodes at a given load step, the corresponding MPCs of those nodes are released, and a RESTART operation is performed from that load step.

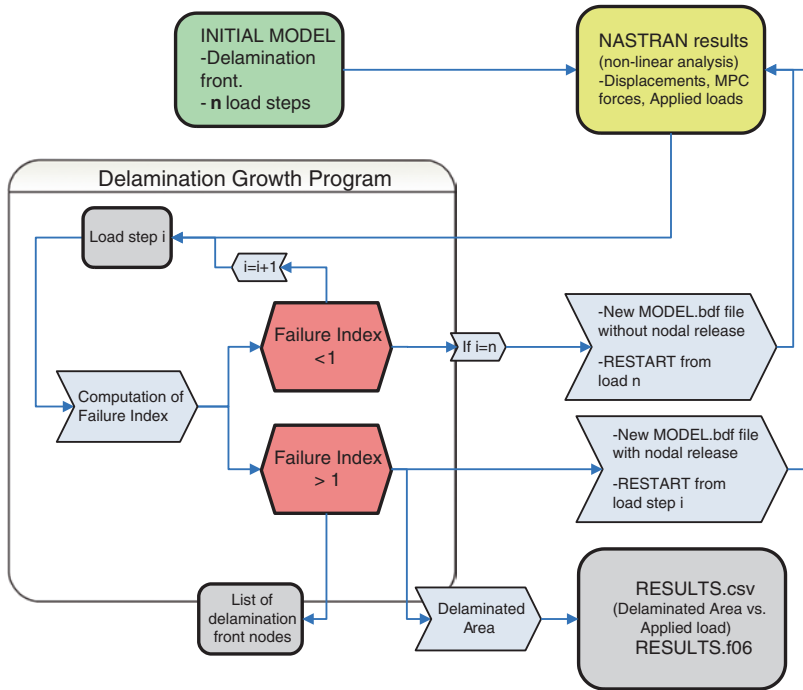


Fig. 3.5 Diagram of the delamination growth algorithm

The RESTART operation, available within MSC. Nastran [16, 17], allows re-initiating a structural analysis from a displacement or stresses state at a used decided load level (load step in non-linear analysis). When a RESTART is done, MSC. Nastran also allows the use of a new FEM model configuration (in this case a new MPC set). The RESTART operation is therefore another key point of the delamination growth tool.

If, for a given load step, no failure criterion is met, the tool just passes to the next load step and RESTART is performed.

This loop is performed up to the last load step, or until there is no-convergence (occurring for our benchmark when the delamination reached the stiffeners).

At the end of the analysis, delamination growth tool generates two results files:

- A *dynamic* Nastran results file (f06). This file is called “dynamic” because it collects the information (displacements, applied loads, information about the nodal release) of all the intermediate results, that actually correspond to different FE models (different delamination fronts, and different MPC sets).
- A csv file with the information of “Delaminated Area versus applied load”. This is the main result of the tool, and it is used to verify the accuracy of the proposed methodology by correlating the numerical curve with the experimental one.

3.2.5 Correlation Between FE Simulations and Tests

Figure 3.6 shows the curve “Delaminated area (mm²) versus applied load (με)” obtained with the in-house delamination growth tool using the most detailed FE model, for five different load steps increments: 0.1, 0.125, 0.15 and 0.2 mm.

Also the experimental curve is shown for comparison purposes. The tests were performed by QinetiQ, they performed static tests until final failure, and post-mortem analyses of several stiffened panels containing impact damages and artificial defects. The damage evolution when applying static compression loads was monitored during the tests, more information about the performed tests can be found in [25].

As expected, the increase of the delamination area starts when the panel buckles. The predicted growth velocity (the slope in the figures) is adequate and similar to the experimental one, although a slight dependence on the load step used has been observed. The load step dependency is studied in next section.

Also a comparison between experimental and numerical delamination shapes across the loading process is introduced. In Fig. 3.7 photos of the delaminated area found by QinetiQ by means of ultrasonic inspections are shown. The photos were

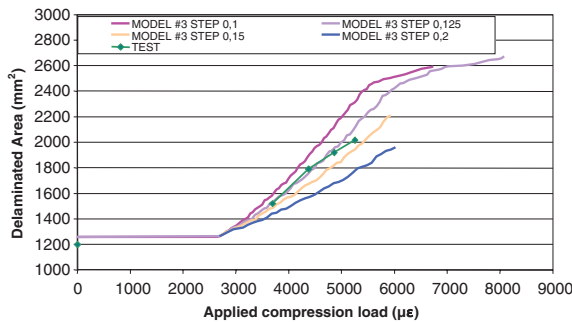


Fig. 3.6 Comparison between experimental delaminated area and FE simulations for different load step sizes (in mm)

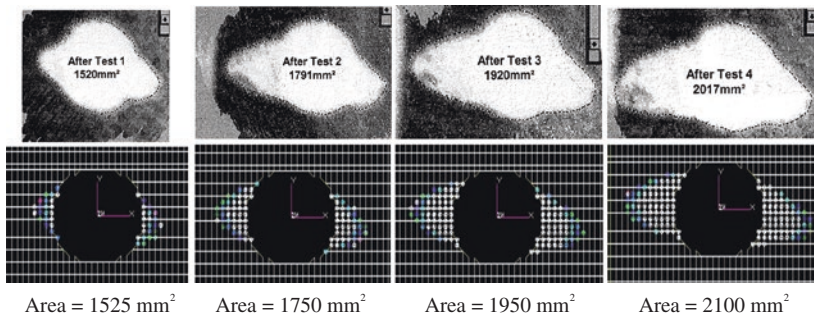


Fig. 3.7 Delamination evolution found experimentally with ultrasonic inspections (©Copyright QinetiQ Ltd) and with the simulation tool

taken without removing the panel from the test frame [25], just after the compressive experimental tests up to 3,692 $\mu\epsilon$ (Test 1), 4,379 $\mu\epsilon$ (Test 2), 4,862 $\mu\epsilon$ (Test 3), and 5,255 $\mu\epsilon$ (Test 4). In the same figure the delamination shapes found by the delamination growth tool at the same load values are shown as well.

As it can be seen the experimental and simulation delamination shapes are quite similar, and the slight asymmetry of the delamination (see pictures above after Tests 3 and 4) is also captured very well by the simulations.

3.2.6 Mesh Size Effect

The three FE models were numerically tested, providing results in good agreement with experimental data. It was found that the optimum FE result depends on the mesh size and the load increment used for the Nastran analysis. This dependency was studied, and it was found that an almost linear correlation exists between the optimal (in terms of experimental data fitting) combinations of these two parameters.

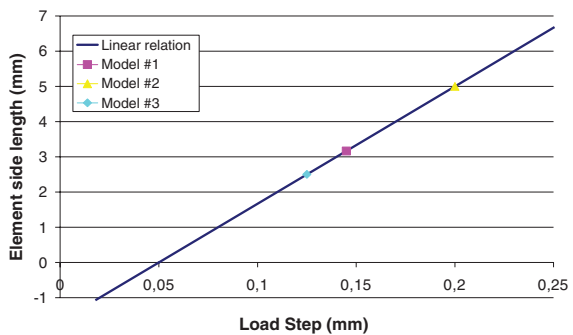
In Fig. 3.8 the optimum correlation between mesh size and load step to be used in the analysis is shown, the mixed-mode failure criterion used in this case is the linear one.

The results of the 3 optimized FE models (each one using its own corresponding optimum load steps) agreed very well with the experimental data, as is shown in Fig. 3.9. As it can be seen the experimental and the 3 optimized simulation curves are quite similar, and the delamination growth velocity is almost identical.

3.2.7 Comparison Among Mixed-Mode Failure Criteria

A comparison has been performed among the different failure criteria implemented in the delamination growth tool: the Linear Criterion (1), Exponential Hackle (2), K Criterion (3), and Quadratic Criterion (4).

Fig. 3.8 Correlation for the different FEM's: element size versus load step



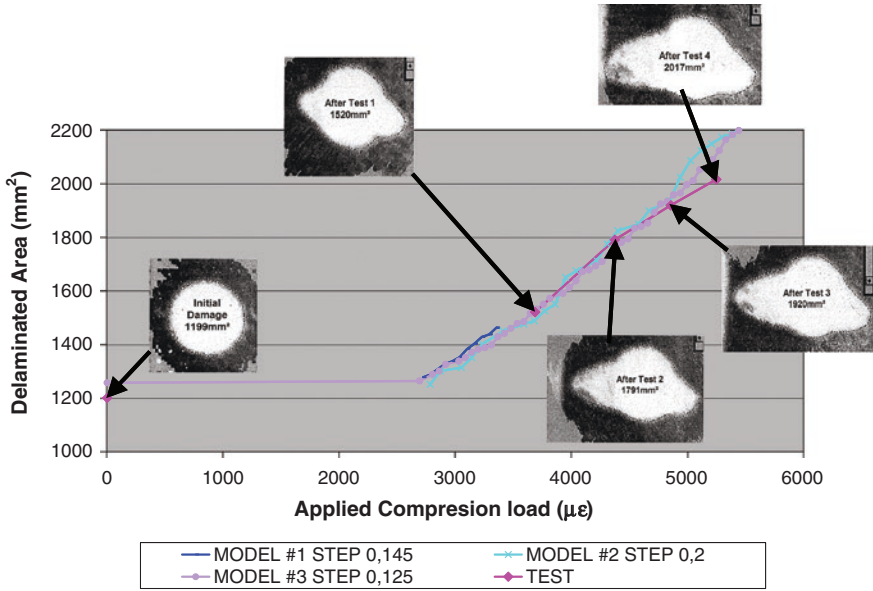
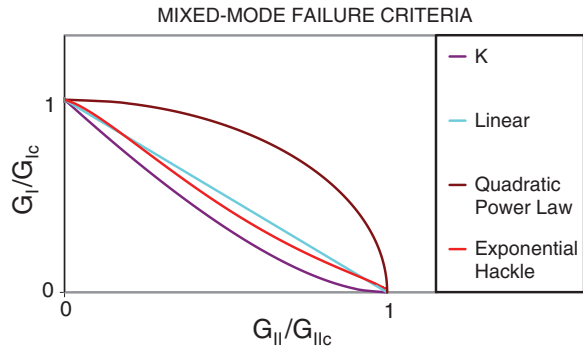


Fig. 3.9 Comparison of *optimized FEMs* and *experimental curves* (delamination photos ©Copyright QinetiQ Ltd)

Fig. 3.10 Comparison among different mixed-mode failure criteria



In Fig. 3.10 the shapes of the failure envelopes for the four criteria are shown. These envelopes are obtained as the combinations of SERR values (G_I and G_{II}) that (according to the different mixed-mode criteria) cause the delamination growth. G_{Ic} and G_{IIc} are, respectively, the inter-laminar fracture toughness for mode *I* and *II*. As already mentioned, the standard experimental tests used to evaluate these toughness are: DCB test for mode *I* [21], ENF test for mode *II*, and MMB test for mixed-mode conditions [22].

In Fig. 3.11 the “Delaminated Area versus Applied Load” curves, found by applying the four criteria, are shown. All the curves have been obtained by

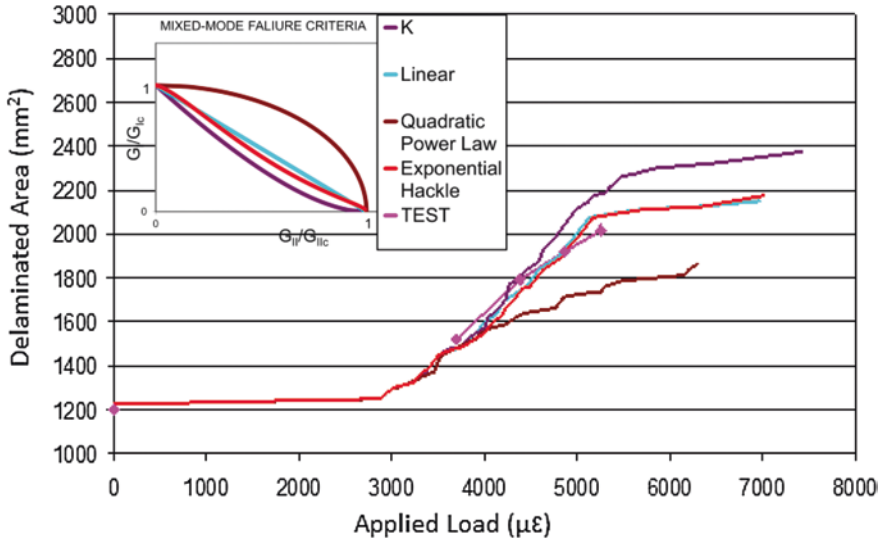


Fig. 3.11 Comparison among applied load—delamination area curves for the different failure criteria (load step 0.125 mm) and experimental results

applying the same displacement increment used in the tests i.e. the optimum load step size for FE model 3 (0.125 mm).

It can be seen that the solution given by the Linear and Exponential Hackle failure criteria are almost identical. This was expected since these two failure criteria are very similar. These two solutions also provide the best fit with experimental data while the worst solution was given by the quadratic failure criterion.

It can be seen from Fig. 3.11, the predicted load at which delamination starts to growth is the same for all the criteria, and the initial slope of the curve is very similar for all the criteria as well.

3.2.8 Conclusions and Future Work

Within the framework of The GARTEUR AG-32 R+D project focused in finding robust and reliable Finite Element Model (FEM) simulation methodologies for damage growth, INTA has developed an in-house numerical tool able to simulate delamination growth. The tool uses as inputs the Nastran solver input and results files. It is completely automated and provides options as growth criteria selection. The tool has been demonstrated to be robust and moderately cheap for a computation time perspective.

The benchmark used for validation purposes is a composite stiffened panel with a single bay delamination, The delamination growth has been supposed limited to the initial interface (no ply migration has been considered).

The main conclusion of the simulation results is that they are quite promising and consistent with experimental results. The following main considerations can be done:

- adequate prediction of delamination growth initiation;
- adequate prediction of delamination growth slope;
- shape of the delamination very similar to the experimental one across the loading process;
- identification of the mesh size dependency. Optimization of the results by providing specific rules to be followed when choosing the mesh size and the load step for the FE analysis;
- investigation on the influence of failure criteria used for delamination growth on the FE solution. Indeed the solution obtained with the Linear and Exponential Hackle failure criteria provides the best fit of the experimental data;
- good FE convergence and moderate computation times.

Therefore, it can be concluded that the feasibility of simulating the delamination growth process in a subcomponent structure, such as a stiffened composite panel, has been tested.

As future work, the investigation of the damage behaviour in other experimental benchmarks is desirable to further validate the procedure and the delamination growth tool. The following topics will be also investigated:

- delamination migration in the FE analysis;
- progressive failure in composites in terms of intra-laminar cracks;
- application of the developed methodology to panels with impact damage and multiple delaminations.

3.3 Debonding Growth

INTA is currently involved in an internal R+D project focused in finding robust and reliable FEM simulation methodologies for bonded structures. This project will be carried out at various levels, up to now work done is only at coupon level: mode I (Double Cantilever Beam or DCB) and mode II (End Notched Flexure or ENF). Two types of adhesives (adhesive film and paste) have been selected, both widely used in aircraft designs and repairs. The work presented in this chapter corresponds to *DCB* coupons using paste adhesive *Epibond 1590*.

INTA has performed detailed FEM simulations of DCB coupons based in Cohesive Zone Methodology (CZM), a Damage Mechanics Theory accounting for irreversible damage at interfaces, that it is well suited to model progressive failure of bonded joints [10–15].

To validate CZ FEM results, DCB tests have been carried out at INTA. A quite detailed correlation Simulations—Tests is shown in the next sections. The results found seem very promising and the correlation achieved is quite accurate. Our goal is to further develop the methodology analysing more complicated structures,

and also dealing with mixed-mode problems, for which no established methodology is still available.

3.3.1 FE Modelling of DCB Coupons

Double Cantilever Beam (DCB) coupons are one of the most used experimental tests to characterize *fracture toughness* of composites or adhesives in mode I (tension mode): G_{IC} . In Fig. 3.12 a scheme of a typical DCB test coupon is shown, basically it is composed of two identical sub-laminates, with an initial debond of length a_0 , and subjected to 2 transverse symmetrical forces F .

The standard used for this test is generally the ASTM 5528 [21], that was written originally to characterize fracture toughness of resins for composite laminates. However, it can be used, as well, to characterize adhesives fracture toughness G_{IC} .

Progressive debonding (growth) takes place in the coupon mid-plane, perpendicular to the loads applied, see Fig. 3.12. During tests, the curve “Applied Force F —Opening displacement δ ” is recorded (see Fig. 3.13), sometimes the physical crack length a is also monitored by optical methods. In [21] several data reduction methods approaches are recommended for calculating G_{IC} , such as the *Modified Beam Theory (MBT)*, the *Compliance Calibration Method (CC)*, and the *Modified Compliance Calibration (MCC) Method*.

The DCB coupons tested at INTA, have been manufactured from pre-preg material system: AS fibre/8552 epoxy resin, with an initial debond a_0 of 51 mm, and with the adhesive paste Epibond 1590 (typically used in repairs). The average adhesive thickness is 0.2 mm. Additional details on dimensions, materials, manufacturing, and laminates lay-ups can be found in [15].

The FE model of the coupon has been prepared by using a classical software tool in aeronautic industry such as Patran [26] for FEM generation and post-processing, Mentat to model adhesive CZ elements. Marc [27, 28] has been adopted as FE solver.

Fig. 3.12 Scheme of a DCB Test

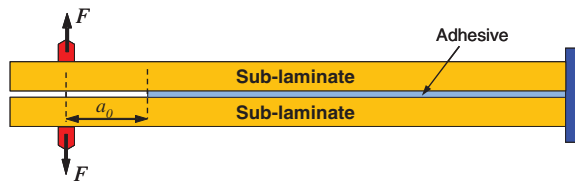


Fig. 3.13 Scheme of DCB Test

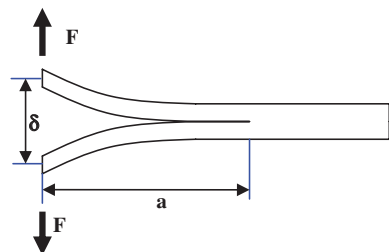


Fig. 3.14 General view of DCB FEM

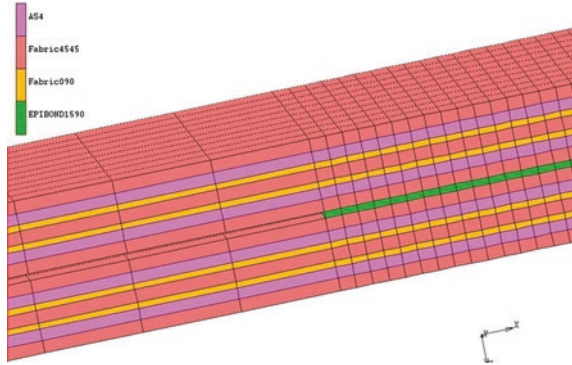
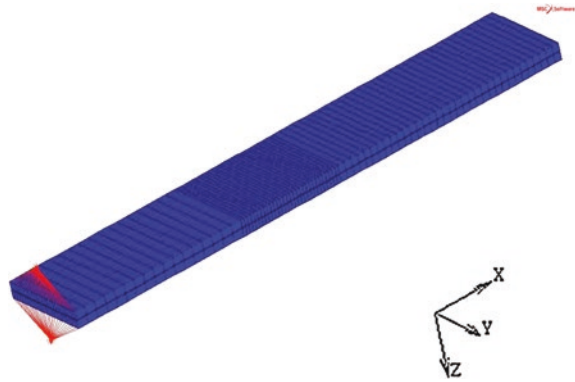


Fig. 3.15 DCB FEM boundary conditions



Regarding the laminates two types of elements were tested: composite solids (Marc element type 149) taking into account the laminate stacking sequence, and homogenous solid elements (Marc element type 7) which require the use of one solid element to model each ply. Although the composite solids seems, in principle, preferable due to the possibility to build FE models characterised by less elements, considerable convergence problems were found using this type of elements, so homogenous solid elements were used. In Fig. 3.14 a general view of the FE model is presented, clearly showing that both UD and fabric plies are modelled by means of solid elements. Adhesive (green colour elements in Fig. 3.14) is represented by *cohesive zone* (CZ) elements (type 188 in Marc), working in mode I tension mode.

Loads are applied by using MultiPoint Constraints (MPC), RBE2 type, as shown in Fig. 3.15.

3.3.2 Cohesive Zone (CZ) Elements

The basic idea of CZ can be dated in early 60s [29], Dugdale and others introduced models avoiding the unrealistic infinite stresses at crack tip characteristic of the Stress Intensity Factors (SIF) approach.

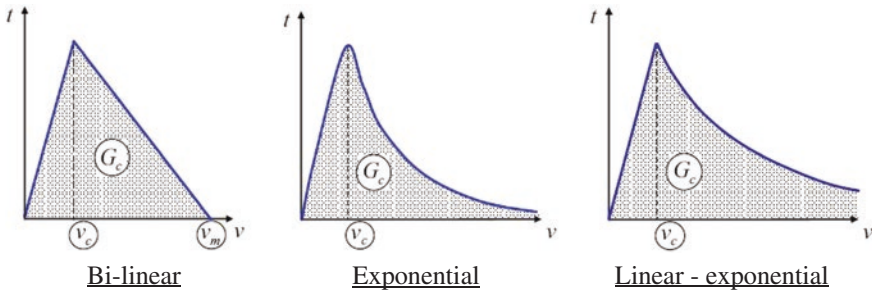


Fig. 3.16 Separation laws for cohesive elements

In FE models, CZ elements can be considered as *interface elements*, the traction vector t includes one normal component (mode I), and two tangential (modes II and III), and its mechanical behaviour follows a *phenomenological separation law* $t = f(v)$, being v the vector of nodal separations (3 components as the traction vector) in the CZ element. The most usual separation laws are bi-linear (used for fragile materials), exponential, and combined linear-exponential (see Fig. 3.16), these approaches are available in most FEM solvers (Marc, ANSYS, ABAQUS, etc.). The area enveloped by the curve corresponds to the material fracture toughness G_C .

The cohesive law considers a high non-linear behaviour: the first part is linear and reversible, but when separation in the element v exceeds the critical value v_c (maximum separation the elastic regime) the element is considered partially damaged and the behaviour is irreversible. If the deformation in the element is high enough ($v = v_m$) the FE solver de-activates the element by eliminating its contribution in transmitting forces. In such a way, the growth of debonding in the structure is simulated.

The three separation laws shown in Fig. 3.16 have been tested with the solver Marc, and the exponential approach was finally selected because it seems to be more adequate to model ductile materials and it allow an easier FE model convergence.

A typical inconvenient of CZ FEMs is how to account for *mixed-mode* analysis [30, 31], problems for which the CZ element support simultaneously forces and separations in modes I , II and III . This is not our case, adhesive in a DCB coupon works only in Mode I : t is the transverse force (peeling) transmitted by the element, v the relative transversal separation of CZ element, and G_C value is G_{IC} .

3.3.3 Mesh Dependency

It is well know that CZ FE models are mesh dependent, or in other words CZ FEM results depend of the mesh size (size of the elements in the relevant direction that represent the adhesive in the FEM). Several researchers have worked on this topic

[14, 15], proposing several solutions. One of the suggested approaches consists in adapting the material allowables. For the application presented in this section, the adhesive maximum peeling stress would become function of the mesh size.

In this section a rather complex theory based on energy considerations, and taking into account the Dugdale model for transverse stresses around a crack tip in a plastic material [29], and CZ FEM stresses based in Irwin/Bazant model [32] is adopted. This theory is represented by the following equation:

$$l_{CZ} = M \frac{E_{33} G_{IC}}{\sigma_o^2} \tag{3.6}$$

being:

- l_{CZ} : *cohesive zone length*: adhesive length that has been irreversibly damaged. It is the distance, along coupon longitudinal axis, between the physical front (end) of the adhesive, and the so-called *mathematical adhesive front* (position of maximum peeling stress in the adhesive).
- M : constant dependent of the CZ model used. The models most typically used are Hillerborg [33]: $M = 1$, and Rice [34]: $M = 9\pi/32 \approx 0.88$.
- G_{IC} : Adhesive fracture toughness in mode I found experimentally (see next section): 211.7 J/m^2 .
- σ_o : adhesive allowable at tension (t value of CZ element curves). For Epibond 1590 it is used a value of 54 MPa. This value has been derived from manufacturer test data on Single Lap Shear (SLS) coupons, using Von-Misses theory.
- E_{33} : Sub-laminate elasticity modulus in transverse direction 3: 10.8 GPa.

More details of how to derive Eq. (3.6) can be found in [14, 15]. To determine an adequate value for the constant M a *detailed* DCB FE model was created using a mesh size of $62.5 \mu\text{m}$, see Fig. 3.17. This FE model is not suitable for progressive debonding analysis (too many elements and difficulties in convergence). The non-linear analysis is performed by applying a load able to make the first CZ adhesive element reaching its maximum deformation capability v_m . Therefore this element transmits almost no stress although it has not been *de-activated*, i.e. still there is no de-bonding propagation.

Fig. 3.17 σ_3 stress (*peeling*) colour plot in the adhesive front (detailed DCB FE model)

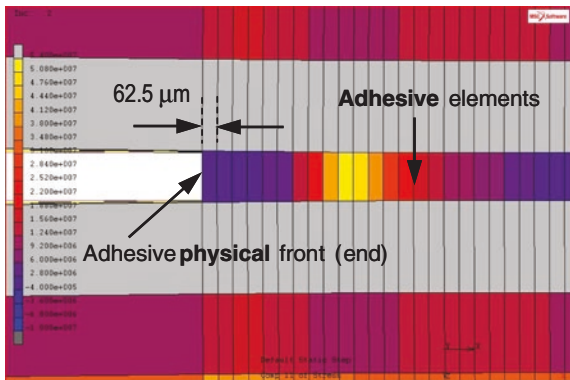
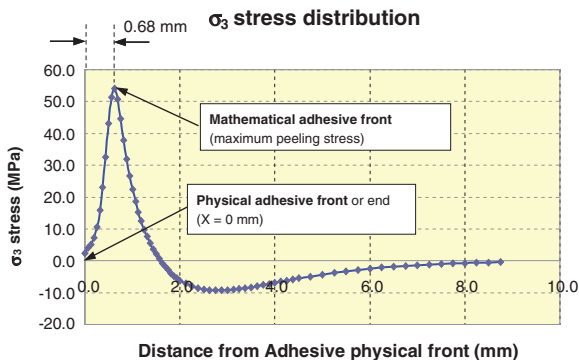


Fig. 3.18 σ_3 stress (peeling) in the adhesive elements



In Fig. 3.18 the σ_3 stress distribution in the CZ adhesive elements is shown. As it can be seen in the Figure, the cohesive zone length l_{CZ} predicted by the FE model is approximately 0.68 mm, that according to formula (3.1) gives an M value of 0.862, very close to the Rice value [34] for M ($9\pi/32 \approx 0.88$).

When using a FE model with a coarser mesh, the CZ length will not be accurately predicted by the FEM because there are not enough elements in the adhesive front to capture the high stress concentration. However there is a relation between the CZ length calculated by the FE model l_{CZ}^* (different from l_{CZ} predicted by the detailed DCB FE model) and the maximum stress in the adhesive σ_{max}^* [14, 15]:

$$l_{CZ}^*(\sigma_{max}^*)^2 = ME_{33}G_{IC} \quad (3.7)$$

So from Eq. (3.7) the σ_{max}^* value (allowable or maximum stress value of the CZ elements) can be considered a function of the CZ length predicted by the FEM l_{CZ}^* . Consequently σ_{max}^* can be considered a function of the mesh size l_e (element length along X axis) if the mesh size is chosen adequately such as $l_e = l_{CZ}^*/N_e$ (being N_e the number of adhesive elements in the CZ length). With such a choice of mesh size and maximum stress, according to Eq. (3.8), it can be expected that the coarser FE model will provide quite accurate results in terms of global behaviour. This is shown in formula (3.7), and explained in more detail in [15]. The general recommendation for N_e is to use a value between 3 and 10.

$$\sigma_{max}^* = \sqrt{\frac{ME_{33}G_{IC}}{N_e l_e}} \quad (3.8)$$

3.3.4 Experimental Results on DCB Coupons

In Fig. 3.19 pictures of the mode I DCB tests carried out at INTA are shown.

In Fig. 3.20, the experimental curves: load applied F (N) versus opening displacement δ (mm), are shown for the 5 coupons tested: **P1** to **P5**. As it can be seen, except for the coupon **P2**, that behaves relatively differently, the other 4 coupons

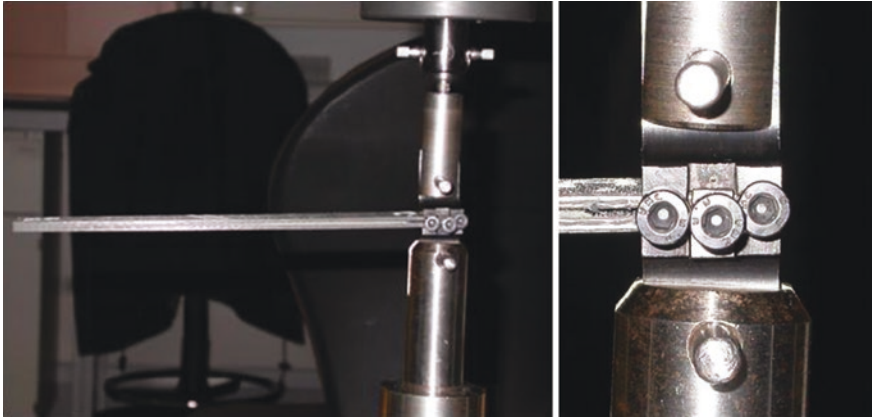
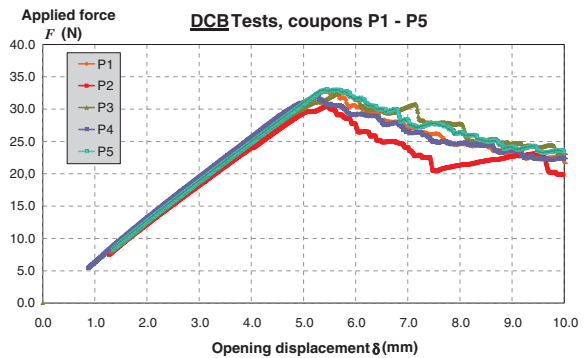


Fig. 3.19 Experimental tests on DCB coupon

Fig. 3.20 Experimental DCB curves: applied force F versus opening displacement δ



show a relatively repeatable mechanical behaviour in terms of *initial slope*, *maximum load*, and *negative curve slope* beyond maximum load.

The reason for the P2 different behaviour can be probably found to the poor surface preparation or to an inadequate quality control of the bonding process. In fact adhesive joints mechanical properties are strongly dependent on the bonding process and the quality control used to prepare the coupons rather than on the specific adhesive used.

Form these curves, by using the recommended methods in [21] *Modified Beam Theory (MBT)*, and *Compliance Calibration method (CC)* the adhesive Mode I Interlaminar Fracture Toughness G_{IC} was derived (see [15] for details). The average value derived from those methods, and later to be used in FEM simulations is 211.7 J/m^2 .

3.3.5 Correlation FE Model Simulation—Tests—DCB Coupons

As above mentioned, a very fine mesh FEM (mesh size 62.5 μm) was created only for “calibration” purposes, i.e. for the derivation of the constant M required to adapt the adhesive peeling allowable σ_o , but not for the simulation of the DCB coupon *progressive debonding*.

To this last purpose, 4 different FE models with coarser meshes were prepared. The element length l_e along X axis (longitudinal coupon axis) in the debonding growth zone has been set, respectively, to 2, 1, 0.5, and 0.25 mm. Details about the total number of elements of each FEM can be found in [15]. In Figs. 3.21 and 3.22 the FE models with l_e set to 2 and 0.25 mm are shown.

As already mentioned, Marc has been used to perform static non-linear analyses, giving in output the stresses in the adhesive elements and node displacements. The adhesive fracture toughness used in the models in mode I is $G_{IC} = 211.7 \text{ J/m}^2$, and the maximum transverse peeling stress σ_o considered for the analysis is 54 MPa. This s_o value has been derived from manufacturer test data.

In Fig. 3.23, the Applied Force versus opening displacement curve predicted with 3 DCB FE models (with l_e set to 0.25, 0.5, and 1 mm) are presented. As it can be seen, the predicted maximum value of the Applied Force increases with mesh size. This behaviour, already reported by other authors, was expected.

Fig. 3.21 FEM of mesh size $l_e = 2$ mm. Total FEM size 7,480 elements

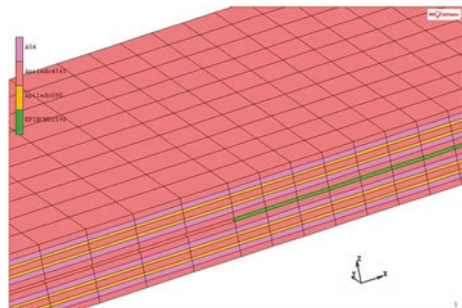
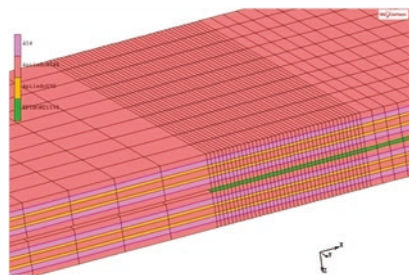


Fig. 3.22 FEM of mesh size $l_e = 0.25$ mm. Total FEM size 12,880 elements



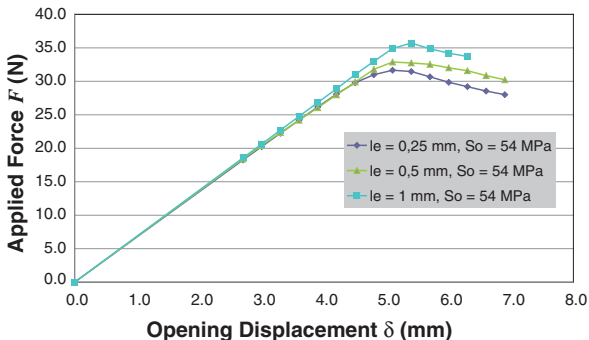


Fig. 3.23 Curves applied force versus opening displacement found by the non-adapted FEM

Therefore, another set of analyses has been carried out by adapting the allowable transverse peeling stress σ_o of the adhesive (maximum value of CZ characteristic curve), as a function of the mesh size along X axis according to formulas (3.7) and (3.8). The analyses have been carried out by using $N_e = 3$ and 5 (i.e. 3 or 5 elements in the CZ length). In Fig. 3.24 the allowable value used in CZ elements for peeling stress σ_o (MPa) in the adhesive, is shown function of the FE model mesh size along X axis (in mm).

In Fig. 3.25, a comparison between experimental and CZ FEM simulation “load applied versus opening displacement” curves is presented. For the experimental tests only the curves of coupons P1, P3, P4 and P5 are presented. The FE models curves have been obtained with the 4 different FE models above explained and $N_e = 5$.

As it can be seen, all experimental and numerical curves are quite similar and the correlation is quite accurate in terms of initial curve slope, maximum load, and negative curve slope beyond maximum load. It can be concluded that the proposed CZ FE methodology is accurate, and, in particular, that the relatively coarse FE model (for instance the one with mesh size of 2 mm) can be used to model progressive coupon debonding with high accuracy. Moreover, the proposed CZ methodology overcomes the problem of mesh size dependence.

Fig. 3.24 σ_o adaptation function of FEM mesh size

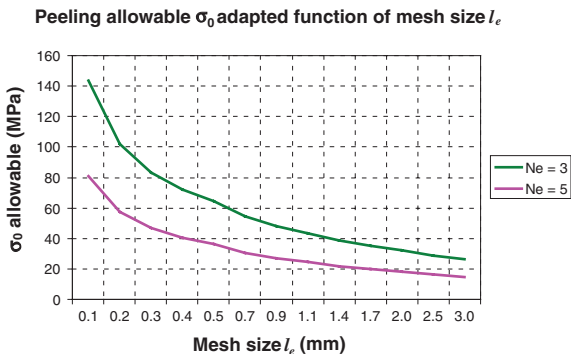
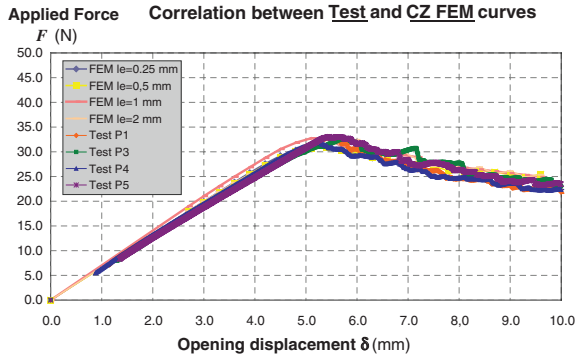


Fig. 3.25 Correlation between experimental and CZ FEM “Load versus opening displacement” curves



Another result, not directly comparable with experiments, has been derived from the CZ FE models and used to verify its robust and coherent behaviour. In Fig. 3.26 the peeling stress σ_3 is shown for the calibration FE model (very fine mesh, element size = 62.5 μm), and for the one with mesh size set to 0.5 mm. As it was already mentioned, being N_e set to 5, the maximum stress σ_3 takes place at the 5th node. Furthermore, the CZ length predicted by the coarser model is much larger than the one predicted by the fine model, while the maximum stress is obviously inferior to the physical adhesive allowable for peeling stress because it was “adapted” to the mesh size.

It is important anyway to recall that the methodology used, makes that global FEM behaviour (for instance concerning the “applied load versus opening displacement” curves) similar for all mesh sizes, but of course “locally” the behaviour is different and not representative for coarse FE models.

In Fig. 3.27, the *crack length* a , i.e. the distance between the force application point and the node in the adhesive with zero peeling stress, is shown as a function of the opening displacement of the DCB coupon. Three curves are shown, representative of the behaviour of the three CZ FE models with mesh sizes set to 2, 1, and 0.5 mm. As it can be seen, the 3 FE models predict basically the same crack growth, so again global FE model behaviour is similar in all cases, and the trick used to avoid mesh dependence seems adequate.

Fig. 3.26 Comparison of σ_3 stress in the adhesive for mesh sizes $l_e = 62.5 \mu\text{m}$ and $l_e = 0.5 \text{ mm}$

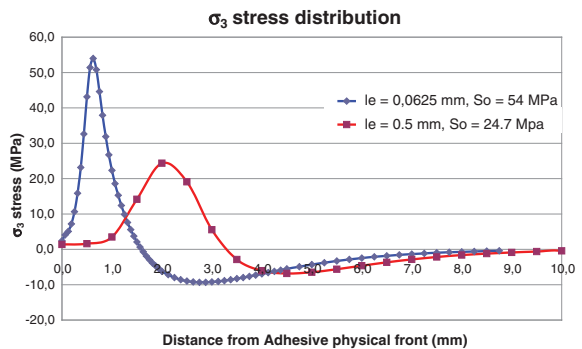
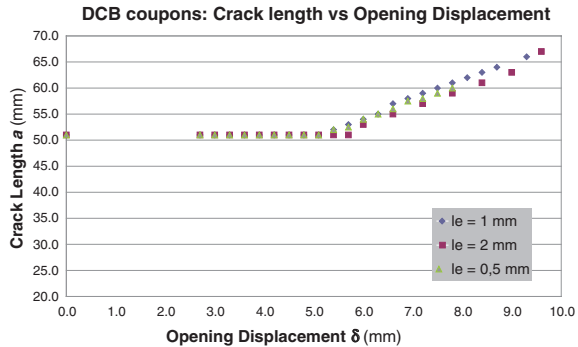


Fig. 3.27 Crack length versus opening displacement



3.3.6 Conclusions and Future Work

In this section a methodology to predict progressive debonding by means of *Cohesive Zone (CZ)* FE models has been introduced. The methodology is able to analyze bonded structures working in mode *I* (tension mode), and has been applied to *Double Cantilever Beam DCB* coupons that has been manufactured and tested at the Spanish research centre for aerospace (INTA).

The following considerations can be drawn:

- CZ FE models have been prepared by using classical software tools in the aeronautic industry: Patran (for the generation of most of the FEM and post-processing), Mentat (to model adhesive CZ elements), and Marc (solver). Elements used are homogenous solid elements.
- Experimental tests were carried out at INTA on 5 DCB coupons, manufactured by pre-preg method with AS fibre and 8552 epoxy resin, adhesive is paste Epibond 1590. For these coupons the curve “applied load—opening displacement” was obtained. Based in these curves, the adhesive fracture toughness in mode *I* G_{IC} was found to be 211.7 J/m^2 .
- A set of FE models using different mesh sizes have been used for the simulations. In each FE model the adhesive allowable peeling stress has been modified as a function of the mesh size. It has been found that all FE models yield the same results, so *mesh size dependency*, a typical drawback of CZ FE models, has been easily solved.
- The correlation between FE simulations and test results has been found quite good. All the relevant parameters of load—opening displacement curve: *initial curve slope*, *maximum load*, and *negative curve slope* beyond maximum load, were found to be very similar in all the CZ FE simulations and comparable to the experimental values.
- Additional results, not directly comparable with experiments, has been derived from the CZ FE models. Indeed the local peeling stress σ_3 in the cohesive length zone and the curve *crack length* function of the applied opening displacement were found to be coherent with theory used to adapt adhesive allowables

to mesh size. The curves found with the different FE models (different mesh sizes), were very similar, so we can be sure that the allowable adaptation methodology does not modify the global FEM behaviour.

The final conclusion, being the presented results quite promising, is that the applied methodology to simulate Progressive Failure Analysis (PFA) of bonded structures in mode *I* has been proved to be robust, computationally efficient, and quite accurate showing a good correlation with experimental data.

It has been shown that mesh size dependency can be compensated by adapting adhesive allowables. Therefore CZ FE models do not require to be very fine to get accurate FPA predictions.

The INTA plan for future work is to extend the proposed methodology to analyse problems in mode *II* (ENF coupons for instance) and *mixed-mode* problems (for which, right now, there is no established methodology). Moreover, in the future, the proposed methodology will be applied to analyze the *progressive failure* of more complex bonded structures.

References

1. Krueger, R.: The virtual crack closure technique: history, approach and applications. NASA/CR-2002-211628, ICASE Report No. 2002-10. ICASE, NASA Langley Research Center, Hampton, Virginia (2002)
2. Nilsson, K.-F., Asp, L.E., Alpmann, J.E., Nystedt, L.: Delamination buckling and growth for delaminations at different depths in a slender composite panel. *Int. J. Solids Struct.* **38**, 3039–3071 (2001)
3. San Millán, J., Castañón, M., Armendáriz, I., Gonzalez, R., García-Martínez, J.: Simulation tools for progressive damage. NAFEMS World Congress, Crete (2009)
4. Krueger, R., Minguet, P.J., O'Brien, T.K.: Implementation of interlaminar fracture mechanics in design: an overview. In: 14th International Conference on Composite Materials (ICCM-14), San Diego (2003)
5. Ullah, H., Harland, A.R., Lucas, T., Price, D., Silberschmidt, V.V.: Finite-element modelling of bending of CFRP laminates: multiple delaminations. *Comput. Mater. Sci.* **52**, 147–156 (2012)
6. Armendáriz, I., González, R., San Millán, J., García-Martínez, J.: Delamination growth in damage tolerance composite structures. In: 9th International Conference on Composite Science and Technology, Sorrento (2013)
7. Shokrieh, M.M., Rajabpour-Shirazi, H., Heidari-Rarani, M., Haghpanahi, M.: Simulation of mode I delamination propagation in multidirectional composites with R-curve effects using VCCT method. *Comput. Mater. Sci.* **65**, 66–73 (2012)
8. Liu, P.F., Hou, S.J., Chu, J.K., Hub, X.Y., Zhou, C.L., Liu, Y.L., Zheng, J.Y., Zhao, A., Yan, L.: Finite element analysis of postbuckling and delamination of composite laminates using virtual crack closure technique. *Compos. Struct.* **93**, 1549–1560 (2011)
9. Xie, D., Biggers Jr, S.B.: Progressive crack growth analysis using interface element based on the virtual crack closure technique. *Finite Elem. Anal. Des.* **42**, 977–984 (2006)
10. Davies, G.A.O., Hitchings, D., Ankersen, J.: Predicting delamination and debonding in modern aerospace composite structures. *Compos. Sci. Technol.* **66**, 846–854 (2006)
11. Chen, J., Crisfield, M., Kinloch, A., Busso, E., Mathews, F., Qiu, Y.: Predicting progressive delamination of composite material specimens via interface elements. *Mech. Compos. Mater. Struct.* **6**, 301–317 (1999)

12. Segurado, J., Llorca, J.: A new three-dimensional interface finite element to simulate fracture in composites. *Int. J. Solids Struct.* **41**, 2977–2993 (2004)
13. Elices, M., Guinea, G.V., Gómez, J., Planas, J.: The cohesive zone model: advantages, limitations and challenges. *Eng. Fract. Mech.* **69**(2), 137–163 (2002)
14. Turon, A., Davila, C.G., Camanho, P.P., Costa, J.: An engineering solution for solving mesh size effects in the simulation of delamination with cohesive zone models. *Eng. Fract. Mech.* **74**, 1665–1682 (2007)
15. San Millán, J., Vázquez, L., González, R., Matías, D., Vergniory, U.: Progressive failure of composite bonded joints. In: *Proceedings of 3rd European Conference for AeroSpace Sciences (EUCASS)* (2009)
16. MSC Nastran 2012: Linear Static Analysis, User's Guide. MSC Software Corporation (2012)
17. MSC Nastran 2012: Quick Reference Guide. MSC Software Corporation (2012)
18. Rybicki, E.F., Kanniken, M.F.: A finite element calculation of stress intensity factors by a modified crack closure integral. *Eng. Fract. Mech.* **9**(4), 931–938 (1977)
19. Orifici, A.C., Krueger, Ronald: Benchmark assessment of automated delamination propagation capabilities in finite element codes for static loading. *Finite Elem. Anal. Des.* **54**, 28–36 (2012)
20. Leski, A.: Implementation of the virtual crack closure technique in engineering FE calculations. *Finite Elem. Anal. Des.* **43**, 261–268 (2007)
21. ASTM D 5528: Standard Test Method for Mode I Interlaminar Fracture Toughness of Unidirectional Fiber-Reinforced Polymer Matrix Composites
22. ASTM D 6671: Standard Test Method for Mixed Mode I-Mode II Interlaminar Fracture Toughness of Unidirectional Fiber Reinforced Polymer Matrix Composites
23. Donaldson, S.L.: Fracture toughness testing of graphite/epoxy and graphite/peek composites. *Composites* **16**(2), 103–112 (1985)
24. Orifici, A.C., Herszberg, I., Thomson, R.S.: Review of methodologies for composite material modelling incorporating failure. *Compos. Struct.* **86**, 194–210 (2008)
25. Greenhalgh, E., Meeks, C., Clarke, A., Thatcher, J.: The performance of post-buckled CFRP stringer-stiffened panels containing defects and damage. In: *44th AIAA Structures, Structural Dynamics and Materials Conference, Norfolk* (2003)
26. Patran 2012 Reference Manual. Part 3: Finite Element Modeling. MSC Software Corporation (2012)
27. Marc 2012 User's Guide. MSC Software Corporation (2012)
28. Marc 2012 Volume A: Theory and User Information. MSC Software Corporation (2012)
29. Dugdale, D.S.: Yielding of steel sheets containing slits. *J. Mech. Phys. Solids* **8**, 100–104 (1960)
30. Ruiz, G., Pandolfi, A., Ortiz, M.: Three dimensional cohesive modelling of dynamic mixed-mode fracture. *Int. J. Numer. Methods Eng.* **52**, 97–120 (2001)
31. De Xie., Wass, A.M.: Discrete cohesive zone model for mixed-mode fracture using finite element analysis. *Eng. Fract. Mech.* **73**(13), 1783–1796 (2006)
32. Bazant, Z.P., Planas, J.: *Fracture and Size Effect in Concrete and Other Quasibrittle Materials*. CRC Press, Boca Raton (1998)
33. Hillerborg, A., Modeer, M., Petersson, P.E.: Analysis of crack formation and crack growth in concrete by means of fracture mechanics and finite elements. *Cem. Concr. Res.* **6**, 773–781 (1976)
34. Falk, M.L., Needleman, A., Rice, J.R.: A critical evaluation of cohesive zone models of dynamic fracture. *J. Phys. IV France* **11 Pr5**, 43–50 (2001)

Chapter 4

Delamination Growth in Composite Plates Under Fatigue Loading Conditions

Aniello Riccio, Andrea Sellitto and Rocco Ricchiuto

4.1 Introduction

Composite materials are usually characterized by very extraordinary specific strength and stiffness properties which can be strongly affected by intra-laminar and inter-laminar damages [1–6]. In particular, delaminations can be strongly influenced by the fatigue induced material degradation which can initiate delamination growth phenomena at a relatively low number of cycles gradually leading to the increase of the damaged area and to the reduction of the overall structural stiffness [7].

Historically, it was a common belief that composite materials did not suffer degradation phenomena under fatigue loading conditions [8]. In 1970, experimental tests on composite material with unidirectional fibers (CFRP) led to the interpretation that these materials had superior fatigue properties than metallic ones, and that the design of the components would not have been limited by their fatigue performances. As a matter of facts, most of the CFRP are extremely stiff along the fibre direction: in such a way, the cyclic loads during the test were well below the damage initiation values leading to no degradation of the material performances even for very high cycle numbers. Indeed, for multi-directional composites, the damage initiation would have led to the weakening of the structure subjected to cyclic loading.

As a matter of facts, despite the composites have excellent fatigue performance, a pre-existing damage in structures can propagate under a fatigue load, leading to a continuous deterioration of the material, a gradual increase of the area of damage and a reduction of the stiffness of the overall structure, up to the final collapse.

A. Riccio (✉) · A. Sellitto · R. Ricchiuto
Department of Industrial and Information Engineering, Second University of Naples,
via Roma n 29, 81031 Aversa, Italy
e-mail: aniello.riccio@unina2.it

The wide range of applications of composite materials and the tendency to design structures by reducing safety factors has increased the need for the understanding and the development of numerical methods to study the behavior of their fatigue life; however, the diversity and the complexity of the mechanisms characterizing the behavior of composite structures subjected to fatigue load make their analysis to be extremely complicated.

Commercial FE platforms usually use built in module to predict the fatigue behavior of structural components. However these fatigue modules, usually are based on linear formulations and cannot be adopted when geometrical non-linearity are involved in computations. This is the case of the compression induced delamination growth taking place as a consequence of the delamination buckling phenomenon which involves large displacements and rotations.

In the present chapter an algorithm is proposed which, by means of non-linear analyses, can correlate the increase of delaminated area to fatigue cycles. The proposed algorithm adopts Paris Law formulation based propagation criterion which can take into account the local damage accumulation along the delamination front.

In order to test the effectiveness of the proposed numerical approach, the fatigue behavior of a delaminated panel with a central hole has been simulated and the obtained numerical results have been compared with literature experimental results [9]. A sensitivity analysis is also introduced showing the influence of delamination size and position on the fatigue induced delamination growth.

4.2 Fatigue Degradation: Linear Approach

The fatigue life may be subdivided in two different stages: crack initiation phase and crack growth phase [10, 11]. High-cycle fatigue loads (elevated number of cycles at a relatively low stress state) are more likely able to induce the crack onset while low-cycle fatigue loads (reduced number of cycles at a relatively high stress state) are critical for the crack growth phase.

To determine the fatigue life by simulations, it is necessary to predict the behaviour of cracks in materials and to establish if a certain component will fail. As a consequence of the investigation of the stress field around the crack tip, Irwin introduced the *stress intensity factor (SIF) K* for static fracture analysis [12]:

$$K = F\sigma\sqrt{\pi a} \quad (4.1)$$

where:

- a is the crack length;
- F is the geometry factor depending on the relative crack length;
- σ is the applied stress;
- K is a parameter to identify the magnitude of the stress range that occurs near the apex of the crack and it is not a characteristic of the material.

If the stress varies between two reference values, σ_{\min} and σ_{\max} , the state of the stress can be characterized by the fluctuation of the stress intensity factor, defined as:

$$\Delta K = K_{\max} - K_{\min} = F(\sigma_{\max} - \sigma_{\min})\sqrt{\pi a} = F \Delta\sigma \sqrt{\pi a} \quad (4.2)$$

Fatigue crack growth models are empirical models generally based on fracture mechanics. In 1961, Paris et al. [13] explained the transition between crack initiation and growth phase as a correlation between crack growth rate, defined as da/dN , the stress intensity factor range, ΔK , and the loading ratio, R , defined as the ratio between the maximum and the minimum load during the cycling phenomenon. Such correlation is defined as:

$$\frac{da}{dN} = f(\Delta K, R) \quad (4.3)$$

Since K is directly proportional to the load during the cycle, the parameter R can also be expressed by the ratio between the maximum and the minimum value assumed by the stress intensity factor:

$$R = \frac{K_{\max}}{K_{\min}} \quad (4.4)$$

The simple empirical equation proposed by Paris applies the Linear Elastic Fracture Mechanics (LEFM) to fatigue and represents the rate of crack propagation. Paris' Law can also be expressed as:

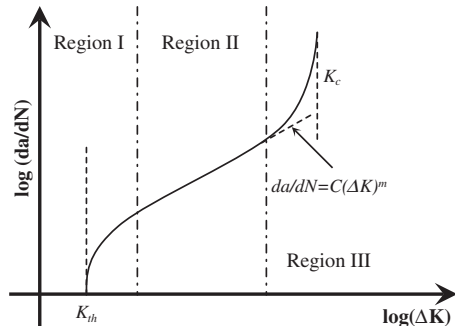
$$\frac{da}{dN} = C(\Delta K)^m \quad (4.5)$$

where C and m are constants which depend on material, temperature, frequency of the load cycles and environment.

The fatigue rate curve is shown in Fig. 4.1 and is divided into three regions defined as Region I, Region II, Region III [14].

Region I represents the early development of the fatigue crack, where the growth rate is 10^{-6} mm/cycle or below. The most important feature in this region is the Fatigue Crack Growth (FCG) threshold, K_{th} . This parameter represents the

Fig. 4.1 Fatigue rate curve



onset value of the fatigue cracks propagation. For SIF ranges below the K_{th} , crack growth would not occur.

Region II is the intermediate zone where growth rates are between 10^{-6} and 10^{-3} mm/cycle. In this region the crack growth is stable and follows a power equation. In this region, the results are strongly influenced by the mean stress. If Region II includes the dominating part of the fatigue life, the phenomenon can be directly estimated by integrating Paris' law.

The last part of the chart, **Region III**, starts where the curve changes curvature, and the growth rates are equal or above 10^{-3} mm/cycle. This high crack growth rates are caused by the rapid and unstable crack propagation prior to final failure. In this region, the curve becomes asymptotic to the value assumed by the fracture toughness, K_c , of the material. The influence of nonlinear properties cannot be ignored due to the presence of a large scale yielding: this leads to the need to adopt the non-linear fracture mechanics instead of the linear approach. The study of the phenomenon in this region is very complex because of the high values of da/dN that results in a very brief fatigue life.

4.3 Fatigue Degradation: Non-linear Approach

The approach shown in Sect. 4.2 is based on linear formulations that cannot be adopted when geometrical non-linearity are involved in computations. This is the case of the compression induced delamination growth taking place as a consequence of the delamination buckling phenomenon which involves large displacements and rotations.

To overcome this issue, an algorithm, first proposed by Shen [9], is adopted, which, by means of non-linear analyses, can correlate the increase of delaminated area to fatigue cycles. The proposed algorithm adopts a propagation criterion which is very similar to the Paris Law formulation and, based on the Energy Release Rate evaluation, can take into account the local damage increase along the delamination front.

The method estimates the cycle number at which the delamination will propagate by performing a non-linear analysis for each fatigue cycle according to the following procedure [15], adopted for each i th fatigue cycle:

- the peak load of the fatigue cycle is applied on the structure, performing a geometrically non-linear Finite Element Analysis;
- the values of the Energy Release Rate at each j th node of delamination front are evaluated;
- the variation of the delaminated area due to the load cycles $\Delta A/\Delta N$ is obtained from the following equation:

$$\frac{\Delta A_j}{\Delta N_j} = c_1 \left(\frac{G_{Ij}}{G_{Ic}} \right)^{c_3} + c_2 \left(\frac{G_{IIj}}{G_{IIc}} \right)^{c_4} \quad (4.6)$$

where c_1 , c_2 , c_3 , and c_4 are material constants to be determined experimentally, ΔA_j is the increase in delaminated area when the j th node on the delamination front is released, G_{Ij} and G_{IIj} are respectively the fracture modes I and II Strain Energy Release Rate components for the j th node of the delamination front, ΔN_j is the equivalent number of cycle at which the j th node will be released leading to the delaminated area variation ΔA_j , G_{Ic} and G_{IIc} are the material fracture toughness for the fracture modes I and II respectively;

- Knowing the increase in delaminated area ΔA_j associated to the releasing of the j th node on the delamination front, the values of ΔN_j are obtained by inverting Eq. (4.6) for each j -th node:

$$\Delta N_j = \frac{\Delta A_j}{c_1 \left(\frac{G_{Ij}}{G_{Ic}}\right)^{c_3} + c_2 \left(\frac{G_{IIj}}{G_{IIc}}\right)^{c_4}} \quad (4.7)$$

- A damage coefficient vector D , that takes into account the effects of the fatigue damage during the cyclic load, is initialized for each node of the delamination front;

$$D_j^{(0)} = 0 \quad (4.8)$$

- The node k , which is the node among the j -th ones on the delamination front which minimize the value expressed in Eq. (4.4), is selected:

$$\Delta N_k^{(i)} \left(1 - D_k^{(i-1)}\right) \quad (4.9)$$

- Assuming the damage will propagate exclusively at the end of the cyclic load, the value ΔN_k is approximated to the smallest integer greater than or equal to it. The damage coefficient vector D_j is updated for each node of the delamination front according to the following relations:

$$\begin{aligned} \Delta D_j^{(i)} &= \frac{\Delta N_k^{(i)}}{\Delta N_j^{(i)}} \left(1 - D_k^{(i-1)}\right) \\ D_j^{(i)} &= D_j^{(i-1)} + \Delta D_j^{(i)} \end{aligned} \quad (4.10)$$

- The m -th node(s) with value of D_j equal or greater than 1 are released allowing delamination growth, and the corresponding damage coefficient is re-set to 0. The actual number of fatigue cycles and the total delaminated area are updated according to Eqs. (4.7) and (4.8) respectively:

$$D_m^{(i)} = 0 \quad (4.11)$$

$$N^{(i)} = N^{(i-1)} + \Delta N_m^{(i)} \left(1 - D_m^{(i-1)}\right) \quad (4.12)$$

$$A^{(i)} = A^{(i-1)} + \Delta A \quad (4.13)$$

The fatigue life has been simulated via non-linear analyses, which provide the distributions of G_I and G_{II} along the delamination front. These distributions are used to estimate the number of cycles associated with the propagation of delamination and the node to be released. The process is iterated until the maximum number of cycles is reached or until the delamination is fully propagated.

4.4 Numerical Application: Delamination Growth in a Composite Panel Subjected to Fatigue Load

The algorithm has been tested over the holed delaminated panel shown in Fig. 4.2.

The thickness of the panel and the position of the delamination through the width are shown in Fig. 4.3.

The panel is modeled according to the geometrical description provided in Fig. 4.2 and to the numerical values provided in Table 4.1; moreover, the delamination has been positioned at a depth t_1 of 0.28 mm, as shown in Fig. 4.3.

Three different zones have been identified:

- The **Zone I**, the green one in Fig. 4.2, is the initial r_2 radius delaminated area. The nodes with identical coordinates that lies on the delaminated interface belonging to the upper and the lower sub-laminates are let free.

Fig. 4.2 Holed panel: zone and boundary conditions

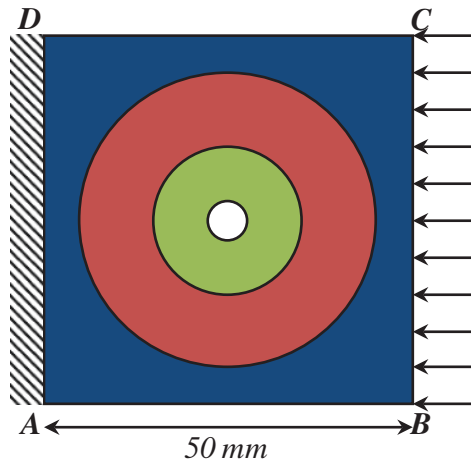


Fig. 4.3 Site of the delamination through the thickness

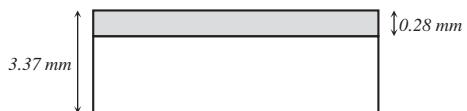


Table 4.1 Geometrical and material data of the panel

<i>Geometry</i>						
AB (mm)	t (mm)	t ₁ (mm)	r ₁ (mm)	r ₂ (mm)	r ₃ (mm)	
50	3.37	0.28	2.5	10	20	
<i>Material</i>						
E ₁ = E ₂ [GPa]	E ₃ (GPa)	G ₁₂ (GPa)	G ₂₃ = G ₁₃ (GPa)	ν ₁₂ = ν ₁₃ = ν ₂₃	G _{Ic} (J/m ²)	G _{IIc} (J/m ²)
42.5	14.5	17.4	0.85	0.22	103	456

Contact criteria have been defined over the interface to avoid element compen-etration during the analysis.

- The **Zone II**, the red one in Fig. 4.2, is the r₃ radius area where delamination is allowed. The corresponding nodes of the upper and lower sub-laminate are initially connected by MPC, and set free if a propagation will occur. As in Zone I, also in Zone II contact criteria have been defined over the interface to avoid compenetration of the propagated elements during the analysis.
- The **Zone III**, the blue one in Fig. 4.2, is the undamaged area. Nodes on the interface are merged and delamination is not allowed in this zone.

According to Fig. 4.2, the side BC of the specimen is subjected to the compressive load of 28 kN, while the side AD of the specimen is clamped. The material adopted is a woven fabric and the panel has been modeled with first-order 3D elements. In Fig. 4.4 the numerical model is shown.

Figure 4.5 shows the local buckling of the upper sub-laminate, while in Fig. 4.6 the values of G_I and G_{II} for a quarter of the structure are reported. The maximum values of the Energy Release Rate have been obtained orthogonally to the applied load, where the growth of the delamination is expected.

The delamination growth under fatigue load has been simulated. Figure 4.7 compares the local buckling relative to the first and to the 287,039th cycle.

Table 4.2 reports the out of plane displacements as well as the delaminated area for a number of fatigue cycles allowing to qualitatively follow the delamination growth evolution during the fatigue analysis.

The numerical results, in terms of propagation of delaminated area as a function of fatigue cycles are in excellent agreement with the experimental data, as reported in Fig. 4.8.

Fig. 4.4 Numerical model

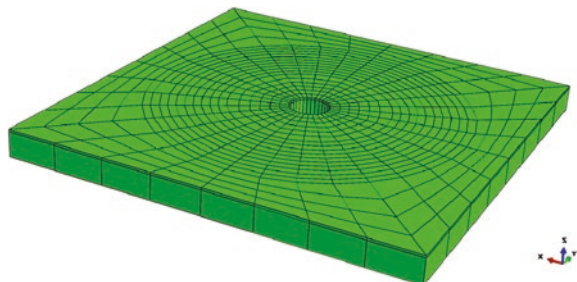


Fig. 4.5 Local buckling

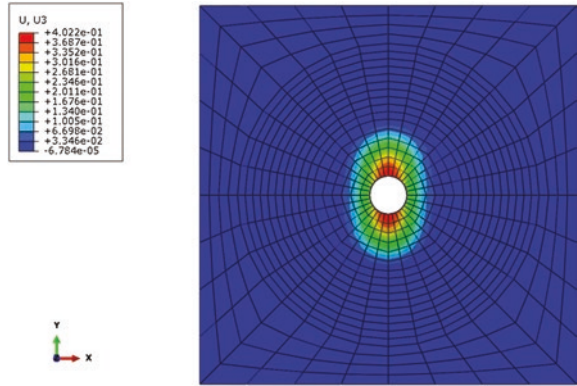


Fig. 4.6 Energy release rate distribution

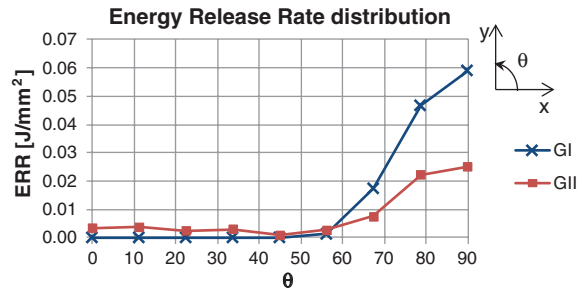


Fig. 4.7 Local buckling relative to cycle number 1 (top) and cycle number 287039 (bottom)

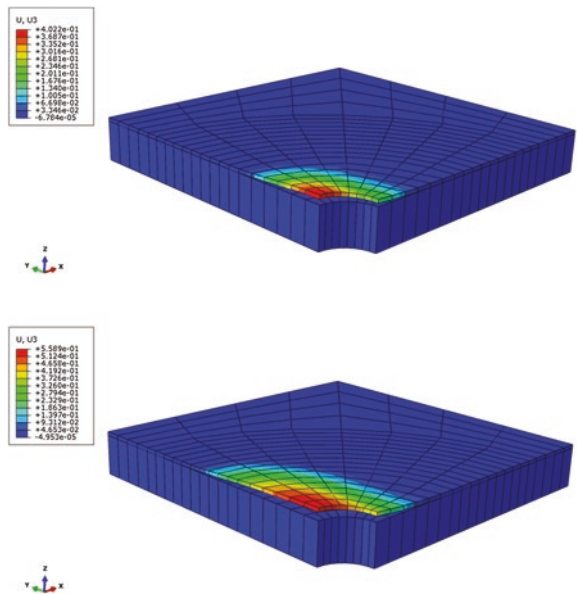

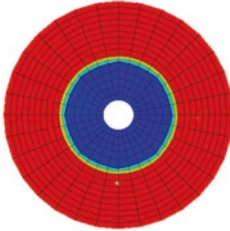

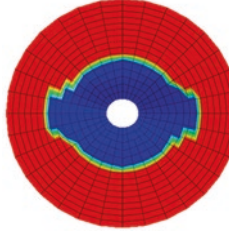
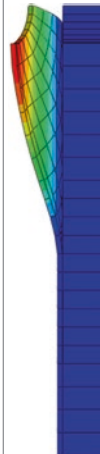
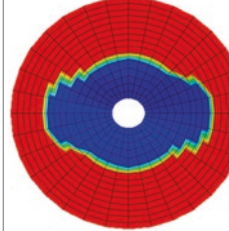


Table 4.2 Out-of-Plane displacements and delaminated area for different cycle numbers

Cycle #	ΔA (mm ²)	Out of plane displacement	Delamination growth
1	0		
18,918	64.30		
36,816	116.84		

(Continued)

Table 4.2 (Continued)

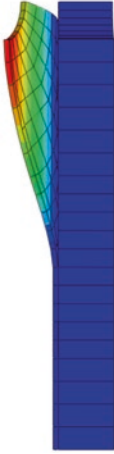
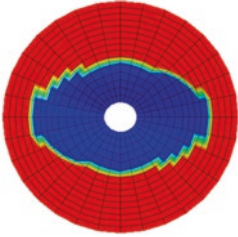

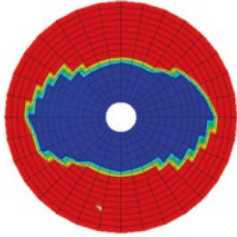
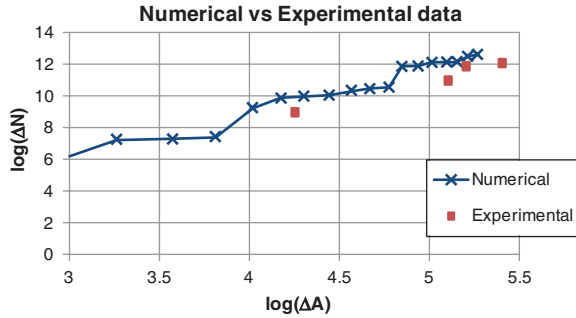
Cycle #	ΔA (mm ²)	Out of plane displacement	Delamination growth
177,771	160.86		
287,039	190.66		

Fig. 4.8 Number of cycle as a function of delaminated area: comparison between numerical and experimental data



4.5 Numerical Application: Sensitivity Analysis of Damage Propagation of a Delaminated Composite Panel Under Fatigue Load

In this subsection, a sensitivity analysis on delamination propagation in composite panels under fatigue loading conditions is presented. Fatigue analyses have been performed on different panels, characterized by different delamination sizes and through the thickness positions, to check the growth sensitivity for a number of load levels. The panels' geometry is detailed in Figs. 4.9 and 4.10 and in Tables 4.3 and 4.4.

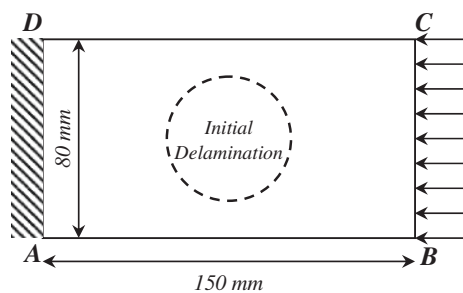
Indeed Table 4.4 summarizes the numerical test matrix adopted for the sensitivity analysis.

The specimens in Table 4.4 have been numerically fatigue tested for both **L1** (50 kN) and **L2** (80 kN) peak loads. The load has been applied according to Fig. 4.9. The numerical model used for the sensitivity analysis is shown in Fig. 4.11.

Table 4.5 shows the results in terms of delamination growth obtained for the **L1** peak load. The number of cycle and the extension of the delaminated area are also reported.

The results in Table 4.5 shows the dependence of the fatigue life of the panel on the depth of the initial delamination and its radius. Actually, an increase of the initial delamination size or depth reduces dramatically the fatigue life of the specimen. Indeed, the panel configuration **DIT2** (small deep delamination) seems to be

Fig. 4.9 Geometrical description and boundary conditions of the panels adopted for the sensitivity analysis



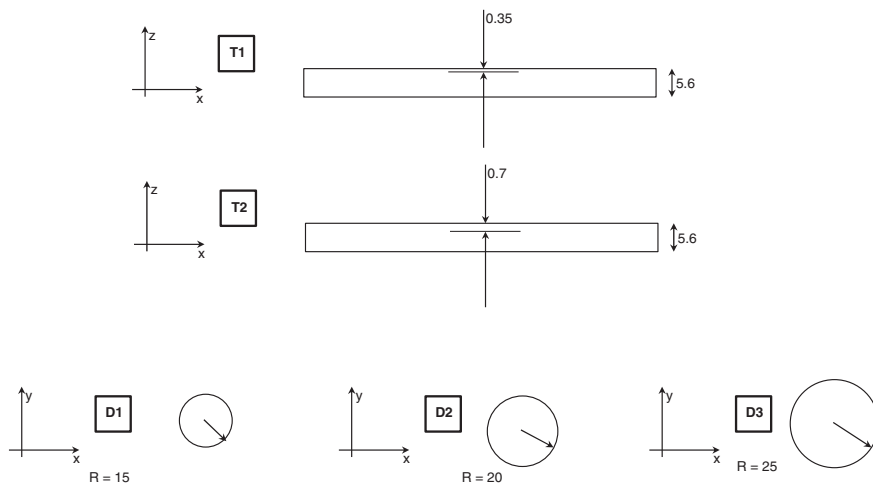


Fig. 4.10 Delamination sizes and positions considered for the sensitivity analysis

Table 4.3 Geometrical parameters and material properties

<i>Panels' fixed geometrical parameters</i>						
Length (mm)	Height (mm)	Thickness (mm)				
150	80	5.6				
<i>Panels' variable geometrical parameters</i>						
D1 (mm)	D2 (mm)	D3 (mm)	T1 (mm)	T2 (mm)	L1 (kN)	L2 (kN)
15	20	25	0.35	0.7	50	80
<i>Material properties</i>						
E_1 [GPa]	$E_3 = E_2$ (GPa)	$G_{12} = G_{23} = G_{13}$ (GPa)	$\nu_{12} = \nu_{13} = \nu_{23}$	G_{Ic} (J/m ²)	G_{IIc} (J/m ²)	
130.05	11.5	6	0.22	180	500	

Table 4.4 Panels defined as combination of the parameters and adopted for the sensitivity analysis

	D1-R = 15 mm	D2-R = 20 mm	D3-R = 25 mm
T1 - $t_1 = 0.35$ mm	D1T1	D2T1	D3T1
T2 - $t_1 = 0.7$ mm	D1T2	D2T2	D3T2

Fig. 4.11 Numerical model adopted for the sensitivity analysis

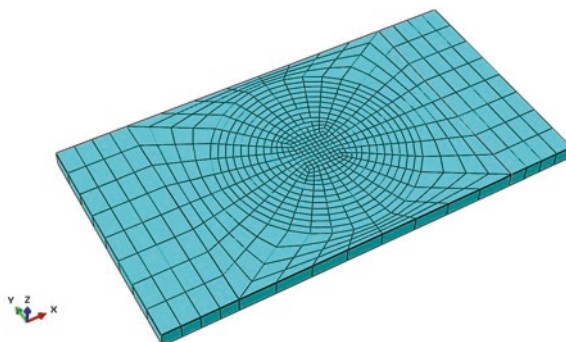
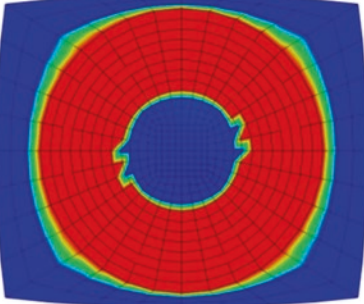
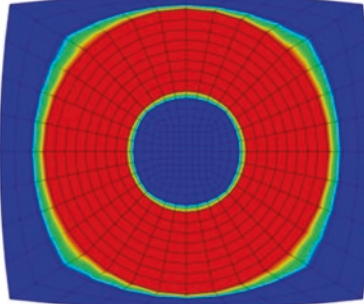
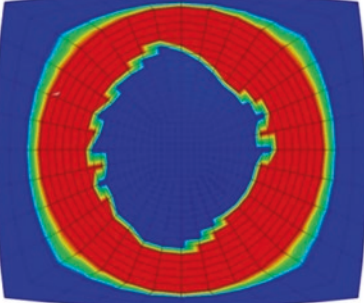
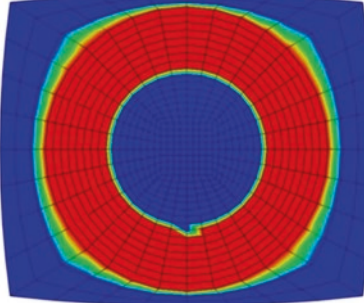
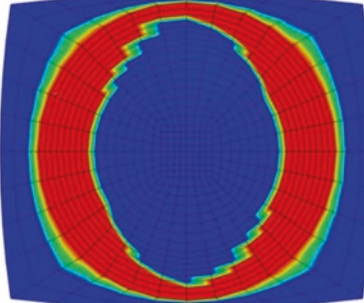


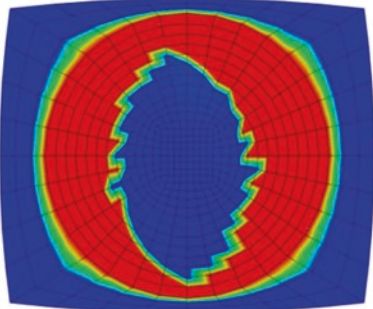
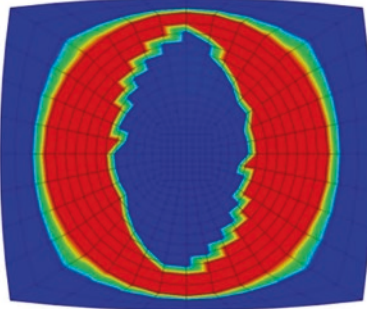
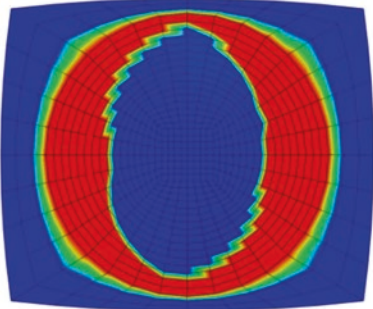
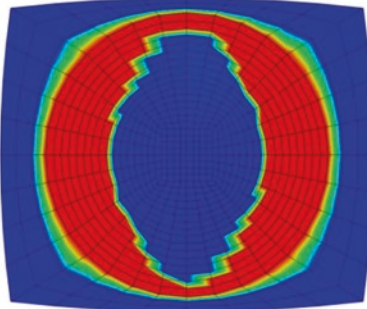
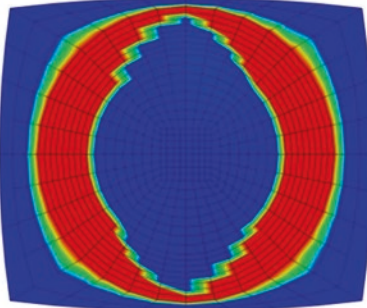
Table 4.5 Results of the sensitivity analysis with the **L1** applied peak load

<i>L1</i>	T1	T2
D1	 <p>Cycle number = 655,501 $\Delta A = 31.72 \text{ mm}^2$</p>	 <p>Cycle number = ∞ $\Delta A = 0 \text{ mm}^2$</p>
D2	 <p>Cycle number = 648,701 $\Delta A = 345.39 \text{ mm}^2$</p>	 <p>Cycle number = 6,231,513 $\Delta A = 7.66 \text{ mm}^2$</p>
D3	<p>The combination of the parameters D3 and T1 strongly reduces the stiffness of the panel in so far as the delamination is fully propagated in the first cycle</p>	 <p>Cycle number = 356,199 $\Delta A = 504.83 \text{ mm}^2$</p>

the best combination in terms of fatigue resistance, while the panel configuration **D3T1** (large superficial delamination) shows a fast delamination growth in the first cycles of the fatigue analysis.

Similar considerations can be done analyzing the results obtained for the **L2** peak load; such results are reported in Table 4.6. As in the previous case, the panel

Table 4.6 Results of the sensitivity analysis with the **L2** applied peak load

L2	T1	T2
D1	 <p>Cycle number = 754 $\Delta A = 850.98 \text{ mm}^2$</p>	 <p>Cycle number = 81,221 $\Delta A = 966.79 \text{ mm}^2$</p>
D2	 <p>Cycle number = 207 $\Delta A = 770.24 \text{ mm}^2$</p>	 <p>Cycle number = 122 $\Delta A = 613.77 \text{ mm}^2$</p>
D3	<p>The combination of the parameters D3 and T1 strongly reduces the stiffness of the panel in so far as the delamination is fully propagated in the first cycle</p>	 <p>Cycle number = 24 $\Delta A = 471.10 \text{ mm}^2$</p>

configuration **D3T1** shows a better fatigue resistance if compared to the panel configuration **D1T2**.

In Fig. 4.12 the Number of Cycle as a function of Delaminated Area is reported for the **L1** peak load. The results show, as expected, a relation between the stiffness of the panel and the fatigue life.

Fig. 4.12 Number of cycle as a function of the delaminated area considering the **L1** applied peak load

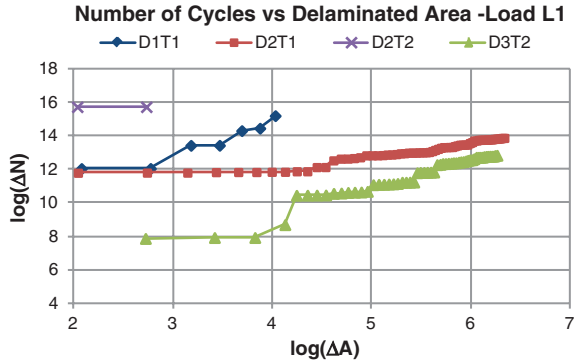


Fig. 4.13 Number of cycle as a function of the delaminated area considering the **L2** applied peak load

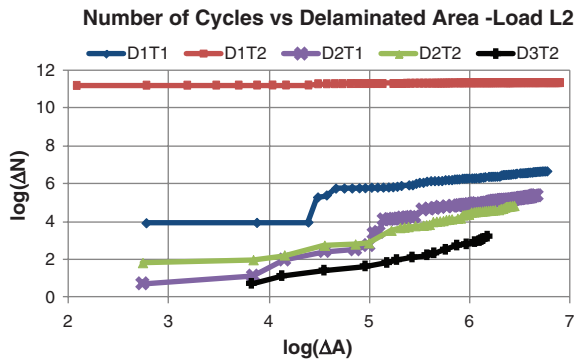
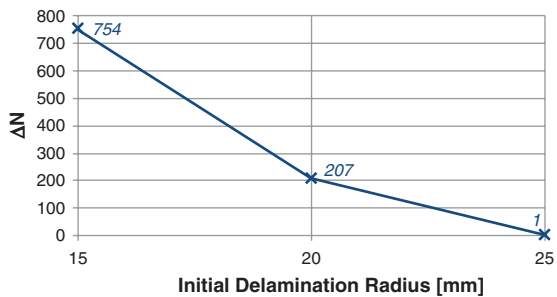


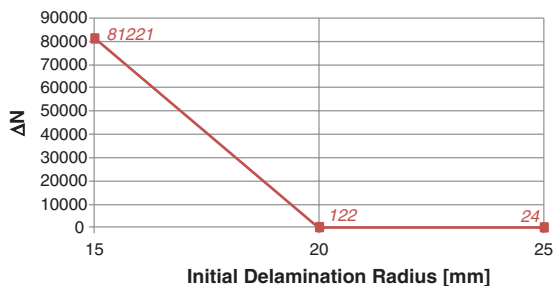
Fig. 4.14 Complete delamination growth cycle versus initial delamination radius at delamination depth **T1** and **L2** applied peak load



A similar trend can be observed in Fig. 4.13, which shows the Number of Cycle as a function of Delaminated Area considering the applied **L1** peak load.

Finally, Figs. 4.14 and 4.15 correlate the number of cycles needed for the delamination full propagation to the initial delamination radius, respectively for a delamination depth of **T1** and **T2** (at the **L2** applied peak load).

Fig. 4.15 Complete delamination growth cycle versus initial delamination radius at delamination depth T2 and L2 applied peak load



4.6 Conclusions

In the present chapter an algorithm is proposed which, by means of non-linear analyses, can correlate the increase of delaminated area to fatigue cycles. The proposed algorithm adopts Paris Law formulation based propagation criterion which can take into account the local damage accumulation along the delamination front.

The effectiveness of the proposed numerical approach in predicting the fatigue behavior of delaminated panels has been verified by comparison with literature experimental data [9]. A sensitivity analysis has been also performed to investigate the influence of delamination size and position on the fatigue induced delamination growth. The relation between delamination radius/depth and fatigue resistance has been quantified for plane delaminated panels. Actually, it has been verified that an increase of the initial delamination size or depth can reduce dramatically the fatigue life of the specimen. Indeed, panel configurations with small deep delamination seem to be the best combination in terms of fatigue resistance, while panel configurations with large superficial delaminations show a fast delamination growth in the first cycles of the fatigue analysis.

References

1. Riccio, A., Raimondo, A., Scaramuzzino, F.: A study on skin delaminations growth in stiffened composite panels by a novel numerical approach. *Appl. Compos. Mater.* **20**(4), 465–488 (2013)
2. Riccio, A., Scaramuzzino, F., Perugini, P.: Influence of contact phenomena on embedded delamination growth in composites. *AIAA Journal* **41**(5), 933–940 (2003)
3. Riccio, A., Raimondo, A., Fragale, S., Camerlingo, F., Gambino, B., Toscano, C., Tescione, D.: Delaminations buckling and growth phenomena in stiffened composite panels under compression. part I: an experimental study. *J. Compos. Mater.* (2013). doi:[10.1177/0021998313502741](https://doi.org/10.1177/0021998313502741)
4. Riccio, A., Raimondo, A., Di Caprio, F., Scaramuzzino, F.: Delaminations buckling and growth phenomena in stiffened composite panels under compression. part II: a numerical study. *J Compos Mater.* (2013). doi:[10.1177/0021998313502742](https://doi.org/10.1177/0021998313502742)
5. Pietropaoli, E., Riccio, A.: On the robustness of finite element procedures based on virtual crack closure technique and fail release approach for delamination growth phenomena. Definition and assessment of a novel methodology. *Compos. Sci. Technol.* **70**(8), 1288–1300 (2010)

6. Pietropaoli, E., Riccio, A.: Formulation and assessment of an enhanced finite element procedure for the analysis of delamination growth phenomena in composite structures. *Compos. Sci. Technol.* **71**(6), 836–846 (2011)
7. Talreja, R.: Fatigue of polymer matrix composites. *Compr. Compos. Mater.* **2**, 529–552 (2000)
8. Harris, B.: *A Historical Review of the Fatigue Behaviour of Fibre-Reinforced Plastics, Fatigue in composites.* Woodhead Publishing, Sawston (2003)
9. Shen, F., Lee, K.H., Tay, T.E.: Modeling delamination growth in laminated composites. *Compos. Sci. Technol* **61**, 1239–1251 (2001)
10. Tada, H., Paris, P.C., Irwin, G.R. *The Stress Analysis of Cracks Handbook.* Del Research (1973)
11. Tada, H., Paris, P.C., Irwin, G.R.: *The Stress Analysis of Cracks Handbook*, 2nd edn. Paris Productions Inc, St. Louis (1985)
12. Irwin, G.R.: *Proceedings of the society for Experimental Stress Analysis.* XVI(1), 93–96, 195
13. Paris, P.C., Gomez, M.P., Anderson, W.P.: A rational analytic theory of fatigue. *The Trend in Eng.* **13**, 9–14 (1961)
14. Vethe, S.: *Numerical Simulation of Fatigue Crack Growth.* University of Science and Technology, Norwegian (2012)
15. Riccio, A., Ronza, F., Sellitto, A., Scaramuzzino, F. Modeling delamination growth in composite panels subjected to fatigue load. *Key Eng. Mater.* **627**, 21–24 (2015)

Chapter 5

Influence of Intralaminar Damage on the Delamination Crack Evolution

Cédric Huchette, Thomas Vandellos and Frédéric Laurin

5.1 Introduction

Composite laminate materials offer very interesting alternative solutions to metallic materials due to their better specific properties in numerous industrial applications and aerospace structures. Nevertheless, the design of composite structures is nowadays limited by the lack of knowledge of the damage behavior of composite materials. In the specific case of Carbon Fiber Reinforced Plastic (CFRP) laminates, it is well known that transverse matrix cracks and delamination cracks can appear early during tensile tests. It is thus necessary to propose a model that permits to predict the initiation of damage and its evolution.

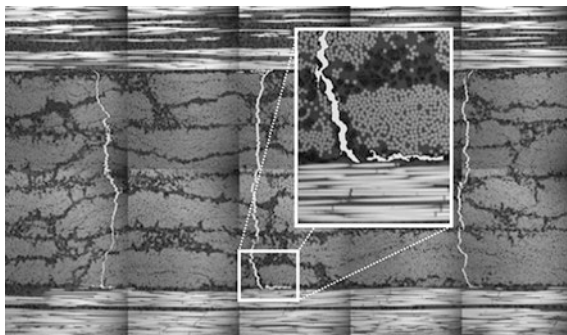
Concerning delamination cracks (interlaminar damage), this kind of damage mechanism in laminated composite structures is often investigated using cohesive zone models, firstly proposed by Dugdale [29] and Barenblatt [11]. These models have the capabilities to describe the onset of a crack and its propagation even in the presence of non-linear behaviors (geometric or material). Several cohesive zone models have been developed to predict delamination in CFRP laminates [3–5, 24, 25, 68] with softening laws presenting different shapes. Whatever the model, two parameters are commonly used: the interlaminar strength, τ_0 , and the critical energy release rate, also called the fracture toughness, G_c . Recent works about the characterization of the interfacial properties have demonstrated (i) the reinforcement

C. Huchette (✉) · T. Vandellos · F. Laurin
Onera—The French Aerospace Lab, 92322 Châtillon, France
e-mail: huchette@onera.fr

T. Vandellos
e-mail: thomas.vandellos@onera.fr

F. Laurin
e-mail: laurin@onera.fr

Fig. 5.1 Local delamination crack observed at the tip of the transverse matrix crack in a cross-ply laminate (detail of the crack deviation in the inset)



of the interfacial strengths under out-of-plane compression/shearing loadings and (ii) the influence of the mixed-mode ratio of the solicitation on the interfacial fracture toughness [12, 31, 60, 63, 73] and on the interfacial strength [18].

Even if in-ply matrix damage (intralaminar damage) is not a catastrophic failure mode for laminated composite structures contrary to delamination, the prediction of the macroscopic behavior or of the failure of composite laminates requires to take into account this damage mechanism [33]. Two kinds of approach have been developed during the last years to simulate the damage evolution (i.e. the onset of damage and its evolution). The first one is based on micromechanics models and permits to identify the relevant parameters required to finely describe the evolution of the transverse crack density in composite laminates (see Berthelot [13] for a review). This type of approach takes into account the reality of the damage pattern in order to explain the influence of the ply thickness or of the local delamination crack present at the tips of the transverse matrix cracks on the matrix crack density evolution (Fig. 5.1). The second approach is based on continuum damage mechanics [15, 44, 47, 66], which is more adapted to structure computation than micromechanics approaches. Nevertheless, the damage variables used in these models correspond to the degradation of the elastic parameters and are not necessarily correlated to the observed damage (transverse cracks, delamination crack, etc.). Moreover they do not take into account the influence of the ply thickness. Several models have thus been developed recently in order to propose a damage constitutive law at the ply level including the discrete aspect of damage and the interaction between local delamination and transverse cracking [35, 45, 67].

In composite structures subjected to various loadings such as tensile tests on open-hole plates or low velocity impact tests on laminates, for instance, intralaminar and interlaminar damage are both involved. It is thus interesting to study the influence of the transverse matrix cracks and of the associated local delamination cracks on the interlaminar damage. Wisnom and Hallett [74] explain that the final failure of open-hole plates presenting different stacking sequences is due to delamination and to the interaction between intralaminar and interlaminar damage. Guinard et al. [32] simulate the delamination induced by low-velocity impacts, taking into account the influence of the damage of each neighboring ply on the

interface under consideration. Ladevèze et al. [45] demonstrate by virtual testing that the behavior of the interface in mesomodel approaches is influenced by the damage in the adjacent plies.

The aim of this chapter is to experimentally demonstrate the influence of the intralaminar damage on the delamination evolution and to propose a model taking into account such a coupling. Section 5.2 will focus on experimental evidences which to demonstrate the influence of matrix cracking on the onset and on the propagation of the delamination cracks. Section 5.3 will propose a mesomodel approach taking into account this coupling. This model will be applied to a structural application in Sect. 5.4 in order to emphasize its contribution for the prediction of damage in laminated composites.

5.2 Influence of Intralaminar Damage on the Interlaminar Damage Evolution

5.2.1 Influence of Intralaminar Damage on Delamination Crack Onset

As mentioned in Sect. 5.1, local delamination cracks are usually observed [36] at the tips of transverse cracks in laminates (Fig. 5.1). This local delamination tends to weaken the considered interface and can lead to premature failure, due to macroscopic delamination, of composite laminated structures such as L-angle specimens. The objective of the present section is thus to demonstrate experimentally the influence of the intralaminar damages (i.e. transverse cracks and the associated local delamination cracks) on the onset of macroscopic delamination, and especially on the out-of-plane tensile strength.

5.2.1.1 Identification of the Intrinsic Out-of-Plane Tensile Strength

Different experimental tests can be found in the Ref. [53] to identify the out-of-plane tensile strength of unidirectional plies. Among these tests, the four-point bending test on L-angle specimens, proposed initially by Jackson and Ifju [38], presents a very interesting ratio between the complexity of the experimental part (manufacturing of the specimen and experimental setup) and the difficulties associated with the analysis of such a test (through analytical solutions [50] or finite element simulations). For these reasons, the four-point bending test on L-angle specimens has been normalized [9] and is currently used in design offices. The principle of such a test is illustrated in Fig. 5.2a. The two cylindrical support bars are fixed and the applied loading is imposed through the two cylindrical loading bars. This loading induces a bending moment at the curved section level, thus leading to unfold the L-angle specimen. In the case of accurately designed L-angle specimens, the observed delamination is only due to the out-of-plane tensile stress generated in the curved section, thus allowing the identification

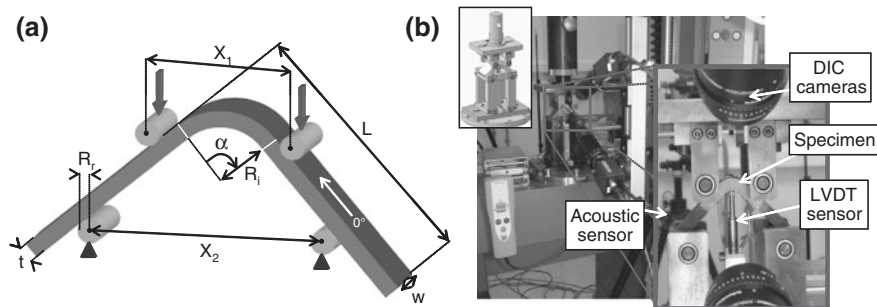


Fig. 5.2 **a** Principle of the four-point bending test on an L-angle specimen and **b** experimental device developed at Onera and the associated multi-instrumentation

of the out-of-plane tensile strength. For all the tested specimens, the propagation of the macroscopic delamination is instantaneous and instable, leading to the final failure of the specimens. This point has also been demonstrated numerically [19]. The characteristic dimensions of a L-angle specimen, also reported in Fig. 5.2a, are the total length of one leg (L), the width of the specimen (w), the total thickness (t), the internal radius of the corner (R_i) and the angle between the two legs (α). Moreover, the cylindrical bars of the four-point bending experimental device are defined by their radius (R_r) and the distances between the cylindrical loading bars (X_1) and between the cylindrical support bars (X_2). The orientation of the 0° plies in the L-angle specimens is also reported in Fig. 5.2a. The most critical parameters in the design of such a test, performed through finite element simulations, are the distances between the loading bars (X_1) and the support bars (X_2). In the present case, these geometrical parameters permit to minimize (i) the out-of-plane shear stress in the radius and in the legs and (ii) the local tensile loading in the inner radius, due to the applied bending, and to avoid transverse cracks initiation prior to macroscopic delamination.

The experimental test campaign has been performed in the framework of the STRENGTH project, under financial support of DGAC and Airbus management. The specimens have been manufactured from T700GC/M21 UD prepreg plies with a weight area of 268 g/m^2 . Two different stacking sequences have been considered to identify the out-of-plane tensile strength (Z_I): (i) a thin quasi-isotropic $[45/0/-45/90]_s$ laminate (8 plies) and (ii) an intermediate disoriented $[45_2/0/-45_2/90/45/0/-45/90]_s$ laminate (20 plies). Each test is repeated three times in order to estimate the scattering.

The experimental device, developed at Onera, for the four-point bending test on L-angle specimens and the associated measurement techniques are reported in Fig. 5.2b. An electro-mechanical Schenk machine (150 kN maximum capacity) is used. The tests are performed in the machine controlled displacement mode and a constant displacement rate is imposed: 0.1 mm/min . The cylindrical bars are machined in steel and can rotate on ball bearings in order to minimize friction and thus to simplify the analysis with FE simulations. Different measurement techniques have been used to improve the understanding of the involved physical

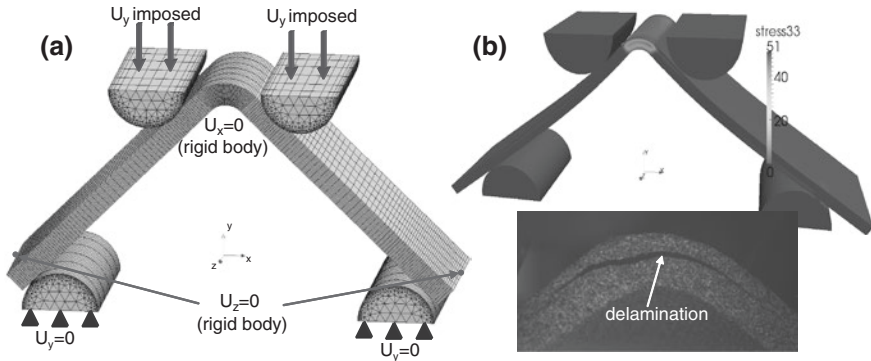


Fig. 5.3 **a** Mesh and boundary conditions of finite element simulations for four-point bending tests on L-angle specimens, and **b** comparison between the predicted out-of-plane stress field and the delamination pattern of a thin quasi-isotropic L-angle specimen

mechanisms and to obtain global and local informations: (i) LVDT sensor for measuring the evolution of the maximum deflection of the L-angle specimen, (ii) acoustic emission for the detection of damage events during loading, (iii) 3D Digital Images Correlation (DIC) on one free-edge of the specimen with black and white paint speckle for tracking the global displacement of the specimen and to obtain an estimate of the in-plane and out-of-plane strains and (iv) pictures taken on the other free-edge which has been properly polished in order to visualize the evolution of the intralaminar damages during the test.

The tests have been analyzed through finite element simulations in order to estimate correctly the stress field in the curved section at the failure load and to determine thus the out-of-plane tensile strength. The meshes of the studied L-angle specimens are performed using one volume linear element in the thickness of the ply. The element size is small in the curved section and under the cylindrical bars and increases in the legs to reduce the time of computation, as illustrated in Fig. 5.3a.

The boundary conditions are also reported in Fig. 5.3a. Half the loading and support bars device is meshed with volume linear elements. The displacement U_y is imposed on the upper faces of the cylindrical loading bars, while the displacement U_y of lower faces of the cylindrical support bars is fixed. Moreover, three nodes have specific conditions in order to avoid rigid body displacements of the specimen. Finally, the contact between the cylindrical bars and the specimen is taken into account while friction is assumed to be zero because of the ball bearings introduced in the experimental device. The behavior of the UD plies prior to final failure due to delamination is assumed linear elastic. This assumption is relevant in the present case since the in-plane and out-of-plane stresses remain rather low at the failure load. Moreover, no acoustic event is recorded prior to the first macroscopic delamination which confirms the absence of transverse crack before failure. Therefore, the elastic properties of the T700GC/M21 UD plies used in the present study are reported in Table 5.1. The steel cylindrical bars are assumed isotropic linear elastic with the following properties $E = 210$ GPa and $\nu = 0.3$.

Table 5.1 Material properties of the T700GC/M21 ply for the intralaminar damage constitutive law and for the cohesive zone model proposed in the present study

Type of parameters	Material properties			
Elastic properties	E_{11} (GPa)	110.0	ν_{12} (-)	0.31
	E_{22} (GPa)	8.0	G_{12} (GPa)	8.2
	ν_{23} (-)	0.40		
In-plane interfiber criterion (Eq. 5.25)	Y_I (MPa)	70.0	S_{12} (MPa)	81.0
	S_{23} (MPa)	90.0		
Effect of transverse cracks ^a (Eq. 5.21)	H_{22}^a/S_{22}^o (-)	0.67	H_{66}^a/S_{66}^o (-)	0.92
	H_{22}^b/S_{22}^o (-)	0.92	H_{66}^b/S_{66}^o (-)	1.80
	H_{22}^c/S_{22}^o (-)	2.51	H_{66}^c/S_{66}^o (-)	0.58
	H_{22}^d/S_{22}^o (-)	4.43	H_{66}^d/S_{66}^o (-)	5.69
Matrix cracking evolution law (Eq. 5.22)	α_I (-)	2.50	α_{II} (-)	0.60
	α_{III} (-)	0.60	n (-)	1
	a_h (-)	0.37	b_h (mm ⁻¹)	0.04
Matrix cracking threshold (Eq. 5.24)	y_I^{oE} (MPa)	0.27	y_{II}^{oE} (MPa)	0.70
	y_{III}^{oE} (MPa)	0.70		
Delay effect (Eq. 5.29)	τ_c (s)	80		
CZM stiffness (Eq. 5.6)	K (MPa mm ⁻¹)	10^6	α_c (-)	10^3
Out-of-plane stress criterion (Eq. 5.8)	Z_t (MPa)	51.0	S_{13}, S_{23} (MPa)	90.0
Evolution of the fracture toughness (Eq. 5.17)	G_{Ic} (J m ⁻²)	340.0	G_{IIc}, G_{IIIc} (J m ⁻²)	1,390.0
	κ (-)	7.4	γ (-)	3.1
	η (-)	1.6		

^aThe other components of the damage effect tensors are zero

Using finite element simulations, it is possible to determine by inverse identification the out-of-plane tensile strength which is assumed to be equal to the maximum out-of-plane tensile stress (in plane $z = 0$ in Fig. 5.3a, i.e. far from the free-edges) at the experimental failure load. As illustrated in Fig. 5.3b, for all the considered specimens, the maximum out-of-plane tensile stress is maximal at the observed failed interface which permits to validate the present identification procedure. The identified out-of-plane tensile strength is equal to $Z_t = 51$ MPa with a standard deviation on the six considered tests equal to 6.1 %. It is important to note that the out-of-plane tensile strength seems to be independent of the considered stacking sequences and of the total thickness of the specimen when no transverse cracking is observed prior to delamination. This point has already been demonstrated experimentally [18, 19] using the same carbon/epoxy material for many other stacking sequences and other total thicknesses (from 16 plies to 48 plies). The determined out-of-plane tensile strength seems to be an intrinsic material property which can be used in a cohesive zone model, as presented in Sect. 5.3.1.

5.2.1.2 Determination of the Influence of Intralaminar Damages on the Onset of Delamination

In the present section, the objective consists in creating transverse cracks in the L-angle specimens prior to final delamination in order to study the coupling existing between the intralaminar damages and the out-of-plane tensile strength. In order to fulfill this objective, two modifications, as compared to the previous section, have been performed. Firstly, by increasing the distances between the cylindrical bars, it is possible to enhance the local tensile loading in the lower part of the curved section which permits to generate transverse cracks in these plies prior to final delamination. Secondly, disoriented stacking sequences, containing many 90° and $\pm 45^\circ$ plies, have been chosen in order to generate more easily transverse cracks in the lower plies prior to rupture. Considering other stacking sequences than those described previously remains relevant in the present study because the out-of-plane tensile strength seems to be independent of the considered lay-up. Two different lay-ups containing 20 plies have been chosen and the stacking sequences are $[90/45/90_2/-45/0/45/90_2/-45]_s$ (noted 10/40/50 laminate) and $[45_2/90/-45_2/0/45/90/-45/0]_s$ (noted 20/60/20 laminate). For these two stacking sequences, two different distances between the cylindrical bars, determined through FE simulations, have been considered in order to generate different transverse crack densities just prior to delamination. This point is essential in order to identify and validate a model taking into account the coupling between the interlaminar and intralaminar damages in laminated composite structures. For each configuration, the test is repeated three times in order to estimate the scattering. The same experimental device and associated instrumentation as described previously have been used for all tests.

The onset and the evolution of the transverse crack density in the disoriented L-angle specimens during the tests have been monitored by different techniques in order to improve the confidence into the measurements. By monitoring the evolution of the cumulative energy, the acoustic emission permits both to detect the onset of intralaminar damages within the structure and to estimate the evolution of the crack density as reported in Fig. 5.4a. This technique permits to detect all the damage events within the structure but does not permit (i) to discriminate a transverse crack from a delamination crack and (ii) to localize the induced defects (only one sensor has been used in the present test campaign).

As a complement to the acoustic emission, analysis of pictures taken on one polished free-edge has been performed in order to distinguish the different damage mechanisms and to determine their locations. Practically, the applied displacement being maintained, some pictures are taken with a 12 bits CCD camera associated with a microscope with different objectives ($\times 2.5$ or $\times 5$). This camera is fixed on micrometer tables thus allowing to take pictures of the different parts of the specimen edge (as reported in Fig. 5.4b). Then, these pictures are assembled to obtain a micrograph of the whole area of interest of the specimen as illustrated in Fig. 5.4b. Finally, the number of cracks is determined in each ply for the different

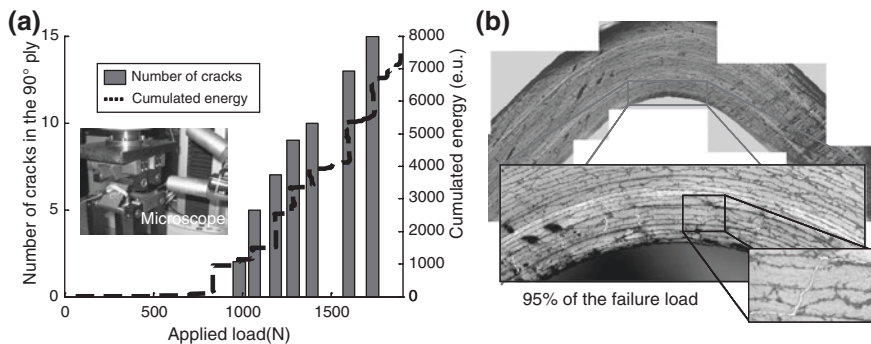


Fig. 5.4 **a** Evolution of the cumulative energy and comparison with the number of cracks detected in the lowest double 90° ply through image analysis as a function of the applied loading for a 10/40/50 L-angle specimen, and **b** visualization of the intralaminar damage pattern in the same specimen at 95 % of the failure load

load levels until the final failure which is attributed to macroscopic delamination. The pictures being taken while the structure is subjected to a bending loading, the transverse cracks are thus opened thereby permitting to detect them more easily. Moreover, local delamination cracks are clearly observed at the tips of the transverse cracks located in the lower plies such as the lowest double 90° plies for the 10/40/50 specimen presented in Fig. 5.4b. It is also worth mentioning that the pictures have been taken as a function of the monitored acoustic events to optimize the monitoring of such a test. Finally, the evolution of the crack density has been compared successfully with the discontinuities observed in the cumulative energy recorded by acoustic emission for the different tested configurations, as presented in Fig. 5.4b for a 10/40/50 specimen.

Moreover, the analysis of the strain fields measured by stereo-digital images correlation can also permit to detect mesoscopic intralaminar cracks in the structure as proposed in [48]. Indeed, when transverse cracks are initiated during loading, a discontinuity is induced in the displacement field and the cracks can be detected using the strain obtained through derivation of the displacement field. The evolution of the crack density can thus be automatically measured and has been successfully compared with the other measurement techniques permitting to improve the confidence in the available experimental data. It can be noted that for the four considered cases (two different geometrical configurations for two different stacking sequences), the measured transverse crack densities just prior to final failure are notably different which should permit to identify the inter/intralaminar damage coupling parameters of a damage model as the one described in Sect. 5.3.3.

For the considered damaged L-angle specimens, the observed failure pattern is drastically different from that observed on specimens in which no transverse cracking is observed prior to delamination. Indeed, as presented in Fig. 5.5a, for a 20/60/20 specimen containing no intralaminar damage prior to final failure (stacking sequence presented in Sect. 5.2.1.1), only the mostly loaded interface,

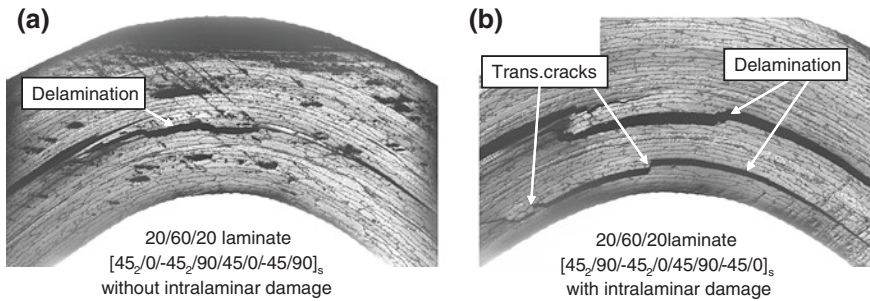


Fig. 5.5 **a** Failure pattern of the disoriented 20/60/20 specimen without intralaminar damage prior to delamination, and **b** failure pattern of the disoriented 20/60/20 specimen with intralaminar damage prior to delamination

located at the mid-thickness of the specimen, failed and led to the final failure of the specimen. Nevertheless, in the present disoriented laminate (in which the positions of the 0° plies have been permuted with those of the 90° plies as compared to the previous lay-up), two main delamination cracks are observed in Fig. 5.5b. The mostly loaded interface still failed but a delamination crack is also observed in the interface between the damaged 45° and 90° plies located near the inner radius. A clear interaction is observed between the transverse cracks in the lowest 90° ply and the delamination crack. The local delamination cracks at the tips of the transverse cracks weaken the interface located between the intralaminar damaged plies and lead to the premature failure of the specimens while the applied out-of-plane stress at this interface remains markedly lower than the out-of-plane tensile strength. The same failure pattern, consisting in several delamination cracks in the interfaces between the damaged plies located near the inner radius, is observed on the other tested stacking sequences and the interaction between the different damage mechanisms is also visible.

Therefore, it has been demonstrated, in this section, that the failure patterns of L-angle specimens are modified due to the presence of intralaminar damages (especially due to the local delamination cracks located at the tips of the transverse cracks). In the present study, these experimental evidences suggest that it is essential to introduce coupling between the onset of delamination and intralaminar damages.

5.2.2 Influence of Intralaminar Damage on Delamination Crack Propagation

It is generally admitted that delamination must be characterized by an onset criterion and a propagation criterion. The propagation criterion represents the evolution of the fracture toughness, i.e. the energy release rate needed to propagate a crack at

the interface, as a function of the mixed-mode ratio often defined as $G_{II}/(G_I + G_{II})$ with G_I (resp. G_{II}) the energy release rate for mode I (resp. mode II). The characterization of the propagation criterion is based on many fracture tests such as the double-cantilever beam (DCB) and the end-notched flexure (ENF) tests for toughness in modes I and II [7, 14, 27, 28, 54, 64, 65]. As a mixed-mode is more likely to occur in structures subjected to in service loadings, several experiments have been developed such as the mixed-mode flexure (MMF) test and the mixed-mode bending (MMB) test allowing a mixed-mode characterization. The MMB test is the most commonly used because it allows investigating all mixed-mode ratios between modes I and II [7, 21, 26, 55, 56, 61, 62]. However, these tests are classically performed on unidirectional (UD) $[0^\circ]_n$ laminates whereas most composite structures subjected to complex loadings involve multidirectional (MD) laminates where delamination fracture mainly occurs in the interfaces between the differently oriented plies. Therefore an increasing amount of researches is devoted to the evaluation of the fracture toughness of MD laminate interfaces [6, 20, 26, 55, 56, 59, 60]. However, one of the major problems in testing those MD specimens is the presence of intralaminar damage. Indeed, with the commonly used fracture tests, this kind of damage is difficult to quantify and its influence on the characterization of the energy release rate during delamination crack growth is also difficult. However this coupling between intralaminar damage and delamination is crucial in order to describe the damage scenario of composite materials in structures. Consequently, a new fracture test, adapted to MD laminate interfaces, has been proposed recently [71]: the Tensile Flexure test on Notched Specimen (TFNS test).

5.2.2.1 The Tensile Flexure Test on Notched Specimen

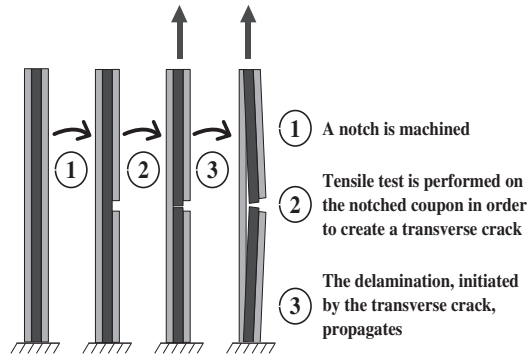
Description of the Experimental Procedure

In order to characterize the propagation of delamination in $\pm\theta^\circ$ plies of unidirectional continuous fiber laminates, a new experimental procedure, based on fracture mechanics, has been proposed. The aim of this new test, called Tensile Flexure test on Notched Specimen (TFNS test), is to determine the fracture toughness of a $0^\circ/\theta^\circ$ interface. In order to study the delamination of the $0^\circ/\theta^\circ$ interface, the most appropriate stacking sequence is $[0_n/\pm\theta_m]_s$. This test procedure is divided into three steps (Fig. 5.6).

In the first step, a notch is machined in the top 0° plies of the laminate in the middle of the specimen in order to introduce a local tensile/bending coupling in the laminate behavior.

The second step is devoted to the specimen preparation (i.e. the initiation of the delamination crack). The tensile loading is applied in a displacement controlled mode for the sake of crack propagation stability. The tensile loading leads to the initiation of a transverse crack under the notch through the $\pm\theta^\circ$ plies. This transverse crack finally reaches the last $0^\circ/\theta^\circ$ interface, leading to

Fig. 5.6 Experimental procedure of the tensile flexure test on notched specimen



local delamination through crack deflection in this interface. Once the local delamination has occurred in the $0^\circ/\theta^\circ$ interface, the specimen is unloaded.

After these two steps, the third step concerns the propagation of the delamination crack front initiated in the $0^\circ/\theta^\circ$ interface on both sides of the transverse crack. The propagation of delamination is thus investigated through a second tensile test. The load, the displacement and the delamination lengths are recorded in order to calculate the fracture toughness. It is worth mentioning that, contrary to other fracture mechanics tests, the delamination occurs without the presence of a Teflon[®] insert as in the test proposed by O'Brien [52]. However, with the TFNS test, the delamination crack is not created by free edge effects (as in [52]), the control of which is very difficult, but results from the deviation of the transverse crack from the θ° ply into the $0^\circ/\theta^\circ$ interface.

Description of the Experimental Device

The TFNS test was performed on an electromechanical testing machine, equipped with a 150 kN load cell, operating in a displacement controlled mode. A digital video microscope is used to observe the damage state at the ply scale (mesoscopic scale) and at the fiber/matrix scale (microscopic scale). This microscope, which is fixed on micrometric displacement tables (Fig. 5.7), allows the measurement of the length of the delamination crack. Numerous displacement plateaus are imposed (every 0.04 mm) thus allowing an accurate observation of the propagation of the delamination crack under loading. The displacement, applied to the specimen, is determined by the variation of the length of the specimen measured during the test at each displacement plateau.

The T700GC/M21 laminate has been chosen because it is a 3rd generation carbon/epoxy material which exhibits a high fracture toughness and experimental results obtained using other experimental devices are available in the literature [60].

The length of the coupon is 100 mm whereas its width is 12 mm. The thickness of the coupon and the notch depth in the middle of the specimen depend on the stacking sequence of the laminate. For instance, in a $[0_n/90_m]_s$ specimen, the

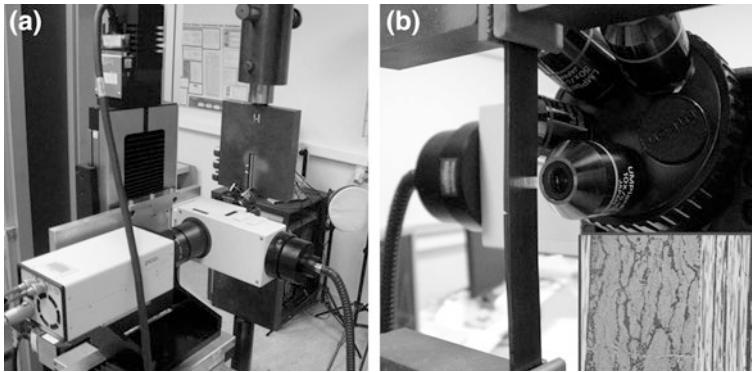


Fig. 5.7 Experimental device: **a** the digital camera fixed on the displacement tables, and **b** micrograph of the sample (inset) during testing provided by the microscopic head of the digital camera

notch depth must be superior to the thickness of the 0° plies since it is essential to avoid that the crack initiates and propagates in the top 0° plies but propagates as a transverse crack in the 90° plies and thus attains the other $0^\circ/90^\circ$ interface in order to deviate in this interface, thus leading to delamination.

Experimental Observations

The evolutions of stress and of crack length versus the imposed displacement for several coupons demonstrate the good reproducibility of the TFNS, as shown in Fig. 5.8 for four $[0_2/90_2]_s$ T700GC/M21 carbon/epoxy specimens. Moreover, the crack growth is stable, without any damage in the plies, as long as the delamination length is short enough (i.e. 1/3 of the total length of the specimen).

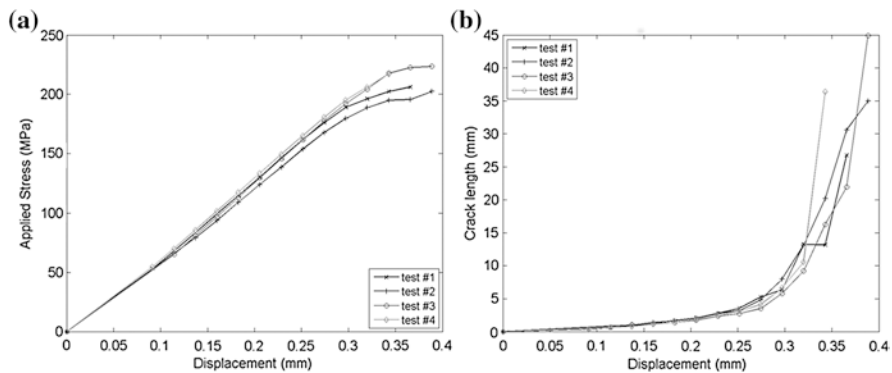


Fig. 5.8 **a** Stress versus imposed displacement, and **b** crack length versus imposed displacement for several TFNS tests on $[0_2/90_2]_s$ T700GC/M21 carbon/epoxy laminates

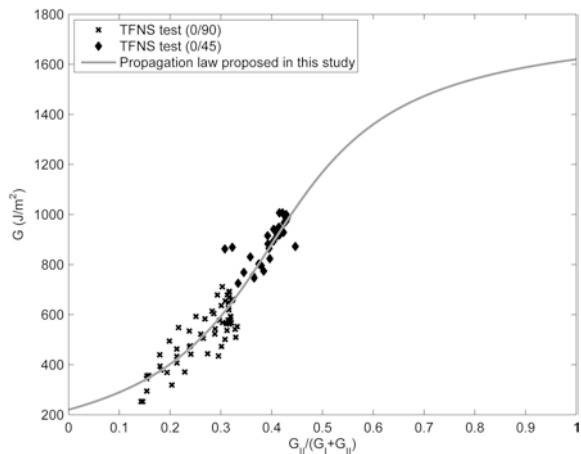
Besides, the delamination crack consists in two cracks propagating with a quasi-symmetrical behavior. It is worth mentioning that the stress-displacement curve is not linear. This behavior is due to the presence of the notch which leads to bending of the specimen under tensile loading.

Identification of the Interface Toughness in a T700GC/M21 Carbon/Epoxy Laminate

From five TFNS tests on $[0_2/90_2]_s$ specimens and two tests on $[0_3/45/-45]_s$ specimens of T700GC/M21 carbon/epoxy laminate, fracture toughness identification was performed using the Modified Virtual Crack Closure Technique (MVCCT) method [43], based on the Linear Elastic Fracture Mechanics. Due to bending of the laminate observed during the tensile test, the calculation assumption of large displacements is made. Using the applied load or the applied displacement measured during the experiment and the measured delamination lengths, it is possible to simulate the experimental conditions and to use this technique to identify the fracture toughness. The application of the MVCCT method on the TFNS test indicates a mixed-mode ratio $G_{II}/(G_I + G_{II})$ evolving with the crack growth.

The results presented in Fig. 5.9 show (i) that the mixed mode evolves from 15 to 35 % of mode II with the $[0_2/90_2]_s$ specimen and from 35 to 45 % of mode II with the $[0_3/45/-45]_s$ specimen and (ii) that the fracture toughness increases as a function of the mixed-mode ratio which increases to 1 (mode II). It should be noted that such results are in good agreement with those reported in Refs. [12, 59]. Moreover, it is worth mentioning that contrary to other tests, the mixed-mode ratio changes. Therefore, the TFNS test permits to obtain, with only one test, the evolution of the fracture toughness of MD laminate interfaces as a function of the mixed mode ratio. The propagation criterion (Eq. 5.17) can be identified using these data (Fig. 5.9).

Fig. 5.9 Identification of a propagation law (Eq. 5.17) based on the fracture toughness identified by MVCCT from the TFNS tests



5.2.2.2 Demonstration of the Influence of Intralaminar Damage on the Interfacial Fracture Toughness

The influence of intralaminar damage on the onset of delamination has been proved in Sect. 5.2.1.2. It seems obvious that the value of the fracture toughness of the interface is also influenced by the intralaminar damage (transverse matrix cracking, local delamination) but its identification remains difficult.

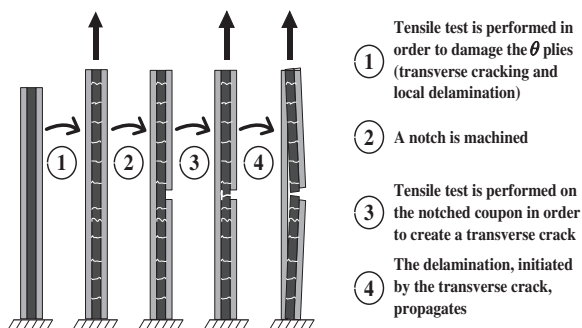
Adding a new step at the beginning of the experimental procedure of the TFNS test, it is possible to study the intralaminar damage effect on the propagation of the delamination crack. Indeed, using a tensile test on the laminated specimen without notch, several transverse cracks are created in the θ° plies. The initial experimental procedure is then followed as shown in Fig. 5.10.

It is important to note that the transverse crack density does not change during the tensile test on the notched specimen. Besides, it is possible to observe the influence of the transverse crack density on the propagation of the delamination crack in the $0^\circ/90^\circ$ interface. Moreover, it is worth mentioning that the experimental device used during the test permits to evaluate, for each displacement plateau, the length of the delamination crack, the number of transverse cracks in the specimen and the length of the local delamination cracks present at the tips of the transverse cracks.

As shown in Fig. 5.11 for several stacking sequences, the transverse cracking rate (i.e. the number of transverse cracks from one unit of length) and the average length of the local delamination depend on the level of the applied stress during the first tensile test. In order to obtain a good compromise, during the TFNS test, between the number of transverse cracks and the length of local delamination cracks, the stacking sequence $[0_2/90_2]_s$ has been chosen.

In order to identify the influence of the level of intralaminar damage on the propagation of the delamination crack, five damage states have been studied. The comparison of the curves representing the evolution of the applied stress as a function of strain shows that the initial slope can not be associated with the different levels of intralaminar damage under consideration. Nevertheless, when the damage level increases, the rigidity seems to decrease sooner (Fig. 5.12a). Moreover, the evolution of the normalized crack length versus strain clearly shows that the

Fig. 5.10 Experimental procedure of the tensile flexure test on notched specimen for studying the influence of intralaminar damage on the propagation of delamination



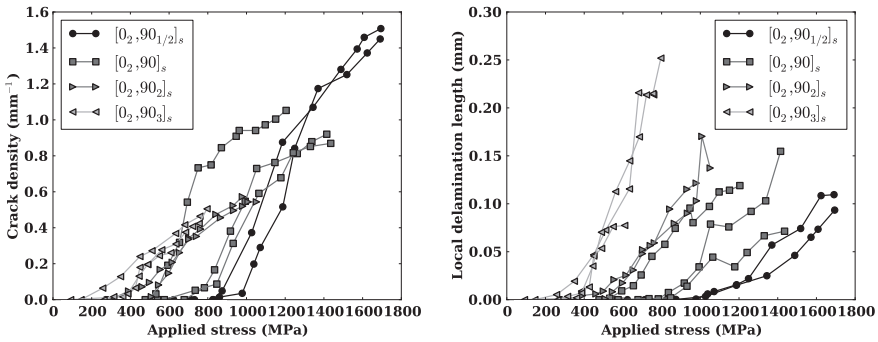


Fig. 5.11 Evolution of the number of transverse cracks by millimeter and of the average local delamination length as a function of the applied stress for several cross-ply T700GC/M21 laminates

propagation of the delamination crack occurs earlier when the intralaminar damage level increases (Fig. 5.12b). Nevertheless, due to the fact that the experimental curves, obtained with intralaminar damage, are included into the dispersion of the experimental curves without intralaminar damage, the identification of the fracture toughness as a function of the intralaminar damage level is not possible.

However, according to numerical simulations of the TFNS test, the effect of the intralaminar damage level on the fracture toughness seems to be realistic. Indeed, the more the fracture toughness of the cohesive zone model (described in Sect. 5.3.1 and used to describe the propagation of the delamination crack at the 0°/90° interface during the TFNS test) decreases, the more the propagation of the crack occurs earlier (Fig. 5.13), as observed during the experimental tests. Therefore, it seems obvious that the fracture toughness has to be influenced by the intralaminar damage level.

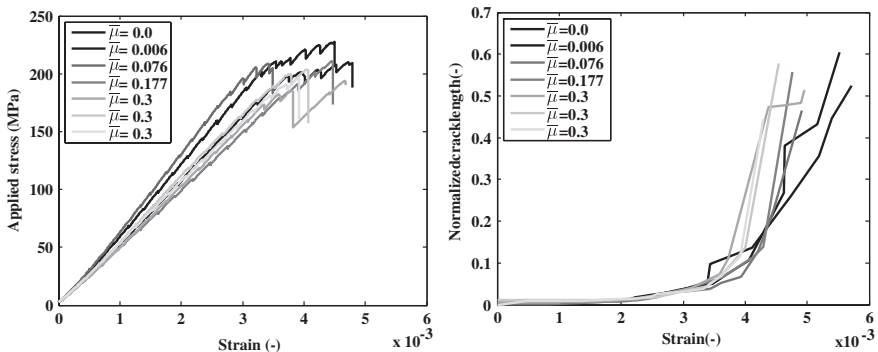


Fig. 5.12 Evolution of the applied stress and normalized crack length as a function of strain for several levels of intralaminar damage obtained from TFNS test on [0₂/90₂]_s T700GC/M21 carbon/epoxy specimens

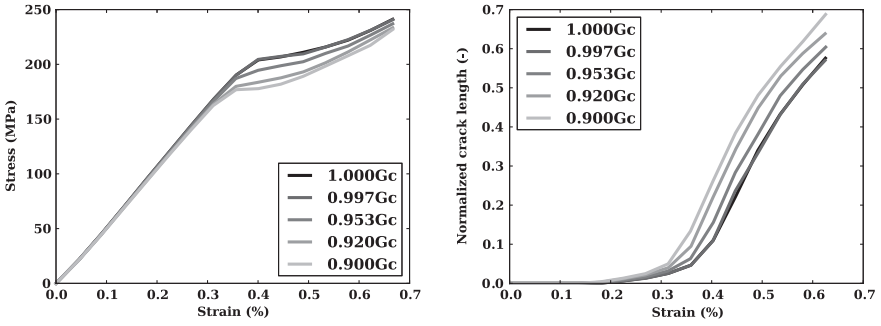


Fig. 5.13 Evolution of the applied stress and the normalized crack length versus strain obtained by the simulation of the TFNS test with several values of the fracture toughness

5.3 Modeling the Effect of Intralaminar Damage on the Interlaminar Damage Evolution

5.3.1 Cohesive Zone Model for Modeling the Interlaminar Damage

5.3.1.1 General Framework of the Cohesive Zone Model

Cohesive zone models are generally used to describe the behavior of interfaces. More precisely, the tractions T_i between the top and bottom surfaces of the interface are related to the relative displacements δ_i , with $i = 1 - 3$ (Fig. 5.14). The value $i = 1$ corresponds to the opening mode of fracture (mode I) whereas the values $i = 2$ and $i = 3$ are related to the shearing modes (mode II and mode III).

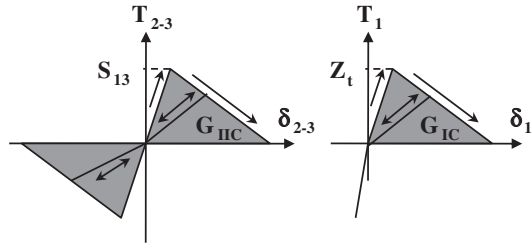
In the general framework, the constitutive law can be written as

$$\begin{cases} \text{if } \delta_1 \geq 0 \\ \left\{ \begin{array}{l} T_1 = K \delta_1 f(\lambda) \\ T_i = K \delta_i f(\lambda) \end{array} \right. & \text{if } \delta_1 < 0 \\ \left\{ \begin{array}{l} T_1 = \alpha_c K \delta_1 \\ T_i = K \delta_i f(\lambda) \end{array} \right. & \text{with } i = 2, 3 \end{cases} \quad (5.1)$$

where δ_1 (respectively δ_2 and δ_3) is the relative displacement in mode I (respectively in mode II and III), T_1 (respectively T_2 and T_3) is the traction force in mode I (respectively in mode II and mode III), K is the initial stiffness of the interface (considered, in this work, as being the same whatever the fracture mode), α_c is a penalization factor for out-of-plane compression, λ is the damage variable, related to the damage kinetics, and $f(\lambda)$ represents the effect of damage. As proposed in [19], the damage variable λ can be then defined from the relative displacement δ and the material parameters δ_0 and δ_f . The relative displacement δ is determined by

$$\delta = \sqrt{(\delta_1)_+^2 + \delta_2^2 + \delta_3^2} \quad (5.2)$$

Fig. 5.14 The constitutive law in single-mode loading



where $\langle \cdot \rangle_+$ are the classical Macaulay brackets defined by

$$\langle x \rangle_+ = \max[0, x] \tag{5.3}$$

It should be noted that, in order to avoid damage under pure out-of-plane compressive normal stress, the normal relative displacement δ_1 is only taken into account in the relative displacement δ when positive. As illustrated in (Fig. 5.15), δ_0 is the relative displacement associated with the damage threshold τ_0 and the interfacial stiffness K , and δ_f is the relative displacement attained when the energy release rate G is equal to the fracture toughness G_c (corresponding to the area under the constitutive law for a constant mixed-mode ratio).

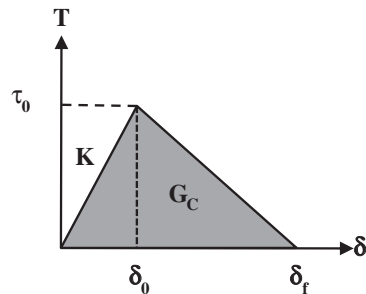
δ_f depends on the shape of the cohesive zone law and on the fracture toughness G_c . It is calculated, for a constant mixed-mode ratio, by

$$G_c = \int_0^{\delta_f} T(\delta) d\delta \tag{5.4}$$

where the value of G_c is experimentally identified by fracture tests. Therefore, the general framework for the definition of a cohesive zone model depends on

- $f(\lambda)$ which represents the damage effect,
- the damage evolution law which is associated with the damage variable λ ,
- δ_0 , determined from an onset criterion (i.e. the evolution of the interfacial strength τ_0 as a function of the mixed-mode ratio),
- δ_f , defined using a propagation law (i.e. the evolution of the interfacial toughness G_c as a function of the mixed-mode ratio).

Fig. 5.15 A bilinear constitutive law for a mixed-mode solicitation according to [16]



5.3.1.2 Damage Evolution Law of the Interlaminar Damage

The proposed framework permits to develop a cohesive zone model based on the experimental characterization and using any shape of law including an elastic part. The bilinear law is implemented in various finite element codes and has been used successfully by different authors [16, 69, 70]. However, questions concerning the influence of the shape of the law on the results and on the convergence (when a quasi-static implicit finite element code is used) are often raised. The tri-linear model presented here is more flexible than the bilinear one and permits to overcome some of its drawbacks [72].

As presented in Fig. 5.16, two parts could be distinguished in the model: a first one (from τ_0 to τ^*) in which the released energy is equal to ω_1 and a second one (from τ^* to 0) in which the released energy is equal to ω_2 . τ_0 is the strength of the interface for a given mixed-mode ratio. τ^* is the maximal damageable stress which represents the admissible stress on the interface at the end of the first part of the damage process. τ^* is defined by $\tau^* = \alpha_\sigma \tau_0$ where α_σ is a shape parameter which is generally a constant (if $\alpha_\sigma = 1$ the shape is trapezoidal). The total energy released during the damage process is equal to G_c with $G_c = \omega_1 + \omega_2$ ($\omega_1 = \alpha_G G_c$). It should be noted that τ_0 and G_c are respectively defined by the initiation criterion and the propagation law experimentally identified (Sect. 5.2).

The evolution of the damage variable is defined by Eq. 5.5 and the damage behavior by Eq. 5.6.

$$\begin{cases} \lambda = 0 & \text{if } \delta \leq \delta_0 \\ \lambda = (\delta_0 - \delta) \frac{\delta^* - \alpha_\sigma \delta_0}{\delta(\delta_0 - \delta^*)} & \text{if } \delta_0 < \delta \leq \delta^* \\ \lambda = \min \left[\frac{\delta(\delta^* - \delta_f) + \alpha_\sigma \delta_0(\delta_f - \delta)}{\delta(\delta^* - \delta_f)}, 1 \right] & \text{if } \delta \geq \delta^* \\ \dot{\lambda} \geq 0 \end{cases} \quad (5.5)$$

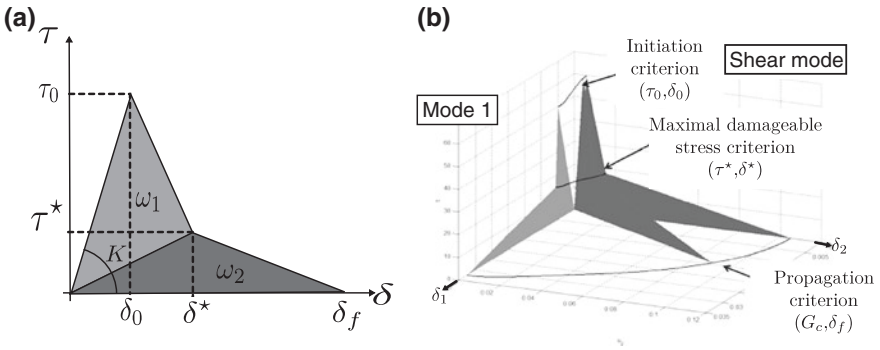


Fig. 5.16 Shape of the tri-linear model **a** for a constant mixed-mode ratio in the (δ, τ) plane, and **b** for mixed-mode ratios between mode I and shear mode

$$\begin{cases} \text{if } \delta_1 \geq 0 \\ T_1 = K(1 - \lambda)\delta_1 \\ T_i = K(1 - \lambda)\delta_i \end{cases} \quad \text{if } \delta_1 < 0 \quad \begin{cases} T_1 = \alpha_c K \delta_1 \\ T_i = K(1 - \lambda)\delta_i \end{cases} \quad \text{with } i = 2, 3 \quad (5.6)$$

$\delta_0, \delta^*, \delta_f$ are material parameters corresponding to the initiation criterion (δ_0) and to the propagation law (δ^*, δ_f). These parameters are defined by

$$\begin{cases} \delta_0 = \frac{\tau_0}{K} \\ \delta_f = 2\frac{\omega_2}{\tau^*} \\ \delta^* = \delta_0 + \alpha_\delta(\delta_f - \delta_0) \end{cases} \quad \text{with } \alpha_\delta = \frac{G_c - 12\tau_0\delta_0}{12\tau_0(\delta_f - \delta_0)} - \alpha_\sigma \quad (5.7)$$

5.3.1.3 Determination of the Onset Criterion with Reinforcement of the Interfacial Strengths Under Out-of-Plane Compression/ Shearing Loadings

The recent work of Charrier et al. [18] has demonstrated the reinforcement of the interfacial strength under out-of-plane compression/shearing solicitations. In order to model this reinforcement, the concept of a positive part of the stress tensor has been used. The concept of this kind of formulation is the determination of the stresses, in the plane of the crack, which are only responsible for the damage, following the procedure proposed in [39]. Besides, the onset criterion can be written as

$$\left(\frac{\sigma_{33}^+}{Z_t}\right)^2 + \left(\frac{\tau_{13}^+}{S_{13}^c}\right)^2 + \left(\frac{\tau_{23}^+}{S_{23}^c}\right)^2 = 1 \quad (5.8)$$

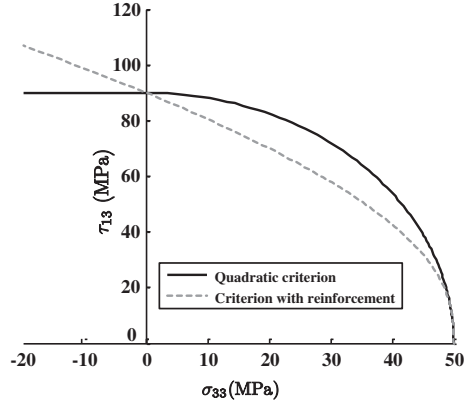
where Z_t is the through-thickness tensile strength identified using a four-point bending test on L-angle laminates (Sect. 5.2.1.2), S_{13}^c and S_{23}^c are the positive shear strengths. $\sigma_{33}^+, \tau_{13}^+$ and τ_{23}^+ are the positive interlaminar stresses defined, following [39], by

$$\begin{cases} \sigma_{33}^+ = \frac{(\lambda^+)^3}{\Omega} \\ \tau_{13}^+ = \frac{\tau_{13}(\lambda^+)^2}{\Omega} \\ \tau_{23}^+ = \frac{\tau_{23}(\lambda^+)^2}{\Omega} \end{cases} \quad \text{with } \begin{cases} \lambda^+ = \frac{(\sigma_{33} + \sqrt{\sigma_{33}^2 + 4(\tau_{13}^2 + \tau_{23}^2)})}{2} \\ \Omega = (\lambda^+)^2 + (\tau_{13}^2 + \tau_{23}^2) \end{cases} \quad (5.9)$$

Positive normal σ_{33}^+ and shear τ_{13}^+ stresses are generated using Eq. 5.9, even under pure shear loading (τ_{13} for instance). In order to respect the identified interlaminar strengths under pure shear loading, the positive shear strengths S_{13}^c and S_{23}^c are defined by

$$S_{13}^c = \frac{S_{13}}{2\sqrt{1 - \left(\frac{S_{13}}{2Z_t}\right)^2}}; \quad S_{23}^c = \frac{S_{23}}{2\sqrt{1 - \left(\frac{S_{23}}{2Z_t}\right)^2}} \quad (5.10)$$

Fig. 5.17 Comparison between the quadratic criterion classically used and the criterion with reinforcement



where S_{13} is the interlaminar strength in mode II (identified using Interlaminar Shear Strength (ILSS) tests on 0° unidirectional (UD) plies [10]) and S_{23} is the interlaminar strength in mode III (identified using ILSS tests on cross-ply laminates [18]). Figure 5.17 shows the difference between the present criterion and the classically used quadratic criterion [22].

For convenience, before onset of failure, the tri-axial stress state is represented using the relative displacement. Thus, the part of the participation of each through-thickness stress is defined using two parameters

$$\begin{cases} \theta = \arccos\left(\frac{\delta_1}{\delta^{\text{eq}}}\right) \\ \omega = \arctan\left(\frac{\delta_3}{\delta_2}\right) \end{cases} \quad (5.11)$$

where ω represents the participation of the interlaminar shear stress in mode III compared with the interlaminar shear stress in mode II and θ the participation of the interlaminar normal stress compared with the interlaminar shear stress. The magnitude of the total relative displacement is defined by

$$\delta^{\text{eq}} = \sqrt{\delta_1^2 + \delta_2^2 + \delta_3^2} \quad (5.12)$$

It should be noted that, compared with the relative displacement δ defined in Eq. 5.4, the total relative displacement takes into account the normal relative displacement, even if it is negative, in order to take into account the effect of the out-of-plane compressive stress on the onset criterion.

Assuming that the stiffness K is the same whatever the loading direction, and reporting Eqs. 5.9 and 5.11 in Eq. 5.8, then the relative displacement at initiation δ_0 is given by

$$\delta_0 = \frac{\delta_0^*}{\sqrt{a_{33}^2 + a_{13}^2 + a_{23}^2}} \quad (5.13)$$

with

$$\begin{cases} a_{33} = \frac{\tilde{a}^3}{\tilde{a}^2 + \sin^2 \theta} \\ a_{13} = \frac{\tilde{a}^2 \sin \theta \cos \omega}{\tilde{a}^2 + \sin^2 \theta} \frac{Z_I}{S_{13}^c} \\ a_{23} = \frac{\tilde{a}^2 \sin \theta \sin \omega}{\tilde{a}^2 + \sin^2 \theta} \frac{Z_I}{S_{23}^c} \\ \tilde{a} = \frac{1}{2} \left(\cos \theta + \sqrt{\cos^2 \theta + 4 \sin^2 \theta} \right) \\ \delta_0^* = \frac{Z_I}{K} \end{cases} \quad (5.14)$$

The evolution of the fracture toughness G_c as a function of the mixed-mode ratio is experimentally characterized using fracture tests [7, 8, 14, 17, 21, 27, 28, 37, 51, 57, 62–65]. This evolution is classically defined by a propagation law such as the power law (Eq. 5.15)

$$\left(\frac{G_I}{G_{Ic}} \right)^\alpha + \left(\frac{G_{II}}{G_{IIc}} \right)^\alpha + \left(\frac{G_{III}}{G_{IIIc}} \right)^\alpha = 1 \quad (5.15)$$

in which α is a material parameter or the Benzeggagh law (Eq. 5.16)

$$\begin{cases} G_c = G_{Ic} + (G_{IIc} - G_{Ic})B^\eta \\ B = \frac{G_{II} + G_{III}}{G_I + G_{II} + G_{III}} \end{cases} \quad (5.16)$$

where η is a material parameter. Nevertheless, the evolution of the fracture toughness as a function of the mixed mode ratio identified by TFNS tests (Sect. 5.2.2.2) is not well described by the precedent propagation laws. In this respect, Vandellos et al. [71] have proposed an improved propagation criterion (Eq. 5.17).

$$\begin{cases} G_c = G_{Ic} + (G_{IIc} - G_{Ic})B^\eta \\ B = \frac{\arctan \left(\frac{\kappa G_{II}}{G_I + G_{II} + G_{III}} - \frac{\kappa}{\gamma} \right) - \arctan \left(-\frac{\kappa}{\gamma} \right)}{\arctan \left(\kappa - \frac{\kappa}{\gamma} \right) - \arctan \left(-\frac{\kappa}{\gamma} \right)} \end{cases} \quad (5.17)$$

in which η , κ , γ are material parameters. A comparison between the identified parameters of this proposed criterion and the experimental data is presented in Fig. 5.9 thereby evidencing a good agreement between the propagation law predictions and the experimental data for the T700GC/M21 carbon epoxy material (see the parameter values in Table 5.1).

Following the definition proposed in [58], the local mixed-mode ratio is defined by

$$\begin{cases} \beta = \arccos \left(\frac{\delta_1}{\delta} \right) \\ \omega = \arctan \left(\frac{\delta_3}{\delta_2} \right) \end{cases} \quad (5.18)$$

Thus, the energy release rates related to the fracture modes are given by

$$\begin{cases} G_I = G_c \cos^2 \beta \\ G_{II} = G_c \sin^2 \beta \cos^2 \omega \\ G_{III} = G_c \sin^2 \beta \sin^2 \omega \end{cases} \quad (5.19)$$

Using Eq. 5.4, an analytical relation can be expressed between the fracture toughness and the maximal admissible displacement δ_f . For instance, this equation for the tri-linear model is

$$\delta_f = \frac{G_c - 1/2\tau_0\delta_0}{1/2\tau_0(\alpha_\delta + \alpha_\sigma)} + \delta_0 \quad (5.20)$$

Thus, reporting in this relation the value of the fracture toughness obtained from the propagation law, the maximal admissible displacement δ_f is evaluated.

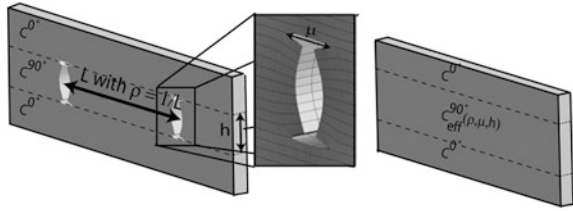
5.3.2 Damage Evolution Law of Intralaminar Damage

Section 5.2 has demonstrated the influence of matrix cracking on the evolution of the delamination crack. Although micromechanics studies [13] have shown the important effect of the local delamination on the saturation of the transverse cracking, only a few continuum damage models [23, 35, 45, 46] take into account the evolution of these two types of matrix damage.

To be able to take into account the influence of intralaminar damage on the delamination evolution, a simplified version of the multiscale hybrid approach for the damage prediction until the final failure of laminated composites developed by Laurin et al. [46] is proposed to simulate the evolution of transverse matrix cracking and local delamination. In this model, two damage variables are used to describe the matrix damage behavior of each ply: $\bar{\rho}$ (the normalized crack density, i.e. the crack density multiplied by the thickness of the considered ply) and $\bar{\mu}$ (the local delamination ratio, i.e. the total length of local delamination cracks divided by the total length of the interface). In order to develop a mesoscopic damage law, it is first necessary to identify the effect of the damage on the stiffness of the damaged ply. Nevertheless, it is very difficult to determine experimentally the stiffness reduction of a cross-ply laminate with a sufficient accuracy, especially for carbon/epoxy composites. Consequently, a numerical approach based on virtual testing has been adopted. In order to determine the stiffness of the damaged cross-ply laminate, a classical assumption on the periodicity of the damage pattern is made [13, 45, 67]. For each crack density and local delamination ratio given, a representative periodic cell is defined (Fig. 5.18).

This unit cell represents a cross-ply laminate. The damage occurs only in the central 90° ply. The behavior of the ply is described by a transverse-isotropic

Fig. 5.18 Definition of the equivalent stiffness tensor as a function of the thickness h and of the damage parameters of the ply ($\rho = \frac{\bar{\rho}}{h}$, $\mu = h\frac{\bar{\mu}}{\rho}$)



elastic behavior. The six elementary strain components are applied to this representative cell and the stiffness of the laminate is defined by the average of the stress field over this cell. By assuming that the laminate stiffness evolution is only due to the loss of stiffness in the 90° ply, an equivalent stiffness of the damaged ply can be identified by a homogenization approach. The effects of the normalized crack density $\bar{\rho}$ and the associated local delamination ratio $\bar{\mu}$, obtained through the virtual test campaign on the damage compliance tensor $\underline{\underline{\tilde{S}}}$ of the damage ply, can be fitted with the following proposed analytical formulations

$$\begin{cases} \underline{\underline{\tilde{S}}} = \underline{\underline{S}}^o + \Delta\underline{\underline{S}}(\bar{\rho}, \bar{\mu}) \\ \underline{\underline{S}}(\bar{\rho}, \bar{\mu}) = \bar{\rho}\underline{\underline{H}}^a + \frac{\bar{\mu}}{1+\bar{\mu}}\underline{\underline{H}}^b + \bar{\rho}^2\underline{\underline{H}}^c + \bar{\rho}\frac{\bar{\mu}}{1+\bar{\mu}}\underline{\underline{H}}^d \end{cases} \quad (5.21)$$

in which, $\underline{\underline{S}}^o$ is the initial compliance tensor of the ply and $\underline{\underline{H}}^a$, $\underline{\underline{H}}^b$, $\underline{\underline{H}}^c$ and $\underline{\underline{H}}^d$ are the damage effect tensors identified through the virtual test campaign. It is worth mentioning that, in order to simplify the identification procedure and especially to guarantee a positive-definite compliance tensor, the effect tensors are assumed diagonal.

In a second step, it is necessary to propose an evolution law for each damage mechanism. In long fiber composite materials, it is now well established that the thickness of the damaged plies is an important parameter [13]. In fact, the damage threshold and the evolution of transverse crack density are a function of the ply thickness (the thicker the ply is, the lower the damage threshold and the higher the kinetics are). The damage kinetics are thus given by the following relations

$$\begin{cases} \bar{\rho} = h(1 - \bar{\mu}) \left[\alpha_I \langle y_I - y_I^o \rangle_+^n + \alpha_{II} \langle y_{II} - y_{II}^o \rangle_+^n + \alpha_{III} \langle y_{III} - y_{III}^o \rangle_+^n \right] \\ \bar{\mu} = \langle a_h \bar{\rho}^2 + b_h \bar{\rho} \rangle_+ \\ \dot{\bar{\rho}} \geq 0 \end{cases} \quad (5.22)$$

where y_I , y_{II} and y_{III} are the driving forces and h is the thickness of the ply. α_I , α_{II} , α_{III} and n are material parameters. y_I^o , y_{II}^o and y_{III}^o are the damage thresholds. a_h and b_h are material parameters which permit to have an explicit formulation of the local delamination ratio ($\bar{\mu}$) as a function of the crack density ($\bar{\rho}$). The use of this explicit formulation avoids the definition of a specific evolution law [35] for the local delamination ratio. Moreover, the local delamination tends to slow down the kinetics of the transverse cracking.

The driving forces are expressed in Eq. 5.23 and depend on the positive part of the stress tensor [39] in order to predict damage for tensile loading or even for combined low transverse compression loading and high shear loading.

$$\begin{cases} y_I = \sigma_2^+ \tilde{S}_{22} \sigma_2 \\ y_{II} = \sigma_6^+ \tilde{S}_{66} \sigma_6 \\ y_{III} = \sigma_4^+ \tilde{S}_{44} \sigma_4 \end{cases} \quad (5.23)$$

where indexes 2 correspond to the in-plane transverse stress components, 6 to in-plane shear components and 4 to the out-of-plane ones. The matrix cracking thresholds are defined by using a coupled criterion [35, 46, 49] which implies that the onset of transverse cracking needs to fulfill two criteria, a stress criterion corresponding to the onset of damage at fiber/matrix scale and an energy criterion to ensure the propagation through the entire ply thickness of the transverse crack. These matrix cracking thresholds are then defined by the following expressions

$$y_i^o = \max \left[\frac{y_i^{oE}}{h}, y_i^{o\sigma} \right] \quad \text{with } i = I, II, III \quad (5.24)$$

in which, y_I^{oE} , y_{II}^{oE} and y_{III}^{oE} are the energy thresholds and $y_I^{o\sigma}$, $y_{II}^{o\sigma}$ and $y_{III}^{o\sigma}$ the stress ones. The energy thresholds are material parameters and the stress ones are the driving forces calculated when the in-plane interfiber criterion, defined in Eq. 5.25, is first fulfilled.

$$\begin{cases} \left(\frac{\sigma_{22}}{Y_t} \right)^2 + \left(\frac{\tau_{12}}{S_{12}} \right)^2 + \left(\frac{\tau_{23}}{S_{23}} \right)^2 = 1 & \text{if } \sigma_{22} \geq 0 \\ \left(\frac{\tau_{12}}{S_{12}} \right)^2 + \left(\frac{\tau_{23}}{S_{23}} \right)^2 = 1 & \text{if } \sigma_{22} < 0 \end{cases} \quad (5.25)$$

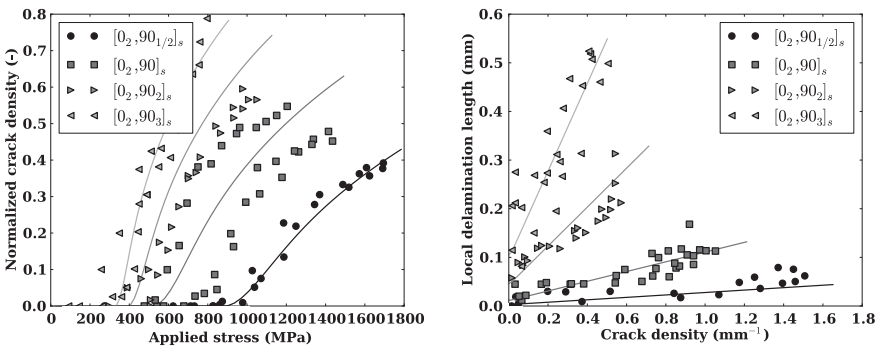


Fig. 5.19 Evolution of the normalized crack density as a function of the applied stress and of the average local delamination length as a function of the crack density for several cross-ply laminates (*in symbols*) and comparison with the prediction of the damage ply behavior (*continuous lines*)

where Y_t , S_{12} and S_{23} are respectively the transverse tensile strength, the in-plane shear strength and the out-of-plane shear strength in the 2-3 plane for a thick UD ply.

Figure 5.19 presents a comparison between the response of the proposed model and the experimental data for T700GC/M21 carbon/epoxy cross-ply laminates with different 90° ply thicknesses. The transverse cracking evolution of the $[0_2/90/0_2]$ laminate is used for the identification of the model parameters (the energy threshold γ_7^{oE} and α_1). The results on the other stacking sequences are used to validate the model (see the parameter values in Table 5.1).

5.3.3 Damage Evolution Law of Delamination Including the Intralaminar Damage Effect

Section 5.2 has demonstrated the influence of ply damage on the onset of delamination cracks and its evolution using experimental data. Even if the identification of this influence is difficult using an established procedure, it seems important to take it into account during the design analysis for the sake of security. Several approaches have been proposed in order to take into account this inter/intralaminar coupling. Ladevèze et al. [45] have developed an approach based on virtual testing in order to define relations between the damage state of the laminate (transverse matrix cracking, local delamination, delamination) and their effects on the out-of-plane part of the laminate behavior (micro-meso bridge approach). Abisset et al. [1] and Daghia and Ladevèze [23] derived from the precedent approach a simple expression for the coupling between delamination and matrix cracking. Abisset et al. [1] applied this expression to predict the rupture of open-hole plates and laid emphasis on the requirement of inter/intralaminar coupling.

From our point of view, the expression of the damage evolution (intralaminar or interlaminar) can not be only deduced from virtual testing and a phenomenological approach must be preferred. Nevertheless, the experimental data presented in Sect. 5.2 only demonstrate the influence of the intralaminar damage on the delamination crack evolution law. Due to the scattering of the experimental results, several assumptions could be made for modeling such a coupling. The first one assumes that the damage variable at the interface (λ defined in Eq. 5.2) and the local delamination ratio ($\bar{\mu}$ defined in Sect. 5.3.2) have the same effect on the interface constitutive law. Under this assumption, it becomes possible to define an effective interface damage variable λ^{eff} as [34]

$$\lambda^{\text{eff}} = \min(\lambda + \bar{\mu}, 1) \quad (5.26)$$

The second assumption adopted by Vandellos et al. [72] and Laurin et al. [46] is based on a geometrical point of view. The local delamination ratio being defined as the total length of the local delamination cracks due to matrix cracking

divided by the total length of the interface, this damage variable could be assimilated to a diffuse damage variable and its effect on the strength of the interface could be defined as

$$\begin{cases} Z_t^{\bar{\mu}} = (1 - \gamma_{\sigma}^{\bar{\mu}} \bar{\mu}) Z_t \\ S_{13c}^{\bar{\mu}} = (1 - \gamma_{\sigma}^{\bar{\mu}} \bar{\mu}) S_{13c} \\ S_{23c}^{\bar{\mu}} = (1 - \gamma_{\sigma}^{\bar{\mu}} \bar{\mu}) S_{23c} \end{cases} \quad (5.27)$$

where $Z_t^{\bar{\mu}}$, $S_{13c}^{\bar{\mu}}$ and $S_{23c}^{\bar{\mu}}$ are the effective interfacial strengths due to the presence of local delaminations at the interface. A similar assumption could be adopted for the propagation law but in order to avoid numerical convergence difficulties, the effective toughnesses $G_{ic}^{\bar{\mu}}$ with $i = I, II, III$ are so defined that the ratio between δ_0 and δ_f (Eq. 5.7) remains constant. Consequently, the effective interfacial toughnesses have the following expressions

$$G_{ic}^{\bar{\mu}} = (1 - \gamma_{\sigma}^{\bar{\mu}} \bar{\mu})^2 G_{ic} \quad \text{with } i = I, II, III \quad (5.28)$$

$\gamma_{\sigma}^{\bar{\mu}}$ in Eqs. 5.27 and 5.28 is a material parameter to be identified and which describes the influence of the intralaminar damage on the interlaminar damage. In the following, the second assumption has been chosen in order to investigate the influence of the parameter identification on the selected application test case.

5.3.4 Implementation in a Finite Element Code

The cohesive zone model and the damage constitutive law of the ply described in the previous sections have been implemented in the implicit finite element solver Zébulon [75]. In order to avoid mesh dependencies due to the damage constitutive law of the ply, a regularization technique is required. Several methods are available [2, 30] but in order to avoid the development of a specific finite element formulation (by a non local approach), the delay effect method has been used. Then, the evolution of the damage variable is defined by a first order ordinary differential equation

$$\frac{d\bar{\rho}}{dt} = \frac{1}{\tau_c} (F(y_I, y_{II}, y_{III}) - \bar{\rho}) \quad (5.29)$$

where $F(y_I, y_{II}, y_{III})$ represents the normalized crack density without regularization defined as

$$\begin{aligned} F(y_I, y_{II}, y_{III}) = h(1 - \bar{\mu}) & \left[\alpha_I \langle y_I - y_I^o \rangle_+^n + \alpha_{II} \langle y_{II} - y_{II}^o \rangle_+^n \right. \\ & \left. + \alpha_{III} \langle y_{III} - y_{III}^o \rangle_+^n \right] \end{aligned} \quad (5.30)$$

Taking into account the coupling between the intralaminar damage and the interlaminar damage in a standard finite element code is not straightforward. In order to transfer the damage state information, i.e. in the present case, the local delamination ratio from the neighboring plies to the interface, several methods are also available, such as the non local approach [34]. Nevertheless, as mentioned previously, this type of method requires the development of a non local finite element formulation and could lead to some difficulties for the numerical convergence of the analysis. In this respect, a post increment method has been adopted. The effect of the local delamination ratio on delamination is then computed at the end of each increment, once the convergence at the global scale is ensured. For each Gauss point in cohesive elements, the maximum of the local delamination ratio computed on the two neighboring plies is retained in Eq. 5.27.

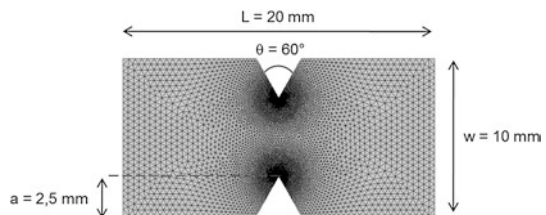
5.4 Application on Structural Test Cases

Tensile tests on T300/914C graphite/epoxy double-edge-notched (DEN) cross-ply laminates specimens were experimentally performed by Kortschot and Beaumont [40–42]. The tests were performed on $[90_j/0_j]_{ns}$ laminates (with $j = 1, 2$ and $n = 1, 2, 4$). Moreover, several ratios of total notch length to specimen width, $2a/w$, were studied. The specimens tested in tension were radiographed during the mechanical tests. Every radiograph has shown a similar cracking pattern where three main forms of damage are visible: (i) splits in the 0° plies from the tips of the notches, (ii) transverse matrix cracks in the 90° plies and (iii) triangular delamination zones at the $0/90$ interfaces.

Due to the presence of intralaminar damage and delamination cracks close to the notches, subjecting DEN specimens to tensile loading seems to be a well adapted test in order to demonstrate the capabilities of the proposed models to describe the influence of intralaminar damages on delamination. The dimensions of the DEN specimens have been chosen as indicated in Fig. 5.20, provided that the $2a/w$ ratio is equal to 0.5. Moreover, the stacking sequence $[90/0]_s$ has been chosen with 0.125 mm for ply thickness, as indicated in [42].

Using the geometrical and material symmetries, the finite element model of the DEN specimen under tension loading is based on 1/8 of the $[90/0]_s$ specimen

Fig. 5.20 Dimensions of the DEN specimen



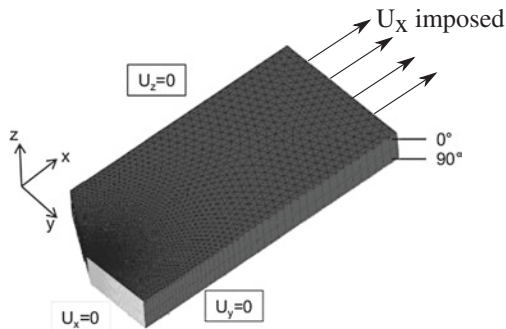


Fig. 5.21 Finite element model of the DEN specimen under tension loading

(Fig. 5.21). Each ply is represented by linear solid elements, with one element through the thickness, and cohesive zone elements are inserted between each ply.

The models used in this work have not been identified on T300/914C laminates but on T700GC/M21 laminates. Therefore, the comparison between the simulations and the experimental observations, reported in [42], will be only qualitative. The material properties used for the simulation are given in Table 5.1. It is important to note that the characteristic time τ_c , used as a delay effect on the damage evolution law of the model (Eq. 5.29), is considered in this work as a numerical parameter which permits to avoid the dependence between the damage rate and the mesh size. For the tensile tests on DEN specimens, simulations in displacement controlled mode with a loading rate of 0.1 mm/min performed with several mesh sizes have shown that the value $\tau_c = 80$ s is satisfying to avoid this numerical dependence.

In order to understand (i) the effect of the behavior of the plies on the interface and (ii) the necessity to take into account the influence of intralaminar damages

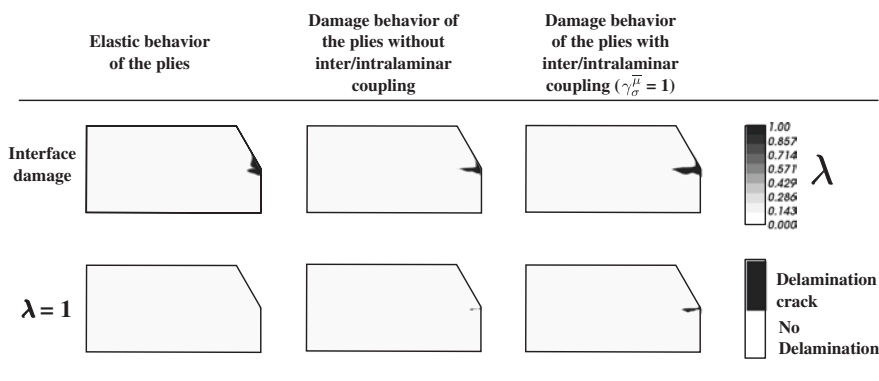


Fig. 5.22 Influence of the ply behavior and of the inter/intralaminar coupling on the delamination zone (interface damage field λ) and on the broken zone ($\lambda = 1$) in the DEN coupon subjected to tension loading

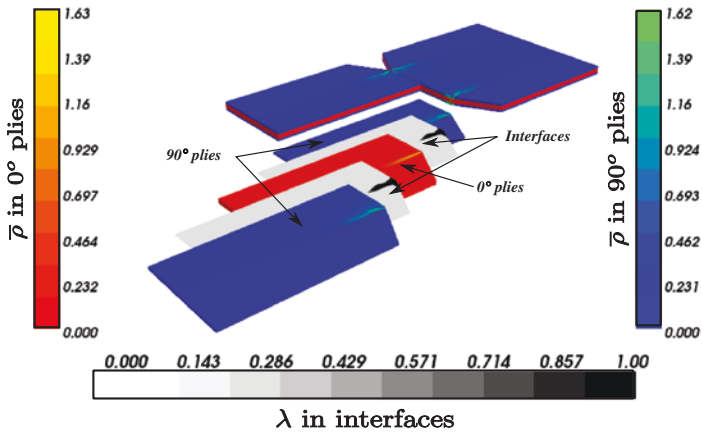


Fig. 5.23 Damage variable fields in the plies ($\bar{\rho}$) and in the interfaces (λ) in the DEN coupon subjected to tension loading for the configuration with a damage model for the plies and inter/intralaminar coupling ($\gamma_{\sigma}^{\mu} = 1$)

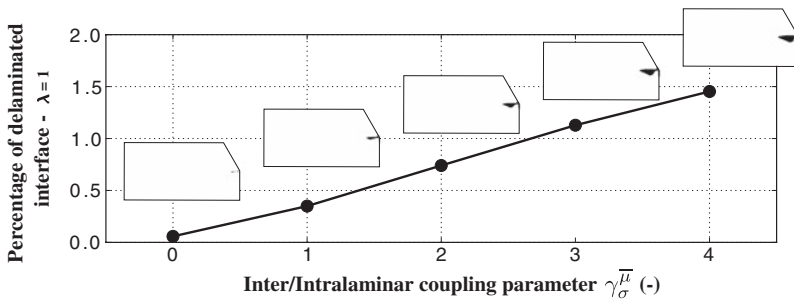


Fig. 5.24 Influence of the inter/intralaminar coupling parameter on the evolution of the percentage of delaminated area in the interfaces in a DEN coupon subjected to tension loading ($\gamma_{\sigma}^{\mu} = 0, 1, 2, 3$ and 4)

on the delamination (i.e. the inter/intralaminar coupling), three configurations have been studied

- without damage model for the plies,
- with damage model for the plies but without inter/intralaminar coupling,
- with the inter/intralaminar coupling in the finite element model.

On the one hand, the comparison between the first two configurations (Fig. 5.22) shows that the ply damage contributes strongly to the propagation of the delamination crack, whose orientation corresponds to the direction of the splits in the 0

plies. Nevertheless, the broken zone (i.e. the delamination zone where the damage variable λ reaches 1) is very localized. In contrast, the last configuration (Figs. 5.22 and 5.23) demonstrates that the inter/intralaminar coupling is essential in order to create a triangular delamination zone at the 0/90 interface, as observed experimentally in [42]. Therefore, it seems crucial to take into account the influence of the intralaminar damage on the delamination and the modeling strategy used in this work appears satisfying to describe this influence. It is worth mentioning that several simulations have been performed in order to choose the increment of time giving a description of the delamination independent of the post increment coupling method used.

On the other hand, the identification of the parameter $\gamma_{\sigma}^{\overline{\mu}}$ used for the inter/intralaminar coupling appears very important. Indeed, with the last configuration, simulations of the DEN specimen under tensile loading have been performed with $\gamma_{\sigma}^{\overline{\mu}} = 0, 1, 2, 3$ and 4. The results presented in Fig. 5.24 demonstrate that the size and shape of the broken zone strongly increase when $\gamma_{\sigma}^{\overline{\mu}}$ becomes higher. Therefore, it seems essential to identify precisely the relation between the interfacial properties and the intralaminar damages, using for instance the experimental characterization procedures proposed in Sect. 5.2.

5.5 Conclusions

In the present chapter, the influence of the intralaminar damage (transverse matrix cracking and local delamination) on the interlaminar damage has been investigated. Using specific device setups and coupons, this influence has been demonstrated experimentally through the analysis of the onset and propagation of delamination cracks. In order to model this inter/intralaminar damage coupling, a cohesive zone model has been developed. It takes into account the local delamination ratio, determined by a continuum damage model in the plies adjacent to the interface, using a post increment method in the implicit finite element analysis. The local delamination ratio is used to decrease the interfacial strength and the fracture toughness of the interface. The application of these models on a double-edge-notched specimen under tensile loading clearly demonstrates the importance of the contribution of the introduced coupling on damage pattern which is very similar to the coupling experimentally observed and reported in Refs. [40–42]. It is worth mentioning that the simulation results are very sensitive to the coupling parameter value, thus implying an improvement in its identification procedure.

Acknowledgments The authors would like to express their sincere gratitude to Dr. R. Valle for valuable and helpful discussions.

References

1. Abisset, E., Daghia, F., Ladevèze, P.: On the validation of a damage mesomodel for laminated composites by means of open-hole tensile tests on quasi-isotropic laminates. *Compos. Part A Appl. Sci. Manuf.* **42**, 1515–1524 (2011)
2. Allix, O., Deu, J.F.: Delayed-damage modelling for fracture prediction of laminated composites under dynamic loading. *Eng. Trans. Rozprawy Inzynierskie* **45**(1), 29–46 (1997)
3. Allix, O., Ladevèze, P.: Interlaminar interface modeling for the prediction of laminate delamination. *Compos. Struct.* **22**, 235–242 (1992)
4. Allix, O., Ladevèze, P., Corigliano, A.: Damage analysis of interlaminar fracture specimens. *Compos. Struct.* **31**, 61–74 (1995)
5. Allix, O., Lévêque, D., Perret, L.: Identification and forecast of delamination in composite laminates by an interlaminar interface model. *Compos. Sci. Technol.* **58**(5), 671–678 (1998)
6. Andersons, J., Knig, M.: Dependence of fracture toughness of composite laminates on interface ply orientations and delamination growth direction. *Compos. Sci. Technol.* **64**, 2139–2152 (2004)
7. ASTM (1994) Standard test method for mode I interlaminar fracture toughness of unidirectional continuous fiber reinforced composite materials. D5528-94A, Philadelphia, PA
8. ASTM (2001) Standard test method for mixed mode I-mode II interlaminar fracture toughness of unidirectional fiber-reinforced polymer matrix composites. D6671-01
9. ASTM (2006a) Standard test method for measuring the curved beam strength of fibre reinforced polymer matrix composite. D6415/D6415M-06a
10. ASTM (2006b) Standard test method for short-beam strength of polymer matrix composite materials and their laminates. D2344/D2344M-00
11. Barenblatt, G.: Mathematical theory of equilibrium cracks in brittle failure. *Adv. Appl. Mech.* **7**, 55–129 (1962)
12. Benzeggagh, M., Kenane, M.: Measurement of mixed-mode delamination fracture toughness of unidirectional glass/epoxy composites with mixed-mode bending apparatus. *Compos. Sci. Technol.* **56**, 439–449 (1996)
13. Berthelot, J.M.: Transverse cracking and delamination in cross-ply glass-fiber and carbon-fiber reinforced plastic laminates: Static and fatigue loading. *Appl. Mech. Rev.* **56**(1), 111–147 (2003)
14. Blackman, B., Kinloch, A.: Fracture tests for structural adhesive joints. In: Moore, D., Pavan, A., Williams, J. (eds.) *Fracture Mechanics Testing Methods for Polymers, Adhesives and Composites*, pp. 225–270. Elsevier, Amsterdam (2001)
15. Caiazzo, A., Costanzo, F.: Modeling the constitutive behavior of layered composites with evolving cracks. *Int. J. Solid Struct.* **38**(20), 3469–3485 (2001)
16. Camanho, P., Dávila, C., de Moura, M.: Numerical simulation of mixed-mode progressive delamination in composite materials. *J. Compos. Mater.* **37**(16), 1415–1438 (2003)
17. Carlsson, L., Gillepsie, J., Pipes, R.: On the analysis and design of the end notched flexure (ENF) specimen for mode II testing. *J. Compos. Mater.* **20**, 594–604 (1986)
18. Charrier, J., Carrère, N., Laurin, F., Bretheau, T., Goncalves-Novo, E., Mahdi, S.: Proposition of 3D progressive failure approach and validation on tests cases. In: 14th European Conference on Composite Materials (ECCM/14) (2010)
19. Charrier, J., Carrère, N., Laurin, F., Goncalves-Novo, E., Mahdi, S.: Proposition d'une méthode d'analyse dédiée aux structures composites soumises à des sollicitations hors-plan. In: 17^{ème} Journées Nationales sur les Composites (JNC 17) (2013)
20. Choi, N., Kinloch, A., Williams, J.: Delamination fracture of multidirectional carbon-fiber/epoxy composites under mode I, mode II and mixed-mode I/II loading. *J. Compos. Mater.* **33**, 73–100 (1999)

21. Crews, J., Reeder, J.: A mixed-mode bending apparatus for delamination testing. Technical report, Langley Research Center, Virginia, USA (1988)
22. Cui, W., Wisnom, M., Jones, M.: A comparison of failure criteria to predict delamination of unidirectional glass/epoxy specimens waisted through the thickness. *Composites* **23**(3), 158–166 (1992)
23. Daghia, F., Ladevèze, P.: Identification and validation of an enhanced mesomodel for laminated composites within the WWFE-III. *J. Compos. Mater.* **47**(20–21), 2675–2693 (2013). doi:[10.1177/0021998313494095](https://doi.org/10.1177/0021998313494095). URL <http://jcm.sagepub.com/content/47/20-21/2675>
24. Daudeville, L., Ladevèze, P.: A damage mechanics tool for laminate delamination. *Compos. Struct.* **25**, 547–555 (1993)
25. Dávila, C., Camanho, P., Turon, A.: Effective simulation of delamination in aeronautical structures using shells and cohesive elements. *J. Aircr.* **45**, 663–672 (2008)
26. de Morais, A., Pereira, A.: Mixed-mode I + II interlaminar fracture of glass/epoxy multidirectional laminates—part 1: analysis. *Compos. Sci. Technol.* **66**, 1889–1895 (2006)
27. de Morais, A., Pereira, A.: Application of the effective crack method to mode I and mode II interlaminar fracture of carbon/epoxy unidirectional laminates. *Compos. Part A Appl. Sci. Manuf.* **38**, 785–794 (2007)
28. de Morais, A., de Moura, M., Marques, A., de Castro, P.: Mode I interlaminar fracture of carbon/epoxy cross-ply composites. *Compos. Sci. Technol.* **62**, 679–686 (2002)
29. Dugdale, D.: Yielding of steel sheets containing slits. *J. Mech. Phys. Solids* **8**, 100–104 (1960)
30. Germain, N., Besson, J., Feyel, F.: Composite layered materials: anisotropic nonlocal damage models. *Comput. Method Appl. Mech.* **196**(4144), 4272–4282 (2007). doi:[10.1016/j.cma.2007.04.009](https://doi.org/10.1016/j.cma.2007.04.009). URL <http://www.sciencedirect.com/science/article/pii/S004578250700182X>
31. Gong, X., Benzeggagh, M.: Mixed mode interlaminar fracture toughness of unidirectional glass/epoxy composite. In: *Composite Materials: Fatigue and Fracture*, vol. 5, pp. 100–123. ASTM STP 1230 (1995)
32. Guinard, S., Allix, O., Guédra-Degeorges, D., Vinet, A.: A 3D damage analysis of low-velocity impacts on laminated composites. *Compos. Sci. Technol.* **62**, 585–589 (2002)
33. Hinton, M., Kaddour, A., Soden, P.: *Failure Criteria in Fibre Reinforced Polymer Composites: The World-Wide Failure Exercise*. Elsevier Science Ltd., Oxford (2004)
34. Huchette, C., Guinot, F.: Experimental and numerical analysis on delamination growth in damaged composite material. In: *13th European Conference on Composite Materials (ECCM/13)* (2008)
35. Huchette, C., Lévêque, D., Carrère, N.: A multiscale damage model for composite laminate based on numerical and experimental complementary tests. In: Sadowski, T. (ed.) *IUTAM Symposium on Multiscale Modelling of Damage and Fracture Processes in Composite Materials*, No. 135 in *Solid Mechanics and Its Applications*, pp. 241–248. Springer, Netherlands (2006). URL http://link.springer.com/chapter/10.1007/1-4020-4566-2_28
36. Huchette, C.: *Sur la complémentarité des approches expérimentales et numériques pour la modélisation des mécanismes d'endommagement des composites stratifiés*. Ph.D. thesis, University of Paris VI—Pierre et Marie Curie, France (2005)
37. ISO (1987) *Adhesives—determination of Tensile Strength of Butt Joints*. ISO 6922
38. Jackson, W., Ifju, P.: Through-the-thickness tensile strength of textile composites. *Composite materials: testing and design 12*, ASTM STP 1274, 218–238 (1996)
39. Ju, J.: On energy-based coupled elastoplastic damage theories: constitutive modeling and computational aspects. *Int. J. Solids Struct.* **25**, 803–833 (1989)
40. Kortschot, M., Beaumont, P.: Damage mechanics of composite materials. I: a damage based notched strength model. *Compos. Sci. Technol.* **39**, 289–301 (1990)
41. Kortschot, M., Beaumont, P.: Damage mechanics of composite materials. II: measurements of damage and strength. *Compos. Sci. Technol.* **39**, 303–326 (1990)
42. Kortschot, M., Beaumont, P., Ashby, M.: Damage mechanics of composite materials. III: prediction of damage growth and notched strength. *Compos. Sci. Technol.* **40**, 147–165 (1991)

43. Krueger, R.: The virtual crack closure technique: history, approach and applications. Technical report, ICASE, Hampton, Virginia (2002)
44. Ladevèze, P., LeDantec, E.: Damage modelling of the elementary ply for laminated composites. *Compos. Sci. Technol.* **43**(3), 257–267 (1992). doi:10.1016/0266-3538(92)90097-M. URL <http://www.sciencedirect.com/science/article/pii/026635389290097M>
45. Ladevèze, P., Lubineau, G., Marsal, D.: Towards a bridge between the micro- and meso-mechanics of delamination for laminated composites. *Compos. Sci. Technol.* **66**, 698–712 (2006)
46. Laurin, F., Carrère, N., Huchette, C., Maire, J.F.: A multiscale hybrid approach for damage and final failure predictions of composite structures. *J. Compos. Mater* **47**(20–21), 2713–2747 (2013). doi:10.1177/0021998312470151. URL <http://jcm.sagepub.com/content/47/20-21/2713>
47. Laurin, F., Carrère, N., Maire, J.F.: A multiscale progressive failure approach for composite laminates based on thermodynamical viscoelastic and damage models. *Compos. Part A Appl. Sci. Manuf.* **38**, 198–209 (2007)
48. Laurin, F., Charrier, J.S., Lévêque, D., Maire, J.F., Mavel, A., Nunez, P.: Determination of the properties of composite materials thanks to digital image correlation measurements. *Procedia IUTAM* **4**, 106–115 (2012)
49. Leguillon, D.: Strength or toughness? A criterion for crack onset at a notch. *Eur. J. Mech. A-Solid* **21**, 61–72 (2002)
50. Lekhnitskii, S.G.: *Theory of Elasticity of an Anisotropic Elastic Body*. Holden-Day Edn. Inc., San Francisco (1963)
51. NASA.: Standard tests for toughened resin composites. Technical report, Langley Research Center, Virginia, USA (1982)
52. O'Brien, T.: Mixed-mode strain energy-release rate effects on edge delamination of composites. In: 836 AS (ed.) *Effects of Defects in Composite Materials*. American Society for Testing and Materials, pp. 125–142 (1984)
53. Olsson, R.: Review—a survey of test methods for multiaxial and out-of-plane strength of composite laminates. *Compos. Sci. Technol.* **71**, 773–783 (2011)
54. Ozdil, F., Carlsson, L.: Beam analysis of angle-ply laminate DCB specimens. *Compos. Sci. Technol.* **59**, 305–315 (1999)
55. Pereira, A., de Morais, A.: Mixed-mode I + II interlaminar fracture of glass/epoxy multidirectional laminates—part 2: experiments. *Compos. Sci. Technol.* **66**, 1896–1902 (2006)
56. Pereira, A., de Morais, A.: Mixed-mode I + II interlaminar fracture of carbon/epoxy laminates. *Compos. Part A Appl. Sci. Manuf.* **39**, 322–333 (2008)
57. Pereira, A., de Morais, A.: Mixed-mode I+III interlaminar fracture of carbon/epoxy laminates. *Compos. Part A Appl. Sci. Manuf.* **40**, 518–523 (2009)
58. Pinho, S., Iannucci, L., Robinson, P.: Formulation and implementation of decohesion elements in an explicit finite element code. *Compos. Part A Appl. Sci. Manuf.* **37**, 778–789 (2006)
59. Prombut, P.: Caractérisation de la propagation de délaminage des stratifiés composites multidirectionnels. Ph.D. thesis, University of Toulouse III—Paul Sabatier, France (2007)
60. Prombut, P., Michel, L., Lachaud, F., Barrau, J.J.: Delamination of multidirectional composite laminates at $0/\pm$ ply interfaces. *Eng. Fract. Mech.* **73**, 2427–2442 (2006)
61. Reeder, J., Crews, J.: Mixed-mode bending method for delamination testing. *AIAA J.* **28**, 1270–1276 (1990)
62. Reeder, J., Crews, J.: Redesign of the mixed-mode bending delamination test to reduce non-linear effects. *J. Compos. Technol. Res.* **14**, 12–19 (1992)
63. Reeder, J.: An evaluation of mixed-mode delamination failure criteria. Technical report, Langley Research Center, Virginia, USA (1992)
64. Schuecker, C., Davidson, B.: Evaluation of the accuracy of the four-point bend end-notched flexure test for mode II delamination toughness determination. *Compos. Sci. Technol.* **60**, 2137–2146 (2000)

65. Sun, C., Zheng, S.: Delamination characteristics of double-cantilever beam and end-notched flexure composite specimens. *Compos. Sci. Technol.* **56**, 451–459 (1996)
66. Talreja, R.: Stiffness properties of composite laminates with matrix cracking and interior delamination. *Eng. Fract. Mech.* **25**(5), 751–762 (1986)
67. Thionnet, A., Renard, J.: Meso-macro approach to transverse cracking in laminated composites using Talreja's model. *Compos. Eng.* **3**(9), 851–871 (1993). doi:[10.1016/0961-9526\(93\)90044-K](https://doi.org/10.1016/0961-9526(93)90044-K). URL <http://www.sciencedirect.com/science/article/pii/096195269390044K>
68. Turon, A.: Simulation of delamination in composites under quasi-static and fatigue loading using cohesive zone models. Ph.D. thesis, Department d'Enginyeria Mecànica i de la Construcció Industrial, Universitat de Girona, Spain (2006)
69. Turon, A., Dávila, C., Camanho, P., Costa, J.: An engineering solution for mesh size effects in the simulation of delamination using cohesive zone models. *Eng. Fract. Mech.* **74**, 1665–1682 (2007)
70. Turon, A., Camanho, P., Costa, J., Renart, J.: Accurate simulation of delamination growth under mixed-mode loading using cohesive elements: definition of intralaminar strengths and elastic stiffness. *Compos. Struct.* **92**, 1857–1864 (2010)
71. Vandellos, T., Hautier, M., Carrère, N., Huchette, C.: Development of a new fracture test to identify the critical energy release rate: the tensile flexure test on notched specimen. *Eng. Fract. Mech.* **96**, 641–655 (2012)
72. Vandellos, T., Huchette, C., Carrère, N.: Proposition of a framework for the development of a cohesive zone model adapted to carbon-fiber reinforced plastic laminated composites. *Compos. Struct.* **105**, 199–206 (2013)
73. Whitcomb, J.: Analysis of instability-related growth of a through-width delamination. Technical report, Langley Research Center, Virginia, USA (1984)
74. Wisnom, M., Hallett, S.: The role of delamination in strength, failure mechanism and hole size effect in open hole tensile tests on quasi-isotropic laminates. *Compos. Part A Appl. Sci. Manuf.* **40**, 335–342 (2009)
75. Zébulon (2014). URL <http://www.zset-software.com/products/zebulon/>

Chapter 6

Microdamage Modeling in Laminates

Janis Varna

6.1 Introduction

During service life structures made of laminated composites are subjected to complex combinations of thermo-mechanical and environmental loads. The final macroscopic failure of composite laminate is preceded by initiation and evolution of several microdamage modes in layers. This is because the transverse tensile strain to failure of unidirectional composites is lower than other failure strain components. Therefore transverse cracking of layers with off-axis orientation with respect to the main load direction, caused by combined action of transverse tensile stress and shear stress, is usually the first mode of damage [1, 2].

The crack, see Fig. 6.1a, is usually well defined, it runs parallel to fibers in the layer and the crack plane is transverse to the laminate middle-plane. Often they cover the whole thickness of the layer and propagate over the whole width of the tensile test specimen (may be except for laminates with very thin layers and/or in low stress cyclic (fatigue) loading). These cracks which in this chapter we call intralaminar cracks are called also matrix cracks, tunneling cracks, transverse cracks or inclined cracks (in off-axis layers with different orientation than 90°).

Intralaminar cracks do not usually cause the final failure of a laminate, but may significantly impair the effective properties of the laminate [3] and serve as a source for other damage modes initiation, such as delamination [4, 5] (Fig. 6.1b), “stitch cracks” [6] and fiber breaks (Fig. 6.1c) in the adjacent plies.

With increasing load or with the number of cycles in fatigue loading the number of cracks increases. Initiation, evolution and effect of these cracks on laminate

J. Varna (✉)
Composites Centre Sweden, Lulea University of Technology,
SE 97187 Lulea, Sweden
e-mail: janis.varna@ltu.se

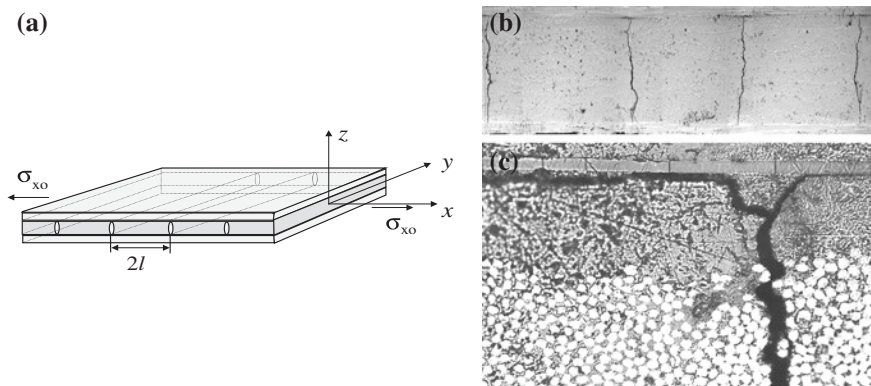


Fig. 6.1 Intralaminar cracks in cross-ply laminate: **a** schematic showing of laminate with cracks; **b** multiple cracks with rather uniform distribution; **c** the crack tip region at the 0/90 interface with local interlayer delamination and fiber breaks in the 0-layer

stiffness has been discussed in many papers, see for example review papers [7, 8]. The extent of cracking in a layer is quantified with an average measure called crack density: number of cracks in a layer over certain distance measured transverse to the crack plane. So the crack density in k th layer is ρ_k (cracks/mm). Number inverse to the crack density is called average crack spacing $2l_k = 1/\rho_k$. Slightly deeper analysis based on features of an elastic stress solution reveals that the distance between cracks measured in, for example, millimeters is what we can measure but it is not the most informative characteristic of the damage state. For example, spacing 1 mm between cracks does not give any information how close to each other they are in the sense of interaction of corresponding stress perturbations. Instead, if we know that the crack dimension in vertical direction (which is equal to the cracked ply thickness t_k) is 1.0 mm we know that the distance between two cracks in the previous example is equal to the crack size as it approximately is in Fig. 6.1b. This is a very high crack density, close to the maximum possible reached in tests (often called saturation region or the region with strong crack interaction). If the spacing between cracks is larger than $4t_k$ cracks may be considered as non-interactive (as a consequence of St. Venant's principle the stress perturbations caused by them do not overlap). Therefore, a proper measure of distance between cracks is so-called normalized crack spacing $2l_{kn} = 2l_k/t_k$ with corresponding normalized crack density $\rho_{kn} = \rho_k t_k$.

Each cracking event in a layer creates two new traction free surfaces. This means that the transverse stress and the in-plane shear stress on the crack surface is equal to zero and new cracks close to existing crack cannot be expected. With increasing distance from the crack the transverse and in-plane shear stresses start to recover and when the distance is large they may asymptotically approach the value as it was in the layer before cracking (called far-field stress). The stress transfer mechanism from the undamaged layer to the damaged is through high

intra-laminar shear stresses at the layer interface in the vicinity of the crack. The efficiency of the stress transfer (the distance needed to recover the far-field stress state) depends on the interface quality. The distance is much shorter in case the interface is not damaged and can be very large in case of delaminations starting from the intralaminar crack. The described stress transfer mechanism resulting in stress recovery in the damaged layer allows for creation of many cracks in the same layer (multiple cracking).

A relevant question following this description is: if the distance from the crack to recover the far-field stresses in a laminate with ply thickness 0.25 mm is only a couple of mm why we do not have at least 50 cracks created simultaneously at the same load in a specimen with gauge length 100 mm? Experiments show that each new crack requires an increase of the applied load. The reason is that the transverse and shear failure properties are not the same along the transverse direction of the layer: there are some weaker positions where the first cracks occur and more strong positions requiring larger macroscopic load. As it will be shown in Sect. 6.3 the transverse failure properties have statistical distribution, for example, it can be Weibull distribution for strength [9–11]. In result only a few cracks are created at relatively low load because there are just a few weak locations. Then the cracking rate increases with increasing load because we are reaching loads where the material has the highest probability density of failure and many positions have almost the same failure properties. After that the multiple cracking slows down because there are only a few positions with high value of failure properties; the probability density curve approaches to zero.

There is another mechanism slowing down the rate of cracking in the high crack density region. The stress distribution between two cracks depends on the distance between them (normalized spacing). When the normalized crack density is very high, there is no enough distance for stress recovery and even the maximum values of the in-plane stresses between two cracks become significantly lower than the far-field value. The creation of a new crack between two existing requires significantly higher macroscopic load being applied to the laminate. This in addition to fact that the remaining positions for cracking are very strong slows down and eventually stops the intralaminar cracking.

Due to progressing microcracking, the macroscopic thermo-mechanical properties of the laminate are degraded. We will illustrate the degradation mechanism on symmetric $[0/90]_S$ cross-ply laminate as an example. Assume that we apply to this laminate macroscopic average tensile stress σ_x^{LAM} and compare its axial deformation before cracking and in the presence of intralaminar cracks in the 90-layer. It is important to realize that in both cases the macroscopic deformation of the 0-layer is equal to the macroscopic deformation of the laminate (this is why strain gauges and extensometers are located on the specimen surface) and therefore the 0-layer strain can be used as a measure of the average axial strain of the laminate ε_x^{LAM} and from there the axial modulus of the laminate E_x^{LAM} is calculated. In undamaged state the stress distribution in layers does not depend on coordinate and the Classical Laminate Theory (CLT), which is based on iso-strain assumption can be used to calculate the strain ε_{x0}^{LAM} and stresses in layers, for example σ_{x0}^{90}

(index 0 is added to specify the case with zero damage) and $\sigma_{x0}^{90^\circ}$. If the 90-layer has a crack the $\sigma_x^{90^\circ}$ at the crack face is zero. Due to stress transfer over layer interface the stress increases with the distance from the crack and somewhere far from the crack it could reach $\sigma_{x0}^{90^\circ}$. So,

$$\sigma_x^{90^\circ} \leq \sigma_{x0}^{90^\circ} \quad (6.1)$$

in any point of the damaged 90-layer. Due to axial force balance the axial force has to be the same in any cross-section of the laminate. This means that because of (6.1) stress $\sigma_x^{0^\circ}$ in any position of the 0-layer is larger than in the undamaged laminate,

$$\sigma_x^{0^\circ} \geq \sigma_{x0}^{0^\circ} \quad (6.2)$$

Larger axial stress results in larger local axial strains in the 0-layer, leading to larger macroscopic deformation of the layer. Obviously, the result is larger laminate strain, $\varepsilon_x^{LAM} \geq \varepsilon_{x0}^{LAM}$ meaning that the damaged laminate axial modulus is lower, $E_x^{LAM} \leq E_{x0}^{LAM}$. Quantitative estimation of the change requires knowledge of the stress distribution between cracks.

The quantification simplifies realizing that the average values of in-plane stresses are governing the stiffness degradation and details of the stress distribution are not important. It can be shown using divergence theorem [12] that the average stress applied to the laminate has a rule of mixtures (RoM) relationship to average stresses in layers. Since the average stress between two cracks is always lower than $\sigma_{x0}^{90^\circ}$, from RoM and the force equilibrium follows that the average stress in the 0-layer is higher than $\sigma_{x0}^{0^\circ}$ with the same consequences as described in the previous paragraph.

The simplest way of accounting for average stress reduction in a damaged ply in a model is by replacing the cracked layer with “effective layer” which has “effective” = reduced thermo-elastic properties. How much the properties have to be reduced is an open question. An extreme case of this approach is the well known ply-discount model, commonly used together CLT. Physically this approach is not correct: thermo-mechanical constants of the material in the damaged layer have not changed. Nevertheless, the reduction of elastic constants is a simple way to incorporate the effect of reduced average stress in the layer, still keeping the concept of iso-strain which in non-bending case builds the basis of CLT. However, the common assumption in this approach that transverse and shear properties of a ply with cracks are zero is very conservative and does not reflect the real situation where the number of cracks is increasing in a stable manner during the service life. The ply-discount assumption corresponds to case with an infinite number of cracks when the in-plane stresses between cracks approach to zero. Therefore, requirement that laminate stiffness with increasing crack density approaches the ply-discount model prediction must be satisfied in all predictions based on stress distribution models.

The basic approach, called micromechanics modeling, (see review for example in [13]), is based on perturbation stress analysis. Most of the models are focused on

an approximate analytical description of the local stress distribution in the repeating element between two cracks. The simplest calculation schemes used are based on shear lag assumption or variational principles [13–16]. Most of the analytical solutions are applicable to cross-ply type of laminates with cracks in 90-layers only. The most accurate numerical routines based on Reissner’s variational principle are presented in [17]. “Equivalent constraint model” was introduced in [18] to determine the effective properties of the damaged layer. In Zhang et al. [18] his approach was used together with shear lag model. With improved stress model it has the potential of accounting for interaction of cracks belonging to different layers of laminates.

Using the calculated stress distributions between cracks one could find the average value of the stress change in the cracked layer to be used to predict laminate stiffness degradation. In this work we will use a different method to account for the average stress change. The change of in-plane average stresses due to cracking is proportional to the average values of the crack face opening (COD) and sliding displacements (CSD). Certainly the change depends also on crack density in the layer as well as elastic and geometrical constants. So, dependent on the suitability of the used model the stiffness change can be expressed in terms of average stress change or in terms of average COD and CSD. The former method is more suitable when analytical stress distributions are available, whereas the latter is preferable when crack face displacements have been calculated (for example, using FEM). Therefore the damaged laminate stiffness can be expressed also in terms of density of cracks and two parameters: average COD a CSD as done in the GLOB-LOC model [19, 20]. These two rather robust parameters depend on the normalized crack spacing (crack density). In Sect. 6.4 stiffness expressions based on COD and CSD approach are given for a general symmetric laminate with cracks in all layers.

The relationship between the average stress change between cracks and the average value of COD and CSD can be easily explained. If we imagine that somehow the corresponding points on both crack faces are kept together (it would require application of tractions to points on crack surfaces), not allowing the crack to open or the faces to slide ($COD = CSD = 0$), the stress between cracks would be the same as in undamaged laminate and the laminate thermo-elastic properties would not change. However, we know that under in-plane tension cracks open; under shear their surfaces slide and under compression they are closed. The latter case with closed cracks is very interesting because, as just described, the stress state is as in undamaged laminate and, hence, the stiffness of the damaged laminate in compression equals to the undamaged laminate stiffness.

In the tensile case, as soon as we allow for separation of points on crack faces (opening or sliding), the stress between cracks is reduced. The larger the COD and CSD, the larger is the average stress reduction. The most extreme case is fully delaminated unit between two cracks. Then there is no stress transfer between layers and in-plane stresses in the cracked layer are zero. This corresponds to the maximum possible COD and CSD which can be easily estimated knowing that the 90-layer material in this case is not deformed and the whole load is carried by the rest of layers.

Most of the existing stiffness models use assumption that cracks are uniformly distributed in the layer, with equal spacing between them. It simplifies analysis and is expected to give sufficient accuracy. However, the crack distribution in the layer may be highly non-uniform. This is more typical in the beginning of the cracking process when the average crack density is relatively low. The reason is the random distribution of transverse failure properties along the transverse direction of the layer. At low crack density the stress distribution between two existing cracks has a large plateau region with constant high stress and any position there is a site of possible failure. At high crack density there is a distinct maximum in the stress distribution between cracks and a new crack most likely will be created in the middle between existing cracks.

The possible inaccuracy introduced in laminate stiffness prediction by using assumption of uniform spacing between cracks in a layer has been addressed in [21, 22]. In [21] so-called “double-periodic” approach was suggested to calculate the COD of a crack in a non-uniform case: the COD is found as average from two solutions for periodic crack systems representing the two different distances to neighbouring cracks. Very good agreement of this approach was found with direct FEM solution for non-uniform cracks. It was shown that at fixed crack density the elastic modulus reduction is highest if the cracks are uniformly distributed and in this sense periodic crack distribution models give lower bond to modulus.

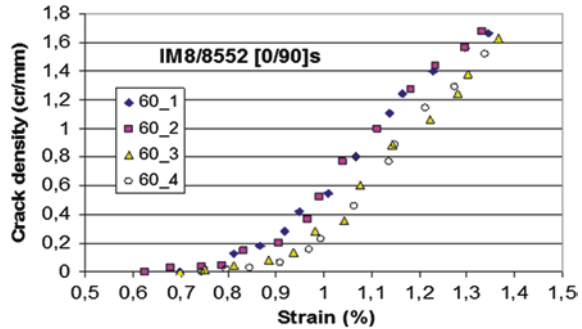
6.2 Experimental Methods for Damage State Characterization

Crack density in a layer enters all expressions for stiffness reduction and it is the main output of damage evolution modeling. Therefore quantification of the damage state is of primary importance for accurate predictions. A short overview of most common experimental methods (optical microscopy, X-ray images, acoustic emission) is given in this section discussing their accuracy, complexity of measurements and other drawbacks.

The effect of each individual crack on stiffness depends on its geometrical features: cracks with large, severe damaged zone at the crack tip and delaminations between layers starting from the crack tip, see Fig. 6.1, lead to more stiffness reduction than “ideal” straight cracks because dependent on these features the crack opening (and the average stress between cracks) may be very different. These details of the damage used in models have to be studied experimentally and below we briefly describe the use of Electronic Speckle Pattern Interferometry (ESPI) for COD measurement and Raman spectroscopy for stress concentration analysis. Stress concentrations caused by intralaminar cracks are triggering new damage modes as interlayer delamination and fiber breaks in adjacent layers and the initial shape of stress concentrations is changing.

Optical observations belong to the simplest group of methods. Specimen edge inspection under microscope is preferable for Carbon fiber (CF) reinforced

Fig. 6.2 Crack density increase with axial strain in 90-layer of CF/EP cross-ply laminate. Different symbols correspond to edge data for different specimens of the same plate. Measurement length was 80 mm along the specimen edge



composite laminates: thermal tensile stresses in layers are high due to high manufacturing temperature and large mismatch in thermal expansion coefficients between layers. In result, intralaminar cracks in CF composites are opened, the polished fiber cross-sections are bright and shiny and even without any applied mechanical load cracks are well seen in a microscope as dark belts, see Fig. 6.1b.

For CF laminates the most accurate is to remove the specimen from the testing machine after loading it to certain level of strain for inspection in a microscope. An example of the crack density dependence on the applied strain level in CF/EP IM8/8552 cross-ply laminate obtained in this way is shown in Fig. 6.2.

For GF laminates this method is not applicable because we would not see any cracks in unloaded specimen (thermal stresses are lower and due to worth reflective properties the contrast is lower). If a small tensile testing machine is linked to the microscope, one can see that applying even small strains we start to see cracks, see Fig. 6.1c. Since this option is not always available, counting can be made on the loaded specimen edge or on the surface without unloading and taking it out from the testing machine. Good accuracy can be achieved adjusting the position and orientation of a light source. Cracks can be counted on edges in reflected light as well as on the specimen surface as dark lines in transmitted light. The surface observations are not decisive if several damaged layers of the same orientation are in the laminate: some cracks are too close to each other and it is not possible to distinguish which crack belongs to which of these layers.

Since the described procedure is rather time consuming, edge replicas are often used: instead of microscopy observation of the specimen edge a replica (“print” of the crack on plastic film) taken from the edge of loaded specimen is analyzed in a microscope after the mechanical test. The advantage is that replicas are taken in loaded state when the crack is most open. Since the quality of replicas is never better than the quality of the polished surface, a thorough calibration of the data obtained from replicas with respect to the direct microscopy has to be performed for every used laminate lay-up and material. Generally speaking in replicas we can lose some cracks and count as cracks some artifacts like polishing scratches. Observing the specimen in microscope and slightly changing the focus we can get more “in-depth” information than observing replicas.

The accuracy of these techniques decreases with decrease of layer thickness, because the crack size is limited by the layer thickness and small cracks at the same applied strain open proportionally less and are difficult to distinguish.

Observation of local interlayer delaminations using optical methods described here is very difficult because the delamination cracks are usually not opened. One can see them in Fig. 6.1b but the measured delamination length would be very uncertain.

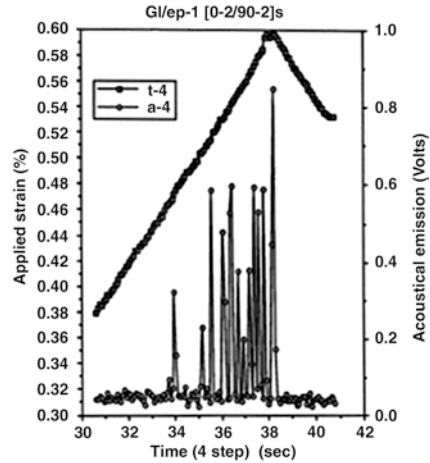
Yet, the most critical in evaluating this method is the question how representative are the observations done on the specimen edge for the bulk of the specimen. First is to check whether the crack density values obtained from both specimen edges are the same. Then the specimen has to be cut longitudinally to introduce two new edges which after careful polishing are inspected and compared with data from edges. Only after this validation the edge data can be used as representative for the material. The differences can be particularly large for laminates with thin layers and especially in fatigue loading: more damage is in the edge region. The differences between edge and the interior can be very large for secondary damage like local delaminations: often they are present on specimen edges only.

X-ray images Penetrant liquid has to fill the crack to obtain X-ray image of the crack and actually what we see is the penetrant. Images, for example, in [23], show cracks in both layers of a cross-ply laminate subjected to tensile fatigue loading. Cracks in 0-layers are due to mismatch in Poisson's ratios between layers and often they are initiated from cracks in the 90-layer. Local delaminations at cracks and especially in their crossing regions can be identified. Similarly as with transmitted light technique, using X-ray technique it is difficult to distinguish between cracks in the top and in the bottom 0-layer of the laminate. A limiting factor is the condition that penetrant has to enter the crack in order it to be seen. This means that the crack to be seen has to be in the surface layer or connected with the specimen edge. Cracks inside the material, not connected with edges, other cracks or surfaces are invisible. The penetrant enters more easily inside of large opened cracks. It can be much more difficult if the size of the tunneling crack in laminate thickness direction is small (thin cracked layer).

Acoustic emission Often the energy released during intralaminar crack propagation is larger than necessary to create the new crack surface. Part of the excess of the energy goes in acoustic signal in the frequency region 10 Hz–100 kHz. Using a sensor on the specimen surface these signals can be recorded. Recording simultaneously the applied strain dependence of time we can determine the number of cracks corresponding to certain level of strain. An example with data recorded for GF/EP cross-ply laminate [23] is shown in Fig. 6.3. The cracking in the 90-layer of this laminate was unstable (after initiation the crack instantaneously propagated across the whole width of the specimen) and the acoustic signals shown as peaks in Fig. 6.3 are very distinct and the number of cracks is easy to count. As follows from Fig. 6.3 the applied strain was increasing linearly until value 0.6 % was reached. After that the strain was reduced. No new cracks (acoustic events) were observed during the unloading.

If a more sophisticated equipment and software is available, two acoustic sensors may be placed on the specimen in two different positions. Then from the time delay in both signals the exact position of the created crack can be

Fig. 6.3 Acoustic signals caused by multiple cracking in 90-layer of GF/EP [02/902] cross-ply laminate during increasing applied strain [23]



identified. This helps to separate signals from cracks in the gauge length region from cracks created outside it (close to the clamping region, under tabs).

The described technique has problems to identify and register cracks at high crack density. The signals become much less distinguishable than in the initial stage of cracking shown in Fig. 6.3. Part of the reason is that the stress state between two existing cracks where the new crack is created is very complex and the new cracks (tunnels) are not so well defined: they are not straight cracks covering the whole thickness and width of the layer. Instead we have curved cracks close to existing ones; so-called “delta cracks” and growing interlayer delamination. The acoustic emission method in the way as it is described here cannot distinguish between these modes of damage or to quantify them.

Another not resolved problem is detection and quantification of stable crack growth or growth in small increments (jumps) as it is typical for cracks in very thin layers and especially during cyclic loading. In these cases the acoustical emission signals are not distinctive: there is an emission but it is not in form of countable peaks with each peak corresponding to one damage event. An alternative in this case would be to obtain the total emitted energy as a function of time and try to correlate it with the damage state. Even in this case there is a problem of separating the acoustic energy corresponding to different simultaneous modes of damage.

Delaminations at the crack tip and deviations from ideal straight crack geometry (branched cracks, delta cracks) affect the opening (COD) and the sliding (CSD) of crack surfaces and in this way the amount of stiffness reduction. Therefore experimental information regarding COD and CSD is required to compare it with values from idealized models. For example, the COD of an ideal straight crack with no damage at the interface would be much smaller than in a case with delamination.

The first measurements of the CODs were reported in [24, 25]. The distance between crack faces as a function of layer thickness coordinate was measured from micrographs and also using image analysis. In spite of measurement errors due to uncertainties in focusing the microscope to the exact crack surface position and due

to filtering when image analysis was used, it was found that the average value of COD depends on stiffness ratio of the cracked and the supporting layer and on their thickness ratio. These findings were later confirmed with FEM calculations.

Recently, more accurate and reliable COD and CSD measurements were performed using one of the methods of full-field strain measurements, the **Electronic Speckle Pattern Interferometry** (ESPI) [26]. The ESPI is based on interference of two coherent laser beams: reference beam and observation beam that form the same angle with respect to the studied surface, so the corresponding speckle patterns also interfere [27]. From recording the phase maps for the initial and the final stress states the relative displacement at each point on the specimen surface is calculated. The discontinuities correspond to the crack locations and are seen as displacement jumps. COD from model with ideal crack geometry was validated for cracks in inside layers [26]. The technique is very time consuming and, whereas it renders very unique information for the research community, is not suitable for industrial application. Since this technique is optical it can be used on the edge and surfaces of the laminate only.

More details regarding the damage state at the intralaminar crack tip (local strain distribution) can be obtained using Raman spectroscopy [27]. The basis of this technique is the fact that, for example, in Kevlar fibers the Raman wavelength depends on the applied stress. This property is used to obtain the strain distribution along the fiber. In order to use the fiber as a local strain gauge, the fiber is first calibrated to obtain the relationship between the applied stress and the Raman wavenumber. The fiber is embedded in the composite with a special function to serve as sensor. This technique has very high resolution, and the strain values are obtained directly from the fiber. Unfortunately, as for all optical techniques, the measurements are on edges and outer surfaces, or the matrix has to be transparent. The method is relatively slow (the data collection time for a single measurement in a fixed position along the fiber takes several seconds).

In [29] this technique was used to measure the local stress concentration distribution in the 0-layer of a cross-ply laminate close to the tip of an intralaminar crack, plotting the stress as a function of the distance from crack tip. It was found that the shape of the stress concentration changes after higher load application: the normalized maximum becomes lower and the concentration zone is wider. This behavior was explained in [29] by fiber breaks introduced in the 0-layer close to the crack tip, see also Fig. 6.1c, which are “softening” part of the 0-layer adjacent to the layer interface.

6.3 Damage Initiation and Growth

6.3.1 *Initiation Stress and Propagation Stress*

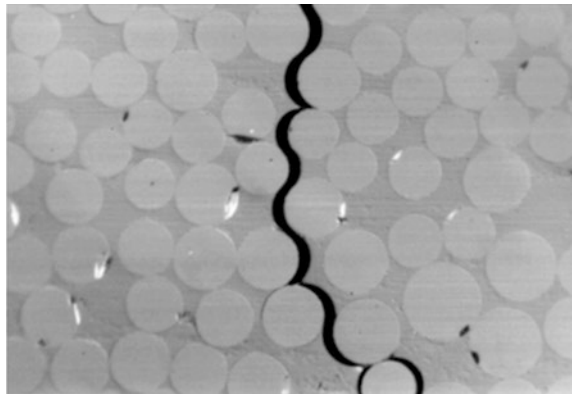
Two phases in development of each individual intralaminar crack can be identified: initiation and propagation (growth). The stress state based analysis is similar in quasi-static and in cyclic (fatigue) loading. We assume that a necessary condition

for intralaminar crack initiation and propagation in the layer under consideration is that the transverse stress, which consists of thermal and mechanical part, is tensile or at least non-negative. Existence of large in-plane shear stresses in the layer contributes to cracking. Many experiments show that the tensile transverse stress has a major role for crack initiation and also for the crack growth: the crack opening mode (Mode I) is the dominant mode of crack propagation. Often in modeling the in-plane shear stresses contribution to the cracking process is even neglected. This simplification of the analysis reflects the fact that the resistance to crack growth in shear (Mode II) is usually much higher than in Mode I. Ignoring the effect of shear stresses in this section is not critical for the simulation methodology described and mixed mode criteria can be easily implemented if available.

First we will give a rather “diffuse” definition of the initiation and propagation terms. Initiation is a process on fiber/resin scale (microscale) which leads to development of a mesoscale damage entity (defect, flaw, crack...?) which further development (propagation) can be analyzed ignoring the microstructure and considering the layer in the laminate as a homogeneous material.

Detailed analysis of initiation is very complex and it is outside the scope of this book. Generally speaking the sequence of micro-events is known: it is a combination of failure of interface leading to prolonged debonds and the resin failure following by coalescence of these small damage entities into large damage entity which starts to grow unstable in the layer thickness direction, see Fig. 6.4. The unstable growth in thickness direction is arrested when the crack approaches the interface with the neighboring layer. This process has been analyzed using Linear Elastic Fracture Mechanics (LEFM) in homogenized layer analytically [30] as well as numerically with FEM [31]. The most probable region for initiation is at specimen edges where the transverse in-plane stress is slightly higher than in the interior of the specimen. Another important parameter is geometrical, it is the local variation of fiber volume fraction: in several locations fibers are very close to each other or even touching. There: (a) the stress concentrations are higher than in a unit cell with average fiber content; (b) due to very limited space between

Fig. 6.4 Intralaminar crack formed in result of coalescence of fiber/matrix interface debonds



fibers impregnation with resin could be of lower quality than in average, leading to reduced interface and resin mechanical properties. These locations are randomly distributed in the specimen.

Since suitable and reliable micromechanics analysis for evaluating the necessary applied strain or stress level for initiation does not exist, we will employ here a pragmatic approach stating that there is a material system dependent stress level σ_{in} required to initiate a defect large enough to grow unstably in thickness direction and then propagate along fibers to become intralaminar crack. Notation σ_{in} can be considered as a symbolic notation for simultaneously acting transverse and shear stress in the layer, most probably expressed through stress invariants. It is convenient to assume that the initiation stress level does not depend on the thickness of the layer. Certainly, a weak reduction with increasing volume (layer thickness) is still possible because of the increasing probability to find locations with very unfortunate combinations of geometrical and failure parameters. For example, changing the thickness several times has a small effect in the Weibull strength distribution [9]. The initiation stress σ_{in} is expected to be higher than the transverse tensile strength of the same unidirectional (UD) composite, σ_T^+ . The reason is that comparing with free standing UD composite the severity of large defects at the layer surface inside the laminate is reduced due to bond with the neighboring layer. Simple analysis in [32] shows that suppressing surface defect growth the initiation stress can be by 50 % higher than the transverse tensile strength

$$\sigma_{in} = 1.12\sqrt{2}\sigma_T^+. \quad (6.3)$$

LEFM can be applied for propagation of the initiated crack: the available potential energy has to be equal or larger than the work required creating a new crack surface. In terms of LEFM for Mode I growth: the Mode I energy release rate has to be equal or larger than its critical value G_{IC} which is material property (energy needed to create a unit of new crack surface). In the presence of in-plane shear stresses mixed mode propagation is possible and a criterion which involves Mode I and Mode II energy release rate as well the corresponding critical values may be required.

The energy release rate, G is proportional to the square of the in-plane stress in the layer in the location of cracking. G is a linear function of the intralaminar crack size in thickness direction which is equal to the cracked layer thickness. From here and the propagation criterion the stress level σ_{prop} for crack growth can be calculated. From the above description we conclude that σ_{prop} depends on the cracked layer thickness t_k .

Two different scenarios can describe what follows after crack initiation. If the stress level which was necessary to initiate the crack is high and the layer thickness is large

$$\sigma_{in} > \sigma_{prop} \quad (6.4)$$

In this case the crack will propagate in unstable manner as soon as it is initiated. In terms of energies it means that at the initiation stress level the available strain

energy release rate is much higher than the critical value G_c . In this case the initiation stress governs the multiple cracking process and fracture mechanics is not an applicable tool for analysis.

On the other hand, if the stress for the initiation, σ_{in} is rather low and/or the ply is very thin,

$$\sigma_{in} < \sigma_{prop} \quad (6.5)$$

the crack after initiation will not propagate. In other words at the initiation stress level the available strain energy release rate for crack propagation is lower than G_c . In this case nothing will happen directly after the initiation and higher stress has to be applied to get the crack propagating. This stress level for propagation can be calculated using fracture mechanics. In this case cracking is propagation governed.

The phenomenon that the laminate strain for first ply failure in thin layers becomes ply thickness dependent was experimentally observed in [34, 35] and called “in-situ strength”. Using critical strain energy release rate based failure criterion the stress for crack propagation σ_{prop} has $1/\sqrt{t_k}$ dependence on ply thickness t_k and therefore stress level for crack propagation in thin layers is higher. So, according to our description in thin layer crack is initiated at roughly the same stress as in thick layers but its propagation is delayed. Unfortunately, the thickness of the layer at which transition takes place from the initiation stress σ_{in} controlled cracking behavior to ply thickness dependent propagation stress σ_{prop} (fracture mechanics) controlled behavior is different for different composite systems and has to be determined in tests. Comparison of crack density curves for several ply thicknesses is the most correct way to find the transition point.

6.3.2 Statistical Nature of Initiation Stress Distribution

We will explain the statistical effects considering transverse stresses only. The ideas and methodology are applicable for general in-plane loading and expressions are easy to generalize.

Statistical distribution of the transverse cracking initiation stress σ_{in} is assumed in simulations. In its transverse direction each layer, where cracks may be expected, is considered as consisting of many small elements. Each element has its individual intralaminar cracking initiation stress. Weibull strength distribution is assumed to describe the variation in σ_{in} between elements but the geometrical position of element with a given σ_{in} is random.

A proper test to obtain the Weibull distribution parameters is tensile loading of cross-ply specimens with counting intralaminar cracks after reaching different loading levels (far-field mechanical + thermal stress in the local axes of the layer with cracks). Two to three specimens usually give enough data for statistical analysis. To obtain initiation stress σ_{in} distribution, test has to be performed on laminates with relatively thick 90-layer (0.5 mm and more). This is necessary to ensure that cracking is initiation governed: the initiated crack propagates at once

through the whole specimen and, hence, the crack counting on the specimen edge is validated. The above is valid assuming that the initiation stress does not depend on the layer thickness.

In our earlier work [36] we found values around $m_\sigma \approx 18$ for the Weibull shape parameter using different composites. In analysis the length of the element in the transverse direction is related to the maximum possible crack density and is selected so that each element may crack not more than once. As a rough estimate, one can assume that in internal layers at highest crack density the average distance between cracks is equal or slightly larger than the k th cracked layer thickness

$$\rho_{k,\max} = \frac{1}{t_k} \quad (6.6)$$

So, the element size has to be taken equal or smaller than the ply thickness. In surface layer the spacing at highest crack density (saturation) is approximately two times larger.

$$\rho_{k,\max} = \frac{1}{2t_k} \quad (6.7)$$

These values are suggested based on observations with many composite systems and are applicable as long as the straight crack assumption is applicable: after crack saturation new damage modes occur with increasing loading (delta cracks, curved cracks, local delaminations) but they are difficult to quantify and to include in models. The effective stiffness of the layer at this stage is already significantly reduced and the laminate stiffness is approaching the ply discount model prediction.

The analysis presented in this section is not a Monte Carlo type of simulation where failure of each individual element is considered explicitly based on local stress distribution and its individual failure properties. In Monte-Carlo simulations each element has to be significantly smaller. Here we express the probability of cracking through crack density without specifying which particular element has failed.

The Weibull distribution for crack initiation stress σ_{in} is in form

$$P_{in} = 1 - \exp \left[-\frac{V}{V_0} \left(\frac{\sigma_T}{\sigma_{in0}} \right)^{m_\sigma} \right] \quad (6.8)$$

In (6.8) P_{in} is the probability that crack is initiated when the transverse tensile stress in the element is σ_T ; m_σ and σ_{in0} are the shape and the scale parameters obtained in tests with reference specimens of element volume V_0 ; V is the volume of the considered element which has to be included if the identified shape parameters are used for cracking probability calculation in layers of different thickness.

Sometimes m_σ is estimated from standard deviation of transverse tensile strength data for UD composite specimens. Then the σ_{in0} value may be estimated from the

average tensile transverse strength σ_T^+ of the UD composite. Due to suppression of surface defect growth when the layer is in a laminate we obtain increase of initiation stress described by relationship (6.3). It is reasonable to assume that the same relationship is valid for scale parameters in Weibull distributions

$$\sigma_{in0} = 1.12\sqrt{2}\sigma_0 \quad (6.9)$$

where σ_0 is the scale parameter we would have for UD composite transverse strength distribution for specimens with volume V_0 . It is related to the average transverse strength σ_T^+ of large US specimens (with volume V_{UD}) [37] by

$$\sigma_T^+ = \sigma_0 \left(\frac{V_0}{V_{UD}} \right)^{1/m_\sigma} \Gamma \left(1 + \frac{1}{m_\sigma} \right) \quad (6.10)$$

In (6.10) Γ is gamma function. From (6.9) and (6.10)

$$\sigma_{in0} = \frac{\sigma_T^+ 1.12\sqrt{2}}{\Gamma \left(1 + \frac{1}{m_\sigma} \right)} \left(\frac{V_{UD}}{V_0} \right)^{1/m_\sigma} \quad (6.11)$$

Even if (6.11) is mathematically correct, it should be used with caution. The volume ratio V_{UD}/V_0 of UD specimen and an element in the cracked layer is very large and the strength recalculation to smaller volumes may be inaccurate, especially if we remember that m_σ value is obtained using data on a limited number of broken UD specimens.

More advisable is to use multiple cracking evolution data (crack density) for 90-layers in cross-ply laminates to determine parameters in (6.8). The probability of initiation P_{in} can be defined as the number of elements with initiated cracks M_{in} versus the total number of elements M in the layer. This definition is valid for low crack densities where cracks are not interacting. The number of initiated cracks in the considered thick layer case is equal to the number of fully developed cracks, $M_{in} = M_{cr}$ and therefore

$$P_{in} = \frac{M_{cr}}{M} \quad (6.12)$$

According to (6.6) the number of elements in interior layer with index k is

$$M = \frac{L}{t_k} = L \cdot \rho_{k,\max} \quad (6.13)$$

In surface layer it is approximately two times different. Similarly, the number of cracks when the stress in the layer is $\sigma_{T0}^{(k)}$ is related to average spacing between them

$$M_{cr} = \frac{L}{2l_k} = L \cdot \rho_k \left(\sigma_{T0}^{(k)} \right) \quad (6.14)$$

Substituting (6.13), (6.14) in (6.12) we obtain relationship linking the probability of crack initiation P_{in} with the crack density at certain stress level in a layer with index k

$$P_{in}^{(k)} = \frac{\rho_k \left(\sigma_{T0}^{(k)} \right)}{\rho_{k,max}} \quad (6.15)$$

Using crack density data for the 90-layer in cross-ply laminate in (6.15) we obtain P_{in}^{90} dependence on transverse stress σ_{T0}^{90} . The stress is calculated using CLT from the applied load (or strain) and from the temperature difference ΔT between manufacturing and testing temperature

$$\sigma_{T0}^{90} = \sigma_{T0}^{90mech} + \sigma_{T0}^{90thermal} \quad (6.16)$$

Index “0” is used for stresses according to CLT i.e. laminate without damage. Then, expecting that (6.8) is valid, standard procedure is applied to the obtained experimental relationship: double logarithm of P_{in}^{90} we plot against $\ln(\sigma_{T0}^{90})$. If the data really follow Weibull distribution, the obtained relationship is linear. Using linear fit to these data (trend line in EXCEL, for example) we obtain parameters m_σ and σ_{in0} from fitting function.

More accurate values of Weibull parameters can be found comparing Monte-Carlo simulations with experiment [37] or using the probabilistic approach developed in [38]. Both approaches require analytical models for stress distribution between two cracks.

Now we will discuss how the Weibull distribution for crack initiation stress (6.8) with known parameters m_σ and σ_{in0} can be used to predict the number (density) of initiated cracks in an arbitrary k th layer of a multidirectional laminate subjected to increasing general thermo-mechanical loading. The proposed approach is simple and has no ambition for high accuracy. The application routine differs dependent on the level of the transverse stress σ_{prop} for propagation with respect to the initiation stress region given by (6.8), (6.15).

In thin layers the propagation stress may be very high and most of the cracks in the layer may be initiated before the transverse stress becomes equal to σ_{prop} . In this situation simulations of growing density of initiated cracks can be performed combining (6.8) and (6.15) (this time for initiated cracks that are not propagating)

$$\rho_k^{in} = \rho_{k,max} \left\{ 1 - \exp \left[- \frac{V}{V_0} \left(\frac{\sigma_{T0}^{(k)}}{\sigma_{in0}} \right)^{m_\sigma} \right] \right\} \quad (6.17)$$

We still assume that only one crack can initiate in each element and therefore in (6.17) $\rho_{k,max}$ is the highest possible crack density in the k th layer discussed above. All initiated cracks are relatively short in the fiber direction and in different elements they can be in different positions along fibers. Because of that interaction between initiated cracks may be neglected and the CLT transverse stress in the layer, $\sigma_{T0}^{(k)}$ can be used in (6.17). Since we use assumption that crack initiation is only weakly dependent on ply thickness, this expression can be used for all layers independent on their thickness.

Another extreme case is when the propagation stress is low and each initiated crack immediately propagates leading to “fully developed” cracks. The transverse stress $\sigma_T^{(k)}$ in any point between two cracks (including the maximum point which is in the middle) is lower than the stress in undamaged layer at the same applied load

$$\sigma_T^{(k)} \leq \sigma_{T0}^{(k)} \quad (6.18)$$

The average value of the stress is also lower

$$\sigma_{T(av)}^{(k)} = k_\sigma \sigma_{T0}^{(k)} \quad k_\sigma < 1 \quad (6.19)$$

Coefficient k_σ depends on the density of fully developed cracks. Expressions (6.8) and (6.15) still are applicable, but the question is what should we use for $\sigma_T^{(k)}$. One obvious option is to use the maximum value of the stress between two cracks but one could argue that even if the stress reaches maximum in one point the strength is randomly distributed. It could be very high in that particular point and the next crack may come where stress is lower but the strength is even lower. Another alternative is to use the average stress between cracks when estimating the probability of occurrence of a new crack. Independent on the choice the expression for crack density in this case is

$$\rho_k^{in} = \rho_k = \rho_{k,max} \left\{ 1 - \exp \left[-\frac{V}{V_0} \left(\frac{\sigma_{T0}^{(k)} k_\sigma}{\sigma_{in0}} \right)^{m_\sigma} \right] \right\} \quad (6.20)$$

The most complex is the case when the propagation stress σ_{prop} is somewhere in the middle of the initiation stress distribution region. In this case as long as $\sigma_{T0}^{(k)} < \sigma_{prop}$ initiation follows (6.21)

$$\rho_k^{in} = \rho_{k,max} \left\{ 1 - \exp \left[-\frac{V}{V_0} \left(\frac{\sigma_{T0}^{(k)}}{\sigma_{in0}} \right)^{m_\sigma} \right] \right\}, \quad \sigma_{T0}^{(k)} < \sigma_{prop} \quad (6.21)$$

Just before $\sigma_{T0}^{(k)} = \sigma_{prop}$ we have initiated crack density ρ_{k0}^{in} . As soon as we reach equality all initiated cracks propagate and instantly become fully developed with crack density $\rho_k = \rho_{k0}^{in}$. Since some scatter in fracture toughness for crack propagation is inevitable in reality the crack density jump will not be instant. With increasing load new cracks initiate but they will immediately grow in fully developed cracks according the rule

$$\rho_k^{in} = \rho_k = \rho_{k,max} \left\{ 1 - \exp \left[-\frac{V}{V_0} \left(\frac{\sigma_{T0}^{(k)} k_\sigma}{\sigma_{in0}} \right)^{m_\sigma} \right] \right\}, \quad \sigma_{T0}^{(k)} k_\sigma > \sigma_{prop} \quad (6.22)$$

In this simulation approach interaction is accounted only for cracks in the same layer. Interaction between cracks in different layers during damage evolution is neglected because at present this problem is not studied sufficiently.

We can summarize the sequence of calculation steps used to construct crack density curves, stress-strain curves using this approach.

- (a) For each layer estimate $\rho_{k,\max}$ according to (6.6) or (6.7) and select an arbitrary set of crack density ρ_k values in the region $[0; \rho_{k,\max}]$.
- (b) Using (6.17)–(6.22) find the corresponding $\sigma_{T0}^{(k)}$ set
- (c) Subtract thermal stresses found using CTL from the $\sigma_{T0}^{(k)}$ set to find the set of pure mechanical stresses in the layer $\sigma_{T0}^{(k)mech}$ responsible for the selected crack densities.
- (d) Use CLT to calculate the set of corresponding strains applied to the laminate ε_{x0}^{LAM} . Since it is linearly related to $\sigma_{T0}^{(k)mech}$, calculation for linear elastic material is simple. More complex macroscopic mechanical loading cases are analyzed similarly
- (e) Plot the crack density in each layer versus ε_{x0}^{LAM} and fit the curves with monotonously increasing functions. From these functions we can find the damage state in each layer at arbitrary selected ε_{x0}^{LAM} to be used in following simulations.
- (f) Use thermo-elastic properties reduction expressions in Sect. 5.4 to find the degraded laminate thermo-elastic properties for these damage states (E_x^{LAM} , ν_{xy}^{LAM} , α_x^{LAM} etc.).
- (g) Calculate damaged laminate strains ε_x^{LAM} using the values of ε_{x0}^{LAM} and the degraded elastic constants.

The last step on this list requires more detailed explanation. When stress σ_{x0}^{LAM} is applied to the laminate the strain in the damaged laminate, ε_x^{LAM} will be larger than the strain in the undamaged laminate, ε_{x0}^{LAM} . It is because the elastic modulus E_x^{LAM} is lower than E_{x0}^{LAM} . The stress-strain relationship for the damaged and undamaged laminate are

$$\sigma_{x0}^{LAM} = E_{x0}^{LAM} \varepsilon_{x0}^{LAM}, \quad \sigma_{x0}^{LAM} = E_x^{LAM} \varepsilon_x^{LAM}, \quad \varepsilon_x^{LAM} > 0 \quad (6.23)$$

From here we obtain expression

$$\varepsilon_x^{LAM} = \frac{E_{x0}^{LAM}}{E_x^{LAM}} \varepsilon_{x0}^{LAM} \quad (6.24)$$

The crack density curves obtained in step (e) as functions of ε_{x0}^{LAM} now can be plotted versus the real laminate strains ε_x^{LAM} using (6.24).

6.3.3 Energy Release Rate Based Analysis of Intralaminar Crack Propagation

Intralaminar crack propagation along the fiber direction in a layer of laminate is illustrated in Fig. 6.5 (L-is the fiber direction). Except for the specimen edge region where the stress state is 3-dimensional and except the very beginning of the

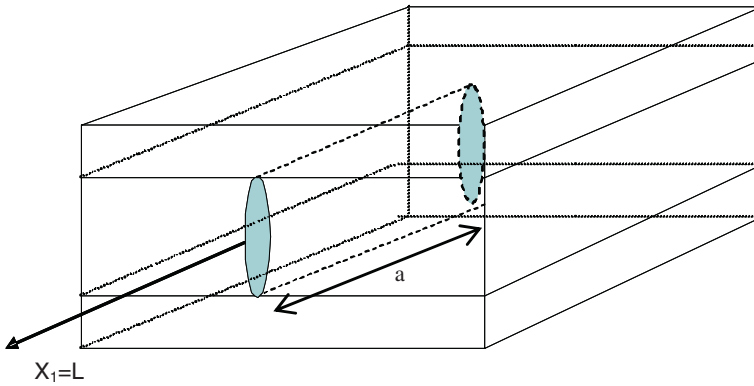
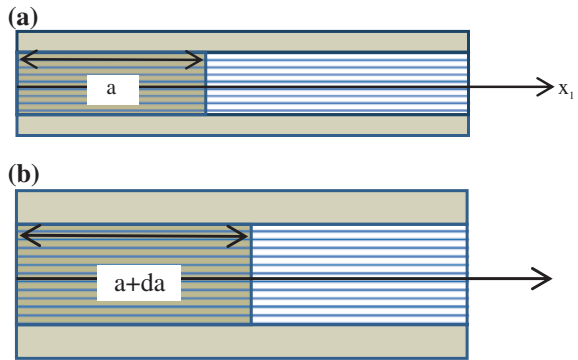


Fig. 6.5 Schematic showing of intralaminar (tunneling) crack with length a propagating parallel to fibers in the layer

Fig. 6.6 Intralaminar crack propagation along x_1 coordinate: **a** crack length; **b** crack length $a + da$



intralaminar crack propagation when the crack is relatively short, the intralaminar growth is in a self-similar manner (so-called steady state growth). Condition for that is that the crack front is far away from both specimen edges.

The meaning of a self-similar propagation is explained in Fig. 6.6 where a section of the laminate parallel to the crack plane in the position of the crack is shown. In Fig. 6.6a the crack length is a . The shape of the crack front and the stress state there are very complex and not known. However, the stress state at the crack front $x_1 = a + da$ in Fig. 6.6b is the same as in Fig. 6.6a at $x_1 = a$, the stress state is just shifted in x_1 direction by da . The stress state at specimen edges is also complex but it is not changing due to crack propagation by da . Using the made assumption that the crack front is far away from specimen edges we conclude that between specimen edges and the crack front we have rather large regions where the stress distribution is not dependent on x_1 (plateau region). When the crack propagates by da the plateau region to the left of the crack front increases by da whereas the plateau region to the right decreases by. This is the only change and the corresponding change of potential energy can be easily calculated.

The new created region of length da in x_1 direction on the left of the crack front is shown in Fig. 6.7b. The middle layer there contains a fully developed crack. The “lost” part of the plateau region to the right of the crack front of the same length da is shown in Fig. 6.7a. It does not contain crack and the stress distribution there can be calculated using CLT.

Obviously the potential energy change in the system, which is needed in fracture mechanics analysis, is equal to the energy change when an element without crack in Fig. 6.7a is replaced with a cracked element in Fig. 6.7b. The change could be determined by first calculating the stress states (for example, using CLT for element in Fig. 6.7a and FEM for element in Fig. 6.7b) and then find strain energy. However, there is a simpler way: the potential energy change is equal to the work which has to be performed on crack surfaces to close it, thus bringing the element back to the undamaged state. We will demonstrate the procedure in details for crack opening case and for a crack which does not interact with other cracks in the same layer (low crack density), see Fig. 6.8.

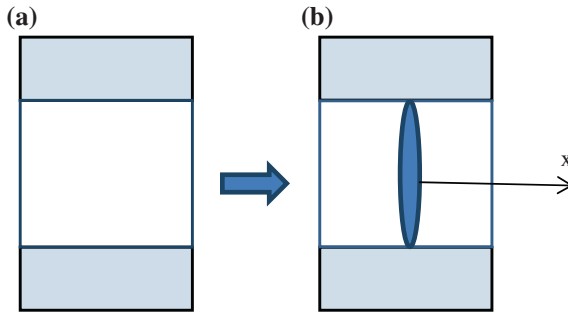


Fig. 6.7 Schematic showing of the undamaged region (a) replaced with region containing crack (b)

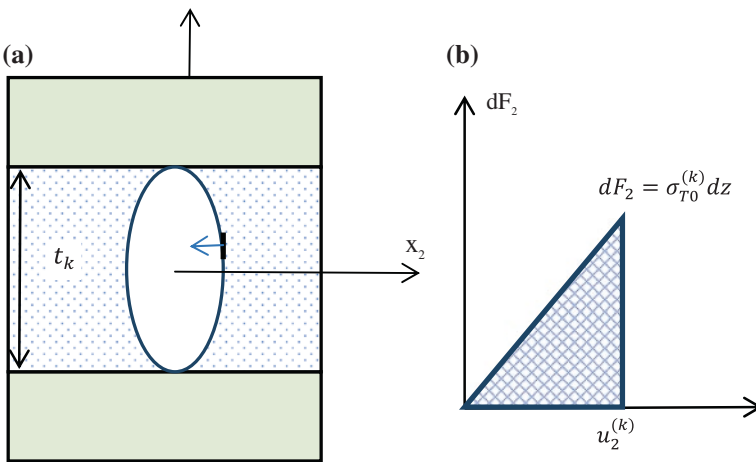


Fig. 6.8 Schematic showing of a force applied to the element on crack surface and the work to move this element to position when the crack is closed

We consider an element with area $dzda$ on the deformed (opened) crack face and apply to it increasing force dF_2 in the x_2 direction until it is closed. To close it we have to apply displacement $u_2^{(k)}(z)$ which is equal to 1/2 of the opening of the crack at this z -coordinate. The transverse stress when it is closed is $\sigma_{T0}^{(k)}$, the same as before cracking. In the definition used in this chapter COD is equal to $u_2^{(k)}(z)$, i.e. it is 1/2 of the distance between corresponding points on both crack surfaces.

The force in the closing instant is $dF_2 = \sigma_{T0}^{(k)} dzda$ and the performed work by closing

$$dW_2 = \frac{1}{2} u_2^{(k)}(z) dF_2 = \frac{1}{2} \sigma_{T0}^{(k)} u_2^{(k)}(z) dzda. \quad (6.25)$$

The work to close both crack surfaces (two surfaces is the reason for coefficient 2 in (6.26)) is

$$W_2 = 2 \cdot \frac{da}{2} \sigma_{T0}^{(k)} \int_{-\frac{t_k}{2}}^{+\frac{t_k}{2}} u_2^{(k)}(z) dz. \quad (6.26)$$

The energy release rate G_I is defined as the work to close the crack divided with area $da \cdot t_k$ and therefore

$$G_I = \sigma_{T0}^{(k)} \cdot \frac{1}{t_k} \int_{-\frac{t_k}{2}}^{+\frac{t_k}{2}} u_2^{(k)}(z) dz. \quad (6.27)$$

Average value of any function $\phi(z)$ in segment $[-\frac{t_k}{2}, +\frac{t_k}{2}]$ is defined as

$$\phi_a = \frac{1}{t_k} \int_{-\frac{t_k}{2}}^{+\frac{t_k}{2}} \phi(z) dz. \quad (6.28)$$

Hence, the integral in (6.27) divided by t_k is the average value of the COD over the crack surface (here assumed independent on X_1)

$$G_I = \sigma_{T0}^{(k)} u_{2a}^{(k)}. \quad (6.29)$$

In (6.29) we see the importance of the average crack opening displacement $u_{2a}^{(k)}$ for the energy release rate in Mode I, G_I . In linear elastic solution all stresses strains and displacements are proportional. Therefore the average COD, $u_{2a}^{(k)}$ is proportional to the far-field transverse stress in the layer, $\sigma_{T0}^{(k)}$ and to the dimensions of the model which can be represented by the transverse size of the crack which is equal to the ply thickness t_k . It motivates to use normalized average COD defined as follows

$$u_{2an}^{(k)} = \frac{u_{2a}^{(k)}}{\sigma_{T0}^{(k)} t_k} E_T = \frac{E_T}{\sigma_{T0}^{(k)} t_k^2} \int_{-\frac{t_k}{2}}^{+\frac{t_k}{2}} u_2^{(k)}(z) dz. \quad (6.30)$$

In (6.30) factor E_T is introduced to have $u_{2na}^{(k)}$ as a dimensionless parameter. In terms of normalized average COD the strain energy release rate given by (6.29) can be rewritten as

$$G_I = \left[\sigma_{T0}^{(k)} \right]^2 \frac{t_k}{E_T} \cdot u_{2an}^{(k)} \quad (6.31)$$

Due to its importance here and also in stiffness reduction predictions, see Sect. 6.4, the normalized average COD, $u_{2an}^{(k)}$ and its dependence on elastic and geometrical parameters of layers and the laminate lay-up has been studied extensively using numerical methods [19, 20, 39–41]. It was found that $u_{2an}^{(k)}$ is a robust parameter slightly dependent on cracked layer and neighboring layer stiffness ratio in direction transverse to the crack and on the thickness ratio of these layers. Simple fitting expressions for $u_{2an}^{(k)}$ obtained in FEM parametric analysis are presented in Appendix.

Similar analysis can be performed for crack face sliding and the strain energy release rate in Mode II cracking. The crack face sliding displacement, $u_1^{(k)}(z)$ is introduced as half of the distance in fiber direction between corresponding points on both crack surfaces. The normalized average CSD is introduced as

$$u_{1an}^{(k)} = \frac{u_{1a}^{(k)}}{\sigma_{LT0}^{(k)} t_k} G_{LT} = \frac{G_{LT}}{\sigma_{LT0}^{(k)} t_k^2} \int_{-\frac{t_k}{2}}^{+\frac{t_k}{2}} u_1^{(k)}(z) dz \quad (6.32)$$

and the energy release rate in Mode II is

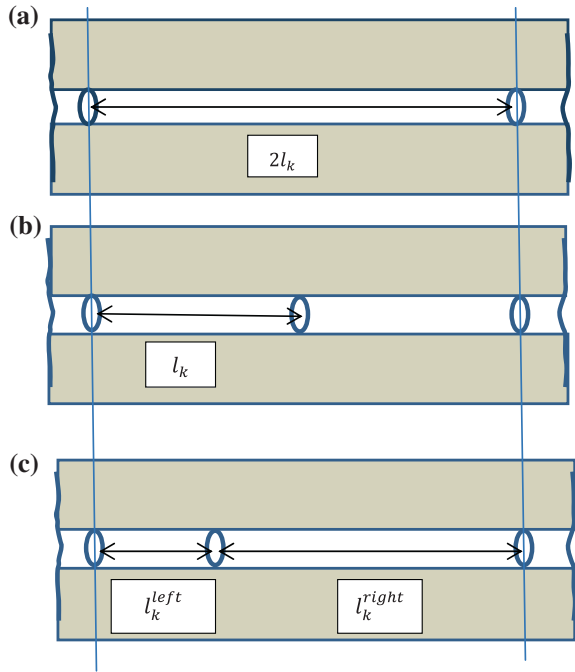
$$G_{II} = \left[\sigma_{LT0}^{(k)} \right]^2 \frac{t_k}{G_{LT}} \cdot u_{1an}^{(k)} \quad (6.33)$$

Expressions (6.31) and (6.33) for energy release rates are applicable only for so-called “non-interactive” cracks when after the crack closing the stress in the crack position is equal to the far-field value which comes from CLT. At higher crack density it is not correct because the stress at the closed crack is lower because of neighboring cracks.

At higher crack density we can assume having 2 cracks with distance between them $2l_k$ as shown in Fig. 6.9a. For simplicity we assume that the considered element between the two vertical lines is a repeating element. First we consider case when the next crack propagates in the middle between these two existing cracks as shown in Fig. 6.9b focusing on Mode I. We have to calculate the strain energy release rate when the new crack is created.

We can use the approach used above and calculate the work to close the crack but the obtained expression would contain the stress $\sigma_T^{(k)}$ in the middle between these two “old” cracks which in an unknown way depends on the “old” crack density (spacing $2l_k$). Instead we will find the work to close the “new” crack in a different way: we can close ALL cracks by first closing the “new” one and then the “old” ones. The work to close all cracks in the repeating element at once is denoted $W_{all \rightarrow 0}$, the work to close the “old” cracks when the “new” crack is already closed is $W_{old \rightarrow 0}$, the unknown work to close the “new” crack in the

Fig. 6.9 A “new” crack propagating between two “old” cracks: **a** damage state with two old cracks; **b** “new” crack in the *middle* between two “old” cracks; **c** “new” crack in an arbitrary position between two old cracks



presence of both “old” cracks is $W_{all \rightarrow old}$. Obviously we can first close the “new” crack and then the “old” cracks and summary work is

$$W_{all \rightarrow 0} = W_{all \rightarrow old} + W_{old \rightarrow 0} \tag{6.34}$$

or

$$W_{all \rightarrow old} = W_{all \rightarrow 0} - W_{old \rightarrow 0}. \tag{6.35}$$

The work to close all cracks at once can be calculated as in the first part of this section, because after closing the stress in the layer is the far-field stress. We have one “new” crack in the middle and two halves of the “old” cracks to close and the crack spacing is l_k .

The expression is

$$W_{all \rightarrow 0} = 2 \left[\sigma_{T0}^{(k)} \right]^2 \frac{t_k}{E_T} \cdot u_{2an}^{(k)}(l_k) \cdot t_k da. \tag{6.36}$$

Notation $u_{2an}^{(k)}(l_k)$ is used to emphasize that the normalized average COD is calculated using (6.30) for crack spacing l_k corresponding to crack density $\rho_k = 1/l_k$. The work to close the “old” cracks (two halves of them belong to the analyzed element) when the “new” is already closed is

$$W_{old \rightarrow 0} = \left[\sigma_{T0}^{(k)} \right]^2 \frac{t_k}{E_T} \cdot u_{2an}^{(k)}(2l_k) \cdot t_k da. \tag{6.37}$$

In (6.37) $u_{2an}^{(k)}(2l_k)$ is the normalized average COD for crack spacing $2l_k$. Expressions (6.36) and (6.37) are substituted in (6.35) obtaining the work to close the “new” crack

$$W_{all \rightarrow old} = \left[\sigma_{T0}^{(k)} \right]^2 \frac{t_k}{E_T} \cdot \left[2u_{2an}^{(k)}(l_k) - u_{2an}^{(k)}(2l_k) \right] t_k da. \quad (6.38)$$

Dividing by the new created surface $t_k da$ we obtain

$$G_I = \left[\sigma_{T0}^{(k)} \right]^2 \frac{t_k}{E_T} \cdot \left[2u_{2an}^{(k)}(l_k) - u_{2an}^{(k)}(2l_k) \right]. \quad (6.39)$$

Similar expression for Mode II cracks propagation reads

$$G_{II} = \left[\sigma_{LT0}^{(k)} \right]^2 \frac{t_k}{G_{LT}} \cdot \left[2u_{1an}^{(k)}(l_k) - u_{1an}^{(k)}(2l_k) \right]. \quad (6.40)$$

Expression for work to close the “new” crack is valid if the crack is in the middle between two “old” cracks. This may not be correct and the distance to the closest crack to the left and right for the “new” crack may be l_k^{left} and l_k^{right} respectively. The COD on the left face of the crack is different than on the right face.

The energy release rate when a crack is not in the middle was analyzed in [21]

$$G_{nonuniform} = \frac{1}{2} \left[\sigma_{T0}^{(k)} \right]^2 \frac{t_k}{E_T} \cdot \left[2u_{2an}^{(k)}(l_k^{right}) - u_{2an}^{(k)}(2l_k) \right. \\ \left. + 2u_{2an}^{(k)}(l_k^{left}) - u_{2an}^{(k)}(2l_k) \right] \quad (6.41)$$

To use the derived expressions for energy release rates criteria for crack propagation have to be formulated. In a simplest case they are $G_I = G_{Ic}$ and $G_{II} = G_{IIc}$. A large variety of mixed mode criteria are available, but at present there is rather limited knowledge about interaction between different fracture modes in composites.

Finally, it has to be reminded that the fracture toughness G_{Ic} and G_{IIc} may have different values in different locations. It is not clear whether the location with the lowest initiation stress has also the lowest fracture toughness. Actually it is not relevant, relevant is a question what is the fracture toughness in the material surrounding the initiation location. It is not difficult to accept the thought about variation of fracture toughness due to non-uniform fiber distribution. However, it is not clear whether the variation can be described by Weibull distribution as it was assumed in [42].

6.4 Stiffness of Damaged Laminate

6.4.1 Calculation Expressions

We consider symmetric N layer laminate the upper part of which is shown in Fig. 6.10. The k th layer of the laminate has thickness t_k and fiber orientation angle θ_k . Direction 1 is fiber direction and direction 2 is transverse to fibers.

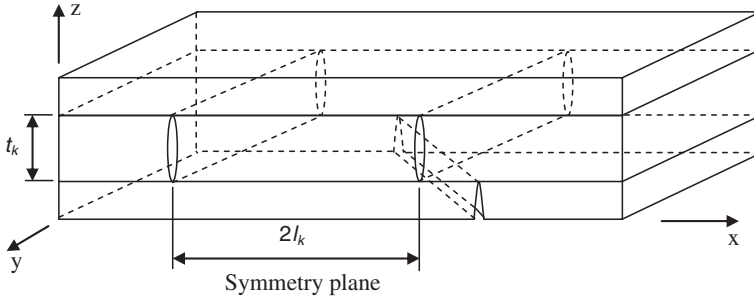


Fig. 6.10 Schematic showing of the *upper part* of symmetric laminate with cracks in different layers

The total thickness of the laminate, $h = \sum_{k=1}^N t_k$. In result of loading layer may contain intralaminar cracks. The damage state is characterized by crack density in the k th layer ρ_k defined as the number of cracks per mm length measured transverse to the crack plane. The crack density in a layer is $\rho_k = 1/(2l_k^{edge} |\sin\theta_k|)$. The average half distance between cracks in the layer measured on the specimen edge is l_k^{edge} . Dimensionless crack density ρ_{kn} in layer is introduced as $\rho_{kn} = t_k \rho_k$. “Vector” and matrix objects are denoted by $\{\}$ and $[\]$ respectively. The macroscopic stiffness matrix of the damaged laminate is $[Q]^{LAM}$ and the stiffness of the undamaged laminate is $[Q]_0^{LAM}$. The laminate compliance matrix $[S]_0^{LAM} = ([Q]_0^{LAM})^{-1}$. The thermal expansion coefficient vectors of the undamaged and damaged laminate are $\{\alpha\}_0^{LAM}$ and $\{\alpha\}^{LAM}$. A bar above the matrix and vector entities in following text indicates layer characteristics in the global coordinate system x, y, z .

In this section exact expressions derived in [19, 20] for macroscale thermoelastic constants of the damaged laminate RVE are presented. They were obtained using so-called “GLOB-LOC” approach establishing link between global thermoelastic properties of damaged laminate and the local stress state close to the crack. Expressions for general symmetric laminate with intralaminar cracks in plies were obtained. The effect of the stress perturbation caused by crack is expressed in terms of crack face opening and sliding displacements whereas the number of cracks is presented by normalized crack density. The expressions are as follow

$$[Q]^{LAM} = \left([I] + \sum_{k=1}^N \rho_{kn} \frac{t_k}{h} [K]_k [S]_0^{LAM} \right)^{-1} [Q]_0^{LAM} \tag{6.42}$$

$$\{\alpha\}^{LAM} = \left([I] + \sum_{k=1}^N \rho_{kn} \frac{t_k}{h} [S]_0^{LAM} [K]_k \right) \{\alpha\}_0^{LAM} - \sum_{k=1}^N \rho_{kn} \frac{t_k}{h} [S]_0^{LAM} [K]_k \{\bar{\alpha}\}_k \tag{6.43}$$

The $[K]_k$ matrix-function for a layer with index k is defined as

$$[K]_k = \frac{2}{E_2} [\bar{Q}]_k [T]_k^T \begin{bmatrix} 0 & 0 & 0 \\ 0 & u_{2an}^k & 0 \\ 0 & 0 & \frac{E_2}{G_{12}} u_{1an}^k \end{bmatrix} [T]_k [\bar{Q}]_k \quad (6.44)$$

The stiffness matrix of the damaged laminate, $[Q]^{LAM}$ is symmetric as requested by thermodynamics considerations. These matrix expressions for thermo-elastic properties contain elastic ply properties, details of laminate lay-up and dimensionless density of cracks in each layer. The influence of each damage entity is represented by the 3×3 displacement matrix in (6.44) which contains the normalized average COD, u_{2an}^k and normalized average CSD, u_{1an}^k of the crack surfaces in k th layer. It is assumed that all cracks in the same layer are equal: they have the same crack face displacements and the crack distribution is uniform. In (6.42) and (6.43) $[I]$ is the identity matrix.

When the distance between cracks in a layer is much larger than the crack size, the stress perturbations of two neighboring cracks do not overlap and cracks in this region are called *non-interactive*. The normalized average COD and CSD in this crack density region are independent on the value of the crack density. Superscript 0 is used to indicate values in this region, u_{1an}^{0k} , u_{2an}^{0k} .

Parametric analysis of u_{1an}^{0k} and u_{2an}^{0k} using FE was performed in [19] to identify the most significant geometrical and material constants affecting crack face displacements. In result simple and relatively accurate fitting expressions were obtained to calculate u_{1an}^{0k} and u_{2an}^{0k} as a function of neighboring layer properties. These expressions, see Appendix, are considered to be sufficiently general to be used for cracks in any laminate. Hence, there is no need to use FEM in any of simulations presented in this paper.

6.4.2 Examples of Calculation and Experiments

The model described in Sect. 6.4.1. has been validated comparing with experimental data and FEM calculations in [19, 20, 40–42]. In this section we will illustrate some results for quasi-isotropic laminate and the agreement with experimental data for cross-ply type of laminates. The material is Glass fiber/epoxy unidirectional layer with longitudinal modulus 44.73 GPa, transverse modulus 12.76 GPa, in-plane shear modulus 3.5 GPa, in-plane Poisson's ratio 0.30 and ply thickness 0.138 mm.

We start with simulations of elastic constants for $[0/+60/-60]_s$ laminates with intralaminar cracks in layers shown in Fig. 6.11.

Two damage states are compared. In the first damage state all layers have the same crack density. It may be the case when cracks are introduced by thermal loading: subjecting the quasi-isotropic specimen to very low temperature transverse tensile thermal stresses in all layers would be the same. We can assume

that it would introduce approximately the same number of cracks in all layers. Certainly it is just an assumption used in elastic properties simulation. In reality differences in crack density may be caused by different layer thickness (-60 layer is two times thicker) and different location of layers (surface layers have different constraint conditions). In the second damage state the laminate has cracks only in off-axis layers. It could be a case when laminate is subjected to axial tensile loading. The crack density is assumed the same. This is also an approximation which may be justified if (1) the ply thickness is sufficiently large and damage state is governed by initiation stress and (2) the crack density is not high because the saturation crack density would be lower for cracks in thick layer.

Disregarding the above discussion about how realistic the two damage states are, we can use Fig. 6.11 to (a) to see how different elastic constants of the laminate are affected by cracking; (b) to evaluate the effect of cracks in the 0-layer on stiffness reduction in this particular laminate. First we see that the axial modulus is not at all affected by cracks in the 0-layer and results in both simulation cases almost coincide. Similar result was earlier obtained analyzing cross-ply laminates

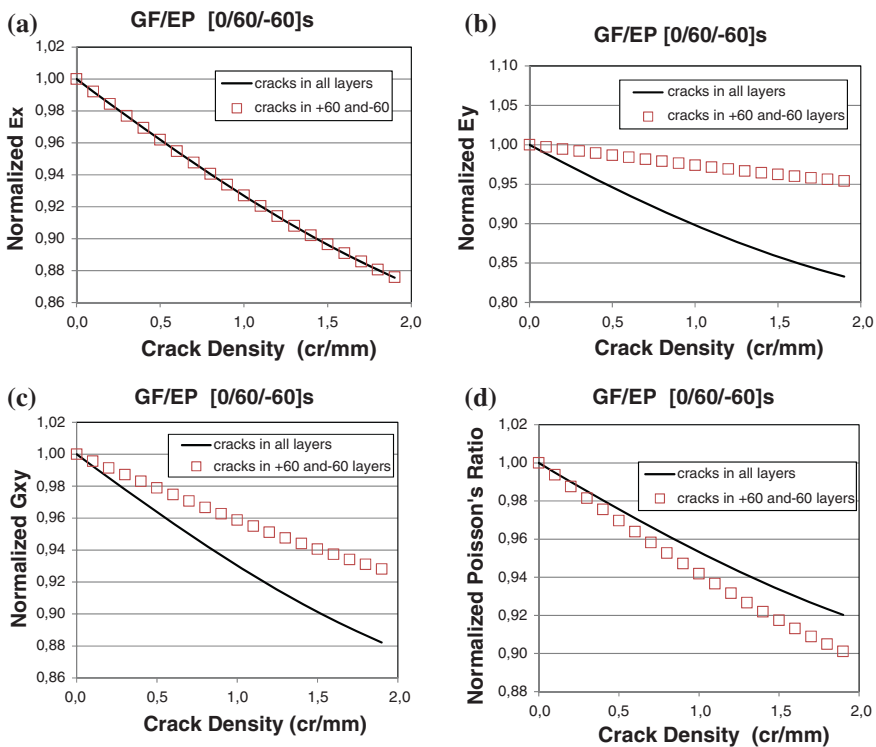


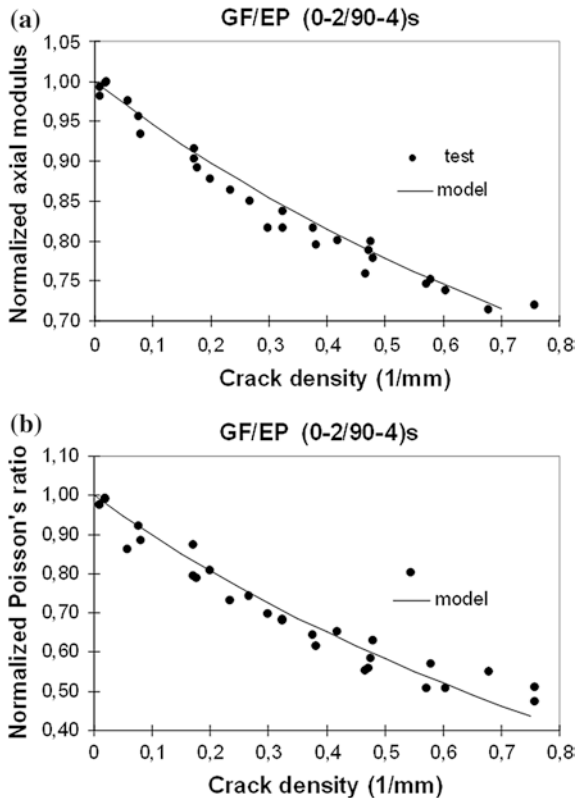
Fig. 6.11 Elastic properties reduction in [0/60/-60]s GF/EP laminate with increasing intralaminar crack density in layers: *solid lines* represent case when the same crack density is in all layers, whereas *symbols* represent results for a case when off-axis layers only have cracks with the same crack density

with cracks in all layers using FEM [19]. This is because cracks in 0-layer are oriented in x-direction which is the loading direction to define E_x . Elastic modulus E_y is reduced much more in presence of 0-layer cracks because in this case these cracks are perpendicular to the loading direction in the defining test. The shear modulus reduction in case of cracks in 0-layer is much more severe and also Poisson's ratio is reduced more than in absence of these cracks. In general, we can see 10–20 % reduction of all elastic constants which in most practical cases would not be acceptable.

Comparison with experimental data has to be the final validation. Some test results are presented in Fig. 6.12 together with simulations. In Fig. 6.12 the axial modulus E_x and the Poisson's ratio ν_{xy} (both normalized with respect to initial values) of GF/EP cross-ply laminate with layer elastic constants given above are shown as dependent on intralaminar crack density in the 90-layer. The agreement with test data is excellent.

The results presented in this section demonstrate the generality of the model to deal with any symmetric laminates with arbitrary intralaminar damage state in layers and the accuracy of the obtained laminate stiffness predictions in cases when the damage state is known from experiments.

Fig. 6.12 Reduction of normalized modulus and Poisson's ratio of [02,904] s GF/EP laminate with increasing crack density in the 90-layer



6.5 Conclusions

The methodology presented in this chapter allows predicting the thermo-elastic properties of laminates with intralaminar cracks in layers. The agreement with test data is good and the methodology can be considered as reliable. The prediction of the damage initiation and growth is still in the development stage. In this chapter strength based approach to initiation of intralaminar cracks was suggested and experimental procedure for parameter determination in the model was described. The damage propagation is expected to follow rules of fracture mechanics with the corresponding methodology described in the chapter. The approach can be used for damage prediction in quasi-static as well as tension-tension fatigue loading.

Appendix: Expressions for COD and CSD

The COD, u_{2an}^0 of *non-interactive crack* is considered in a coordinate system where the cracked layer has 90-orientation with respect to x-axis. In other words x-direction is direction 2 for the layer with crack. Index k denoting the layer is omitted in expressions below. A distinction has to be made between cracks in surface layers and cracks in inside layers. Obviously the normalized average COD of surface cracks is larger because the cracked layer is supported only from one side. The fitting expressions are presented for symmetric case where the bottom support layer has equal properties, orientation and geometry as the top support layer. The expression for u_{2an}^0 is

$$u_{2an}^0 = A + B \left(\frac{E_2}{E_x^S} \right)^n \quad (6.45)$$

In (6.45) E_x^S is the Young's modulus of the support layer measured in the x-direction which is the transverse direction for the cracked layer. For a crack in *internal layer*

$$\begin{aligned} A &= 0.52 \quad B = 0.3075 + 0.1652 \left(\frac{t_{90}}{2t_s} - 1 \right) \\ n &= 0.030667 \left(\frac{t_{90}}{2t_s} \right)^2 - 0.0626 \frac{t_{90}}{2t_s} + 0.7037 \end{aligned} \quad (6.46)$$

In (6.46) t_s is thickness of the adjacent support layer and t_{90} is thickness of the cracked layer.

For a crack in *surface layer*

$$\begin{aligned} A &= 1.2 \quad B = 0.5942 + 0.1901 \left(2 \frac{t_{90}}{t_s} - 1 \right) \\ n &= -0.52292 \left(\frac{t_{90}}{t_s} \right)^2 + 0.8874 \frac{t_{90}}{t_s} + 0.2576 \end{aligned} \quad (6.47)$$

Suggestions for calculations in more realistic cases when the support layers from different sides are different are given in [42].

Crack face sliding displacements (CSD), u_{1an}^0 , see [20] for details, also follows a power law

$$u_{1an}^0 = A + B \left(\frac{G_{12}}{G_{xy}^S} \right)^n \quad (6.48)$$

In (6.48) G_{xy}^S is the in-plane shear modulus of the support layer.

For cracks in *internal layer*

$$A = 0.3 \quad B = 0.066 + 0.054 \frac{t_{90}}{2t_s} \quad n = 0.82 \quad (6.49)$$

For cracks in *surface layer*

$$A = 0.6 \quad B = 0.134 + 0.105 \frac{t_{90}}{t_s/2} \quad n = 0.82 \quad (6.50)$$

Expressions (6.45)–(6.47) and (6.48)–(6.50) show that the normalized average COD and CSD are larger for less stiff surrounding layers and approach to certain asymptotic value with increasing support layer and cracked layer stiffness ratio. For thicker support layers the COD and CSD is smaller. This effect of neighbouring layers on the crack face displacements is called “constraint effect”.

Due to nonlinear shear stress-shear strain response the secant shear modulus of the layer will change with increasing laminate strain and will affect the value of u_{1an}^0 calculated according to (6.48).

When the distance between cracks decreases (high dimensionless crack density) the stress perturbation regions of individual cracks overlap and the normalized average COD and CSD start to decrease. The u_{2an}^k has been related to COD of non-interactive cracks, u_{2an}^{0k} by relationship [40]

$$u_{2an}^k = \lambda_k(\rho_{kn})u_{2an}^{0k} \quad (6.51)$$

The crack interaction function λ is a function of the crack density in the layer and generally speaking it depends on material and geometrical parameters of the cracked layer and surrounding layers. For non-interactive cracks $\lambda = 1$.

Detailed analysis of the effect of different parameters on interaction function was performed in [40] using FEM. Weak interaction (2–5 %) is observable at normalized spacing $2l_{90}/t_{90} = 2.5$. Further decrease of spacing leads to dramatic drop of the values of the interaction function to 0.3. The interaction of cracks in Glass fiber/epoxy laminates is stronger than in Carbon fiber/epoxy laminates. In the latter at high stiffness ratio the interaction function is not sensitive to layer thickness ratio. In the former with lower layer stiffness ratio the interaction is stronger if the support layer is thicker.

The calculated values of the interaction function were fitted by an empirical relationship with an origin in a simple shear lag model. The interaction function according to the shear lag model is

$$\lambda_k = \tanh\left(\frac{k}{\rho_{kn}}\right) \quad (6.52)$$

The shape function (6.52) was used to obtain the k value from the best fit. The best fit with this function to data corresponding to CF laminates ($k_{CF} = 1.12$) and for GF laminate ($k_{GF} = 0.84$). The interaction effect on u_{2an}^k for cracks in surface layer was analyzed in [41] where also more accurate interaction functions for internal cracks are presented. The effect of nonuniform crack distribution on COD was analyzed in [21].

References

1. Parvizi, A., Bailey, J.E.: On multiple transverse cracking in glass fibre epoxy cross-ply laminates. *J. Mater. Sci.* **13**, 2131–2136 (1978)
2. Jamison, R.D., Schulte, K., Reifsnider, K.L., Stinchcomb, W.W.: Characterization and analysis of damage mechanisms in tension-tension fatigue of graphite/epoxy laminates. In effects of defects in composite materials. ASTM STP 836, American Society for Testing and Materials, pp. 21–55. (1984)
3. Ogin, S.L., Smith, P.A., Beaumont, P.W.R.: Matrix cracking and stiffness reduction during the fatigue of a [0/90]s GFRP laminate. *Compos. Sci. Technol.* **22**, 23–31 (1985)
4. Kashtalyan, M., Soutis, C.: Analysis of composite laminates with intra and interlaminar damage. *Prog. Aersp. Sci.* **41**, 152–173 (2005)
5. Takeda, N., Ogihara, S., Kobayashi, A.: Microscopic fatigue damage progress in CFRP cross-ply laminates. *Composites* **26**, 859–867 (1995)
6. Bechel, V.T., camping, J.D., Kim, R.Y.: Cryogenic/elevated temperature cycling induced leakage path in PMCs. *Compos. B Eng.* **36**(2), 171–182 (2005)
7. Nairn, J., Hu, S.: Matrix microcracking. In: Pipes, R.B., Talreja, R. (ed.) *Computational Materials series. Dam. Mech. Comp. Mater.* vol. 9, pp. 187–243. Elsevier, Amsterdam (1994)
8. Berthelot, J.-M.: Transverse cracking and delamination in cross-ply glass-fiber and carbon-fiber reinforced plastic laminates: static and fatigue loading. *Appl. Mech. Rev.* **56**(1), 111–147 (2003)
9. Peters, P.W.M.: The strength distribution of 90-plyies in 0/90/0 Graphite-Epoxy laminates. *J. Compos. Mater.* **18**, 545–556 (1984)
10. Varna J.: Quantification of damage and evolution modeling in multidirectional laminates. In: *Proceedings of the 27th RISØ International Symposium on Material Science*, Roskilde, Denmark, pp. 349–356 (2006)
11. Huang, Y., Varna, J., Talreja, R.: The effect of manufacturing quality on transverse cracking in cross ply laminates. In: *Bhattacharyya, D., Lin, R., Srivatsan, T. (eds.) Processing and Fabrication of Advanced Materials. Centre for Advanced Composite Materials*, vol. XIX, s. 552–559, 8 s. University of Auckland, Auckland (2011)
12. Allen, D.H., Yoon, C.: Homogenization techniques for thermo-viscoelastic solids containing cracks. *Int. J. Solids Struct.* **35**, 4035–4053 (1998)
13. Smith, P.A., Wood, J.R.: Poisson's ratio as a damage parameter in the static tensile loading of simple cross-ply laminates. *Compos. Sci. Technol.* **38**, 85–93 (1990)
14. Hashin, Z.: Analysis of cracked laminates: a variational approach. *Mech Mater.* **4**, 121–136 (1985)

15. Varna, J., Berglund, L.A.: Multiple transverse cracking and stiffness reduction in cross-ply laminates. *J. Compos. Technol. Res. JCTRER* **13**(2), 97–106 (1991)
16. Varna, J., Berglund, L.A.: Thermo-elastic properties of composite laminates with transverse cracks. *J. Compos. Technol. Res.* **16**(1), 77–87 (1994)
17. McCartney, L.N., Schoeppner, G.A., Becker, W.: Comparison of models for transverse ply cracks in composite laminates. *Comp. Sci. Technol.* **60**, 2347–2359 (2000)
18. Zhang, J., Fan, J., Soutis, C.: Analysis of multiple matrix cracking in $[\pm\theta_m/90_n]$ s composite laminates. Part 1. In-plane stiffness properties. *Composites* **23**(5), 291–304 (1992)
19. Lundmark, P., Varna, J.: Constitutive relationships for laminates with ply cracks in in-plane loading. *Int. J. Damage Mech.* **14**(3), 235–261 (2005)
20. Lundmark, P., Varna, J.: Crack face sliding effect on stiffness of laminates with ply cracks. *Compos. Sci. Technol.* **66**, 1444–1454 (2006)
21. Loukil, M.S., Varna, J., Ayadi, Z.: Applicability of solutions for periodic intralaminar crack distributions to non-uniformly damaged laminates. *J. Compos. Mater.* **47**(3), 287–301 (2012)
22. McCartney, L.N., Schoeppner, G.A.: Predicting the effect of non-uniform ply cracking on the thermo-elastic properties of cross-ply laminates. *Compos. Sci. Technol.* **62**, 1841–1856 (2000)
23. Joffe, R., Varna, J., Berglund, L.A.: Acoustic emission signals from composite laminates with well known fatigue damage characteristics. AECM-5, 10–14 July 1995, Sundsvall, Sweden, pp. 179–186
24. Varna, J., Berglund, L.A., Talreja, R., Jakovics, A.: A study of the crack opening displacement of transverse cracks in cross ply laminates. *Int. J. Damage Mech.* **2**, 272–289 (1993)
25. Varna, J., Joffe, R., Akshantala, N.V., Talreja, R.: Damage in composite laminates with off-axis plies. *Compos. Sci. Technol.* **59**, 2139–2147 (1999)
26. Loukil, M., Ayadi, Z., Varna, J.: ESPI analysis of crack face displacements in damaged laminates. *J. Compos. Sci. Technol.* **94**, 80–88 (2014)
27. Moore, A.J., Tyrer, J.R.: An electronic speckle pattern interferometer for complete in plane displacement measurement. *Meas. Sci. Technol.* **1**, 1024–1030 (1990)
28. Parthenios, J., Katerelos, D.G., Psarras, G.C., Galiotis, C.: Aramid fiber: a multifunctional sensor for monitoring stress/strain fields and damage development in composite materials. *Eng. Fract. Mech.* **69**, 1067–1087 (2002)
29. Katerelos, D., Varna, J.: Secondary damage effect on stress redistribution in laminated composites. *Int. J. Damage Mech.* **22**(5), 752–769 (2013)
30. Varna, J., Berglund, L.A.: Two-dimensional transverse cracking in $[0_m/90_n]$ s cross-ply laminates. *Eur. J. Mech. A. Solids* **12**(5), 699–723 (1993)
31. Paris, F., Blazquez, A., McCartney, L.N., Mantic, V.: Characterization and evolution of matrix and interface related damage in $[0/90]$ s laminates under tension. Part I: numerical predictions. *Compos. Sci. Technol.* **70**(7), 1168–1175 (2010)
32. Berglund, L.A., Varna, J., Yuan, J.: Effect of intralaminar toughness on the transverse cracking strain in cross-ply laminates. *Adv. Compos. Mater. (the Official Journal of the Japan Society for Composite Materials)* **1**(3), 225–234 (1991)
33. Parvizi, A., Bailey, J.E.: On multiple transverse cracking in glass fibre epoxy cross-ply laminates. *J. Mater. Sci.* **13**, 2131–2136 (1978)
34. Flaggs, D.L., Kural, M.H.: Experimental determination of the in situ transverse lamina strength in graphite/epoxy laminates. *J. Compos. Mater.* **16**, 103–115 (1982)
35. Varna, J., Berglund, L.A., Björberg, H.: On the determination of transverse strain to failure in composites. In: 2nd European Conference on Composites ECCM CTS 2, 13–15 Sept 1994, Hamburg, pp. 267–276
36. Hull, D.: *An Introduction To Composite Materials*. 1st edn, Solid State Science Series, Cambridge (1981)
37. Joffe, R., Varna, J.: Damage evolution in multi-directional laminates and the resulting inelastic response. In: Proceedings of ICCM-12, CD, Paris, July 1999, 10p
38. Huang, Y., Varna, J., Talreja, R.: Statistical assessment of manufacturing quality for transverse cracking in cross ply laminates. *J. Compos. Sci. Technol.* (2014)

39. Joffe, R., Krasnikovs, A., Varna, J.: COD-based simulation of transverse cracking and stiffness reduction in [S/90n]s laminates. *Compos. Sci. Technol.* **61**, 637–656 (2001)
40. Lundmark, Peter, Varna, Janis: Stiffness reduction in laminates at high intralaminar crack density: effect of crack interaction. *Int. J. Damage Mech.* **20**, 279–297 (2011)
41. Loukil, M.S., Varna, J., Ayadi, Z.: Engineering expressions for thermo-elastic constants of laminates with high density of transverse cracks. *Composites A* **48**, 37–46 (2013)
42. Varna, J.: Modeling Mechanical Performance of Damaged Laminates. *J. Compos. Mater.* **47**(20–21), 2443–2475 (2013)

Part II
Fast Methodologies for Damage Growth
in Aerospace Composites

Chapter 7

Finite Element Study of Delaminations in Notched Composites

Sören Nilsson, Alann André and Anders Bredberg

7.1 Finite Element Delamination Study of a Notched Composite Plate

Cohesive elements implemented in ABAQUS [1] are a powerful tool to model delamination onset and growth in composite materials. The theoretical background is well described in [1, 2]. The use of cohesive elements together with a bilinear traction separation law (TSL, Fig. 7.1) is outlined below.

The debonding or delamination processes of composite material occur in two main steps: damage initiation and damage propagation.

The cohesive laws for mode I and II capture the linear elastic and softening behaviour before fracture, and can be obtained by performing double cantilever beam tests and end notched flexural beam tests.

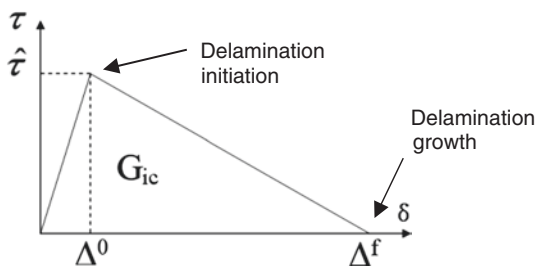
Cohesive elements can be defined by a linear elastic response, a strength criteria and a damage evolution law based on energies. The damage initiates when a quadratic stress criterion is fulfilled ($\delta = \Delta^0$), see Eq. (7.1). The strength of the composite in the normal and shear directions are used as input data

$$\left(\frac{\sigma_{33}}{\hat{\sigma}_{33}}\right)^2 + \left(\frac{\tau_{13}}{\hat{\tau}_{13}}\right)^2 + \left(\frac{\tau_{13}}{\hat{\tau}_{13}}\right)^2 = 1 \quad (7.1)$$

S. Nilsson (✉) · A. André
Composite Structures, Swerea SICOMP, 431 22 Mölndal, Sweden
e-mail: soren.nilsson@swerea.se

A. Bredberg
Saab Aeronautics, Linköping, Sweden

Fig. 7.1 Bilinear traction separation law



The damage evolution is governed by a damage parameter which describes the rate of stiffness softening after damage initiation ($\delta = \Delta^0$). The damage propagation ($\delta = \Delta^f$) is studied in terms of energy release rate and fracture toughness. To accurately predict delamination growth for mode I and mode II loading conditions [2], the Benzeggagh-Kenane criteria are used [3], as expressed in Eq. (7.2).

$$G_k + (G_{IIk} + G_k) \left(\frac{\beta}{1 + 2\beta^2 - 2\beta} \right)^\eta = G_{mc} \tag{7.2}$$

with

$$\beta = \frac{\Delta_{shear}}{\Delta_{peel} + \Delta_{shear}}$$

where G_{IC} and G_{IIC} are the fracture toughness in mode I and II respectively. The exponent η is chosen to 1.45. β is the parameter determining the mixed mode ratio based on the current values of the peel and shear opening in the TSL for mode I and II respectively. The mechanical properties of the ply are reported in Table 7.1.

The material parameters for the cohesive layer are shown in Table 7.2. The stiffness of the elastic part of the traction separation laws is calculated using the stiffness of the composite and the thickness of the cohesive layer [1].

Table 7.1 Hexcel HTA/6376C—approximated mechanical properties

Composites: engineering constants [(GPa) (except Poisson’s ratios)]									
	E ₁₁	E ₂₂	E ₃₃	G ₁₂	G ₁₃	G ₂₃	ν ₁₂	ν ₁₃	ν ₂₃
HTA/6376C	140	10	10	5.0	5.0	3.0	0.30	0.30	0.50

Table 7.2 Approximated cohesive layer properties

Interface: cohesive properties			
$\hat{\sigma}$ (MPa)	$\hat{\tau}$ (MPa)	G _{IC} (J/m ²)	G _{IIC} (J/m ²)
20	30	300	700

7.1.1 Element Type, Mesh, Boundary Condition and Applied Load

The model has been divided into a maximum of 12 different parts: two roller supports, a composite laminate part with a cut in the vicinity of the hole, 5 composite laminate parts in the vicinity of the hole and the cohesive layers were inserted between the layers where delaminations were observed.

The mesh and the assembly of the different parts considered in the model are shown in Fig. 7.2. All parts were joined by surface to surface tie constraints.

To reduce the computing time, symmetry is often used to model a half or a quarter of composite laminates loaded in bending. The quasi-isotropic lay-up considered in this study did not offer this possibility because of the unsymmetrical $\pm 45^\circ$ layers.

The loading was applied through a controlled displacement of 80 mm. All nodal displacements on the bottom surface of the roller support were restrained.

7.1.2 Assumption and Particular Settings

The roller supports used on the 4-point bending experiments are often neglected in FE models and replaced by boundary conditions restricting nodal displacement along the contact line. Due to large displacements during the experiments (deflection over 80 mm) and large sliding of the specimen on the roller supports this assumption has not been made because it could have led to the uncorrected determination of the reaction forces. Consequently, the roller support was modelled explicitly. This introduced a cost demanding contact interaction in the FE-model. Since the objective was to determine the delamination onset and growth, the contacts were defined with a coarse mesh to decrease the computing time. In ABAQUS, the interaction “composite laminate-steel support” was defined using a finite sliding formulation together with a node to surface discretization method. Non linear effects due to large deformations were taken into account in the FE-model.

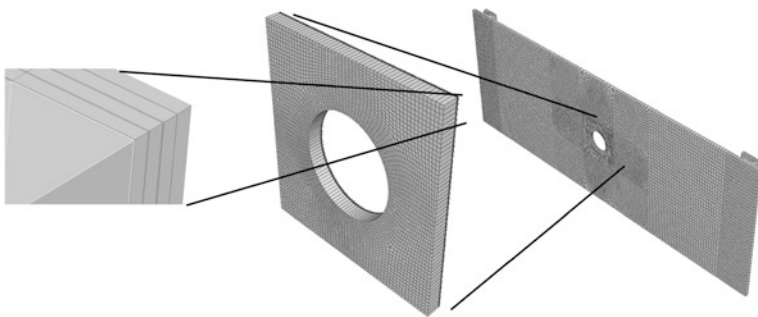


Fig. 7.2 Mesh of the whole model

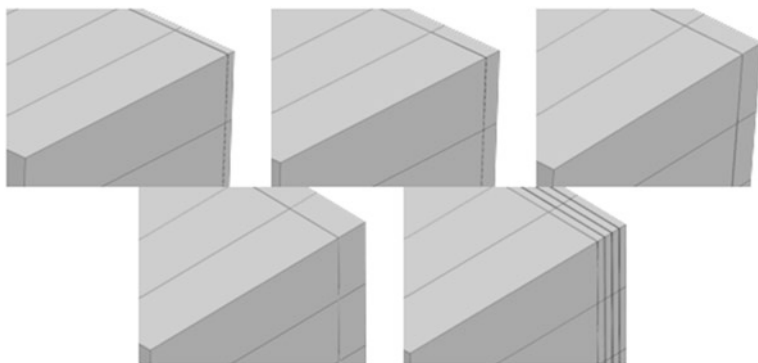


Fig. 7.3 The five models with cohesive elements positioned at different composite layer interfaces on the tension side

Damage models where material softening occurs are often generating convergence difficulties in ABAQUS standard. Therefore, it is useful to include artificial damping in the model in order to overcome these problems. In all models, a damping value of 3×10^{-4} was used. By comparison of the viscous damping energy with the total strain energy, it was verified that the artificial damping did not yield inaccurate solutions.

7.1.3 Method

Four models employing one cohesive layer were analysed. In these models, the cohesive layer was positioned at the first interface on the tension side in the first model, at the second interface in the second model, and so on. In a fifth model the cohesive layers were placed at the first four interfaces on the tension side, see Fig. 7.3.

Model 1, with cohesive elements at the first interface, i.e. between the 0° and 90° layers on the tension loaded side, has been analysed with 3 different element sizes for the cohesive elements: 0.5, 0.25 and 0.125 mm.

7.2 Results

7.2.1 Structural Response

It can be seen that there is no difference between the 5 models in terms of load-deflection behaviour of the specimen in bending. The maximum load obtained from FE models is 3.8 kN (at $w = 80$ mm), which is in good agreement with the experimental result of 3.9 kN at the same deflection (Fig. 7.4).

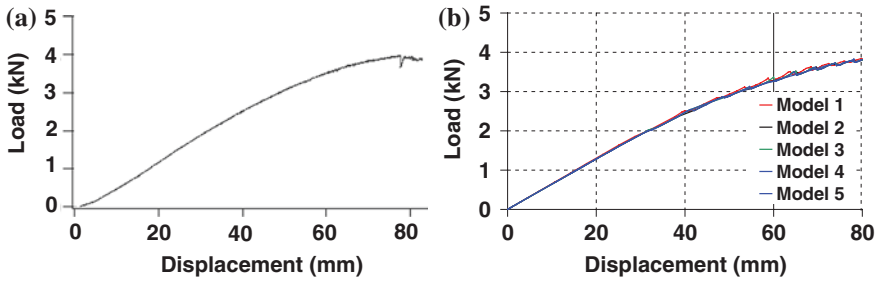
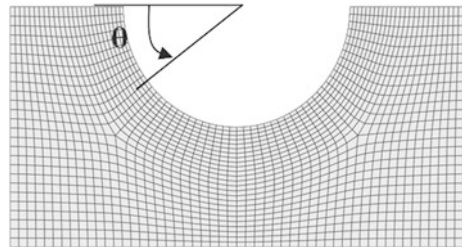


Fig. 7.4 Load-displacement curves—**a** Experiment; **b** FE models

Fig. 7.5 Nodal cylindrical coordinate system at the periphery of the hole



7.2.2 Delamination

The damage initiation criterion and the delamination growth are investigated along the holes edges. The polar position used is referring to the position of the nodes as described in Fig. 7.5.

7.2.2.1 Delamination Initiation

The delamination initiation load (i.e. the load at which $\delta = \Delta^0$) was investigated for all FE models. In models where cohesive layers are studied separately (models 1–4), the damage criteria was fulfilled at 0.7, 0.9, 0.7 and 0.45 kN for the models with cohesive elements positioned at interfaces 1, 2, 3 and 4 respectively. In the model where four cohesive layers are considered (model 5), damage onset was predicted in cohesive layers at interfaces 1, 2 and 4 at 0.9 kN. The criterion was fulfilled at a load of 1.0 kN at interface 3. Consequently, model 5 predicted damage initiation at slightly higher loads than models 1–4, which only considered delamination at a single interface.

The predicted angle, θ , where delamination initiates varies slightly between models 2–5 and 3–5. The results are reported in Table 7.3. The discrepancies are however small enough to consider that prediction is not influenced by the number of cohesive layers.

Table 7.3 Delamination initiation: angular position (θ)

Interface	Model 1	Model 2	Model 3	Model 4	Model 5
1	66° and 114°	–	–	–	66° and 113°
2	–	90°	–	–	104°
3	–	–	104°, then 63° dominant	–	62°
4	–	–	–	73°	74°

7.2.2.2 Delamination Growth

The delamination growth is monitored in ABAQUS by controlling the value of the stiffness degradation, which takes the value 1 at $\delta = \Delta^f$ (see Fig. 7.1).

Figure 7.6 shows contour plots of the delamination growth for each cohesive layer at 3.8 kN. If comparing these contour plots, it can be shown that the damaged area is smaller in the cohesive layers of the model with 4 cohesive layers (highly damaged area are represented in dark grey).

It was verified that the size of the cohesive elements did not influence the structural response of the laminate.

The delamination initiation at maximum load was investigated from the results of the element size parametric study. Paths were created around half the circumference of the hole (Fig. 7.2). The stiffness degradation at the edge of the hole, as a function of the polar position of the nodes is plotted in Fig. 7.4a. All models predicted delamination growth in the region ranging from $\theta \approx 45^\circ$ to $\theta \approx 135^\circ$. Only an increase of the stiffness degradation, from 0.78 to 0.85, due to higher stress level in smaller elements, was registered close to the 0° and 180° polar positions.

The shear stresses have been plotted along a path created in the areas where large delamination was observed. As expected, the shear stress slightly increases

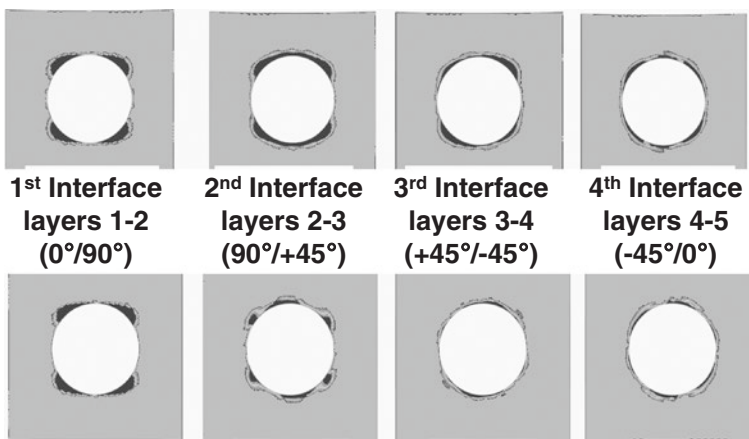


Fig. 7.6 Delamination growth around the hole at $P = 3.8$ kN. Models with one cohesive layer on the *upper line*, and model with 4 cohesive layers on the *lower line*

while decreasing the element size. The shear stress level at the edge of the hole, where elements are almost fully damaged is slightly lower in the model with 0.125 mm element size. Additionally, it can be noticed that the shear stress decreases along a shorter distance after the peak value is reached while decreasing the element size (Fig. 7.4b), which means that higher stresses are predicted ahead of the crack tip when coarser mesh is used.

The element size parametric study shows that there is no need in this particular case to use element smaller than 0.5 mm, since no significant differences have been observed. An explanation is the predominance of mode II, where larger cohesive zone allow coarser mesh to be used. The mode mix ratio, β , is estimated to be greater than 95 % (see Eq. 7.2).

7.3 Comparison and Discussion

Some results of the fractographic analysis carried out on samples from experimental tests are presented in Fig. 7.7. Delaminations were observed between multiple layers at the tension loaded side (between layers 1–2, layers 2–3, layers 4–5, layers 7–8 and layers 9–10).

From the ultrasonic C-scan study, the size and the direction in which the damage propagates are clearly identified. Figure 7.7b shows an extensive delamination damage area at the second interface, i.e. between 90° and 45° layers. Delamination growths in the transverse direction with respect to the load, with a delaminated area extended up to 20 mm from the hole edges at a maximum load of 3.9 kN. The results from the FE models 1, 2 and 5 show delamination direction of growth in good agreement with the experiment. However, the size of the delaminated area,

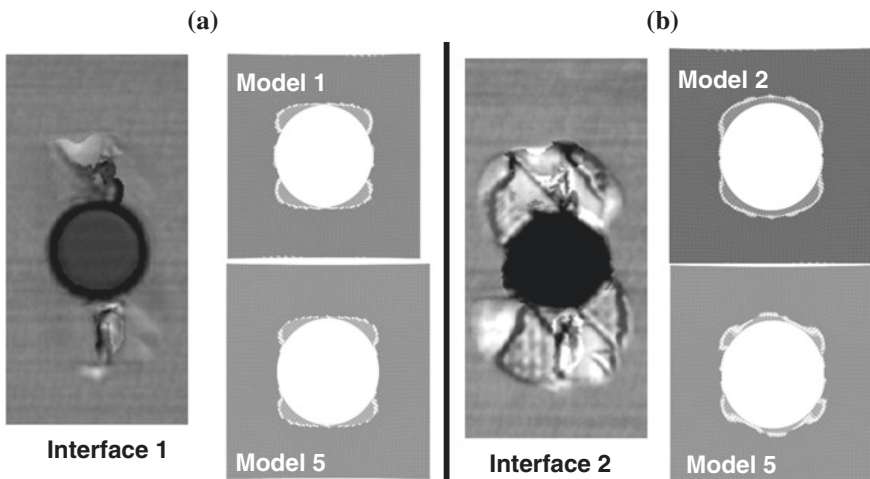


Fig. 7.7 **a** Damage observed by ultrasonic C-Scan microscopy at interface 1 and **b** interface 2. Predicted damage from FE models are shown on the *right*

which is represented in light grey in Fig. 7.7, is much smaller, extended at its maximum from 2 to 3 mm from the edges of the notch.

Regarding the comparison between FE model 5 and FE models 1, 2, 3 and 4, it can be seen that the number of cohesive layers being modelled influence the amount of damage and the size of the delamination at similar load levels. This is resulting from the distribution of damage in all cohesive layer in model 5, while damage is concentrated in one cohesive layer only for models 1–4.

The FE models adopted in this study underestimate the damage area compared to the experimental results. The difference can be explained by the fact that intralaminar damage like matrix cracking, which contributes to the delamination process, has not been considered as a possible damage mechanism in the present FE study. Shear cracks were observed in the first 90° layer on the tension side. These cracks run through the layer and delaminations were observed on both sides of the layer (between the layers 1 and 2 and layers 2 and 3). Another explanation is the modelling of all cohesive layers using fracture toughness values for delamination in unidirectional laminates (i.e. $0^\circ/0^\circ$). The laminate used in the study shows delaminations between layers with different orientation angle where the fracture energy may be lower [4], which influence the delamination onset and growth.

A particular feature of delamination in multidirectional laminates, not considered in this study, is the possibility for the crack to migrate from one interface to another, since the change in fibre orientation does not confine the crack at the interface where it initiated [5]. This delamination mechanism (multi-plane delamination) interacts with intralaminar damage. Without considering it, the delamination has no longer the possibility to grow through the weakest region of the laminate. This artificial restriction would probably yield accurate results for particular loading modes and laminate lay-up, where in-plane damage is not a driving damage mode. In the present case of notched multidirectional laminates loaded in bending, considering delamination only is not sufficient.

Previous papers [6, 7] have pointed out the complexity of predicting interacting intralaminar and interlaminar damage growth. The finite element models are either conducted by implementing user-defined commands in finite element codes, or restricted to predefinition of possible failure regions.

7.4 Conclusions

A need for a method to predict the strength of a laminate loaded in a combination of in-plane and out of plane loads (bending) during the design phase has been recognised. There is a potential with a methodology that can handle the difference in failure strain and failure mode, i.e. make use of the higher failure strain in bending. The tests presented in this work are an initial step to increase the knowledge needed to determine such a tool.

The delamination onset and growth in notched composite laminates has been investigated using finite element analysis and compared to experimental results.

From experimental C-scan and microscopic study of a tested specimen the delaminated and damaged areas were determined. Cohesive elements have been used to model delamination onset and growth between the observed delaminated layers of the notched laminate under flexural load.

The influence of the number of delaminated areas modelled is shown by five different models with either cohesive elements positioned between different layers or with cohesive elements positioned between all layers subjected to delamination. The models with only one cohesive layer show different results than the model with four cohesive layers in terms of the size of the delaminated area. No significant influence on the load displacement curves is noticed. The delamination process is probably too local to globally influence the behaviour of the composite plate.

The element size parametric study showed that there is no need in this particular case to use element smaller than 0.5 mm, since no significant differences in terms of load-displacement behaviour, size of the damage area or stresses have been observed. All models predict delamination to initiate in the region ranging from $\theta \approx 66^\circ$ to $\theta \approx 114^\circ$. Predicted position of delamination initiation and direction of growth correspond to experimental observations for all models. However, the extent of delamination growth is significantly underestimated for the second interface ($90^\circ/45^\circ$) on the tension loaded side. This discrepancy may be explained by an overestimate of the fracture toughness for the $90^\circ/45^\circ$ interface, employing fracture toughness data for a $0^\circ/0^\circ$ interface.

In-plane damage like matrix cracking occurs prior to delamination was also observed experimentally. It is therefore not enough to consider a FE model with only cohesive element to model the delamination process in notched composite plate. There is a need to model simultaneously progressive damage and delamination to accurately capture damage initiation and growth in notched composite plate under flexural loading. To predict final collapse it is also necessary to include in-plane fiber failure.

References

1. ABAQUS version 6.7-1 User Manual Abaqus Inc. (2007)
2. Camanho, P.P., Davila, C.G.: Mixed-mode decohesion finite elements for the simulation of delamination in composite materials. NASA/TM-2002-211737, 1-37 (2002)
3. Benzeggagh, M.L., Kenane, M.: Measurement of mixed-mode delamination fracture toughness of unidirectional glass/epoxy composites with mixed-mode bending apparatus. *Compos. Sci. Technol.* **56**, 439-449 (1996)
4. Gordniana, K., Hadaviniaa, H., Masona, P.J., Madenci, E.: Determination of fracture energy and tensile cohesive strength in mode I delamination of angle-ply laminated composites. *Compos. Struct.* **82**, 577-586 (2008)
5. Singh, S., Greenhalgh, E.: Micromechanisms of interlaminar fracture in carbon-epoxy composites at multidirectional ply interfaces. In: 4th International Conference on Deformation and Fracture of Composites, Manchester, UK (1997)
6. Kashtalyana, M., Soutis, C.: Analysis of composite laminates with intra- and interlaminar damage. *Prog. Aerosp. Sci.* **41**, 152-173 (2005)
7. Hallett, S.R., Green, B.G., Jiang, W.G., Wisnom, M.R.: An experimental and numerical investigation into the damage mechanisms in notched composites. *Compos. A* **40**, 613-624 (2009)

Chapter 8

Effect of the Damage Extension Through the Thickness on the Calculation of the Residual Strength of Impacted Composite Laminates

Sören Nilsson, Anders Bredberg and Tonny Nyman

8.1 Introduction

One of the most common failure modes for composite structures is the interlaminar delamination. Delamination as a result of impact, high stress concentrations from geometrical discontinuity or a manufacturing defect can cause a significant reduction in the compressive load-carrying capacity of a structure. When a delamination is subjected to in-plane compressive dominated load, local buckling of the delaminated region may occur before global buckling of the laminate. In some cases a mixed mode buckling may occur, which is a combination of local and global buckling as shown in Fig. 8.1. Often, the global buckling load represents the failure load of the delaminated composite panel at global buckling, and no post buckling behaviour of the delamination needs to be analysed [1]. Hence, the global buckling mode has not been taken into account in the method described in this chapter. For local and mixed buckling modes, growth of delamination is generally the main mechanism leading to the failure of the delaminated composite and post buckling analysis of the delamination is therefore necessary.

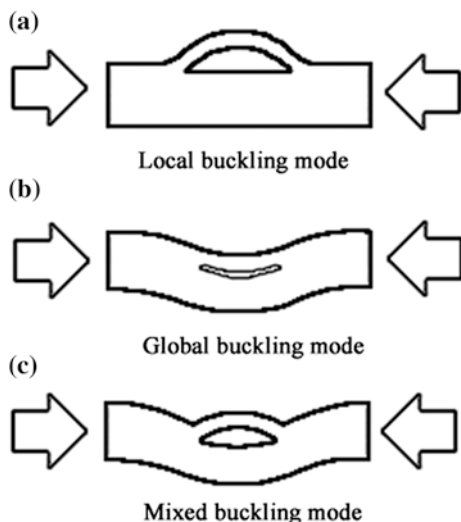
The laminate's lowered ability to resist to compressive loads greatly depends on the location of the delamination in the through-the-thickness direction but also on the area and shape of the delamination. An increase of the delamination area leads to a decrease in buckling load; an effect which is more pronounced when the delamination is located closer to the surface. The delamination location has a significant influence, especially on the buckling mode.

S. Nilsson (✉)

Composite Structures, Swerea SICOMP, SE-431 22 Mölndal, Sweden
e-mail: soren.nilsson@swerea.se

A. Bredberg · T. Nyman
Saab Aeronautics, Linköping, Sweden

Fig. 8.1 Possible delamination buckling modes



Delaminations closer to the surface of the laminate generally buckle at a lower load. However, immediate failure will not occur if the delamination does not grow, since the energy level in the buckled plies is low. Experiments confirm that delaminated composite plates may sustain an increase in load after the buckling event up to the delamination growth. Therefore, it is necessary to both understand the effects of delamination buckling and delamination growth initiation to determine the residual strength after impact, commonly named Compression After Impact (CAI).

A Rayleigh-Ritz method is used to formulate an eigenvalue buckling problem and to predict buckling loads and deformation mode shapes. The method is used to determine the strain at which delamination buckling will occur for a composite plate containing a single delamination. The two-dimensional analysis assumes a delamination elliptical or circular in shape. Most analyses of delamination growth are based on the fracture mechanics approach and on the evaluation of the energy release rate. Post-buckling behaviour and delamination growth can not be predicted by the eigenvalue buckling problem as it is beyond the capability of this eigenvalue analysis. The delamination buckling theory and the theory of delamination growth will together determine the residual strength in delaminated composite plates. The theories of delamination buckling and determination of critical strains at crack growth that are described below have been implemented in the Fortran code CODEIN together with a new methodology for the characterization of impact induced damage along the thickness. All these methodologies provide a first fast evaluation of the residual strength of impacted composite laminates

8.2 Delamination Buckling and Growth

A plate, contain a single delamination, is assumed to be thin relative to its span, such that buckling instead of compressive failure occurs. The delamination is assumed to be elliptical or circular in shape, with local axes of symmetry which coincide or may be at an angle relative to the global axes. The origin of the delamination coincides with the origin of the global axes. The delamination is oriented by an angle θ between the local coordinate system (x', y') and the global coordinate system (x, y) , and its size is described by the lengths $2a$ and $2b$ along the x' - and y' -axes, see Fig. 8.2.

The damaged region of the plate is divided into two sub laminates. The sub laminates located above and beneath the delamination are referred to as the delaminated region and the base laminate (or base region), respectively (Fig. 8.3). To avoid misunderstanding, the term “sub laminate” will also refer to the delaminated region. The base laminate is assumed to be rigid and only the delaminated region will be

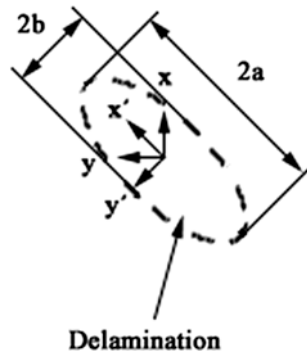


Fig. 8.2 Size, shape and orientation of a delamination

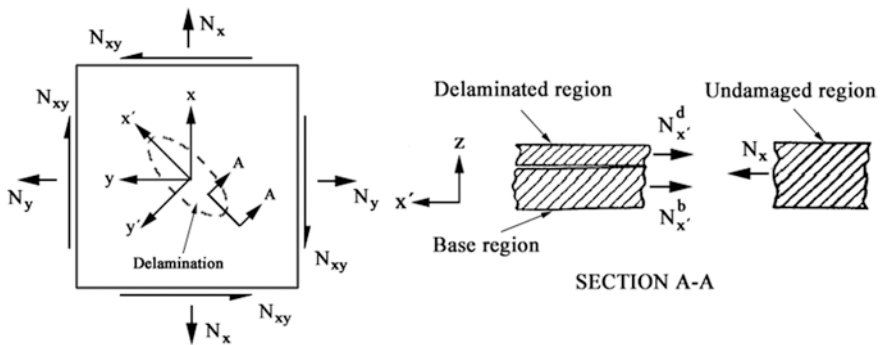


Fig. 8.3 Schematic partition of the delaminated plate

subjected to local buckling. In other words, thin plate linear buckling theory is assumed to be valid.

When analysing elliptical delaminations the present buckling analysis is strictly valid only for those load cases where the shear component is relatively small. In the analysis the load is transformed to a load which coincides with the principle axes of the sub laminate in the $x'y'$ -system. For example, in the case of pure shear the loading is rotated 45° resulting in a compressive-tensile loading with no applied shear.

For circular delaminations no restriction on load cases exists. For engineering purposes, when designing an aircraft structure, it is most practical to consider circular delaminations with diameter equal to the largest of $2a$ and $2b$ as measured on impact specimens. This is a conservative approach.

8.2.1 Delamination Buckling Theory

The theory is based on the Rayleigh-Ritz method, which is used for calculating buckling strains of elliptic and circular delaminations in orthotropic plates. The procedure is divided into the following main steps: (1) Selection of an admissible transverse displacement function. (2) Calculation of the total potential energy. (3) Creation of eigenvalue equation.

The following assumption on transverse displacement field for the delaminated region is made:

$$w = \left[1 - \left(\frac{x'}{a} \right)^2 - \left(\frac{y'}{b} \right)^2 \right]^2 \left(C_0 + C_1 \left(\frac{x'}{a} \right)^2 + C_2 \left(\frac{y'}{a} \right)^2 \right) \quad (8.1)$$

where C_0 , C_1 and C_2 are the so called generalized displacements.

The total potential energy, Π , of the sub laminate is the sum of the strain energy, U , and the potential energy of applied loads, V .

$$\Pi = U + V \quad (8.2)$$

The assumed transverse displacement field, w , is substituted into the expressions for the strain energy and potential energy of external loads. After necessary differentiation and integration the strain energy is given by

$$U = \{C\}_0^T [K] \{C\}_0 \quad (8.3)$$

and the potential energy of external loads is given by

$$V = \{C\}_0^T [K_g] \{C\}_0 \lambda \quad (8.4)$$

where $\{C\}_0^T = (C_0, C_1, C_2)$, $[K]$ and $[K_g]$ are two different stiffness matrices and λ is a scalar factor of the reference load. The subscript “0” in $\{C\}_0^T$ indicates that the vector is normalized. An eigenvalue problem is created by taking the first invariant of the total potential energy:

$$[K] \{C\}_0 + [K_g] \{C\}_0 \lambda = 0 \quad (8.5)$$

The solution of Eq. (8.5) results in three eigenvalues corresponding to three different buckling modes. The lowest absolute eigenvalue corresponds to the first buckling mode, hence the only one of interest. The critical strain, $\varepsilon_{\text{buck}}$, is given by the lowest eigenvalue multiplied with the applied strain.

8.2.2 Approximate Calculation of Strain Energy Release Rate

The adopted method for the calculation of the Strain Energy Release rate is based on work done by Chai and Babcock and Kachanov [2–4].

The analysis of initial growth of delaminations is based on a fracture mechanic approach and Griffith's [5] linear elastic theory for crack propagation. Griffith based his considerations on a global balance of energy in an entire structure. The energy balance equation deals with the energy needed to create a new crack, energy stored in the structure as elastic strain energy, and the work done by external loads. When a crack grows it obtains an increment in length while the potential energy of the body decreases and there is an energy release. According to Griffith's theory of brittle fractures the energy release is used to create new crack surfaces. The total potential energy, Π , of the sub laminate is the sum of the strain energy, U , and the work done by applied loads, V .

$$\Pi = U + V \quad (8.6)$$

Crack growth is possible when the energy release rate, G , reaches a critical value, i.e. when

$$G = G_{\text{crit}} \quad (8.7)$$

where the energy release rate is defined as

$$G = -\frac{d\Pi}{dA} \quad (8.8)$$

The calculations of the total potential energy is divided into two stages; pre buckling ($\varepsilon < \varepsilon_{\text{buck}}$) and in buckling ($\varepsilon > \varepsilon_{\text{buck}}$). The strain energy and the potential energy of external loads are calculated differently in the two stages and the terms (Π_0 , U_0 , V_0) and (Π , U , V) refer to pre buckling and in buckling, respectively. In brief, pre buckling, no transverse deflection is assumed to take place and membrane energy is dominating. In buckling, the potential energy consists of membrane energy and bending energy but the bending energy is dominating if the deflection is larger than the thickness of the sub laminate.

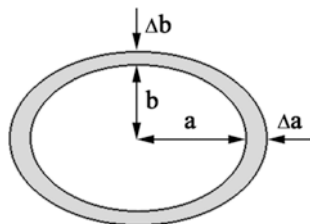
Pre buckling ($\varepsilon < \varepsilon_{\text{buck}}$), the elastic potential energy, Π_0 , is given by

$$\Pi_0 = U_0 + V \quad (8.9)$$

and in buckling ($\varepsilon > \varepsilon_{\text{buck}}$)

$$\Pi_0 = U_0 + V + \Pi_0 \quad (8.10)$$

Fig. 8.4 Geometry of the ellipse for the evaluation of the energy release rates



No interlaminar stress, and consequently no energy release rate, develops at the delamination front until the delaminated region buckles. Therefore, in buckling, the total energy release rate of the ellipse becomes:

$$\begin{aligned} G_a &= \left(-\frac{1}{\pi b} \frac{\partial(\Pi)}{\partial a} \right) \\ G_b &= \left(-\frac{1}{\pi a} \frac{\partial(\Pi)}{\partial b} \right) \end{aligned} \quad (8.11)$$

where G_a and G_b are the energy release rate along the “a” axis (“b” fixed) and along “b” axis (“a” fixed), respectively (see Fig. 8.4). The potential energy, Π_0 , is calculated using the strains and the load intensities referring to the initial buckling state.

In buckling, the derivatives of the bending energy with respect to a and b may be expressed by

$$\begin{aligned} \frac{\partial(U + V)}{\partial a} &= \frac{\partial}{\partial a} \left(\{C\}^T [K] \{C\} + \{C\}^T [K_g] \{C\} \lambda \right) \\ \frac{\partial(U + V)}{\partial b} &= \frac{\partial}{\partial b} \left(\{C\}^T [K] \{C\} + \{C\}^T [K_g] \{C\} \lambda \right) \end{aligned} \quad (8.12)$$

where λ is a scalar factor of the reference load. Thus, λ is equal to the eigenvalue when buckling occurs. The normalized eigenvector $\{C\}_0^T = (C_0, C_1, C_2)$ is obtained when solving the eigenvalue problem, Eq. (8.5). The vector represents the buckling shape (not its size). To be able to calculate G , the scalar factor (D_0/C_0) needs to be determined in $\{C\}^T = (D_0/C_0)(C_0, C_1, C_2)$. The constant D_0 is simply referring to the height at the centre of the buckle. Kachanov [3] presents an approach using a strip model to determine this constant (see Fig. 8.5).

The contraction Δ_1 of the strip due to bending (in buckling) is

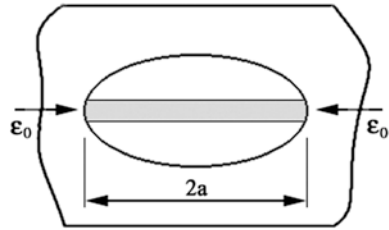
$$\Delta_1 = \frac{1}{2} \int_{-a}^a \left(\frac{\partial w}{\partial x'} \right)^2 dx' \quad (8.13)$$

The contraction Δ_2 due to compression after initial buckling is

$$\Delta_2 = \varepsilon_0 2a \quad (8.14)$$

where the strain ε_0 refers to the added strain after buckling, i.e. $\varepsilon_0 = \varepsilon - \varepsilon_{\text{buck}}$ where ε is the applied strain.

Fig. 8.5 Strip model proposed by Kachanov to determine the constant D_0



Equating $\Delta_1 = \Delta_2$ leads to an expression for D_0

$$D_0 = \sqrt{\left(\frac{1153 \epsilon_0 a^0 C_0^2}{32(C_1^2 + 11C_0^2)} \right)} \tag{8.15}$$

When initial buckling occurs, the energy release rate is calculated by setting the applied strain equal to the buckling strain, $\epsilon = \epsilon_{\text{buck}}$. If the critical energy release rate is reached when buckling occurs, the buckling strain is set to be the critical strain. Otherwise the critical far field strain, ϵ_{crit} , related to the critical strain energy release rate, G_{crit} , is found iteratively by changing the applied loads, (hence changing the height D_0). The critical strain thus depends on the C-vector, through the increase of the buckle height (D_0), and the external loads, which contributes to the performed work.

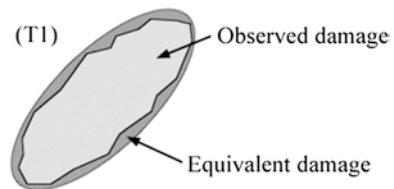
8.3 Characterization of Damage

Three techniques to characterise impact damage are discussed with the proposed method. So far one of the techniques (T1) is fully implemented in the numerical platform CODEIN. According to the first technique (T1), it is assumed that an ellipse covers the projected damage area and each individual delamination is assumed to have the same size as the ellipse (see Fig. 8.6). According to the second (T2) and third techniques (T3), each delamination is assumed to have a peanut shape in the direction of the neighbouring lower ply. In this chapter, only the first technique is considered.

8.3.1 Numerical Implementation

The methodologie above introduced have been implemented in the Fortran code CODEIN. The CODEIN flow chart is shown in Fig. 8.7. The input data are the

Fig. 8.6 Damaged area evaluated according the T1 technique



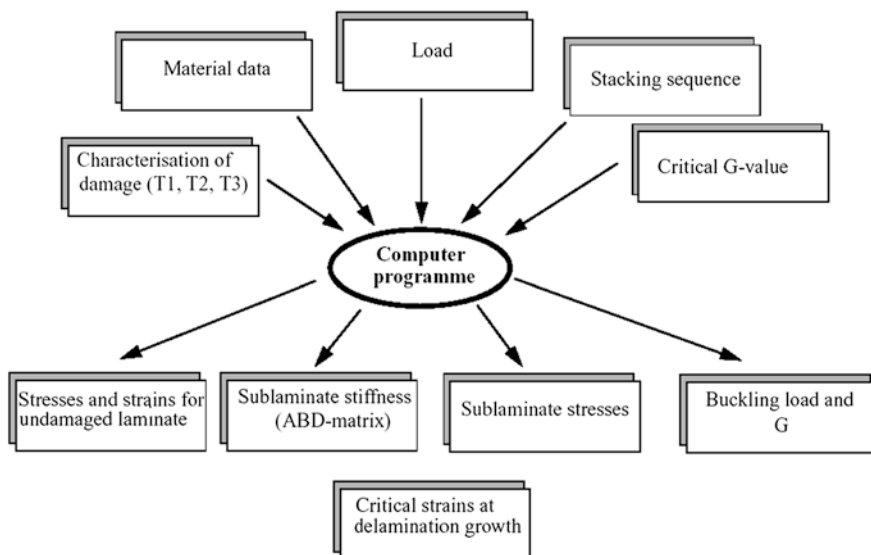


Fig. 8.7 Schematic representation of the method's numerical implementation

material properties, the ply thickness, the dimensions of the elliptical or circular damage (the major axis a and the minor axis b of the ellipse), the in-plane loads, the stacking sequence, the critical strain release rate value, G_{crit} . Depending on the characterization of the damage, three techniques T1, T2 and T3 can be used in CODEIN.

The code allows the single delamination to advance through the stack of the laminate. The buckling strains and the critical strains are determined for each sub laminate. According to the flow chart below the strains and stresses are calculated for the undamaged laminate. Further on, the stiffness and the stresses of the sub laminate are determined. The stresses are transformed to the local coordinate system of the ellipse, i.e. the local x -axis coincides with the major axis of the ellipse. The eigenvalue problem is created in the local system. The solution of eigenvalue problem results in three eigenvalues corresponding to three different buckling modes. The lowest absolute eigenvalue corresponds to the first buckling mode, (hence it is the only one of interest). The eigenvalue multiplied by the applied strain determines the initial buckling strain. Finally, the critical strain is determined.

8.3.2 Description of Method

The introduced method for the characterization of damage assumes that there is a constant projected damage size through the laminate thickness. Actually, there is a variation of damage size through the thickness and for thick laminates the damage

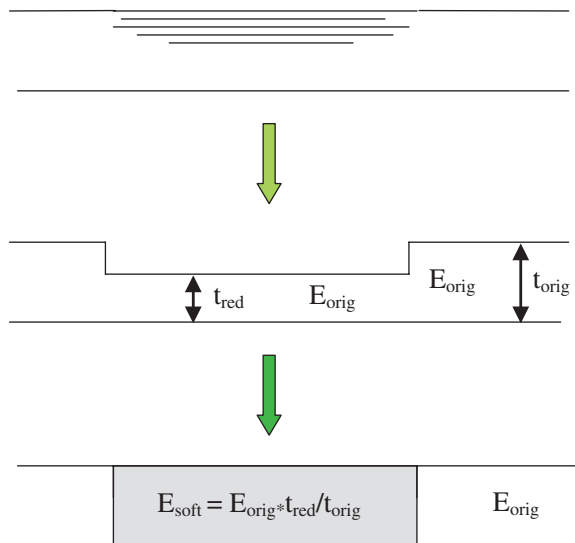
only extends through a part of the thickness. The consequence of this assumption (constant damage size along the thickness) is that the method becomes too conservative for thicker laminates.

In this chapter is an approach of an extended method to predict failure in a composite laminate with an impact damage presented. The development work is ongoing and that the approach could be changed. No validation activity has been performed at the moment.

The approach is:

- An analytical tool to predict damage extension at impact of a composite laminate in all directions is used (development ongoing) or the damage area is already known.
- Damaged area is handled as the damaged material doesn't carry any load, i.e. circular hole with a specified depth
- The remaining material is treated as a soft inclusion
- The stiffness of the soft inclusion is assumed to be scaled with respect to the relationship between undamaged laminate thickness at the impact damage and the original laminate thickness
- An analytical tool to calculate stress/strain field in a plate with a soft inclusion for arbitrary in-plane load is used (existing tool Saab)
- Failure load is determined by comparing max strain at the soft inclusion with allowed strain
- In parallel calculations using the current method based on delamination buckling and damage growth (CODEIN) is performed
- Finally failure load is selected based on strain in a soft inclusion and/or prediction with the current method CODEIN on delamination buckling and growth. The final strategy for this selection is to be determined (Fig. 8.8).

Fig. 8.8 Scheme of the steps implemented in this method



8.3.3 Analytical Tool to Predict Damage Extension

Development of an analytical tool to predict damage extension is ongoing. With help of equations given by Prasad et al. [6] it is possible to determine the inter-laminar stresses for a plate subjected to an impact force.

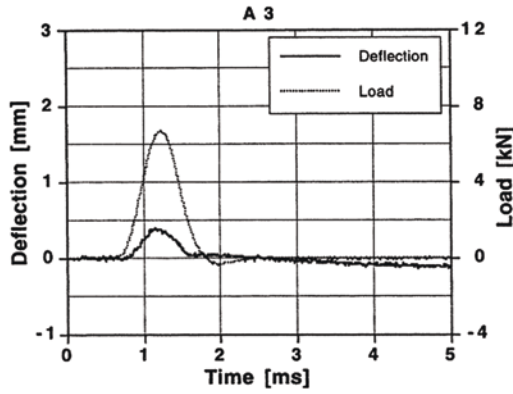
$$\begin{aligned}
 \sigma_z &= \left(\frac{h^3}{48}\right) \left(\left(1 + \left(\frac{2z}{h}\right)^3\right) - 3 \left(1 + \left(\frac{2z}{h}\right)\right) \right) \left((\alpha^3 Q_{11} + \alpha\beta^2(2G_{12} + Q_{12}))X \right. \\
 &\quad \left. + (2G_{12} + Q_{12})\alpha^2\beta + \beta^3 Q_{12} \right) Y \\
 \sigma_{xz} &= -\left(\frac{h^2}{8}\right) \left(1 + \left(\frac{2z}{h}\right)^2\right) \left((\alpha^2 Q_{11} + \alpha\beta^2)X \right. \\
 &\quad \left. + ((G_{12} + Q_{12})\alpha\beta Y) \cos(\alpha x) \sin(\beta y) \right) \\
 \sigma_{yz} &= -\left(\frac{h^2}{8}\right) \left(1 + \left(\frac{2z}{h}\right)^2\right) \left((\alpha^2 Q_{11} + \alpha\beta^2)X \right. \\
 &\quad \left. + ((G_{12} + Q_{12})\alpha\beta Y) \sin(\alpha x) \cos(\beta y) \right)
 \end{aligned} \tag{8.16}$$

Where X and Y are defined as

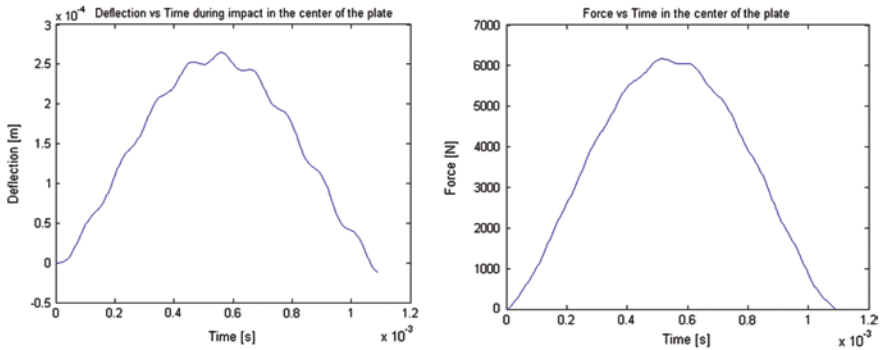
$$\begin{bmatrix} M_{11} & M_{12} & M_{13} \\ M_{21} & M_{22} & M_{23} \\ M_{31} & M_{32} & M_{33} \end{bmatrix} \begin{bmatrix} \ddot{W}_{mn} \\ \ddot{X}_{mn} \\ \ddot{Y}_{mn} \end{bmatrix} + \begin{bmatrix} c_{11} & c_{12} & c_{13} \\ c_{21} & c_{22} & c_{23} \\ c_{31} & c_{32} & c_{33} \end{bmatrix} \begin{bmatrix} W_{mn} \\ X_{mn} \\ Y_{mn} \end{bmatrix} = \begin{bmatrix} Q_{mn} \\ 0 \\ 0 \end{bmatrix} \tag{8.17}$$

The impact force is modeled as a dynamic cosine-cosine distributed load over a rectangular area that can be iteratively determined. The force can be determined by solving

$$\begin{aligned}
 \left(\frac{F}{S}\right)^{2/3} &= v_0 t - \frac{1}{m_2} \int_0^t dt \int_0^t F dt \\
 &\quad - \frac{1}{m_1 u^2 v^2} \sum_{m=1}^{\infty} \sum_{n=1}^{\infty} \frac{\sin\left(\frac{m\pi\xi}{a}\right) \sin\left(\frac{n\pi\eta}{b}\right)}{\omega_{mn}} \\
 &\quad \frac{\sin\left(\frac{m\pi x}{a}\right) \sin\left(\frac{n\pi y}{b}\right) \cos\left(\frac{m\pi u}{2a}\right) \cos\left(\frac{n\pi v}{2b}\right)}{\left(\frac{m}{a} - \frac{1}{u}\right) \left(\frac{m}{a} + \frac{1}{u}\right) \left(\frac{n}{b} - \frac{1}{v}\right) \left(\frac{n}{b} + \frac{1}{v}\right)} \\
 &\quad \int_0^t F(\tau) \sin(\omega_{mn}(t - \tau)) dt
 \end{aligned} \tag{8.18}$$



Test by Daniele Giugno, FFA, 1998



Simulations

Fig. 8.9 Comparison between an experimental test (diagram in the upper side of the figure) and numerical results (diagrams in the lower side of the figure)

The matrix failure mode is determined using equations suggested by Hashin [7].

$$\sigma_{mu}^2 = \frac{1}{\sin^2(\theta) \left(\frac{\sin^2(\theta)}{\sigma_T^2} + \frac{\cos^2(\theta)}{\tau_A^2} \right)} \tag{8.19}$$

An example of predicted force versus time and deflection versus time is presented below and compared with test result on a 6.24 mm thick plate (Fig. 8.9).

8.4 Benefits and Limitations of the Method and Added Value with Respect to the State of the Art

Benefits

- Influence from damage extension through thickness can be handled
- Damage extension is calculated, i.e. must not be measured by NDT
- Not only restricted to the 'no growth' philosophy

Limitations

- Still an approximate method used for initial judgement. Finally testing is needed
- Some fitting of method for correlation with test results may be needed
- Some limitations regarding plate size and impact event.

References

1. Benzeggagh, M.L., Kenane, M.: Measurement of mixed-mode delamination fracture toughness of unidirectional glass/epoxy composites with mixed-mode bending apparatus. *Compos. Sci. Technol.* **56**, 439–449 (1996)
2. Chai, H., Babcock, C.D., Knauss, W.G.: One dimensional modelling of failure in laminated plates by delamination buckling. *Int. J. Solids Struct.* **17**(11), 1069–1083 (1981)
3. Kachanov, L.M.: Delamination buckling. In: *Delamination Buckling of Composite Materials*, vol. 14, pp 19–56. Springer, (1988)
4. Kachanov, L.M.: Delamination growth. In: *Delamination Buckling of Composite Materials*, vol. 14, pp 57–87. Springer, (1988)
5. Griffith, A.A.: The phenomena of rupture and flows in solids. *Phil. Trans. Roy. Soc. (Lon.) A* **221**, 163–198 (1920)
6. Prasad, C.B., Ambur, D.R., Starnes J.H.: Response of laminated composites plates to low-speed impact by airgun-propelled and dropped-weight impactors. AIAA paper 93-1402-CP, pp. 887–900, (1993)
7. Hashin, Z.: Failure criteria for unidirectional fiber composites. *J. Appl. Mech.* **57**, 329–334 (1980)
8. Nyman, T.: Fatigue and residual strength of composite aircraft structures. Doctoral thesis, Report 99-26, Royal Institute of Technology, Department of Aeronautics

Chapter 9

A Fast Numerical Methodology for Delamination Growth Initiation Simulation

Aniello Riccio and Michele Damiano

9.1 Introduction

Carbon Fibres Reinforced Plastics composites have been demonstrated particularly suitable for aerospace structural applications due to their high specific strength and stiffness. Nevertheless, the relevant costs related to composites manufacturing and the difficulties in predicting their failure mechanisms have considerably slowed down their integration in the aerospace industry. Furthermore, the lack of robust numerical tools, able to take into account the damage tolerance of composite structures, especially in the preliminary design phases, has led to an over-conservative design, not fully realising the promised economic benefits.

Among their several and complex failure mechanisms, composite structures have been demonstrated to be highly sensitive to delaminations arising after impact with foreign objects or caused by manufacturing defects. Hence, in order to design less conservative aerospace composite structures, it is mandatory to account for the effects of delaminations and their evolution even in the earlier stages of the design process. In order to achieve this goal, newer and faster numerical procedures representing the main phenomenological features governing the structural behaviour of damage tolerant composite structures, such as the delamination growth, needs to be developed.

The mechanical behaviour of composite structures with delaminations has been widely investigated in literature. Indeed, a number of delaminations' numerical models characterised by different degrees of complexity have been proposed and

A. Riccio (✉) · M. Damiano
Department of Industrial and Information Engineering,
Second University of Naples, via Rome n 29, 81031 Aversa, Italy
e-mail: aniello.riccio@unina2.it

“ad hoc” experimental tests have been performed on delaminated composite structures. The experimental activity on through-the-width and embedded delaminations presented respectively in [1–5] has given a valuable contribution to improve the knowledge on these defects, providing at the same time a useful database for the validation of novel numerical tools. Recently, some interesting experimental works have been published regarding the evaluation of toughness properties of composite materials enhanced by carbon nanotubes [6, 7] and thin-ply prepregs [8], which could help to improve and to validate both traditional and novel numerical methodologies.

The numerical activity has been focused on the simulation of the mechanical behaviour of composite structures with delaminations. Various mono-dimensional and 2-dimensional models for the analysis of through-the-width delaminations are introduced in [9–12]. An example of mono dimensional analytical approach is given in [9], where a second order shear-thickness deformation beam theory is introduced to cope with fracture mode I in angle-ply laminated composites while 2-dimensional numerical delamination models focused on the post-buckling behaviour of plates with through-the-width delaminations are proposed in [10–12].

Fully 3-dimensional approaches, both analytical [13, 14] and numerical [15–20], have been found mandatory for the simulation of the mechanical behaviour of composite plates with embedded delaminations. In [13, 14] the post-buckling behaviour of composite plates with embedded delaminations under compression is investigated and appropriate analytical models are introduced to detect the delamination growth initiation based on the Strain Energy Release Rate evaluation. Relevant steps towards the realistic modelling of delamination have been made in [15, 16], where the influence of the geometrical parameters of embedded delaminations on the buckling modes of delaminated composite panels have been investigated by means of numerical analyses. The importance of a suitable model for the contact phenomena between the sub-laminates has been highlighted in [17, 18] where a numerical approach based on unilaterally constrained, finite, rectangular plates has been employed. In [19, 20] the influence of contact phenomena between the sub-laminates on the strain Energy Release Rate (ERR) distribution along the embedded delaminations front has been investigated in detail for composite panels with a single delamination.

As a matter of facts, none of the above mentioned papers presents models able to simulate the growth of delaminations. On the contrary, in [21–29] more complex models, taking into account the delamination growth, are introduced. In [21, 22] a 2-dimensional approach for the simulation of the delamination growth in composite panels with through-the-width delaminations is presented. This approach is based on the Modified Virtual Crack Closure Technique (MVCCT) for the calculation of the Energy Release Rate and on the Penalty Method (PM) for the simulation of the contact phenomena.

In [23], although a detailed investigation on embedded delaminations’ growth has been carried out, only panels with a single delamination have been investigated reporting no information on the contributions of the single opening crack modes on the total strain Energy Release Rate.

The contribution of each opening crack mode on the overall Energy Release Rate distribution has been investigated in [24–26] where the approach adopted in [21, 22] has been extended and validated for single [24, 25] and multiple [26] embedded delaminations. An interface element able to address the problems of initiation and propagation of delaminations in laminated composites has been developed in [27] while cohesive surface approaches based on meso-mechanical models are introduced in [28, 29]. An accurate 3-D model based on continuum damage mechanics/Cohesive zone and able to determine the delamination growth shape by predicting inter-laminar crack onset and propagation is introduced in [30]. Both Virtual Crack Closure technique and Cohesive zone based approaches are progressively being implemented into commercial Finite Element codes which allow for detailed simulation of delamination initiation and growth [31].

The improvement of knowledge on the delamination growth phenomena, gained during the last decades, has favoured the research activities upon delamination evolution in complex composite structures such as the stiffened panels which are more representative from a design perspective. In [32, 33], experimental activities on stiffened composite panels containing delaminations have been performed and the influence of delamination position (in bay or under stringer) on its growth has been deeply investigated. A detailed numerical model for delamination growth based on the VCCT is applied to stiffened panels in [34]. This model is proven to be able to simulate the influence of the delamination size and position on the growth load and shape. In [35] stiffened panels with artificial partial debonding between stringer and skin and with delaminations in different positions have been numerically investigated by the VCCT. Influence of delamination size and position on the global buckling behaviour of the panels was the focus of the study.

For complex structural and material configurations such as stiffened composite panels, analytical approaches for the determination of the Energy Release Rate are clearly not easily applicable, therefore numerical (FEM for instance) methods are necessary. These numerical methodologies are, usually, employed to determine the complex state of forces acting around the delamination and the displacement field for the part of structure which has locally buckled. In general, due to the presence of geometrical non-linearity, related with the buckling phenomenon, numerical technique based on non-linear algorithms are required: as a consequence, the computational costs associated to such analyses may be quite relevant and time consuming. High computational costs are, generally, acceptable when detailed verification analyses are performed; whereas, for preliminary design and optimisation purposes, less expensive procedures are needed.

Thus, the study presented in this chapter has been aimed at developing a linear approach useful to improve the preliminary design and optimisation of stiffened composite panels tolerant to low velocity impacts induced damage. In the next sections the theoretical background of the proposed approach and the Finite Element implementation are detailed. Finally a numerical application consisting in a sensitivity study on stiffened composite panels with embedded delamination (with varying delamination size position in the skin and position along the thickness) is presented and discussed.

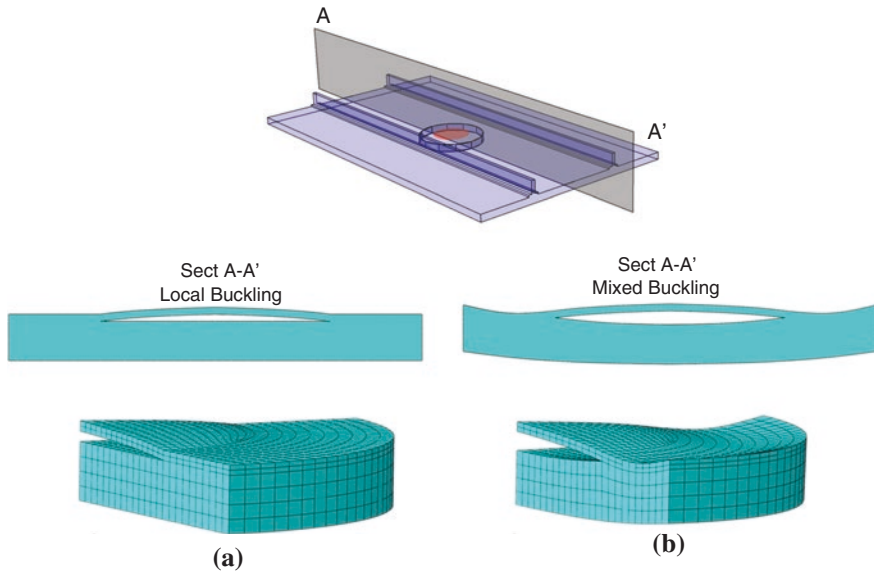


Fig. 9.1 Schematic representation of possible delamination scenarios in composite structures (the initially delaminated area is highlighted in *red* onto the panel sketch): **a** local buckling of the thinner sub-laminate; **b** “global” buckling of the delaminated area

9.2 Description of the Method: Theoretical Background

It is well known that, under compression load, composite structures [36] and in particular delaminated stiffened panels [32–34] can exhibit localised buckling phenomena. More precisely, for bay delaminations of appropriate sizes and localised at relatively small depths, two main scenarios can be singled out: the thinner sub-laminate buckles locally while the thicker sub-laminate remain unaffected (Fig. 9.1a); both sub-laminates buckle exhibiting a sort of mixed buckling mode: such a mode can often be seen as a local mode with respect to the rest of the surrounding structure, however it involves the whole delaminated area (Fig. 9.1b).

Often, the buckling of the thinner sub-laminate occurs, first, during the loading process, while the buckling in the thicker sub-laminate is somehow dictated by the geometrical arrangements of the structure, such as bay delamination size and depth.

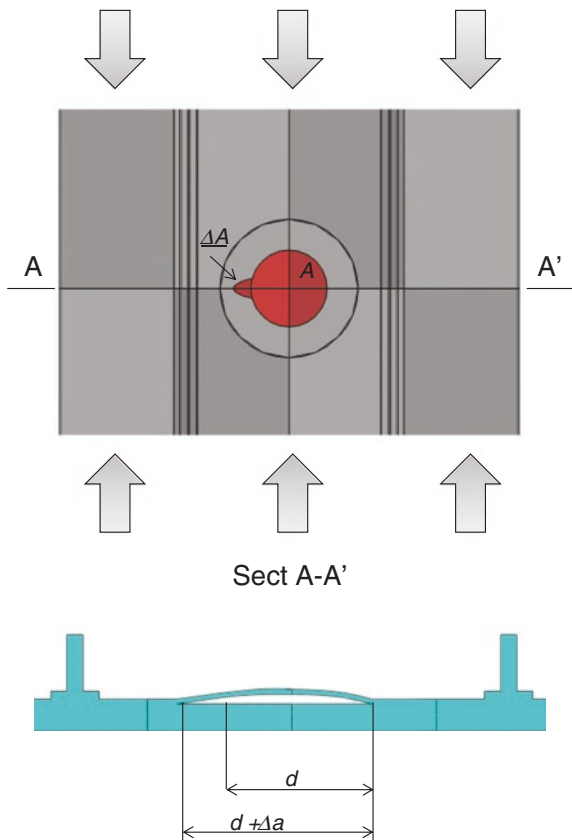
Usually, under compressive load, in stiffened composite panels with thin bay delaminations, the first scenario may evolve, due to delamination growth, and it may lead to the occurrence of the second-like scenario, in which the entity of damage is much more critical triggering more dangerous forms of buckling/failure phenomena. The first-like delamination scenario could be induced by accidental sources of damage, such as impacts or manufacturing defects. Therefore, in order to design damage tolerant stiffened composite panels, it is extremely important to evaluate and to predict when, starting from the first-like delamination scenario,

bay delaminations may propagate leading to the second-like delamination scenario. The evolution mechanisms of bay delaminations in composite stiffened panels drives the attention of the authors, in this chapter, toward the first-like scenario (Fig. 9.1a), which can be considered as the crucial stage for the evaluation of the embedded delaminations effects on structural integrity under compression loads. Theoretically, delaminations can be handled like cracks in brittle materials; hence the principles of linear elastic fracture mechanics for brittle materials hold. According to these principles, the propagation initiation of a delamination at a generic location along the delamination front, schematically shown in Fig. 9.2, can be considered governed by the expression (9.1) defining the Energy Release Rate as the variation of the potential energy ΔE associated to an increase ΔA of the delaminated area A .

When this Released Energy reaches a critical value G_C , which depends only upon the material properties, the delamination is supposed to growth.

$$G = -\frac{\Delta E}{\Delta A} = G_c \tag{9.1}$$

Fig. 9.2 Propagation of the delamination front (first scenario) under compression load

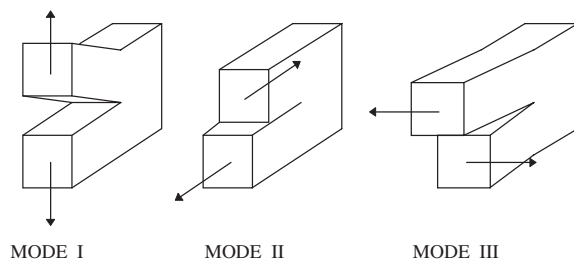


It is possible to distinguish among three different Energy Release Rate contributions associated to the three basic fracture modes: mode I, mode II and mode III schematically shown in Fig. 9.3. For the first delamination scenario, when the thickness of the buckled sub-laminate is much smaller than the total laminate thickness, the contributions of fracture mode II and mode III can be neglected (first assumption) because the first opening mode is clearly predominant over the remaining two. This consideration is demonstrated by both numerical analyses and analytical solutions in other published papers as [19, 25, 37].

The calculation of the energy released due to an increment in the delamination size and its relation with the applied load determines when the delamination advances. The Energy Release Rate distribution, along the embedded delamination front, is non uniform mainly due to the orthotropy character of the materials, the non uniformity of load distribution and the complexity of the surrounding structure. In particular, the Energy Release Rate can locally exceed its critical value, leading to a non-uniform progression of the delamination front (as schematically shown in Fig. 9.2). However, for the first-like delamination scenario, when the buckled sub-laminate thickness is considerably smaller than the total laminate thickness and when there is no delamination buckling mode shape jump between the first delamination buckling event and the delamination growth [38], the Energy Release Rate distribution can be assumed (second assumption) mostly influenced by the out of plane displacements along the delamination front [22, 25, 26, 34] on first delamination buckling.

For complex structural and material configurations such as stiffened composite panels, analytical approaches for the determination of the Energy Release Rate are clearly not easily applicable, therefore numerical (FEM for instance) methods are necessary. These numerical methodology are, usually, employed to determine the complex state of forces acting around the delamination and the displacement field for the part of structure which has locally buckled. In general, due to the presence of geometrical non-linearity, related with the buckling phenomenon, numerical technique based on non-linear algorithms are required: as a consequence, the computational costs associated to such analyses may be quite relevant and time consuming. High computational costs are, generally, acceptable when detailed verification analyses are performed; whereas, for preliminary design and optimisation purposes which are of main interest in this chapter, less expensive procedures are needed. In the next section, a new linear approach, applicable to the

Fig. 9.3 Basic fracture modes



first delamination scenario under the previously cited assumptions, is introduced. Such a procedure, can result extremely useful when designing stiffened composite panels capable to avoid the delamination growth event by predicting, the external load which causes the progression of a initial given delamination and by predicting the growth location along the delamination front. Indeed, considering only the first delamination scenario under the two main assumptions previously introduced (mode I predominance and Energy Release Rate distribution mostly influenced by the first delamination buckling out of plane displacements' distribution along the delamination front), restricts the applicability of the linear method to stiffened composite panels with thin bay delaminations.

Nevertheless, it should be noted that thin bay delaminations are of major concern in aerospace design with composite materials because they represent one of the most frequently occurring damage typology as a consequence of low velocity impact treats. Hence the proposed linear approach can be properly considered as finalised to the improvement of preliminary design and optimisation of stiffened composite panels tolerant to low velocity impacts induced damage.

The new proposed methodology could be schematised in the following steps:

1. calculation of the local buckled shape (mode) of the thinner sub-laminate (delamination buckling) by means of a linearized buckling analysis;
2. determination of the location along the delamination front with maximum Energy Release Rate according to out of plane buckling displacements.
3. calculation of the energy released by the structure at delamination growth initiation by means of a linearized buckling analysis together with two linear static analyses;
4. evaluation of the delamination growth initiation load;
5. determination of the Energy Release rate distribution along the delamination front at growth initiation according to out of plane buckling displacements.

The first linearised buckling analysis is meant to calculate the first buckling load and mode. In Fig. 9.4 a schematic representation of the analysed delamination scenario is presented. This representation, used to simplify the description of the proposed methodology, will be proven to fit very well with the adopted Finite Element Modelling.

Considering the overall structure subjected to an external compressive load F , when the elastic stability threshold is reached, the thinner sub-laminate (labelled as 1 in Fig. 9.4) buckles: an eigenvalue analysis (linearized buckling analysis) can give the delamination buckling load (eigenvalue) and mode (eigenvector). Hence, at each position i along the delamination front, it is possible to univocally determine the *normalized out of plane displacements*, $\frac{\Delta w^i}{\Delta w^k}$ ($i, k = 1 \dots N$), where N is the total number of considered locations along the delamination front (Fig. 9.5).

Beyond the delamination buckling event, characterised by the critical load F^{cr} , the residual non-linear contribution of the buckled thinner sub-laminate to the global stiffness can be neglected when the thickness of the buckled sub-laminate is much smaller than the total laminate thickness (this, as already anticipated in

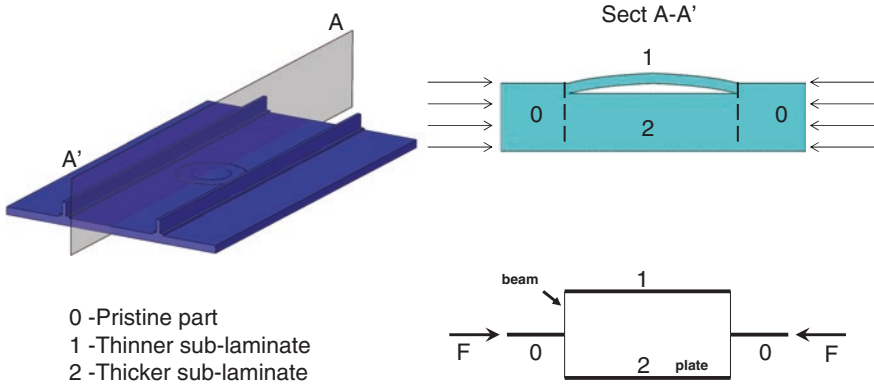
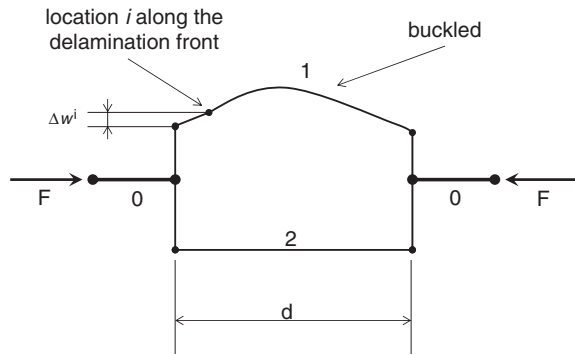


Fig. 9.4 Locally delaminated stiffened panel and its schematic representation

Fig. 9.5 Delamination buckling out of plane nodal displacements Δw^i along the delamination front



the previous section, does not limit the present formulation for the applications of interest). In this situation, even long after the first buckling event, the non-linear stiffness contribution due to large displacements and rotations of the buckled sub-laminate is extremely smaller if compared to the global laminate stiffness. Thus the stiffness K^A of the overall post-buckled structure with a delamination size A , can be approximately calculated by removing the sub-laminate labelled as (1) in Fig. 9.5. The same considerations can be repeated when the delamination size is $A + \Delta A$ (see Fig. 9.2); hence a new delamination buckling load $F^{cr'}$ and a new stiffness of the post-buckled structure $K^{A+\Delta A}$ can be defined.

In Fig. 9.6 a graphical representation of the global structural stiffness evolution is given for both structures, characterised by the two different delamination sizes through the loading process. Starting from the pre-buckling global stiffness value K^0 , the delamination buckling, for the two analysed delamination sizes reduces the global stiffness respectively to K^A and $K^{A+\Delta A}$ opening two distinct equilibrium paths.

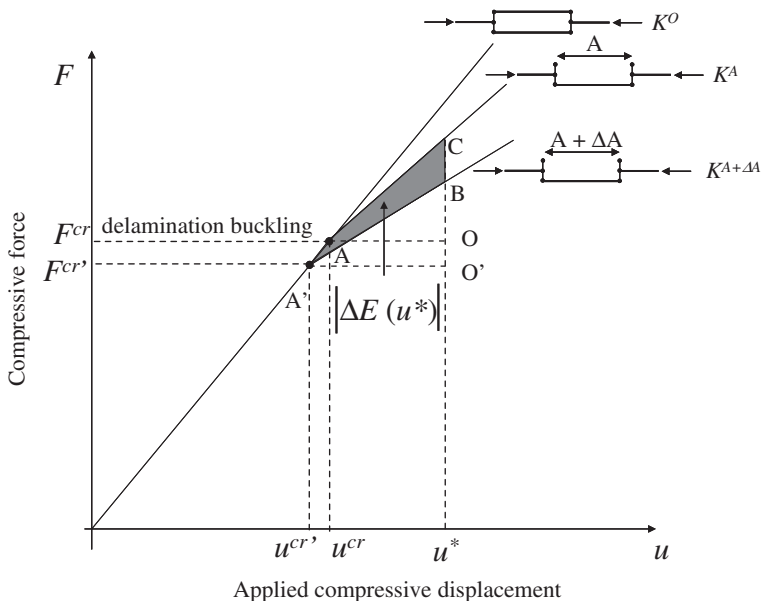


Fig. 9.6 Stiffness evolution of the stiffened composite panel under compression, before, after the delamination buckling and after the delamination propagation

With reference to Fig. 9.6, the progressive quasi-static increase of the delamination size, from A to $A + \Delta A$, for a structural element subjected to compressive displacements, can be reduced to a jump from the former to the latter equilibrium path [24]. Hence, for each displacement value u^* , the overall energy loss $\Delta E(u^*)$ [area $(A'ACB)$ in Fig. 9.6], related to the delamination size increment ΔA , is given by:

$$\begin{aligned}
 \Delta E(u^*) &= E^A(u^*) - E^{A+\Delta A}(u^*) = \text{area}(A'ACO') - \text{area}(A'BO') \\
 &= \text{area}(ACO) + \text{area}(A'A OO') - \text{area}(A'BO') \\
 &= \frac{1}{2}K^A(u^* - u^{cr})^2 + \frac{1}{2}K^0(2u^* - u^{cr'} - u^{cr})(u^{cr} - u^{cr'}) \\
 &\quad - \frac{1}{2}K^{A+\Delta A}(u^* - u^{cr'})^2
 \end{aligned} \tag{9.2}$$

where $E^A(u^*)$ and $E^{A+\Delta A}(u^*)$ are the elastic energies absorbed as a consequence of the applied displacement u^* , by the structures respectively with the delamination size A and $A + \Delta A$. Introducing the quantities:

$$\begin{aligned}
 \Delta u &= (u^* - u^{cr}) \\
 \Delta u' &= (u^* - u^{cr'})
 \end{aligned} \tag{9.3}$$

Equation (9.2) can be rewritten as:

$$\begin{aligned}
 \Delta E(u^*) &= \frac{1}{2}K^A(\Delta u)^2 + \frac{1}{2}K^0(\Delta u + \Delta u')(\Delta u' - \Delta u) - \frac{1}{2}K^{A+\Delta A}(\Delta u')^2 \\
 &= \frac{1}{2}(K^A - K^0)(\Delta u)^2 + \frac{1}{2}(K^0 - K^{A+\Delta A})\left[\Delta u + (u^{cr} - u^{cr'})\right]^2 \\
 &= \frac{1}{2}(K^A - K^{A+\Delta A})(\Delta u)^2 + (K^0 - K^{A+\Delta A})(u^{cr} - u^{cr'})\Delta u \\
 &\quad + \frac{1}{2}(K^0 - K^{A+\Delta A})(u^{cr} - u^{cr'})^2
 \end{aligned} \tag{9.4}$$

and it can be compacted in:

$$\Delta E(u^*) = \text{Coeff}A \cdot (\Delta u)^2 + \text{Coeff}B \cdot \Delta u + \text{Coeff}C \tag{9.5}$$

where:

$$\begin{aligned}
 \text{Coeff}A &= \frac{1}{2}(K^A - K^{A+\Delta A}) \\
 \text{Coeff}B &= (K^0 - K^{A+\Delta A})(u^{cr} - u^{cr'}) \\
 \text{Coeff}C &= \frac{1}{2}(K^0 - K^{A+\Delta A})(u^{cr} - u^{cr'})^2.
 \end{aligned} \tag{9.6}$$

Equation (9.5) represents the total amount of energy released during the delamination propagation as a quadratic function of the difference between the applied displacement and the critical buckling displacement. Considering that the delamination growth initiation is a local phenomenon occurring only at the location of delamination front, where the Energy Release Rate is maximum, the correct evaluation of the of $K^{A+\Delta A}$ and the $F^{cr'}$, respectively, the stiffness and the critical buckling load for the configuration with delamination size $A + \Delta A$, necessarily requires the determination of the location characterised by the maximum ERR.

According to the assumptions made in the previous section, and to the further reasonable assumptions:

1. geometrical and material configurations onto the delamination front nearly constant
2. local delamination bending stiffness nearly constant

it can be realistically assumed that the ERR distribution, related to the delamination size increment $G^i(u^*)$ follows the same distribution as the square of the first delamination buckling out of plane displacements Δw :

$$\begin{aligned}
 \frac{G^i(u^*)}{G^k(u^*)} &= \left(\frac{\Delta w^i}{\Delta w^k} \right)^2 \\
 i &= 1 \dots N \\
 k &= 1 \dots N
 \end{aligned} \tag{9.7}$$

and, in particular the following relation holds:

$$\frac{G^m(u^*)}{G^k(u^*)} = \max_i \left\{ \frac{G^i(u^*)}{G^k(u^*)} \right\} = \max_i \left\{ \left(\frac{\Delta w^i}{\Delta w^k} \right)^2 \right\}$$

$$i = 1 \dots N$$

$$k = 1 \dots N$$
(9.8)

With the superscripts i and k referring to a particular location along the delamination front, over the N total considered, and with the superscripts m indicating the location with maximum Energy Release Rate. By means of relation (9.6) it is possible to determine the location m by evaluating the value of the square of the first delamination buckling relative out of plane displacements Δw^i and Δw^k at each location i .

The further assumption of delamination buckling and delamination growth initiation events close each other let us to consider the Energy Release rate distribution along the delamination front constant with the increase of load. Hence relations (9.7) and (9.8) continues to hold and the maximum ERR location m does not change and the delamination growth will initiate at this location when the local Energy Release Rate will reach the critical value G_{IC} . Indeed at growth initiation the following relation must hold:

$$\frac{G^m(u^*)}{G_{IC}} = \frac{\Delta E(u^*)}{\Delta A^m \cdot G_{IC}} = 1$$
(9.9)

where ΔA^m is the increment of delamination size at the maximum ERR location. Substituting relation (9.5) into Eq. (9.9), it is possible to write:

$$\frac{[CoeffA \cdot (\Delta u)^2 + CoeffB \cdot \Delta u + CoeffC]}{\Delta A^m \cdot G_{IC}} = 1$$

$$\Rightarrow CoeffA \cdot (\Delta u)^2 + CoeffB \cdot \Delta u + CoeffC - \Delta A^m \cdot G_{IC} = 0$$
(9.10)

By solving Eq. (9.10) for Δu (hence for the applied compressive displacement u^*), it is possible to find the critical displacement u^{del} at which *initiation of delamination growth* is expected. Substituting this found displacement, u^{del} , in Eq. (9.9) it is possible to determine the value of the Energy Release Rate at location m at growth initiation. Finally, from Eq. (9.7), it is possible to evaluate the reference value $G^k(u^*)$ and the Energy Release Rate value at growth initiation for each location, i , along the delamination front.

The last step, in the proposed methodology is represented by the evaluation of the applied external compressive load, required to trigger the delamination growth; this load value can be computed by using relation reported in Eq. (9.11).

$$F^{del} = F^{cr} + K^A (u^{del} - u^{cr}).$$
(9.11)

9.3 Finite Element Implementation

The above presented methodology has been implemented in the ANSYS FEM code [39] by using a macro written in the Ansys Parametric Design Language (APDL). The FEM model needs to be accurate especially near the delamination front in order to correctly predict the local buckling modes pertaining to the delaminated part of the structure. The number and size of the finite elements have been selected according to suitable convergence studies, whose results are not presented here for the sake of brevity.

The delaminated stiffened panel is modelled by means of eight nodes layered shell elements, rigid-links and interface elements based on multipoint constraints. In Fig. 9.7, the shell finite element model of the stiffened panel with a bay delamination is presented while in Fig. 9.8a the different parts of delamination model, labelled according to the notation of Fig. 9.5, are illustrated and in Fig. 9.8b the thickness representation of the shell is shown.

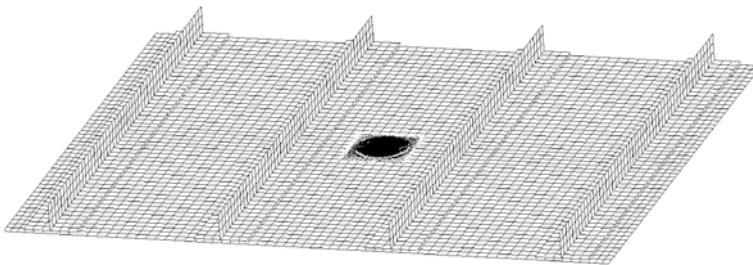


Fig. 9.7 FEM model of the stiffened panel with bay delamination

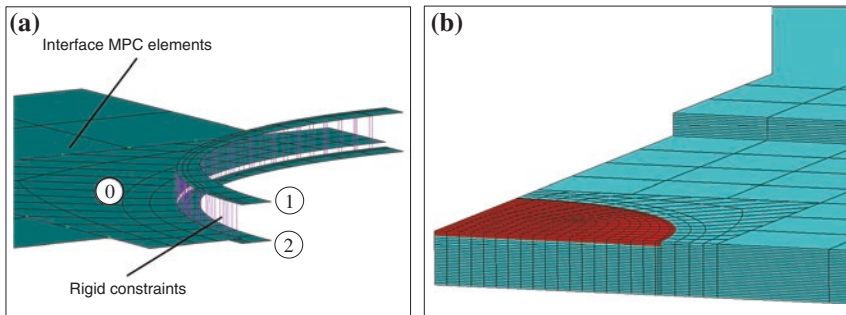


Fig. 9.8 Modeling details: **a** delamination modelling with shell elements, rigid links and interface MPC elements; **b** thickness representation of shell element

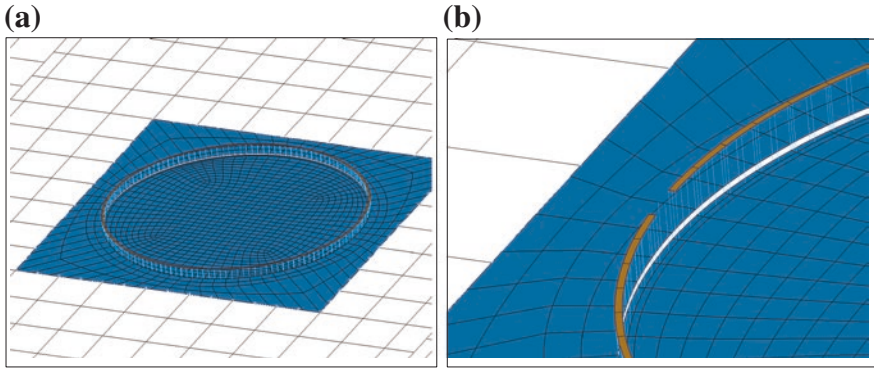


Fig. 9.9 Finite element model of the delaminated area with suppressed thinner sub-laminate. **a** Delamination size A ; **b** delamination size $A + \Delta A$

The dimensions of shell elements close to the delamination boundaries have been chosen accordingly to the convergence study performed in [40]. Eight nodes Shell99 layered elements are used to model the skin, the stringers and the delaminated sub-laminates; CERIG (rigid constraints connecting all the dofs) are used to connect stringer feet to the skin and they are also uniformly distributed along the delamination front at the delamination tip, to connect the sub-laminates to the rest of the skin. CONT elements with multipoint constraints are adopted to connect the delaminated area to the rest of panel without transition mesh (see the ANSYS operation manual [39] for further details on the adopted element formulations).

The ANSYS APDL macro can launch the ANSYS solver according to the computational steps previously introduced. First, an eigenvalue buckling problem (linearised buckling) is solved giving the delamination buckling frequency and mode for the structure with delamination size A . Then, the critical compressive load F^{cr} , the critical displacements u^{cr} and the normalized nodal displacements $\frac{\Delta w_i}{\Delta w_k}$ for the structure with delamination size A , are evaluated. Using these latter displacement values, the node with maximum Energy Release Rate is identified implementing relation (9.8). A further eigenvalue analysis is performed on the structure with the delamination size $A + \Delta A$ (delamination size increased at the location with the maximum energy release rate) in order to find the $F^{cr'}$ and $u^{cr'}$ values needed for the Energy Release Rate computation. Then the evaluation of the stiffness K^0 of the intact structure, the post-buckling stiffness K^A of the structure with the delamination size A and the post-buckling stiffness $K^{A+\Delta A}$ of the structure with the delamination size $A + \Delta A$ is performed (examples of the FEM models, with suppressed thinner sub-laminate, adopted to determine K^A and $K^{A+\Delta A}$ are respectively given in Fig. 9.9a, b). Finally the values of the applied displacements and loads at growth initiation are computed along with the Energy Release Rate at delamination front respectively, by solving Eqs. (9.10), (9.11) and (9.7).

9.4 Numerical Application: Sensitivity Analysis on a Stringer-Stiffened Panel with an Embedded Delamination

The procedure previously described is suitable to the fast evaluation of the delamination tolerance in the preliminary design phase. A parametric study conducted on a stringer stiffened panel (see Fig. 9.10) shows the influence of several parameters on the delamination growth load. For a given stacking sequence and geometrical configuration, the effect on the delamination tolerance due to the depth of the delamination, its position within the three bays and the delamination size have been analysed.

In Fig. 9.11 the geometric description of the structure used to evaluate the delamination propagation is reported.

In Table 9.1 the relevant stacking sequences of the stiffened panel components are presented.

The properties of the material systems adopted in this study are shown in Table 9.2.

The evaluation of the damage propagation load has been performed for different delamination sizes, position over the skin and depth. The results, in terms of

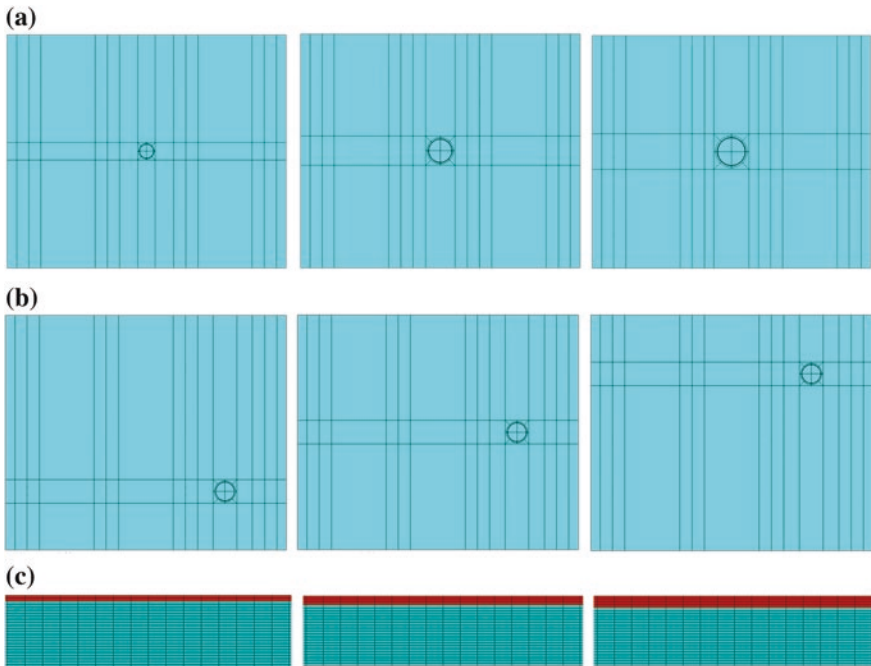


Fig. 9.10 Overview of several analyzed configurations varying: **a** radius, **b** delamination location and **c** thickness of sub-laminate

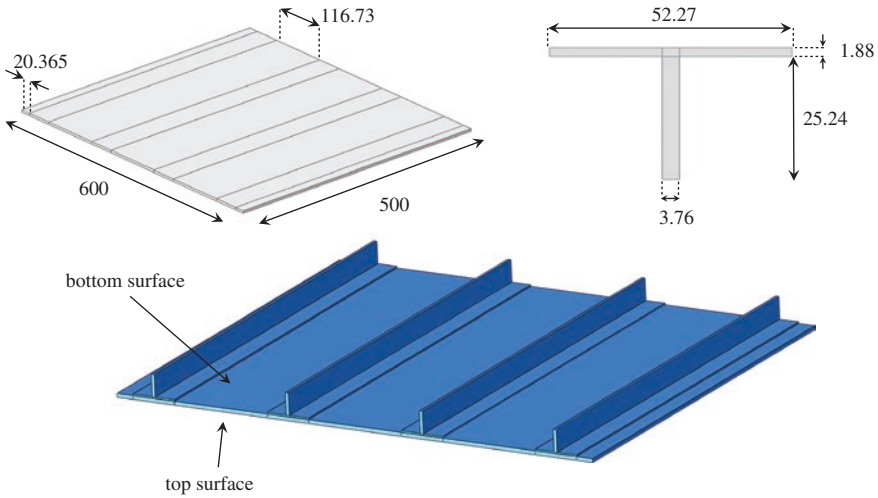


Fig. 9.11 Stiffened panel geometry overview

Table 9.1 Stacking sequences of the stiffened panels components

Component	Stacking sequence
Skin	[45, 0, 90, -45] _{3S}
Cap stringer	[45, -45, 0, 0, 90] _S
Web stringer	[45, -45, 0, 0, 90] _{2S}

Table 9.2 Properties of the material system considered for the stiffened composite panels

AS4/3501-6		
E_{11}	147.0 GPa	Longitudinal young's modulus
$E_{22} = E_{33}$	9.0 GPa	Transverse young's modulus
$G_{12} = G_{13}$	5.0 GPa	Shear modulus
G_{23}	3.0 GPa	
$\nu_{12} = \nu_{13}$	0.33	Poisson's ratio
ν_{23}	0.42	
G_{Ic}	175 J/m ²	Critical ERR for mode I
G_{IIc}	532 J/m ²	Critical ERR for mode II
G_{IIIc}	532 J/m ²	Critical ERR for mode III
t	0.188 mm	Ply thickness

propagation load as a function of the delamination radius, are shown in Fig. 9.12. Results presented in Fig. 9.12 have been obtained for bay circular delaminations centered at 131 × 250 mm (side bay delamination) and placed between the third and fourth ply at 0.564 mm from the bottom skin.

The critical load, reported in Fig. 9.12, decreases, as expected, for delamination radii between 15 and 25 mm. On the other hand, an increase in delamination

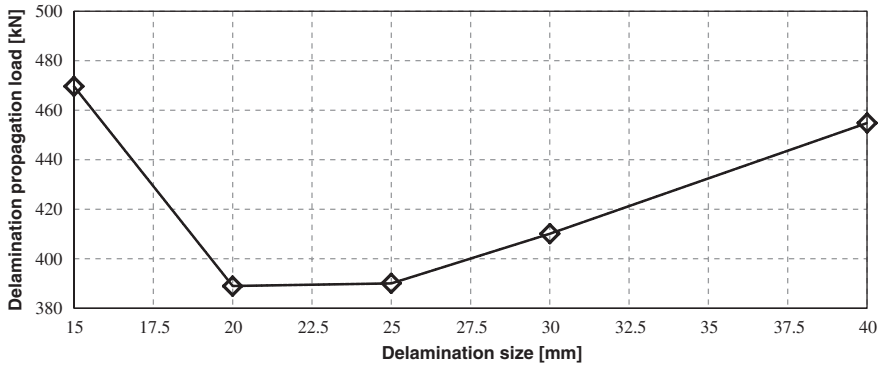


Fig. 9.12 Propagation load as a function of the delamination radius for configurations with a side bay delamination positioned at 131×250 mm and at 12.5 % of the panel thickness

growth initiation load can be appreciated for delamination radii between 25 and 40 mm; this behaviour is probably due to the stringer effect that improves the local stiffness at delamination front and become noticeable as the delamination radius increases and delamination front approaches the stringer foot.

The effect of delamination depth on growth initiation can be appreciated in Fig. 9.13 where three different thickness positions have been considered: 0.386, 0.564 and 0.752 mm from the bottom surface of the skin. Indeed, in Fig. 9.13 the influence of delamination depth on the distribution of energy release rate at growth initiation along the delamination front can be appreciated. Results shown in Fig. 9.13 have been obtained for delamination with a 20 mm radius located in the side bay near panel edge at 131×125 mm.

The energy release rate distribution at growth initiation along the delamination front, of the analysed cases, shows a noticeable dependency on the sub-laminate thickness resulting also in a different direction of damage growth.

In Fig. 9.14 the energy release rate distributions at growth initiation along the delamination front for several positions of the delamination in central and lateral bays are illustrated.

Figure 9.14 clearly shows that there is no relevant influence of delamination position in the skin on the energy release rate distribution and consequently on the angle of delamination growth.

The sensitivity study, here briefly presented, has shown the ability, of the developed linear procedure for delamination growth initiation prediction, to provide useful data in terms of limit load for the growth of a circular delamination and energy release rate distribution along the front. As expected, the applicability of the linear model to a specific configuration strictly depends on the capability of this geometrical configuration to fulfill the assumptions on which the linear model is based. In Table 9.3 the results obtained from the performed sensitivity analysis are summarized.

In Fig. 9.15 contour plots of the out-of-plane-displacements are illustrated both on the local zone of the model and for the whole structure. For the latter case a scale factor has been applied to emphasize the direction of damage propagation.

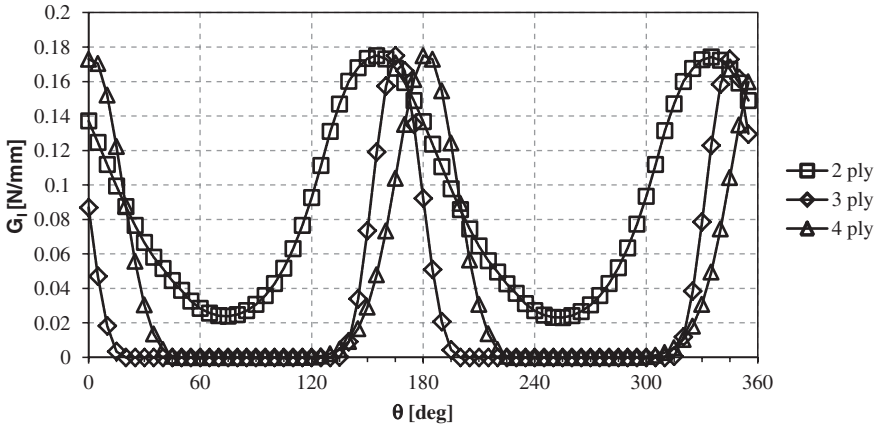


Fig. 9.13 Energy release rate distributions at growth initiation for configurations with side bay delamination (20 mm radius) located at 131 × 125 mm

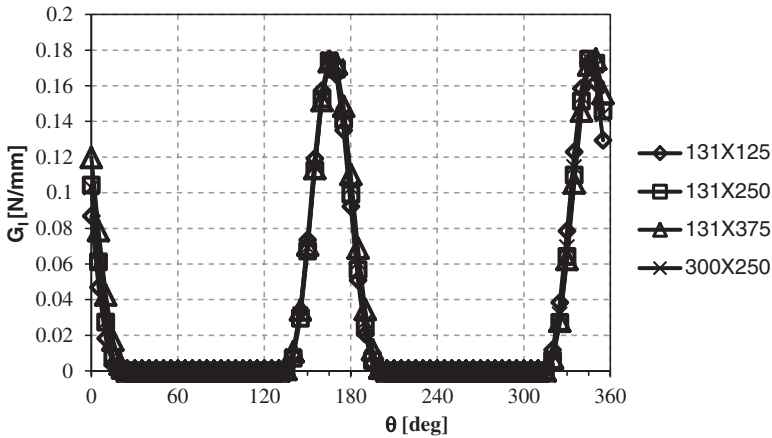


Fig. 9.14 Energy release rate distributions at growth initiation for several position of delamination (with 0.564 mm sub-laminate thickness and 20 mm radius)

9.5 Benefits and Limitations of the Method and Added Value with Respect to the State of the Art

The cited techniques for the numerical simulation of delamination growth, such as the VCCT and the cohesive zone, due to their strict relation between the delamination propagation and buckling phenomenon, are based on geometrically non-linear models which can be computationally expensive, especially for complex geometrical shapes (as in the case of stiffened panels). A first attempt in limiting the computational time has been made in [41] where a loose global local coupling

Table 9.3 Results of the sensitivity study

(a)		20 mm			
Delamination radius		3 plies depth	3 plies depth	3 plies depth	4 plies depth
Thickness position		131 mm × 125 mm	131 mm × 250 mm	131 mm × 375 mm	131 mm × 125 mm
Delamination center position		43,1423	43,1426	43,1423	43,1423
Initial stiffness (N/mm)		40,8256	39,4690	39,3447	53,4371
Critical load—for propagation (N)		1,893	1,830	1,824	2,477
Critical strain—for propagation (μ ϵ)		165	345	350	180
Angle of propagation (deg)		1.5402	1.542	1.5383	1.5403
Critical displacement—global buckling (mm)					
(b)		15 mm			
Delamination radius		3 plies depth	3 plies depth	3 plies depth	3 plies depth
Thickness position		300 mm × 250 mm	300 mm × 250 mm	300 mm × 250 mm	300 mm × 250 mm
Delamination center position		43,1362	43,1416	43,1301	43,0963
Initial stiffness (N/mm)		46,9611	38,8989	39,0081	45,4835
Critical load—for propagation (N)		2,177	1,803	1,809	2,115
Critical strain—for propagation (μ ϵ)		165	345	165	345
Angle of propagation (deg)		1.5442	1.5428	0	0
Critical displacement—global buckling (mm)					

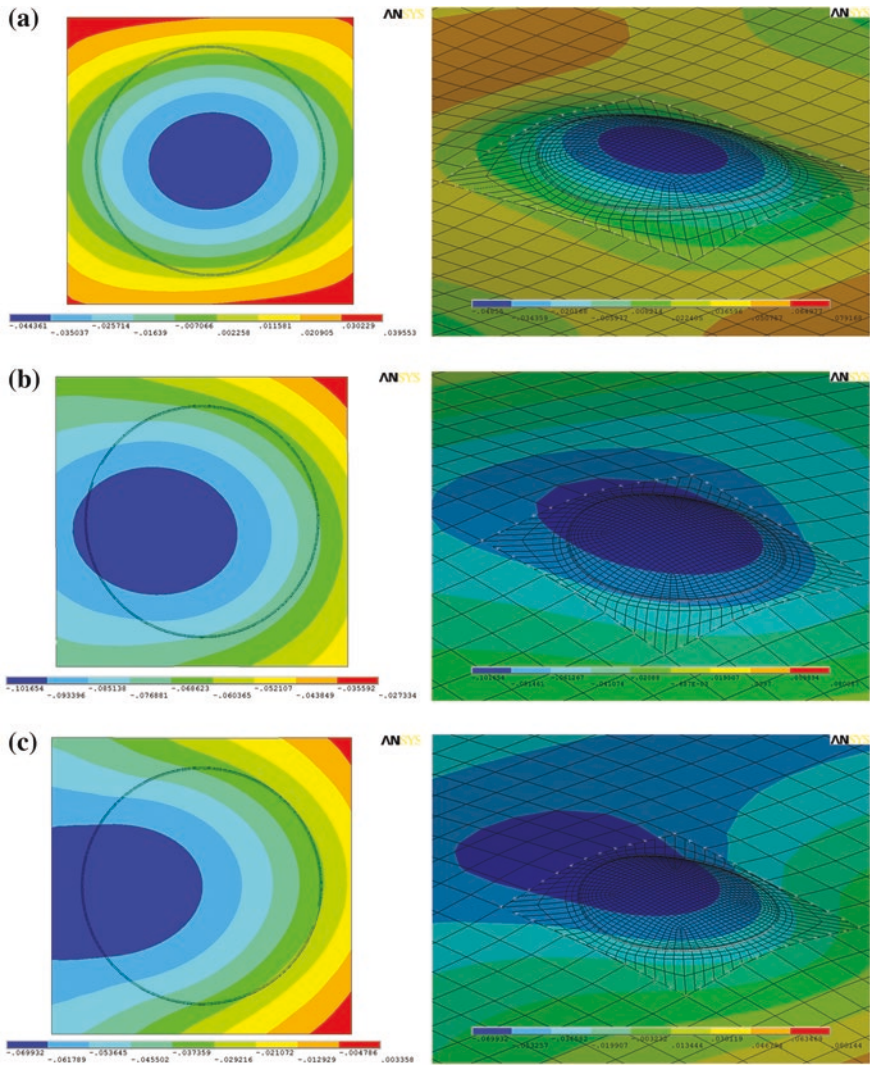


Fig. 9.15 Contour plot of the out-of-plane displacements for three investigated configurations: **a** central bay with a 30 mm radius, 0.564 mm thickness, **b** left bay, 20 mm radius and 0.376 mm thickness, and **c** central bay 0.564 mm thickness and 20 m radius

technique has been adopted for optimisation purposes on damage tolerant composite panels. However, the use of non-linear techniques [42] for delamination growth simulations, even if accompanied by global-local coupling, is still unsuitable for preliminary design and optimisation of stiffened composite panels; hence newer fast numerical methodologies for delamination growth simulation (possibly based on linear calculations) are desirable in order to support the effective “damage tolerant” design of composite structures.

The activities performed at CIRA within the GARTEUR AG-32 have been focused on the development of a linear delamination growth initiation approach for the preliminary design of delaminated stiffened composite panels. The new methodology is derived by the one introduced and validated in [37] enabling the simulation of delamination growth by means of four linear analyses. The first linearised buckling analysis is needed to determine the delamination buckling shape and load. The second linearised buckling analysis along with two linear static analyses are employed to evaluate the amount of energy released by the delamination propagation by means of the elastic energy balance. Under certain hypotheses, which can be considered acceptable in the preliminary design and optimisation phases, the new approach developed can provide the delamination growth load and location in delaminated composite structures.

References

1. Ashizawa, M.: Fast interlaminar fracture of a compressively loaded composite containing a defect. In: Proceedings of the Fifth DOD/NASA Conference on Fibrous Composites in Structural Design. NASA Ames Research Center, pp. 1–269 (1981)
2. Ramkumar, R.L.: Fatigue Degradation in compressively loaded composite laminates. NASA CR-165681 (1981)
3. Ramkumar, R.L.: Performance of a quantitative study of instability-related delamination growth. NASA CR-166046 (1983)
4. Byers, B.A.: Behaviour of damaged graphite/epoxy laminates under compression loading. NASA CR-159293 (1980)
5. Chai, H., Knauss, W.G., Babcock, C.D.: Observation of damage growth in compressively loaded laminates. *J. Exp. Mech.* **23**(3), 329–337 (1983)
6. Arai, M., Noro, Y., Sugimoto, K.-I., Endo, M.: Mode I and mode II interlaminar fracture toughness of CFRP laminates toughened by carbon nanofiber interlayer. *Compos. Sci. Technol.* **68**(2), 516–525 (2008)
7. Tong, L., Sun, X., Tan, P.: Effect of long multi-walled carbon nanotubes on delamination toughness of laminated composites. *J. Compos. Mater.* **42**(1), 5–23 (2008)
8. Yokozeki, T., Aoki, Y., Ogasawara, T.: Experimental characterization of strength and damage resistance properties of thin-ply carbon fiber/toughened epoxy laminates. *Compos. Struct.* **82**(3), 382–389 (2008)
9. Gordnian, K., Hadavinia, H., Mason, P.J., Madenci, E.: Determination of fracture energy and tensile cohesive strength in mode I delamination of angle-ply laminated composites. *Compos. Struct.* **82**(4), 577–586 (2008)
10. Whitcomb, J.D.: Approximate analysis of postbuckled through-the-width delaminations. *Compos. Technol. Rev.* **4**(3), 71–77 (1982)
11. Whitcomb, J.D.: Parametric analytical study of instability-related delamination growth. *Compos. Sci. Technol.* **25**(1), 18–48 (1986)
12. Chai, H., Babcock, C.D., Knauss, W.G.: One delamination modelling of failure in laminated plates by delamination buckling. *Int. J. Solids. Struct.* **17**(1), 1069–1083 (1981)
13. Shivakumar, K.N., Whitcomb, J.D.: Buckling of a sublaminates in a quasi-isotropic composite laminate. *Int. J. Compos. Mater.* **19**, 2–18 (1985)
14. Whitcomb, J.D., Shivakumar, K.N.: Strain-energy release rate analysis of a laminate with a postbuckled delamination. numerical methods in fracture mechanics. NASA TM-89091 (1987)

15. Kim, H.J., Hong, C.S.: Buckling and postbuckling behaviour of composite laminates with an embedded delamination. In: Proceedings of ICCM-10 Whistler, B.C. (1995)
16. Singh, K.L., Dattaguru, B., Ramamurthy, T.S., Mangalgi, P.D.: Delamination tolerance studies in laminated composite panels. *Sadhana* (printed in India) **25**(4), 409–422 (2000)
17. Shahwan, K., Waas, A.M.: Unilateral buckling of rectangular plates. *Int. J. Solids Struct.* **31**(1), 75–89 (1994)
18. Shahwan, K., Waas, A.M.: Buckling of unilaterally constrained plates: application to the study of delaminations in layered structures. *J. Franklin Inst.* **335B**(6), 1009–1039 (1998)
19. Whitcomb, J.D.: Analysis of a laminate with a postbuckled embedded delamination, including contact effects. *Int. J. Compos. Mater.* **26**(10), 1523–1535 (1992)
20. Whitcomb, J.D.: Three dimensional analysis of a postbuckled embedded delamination. *Int. J. Compos. Mater.* **23**, 862–889 (1989)
21. Perugini, P., Riccio, A., Scaramuzzino, F.: Influence of delamination growth and contact phenomena on the compressive behaviour of composite panels. *Int. J. Compos. Mater.* **33**(15), 1433–1456 (1999)
22. Riccio, A., Perugini, P., Scaramuzzino, F.: Modelling compression behaviour of delaminated composite panels. *Comput. Struct.* **78**, 73–81 (2000)
23. Nilsson, K.-F., Thesken, J.C., Sindelar, P., Giannakopoulos, A.E., Storakers, B.: A theoretical and experimental investigation of buckling induced delamination growth. *J. Mech. Phys. Solids.* **41**(4), 749–782 (1993)
24. Gaudenzi, P., Perugini, P., Riccio, A.: Post-buckling behaviour of composite panels in the presence of unstable delaminations. *Compos. Struct.* **51**(3), 301–309 (2001)
25. Riccio, A., Perugini, P., Scaramuzzino, F.: Embedded delamination growth in composite panels under compressive load. *Compos. B Eng.* **32**(3), 209–218 (2001)
26. Riccio, A., Scaramuzzino, F., Perugini, P.: Influence of contact phenomena on embedded delamination growth in composites. *AIAA J.* **41**(5), 933–940 (2003)
27. Davies, G.A.O., Hitchings, D., Ankersen, J.: Predicting delamination and debonding in modern aerospace composite structures. *Compos. Sci. Technol.* **66**, 846–854 (2006)
28. De Borst, R., Remmers, J.J.C.: Computational modelling of delamination. *Compos. Sci. Technol.* **66**, 713–722 (2006)
29. Allix, O., Blanchard, L.: Mesomodelling of delamination: towards industrial applications. *Compos. Sci. Technol.* **66**, 731–744 (2006)
30. Gudmundson, P.: Micromechanically based constitutive models for damage evolution in composite laminates. *Int. J. Damage Mech.* **9**(1), 29–39 (2000)
31. ABAQUS MANUAL (revision 6.5-1): Theory
32. Greenhalgh, E., Singh, S., Hughes, D., Roberts, D.: Impact damage resistance and tolerance of stringer stiffened composite structures. *Plast. Rubber Compos. Process. Appl.* **28**(5), 228–251 (1999)
33. Greenhalgh, E., Meeks, C., Clarke, A., Thatcher, J.: The effect of defects on the performance of post-buckled CFRP stringer-stiffened panels. *Compos. A Appl. Sci. Manuf.* **34**(7), 623–633 (2003)
34. Greenhalgh, E., Singh, S., Nilsson, K.-F.: Mechanisms and modeling of delamination growth and failure of carbon-fiber reinforced skin-stringer panels. *ASTM Spec. Tech. Publ.* **1383**, 49–71 (2000)
35. Suemasu, H., Kurihara, K., Arai, K., Majima, O., Ishikawa, T.: Compressive property degradation of composite stiffened panel due to debonding and delaminations. *Adv. Compos. Mater: Official J. Jpn Soc. Compos. Mater.* **15**(2), 139–151 (2006)
36. ANSYS MANUAL (revision 5) Volume III: Elements DN-R300:50-3
37. Riccio, A., Gigliotti, M.: A novel numerical delamination growth approach for the preliminary design of damage tolerant composite structures. *J. Compos. Mater.* **41**(16), 1939–1960 (2007)
38. Faggiani, A., Falzon, B.G.: Optimization strategy for minimizing damage in postbuckling stiffened panels. *AIAA J.* **45**(10), 2520–2528 (2007)

39. Guédra-Degeorges, D.: Recent advances to assess mono-and multi-delaminations behaviour of aerospace composites. *Compos. Sci. Technol.* **66**, 796–806 (2006)
40. Bruno, D., Greco, F.: Mixed mode delamination in plates: a refined approach. *Int. J. Solids Struct.* **38**, 9149–9177 (2001)
41. Gaudenzi, P., Perugini, P., Spadaccia, F.: Post-buckling analysis of a delaminated composite plate under compression. *Compos. Struct.* **40**(3), 231–238 (1998)
42. Krueger, R.: The virtual crack closure technique: history, approach and applications. NASA/CR-2002-211628, ICASE Report No. 2002-10 (2002)

Part III
Manufacturing and Testing

Chapter 10

An Experimental Study on the Strength of Out of Plane Loaded Composite Structures

Sören Nilsson, Alann André and Anders Bredberg

10.1 Introduction

More and more composite materials are used within primary load carrying aircraft structures. Examples are Boeing 787 and Airbus A350XWB where the composite content has increased up to 50–60 % by weight.

With the aim to decrease manufacturing cost the structures are given a higher degree of integration and complexity. More integrated structures give fewer articles and fewer steps in the manufacturing chain. In many cases new innovative design solutions are a requirement to enable integrated structures. Good examples of this are Saab Aerostructures redesign of the A320 aileron and design of Boeing 787 “Bulk Cargo Door”, where manufacturing costs have been reduced considerably by innovative design solutions. Also the maximum thickness of laminated composite structures is increasing in aircraft structures. For example, the wing spars of the inner wings as well as the central wing box in modern aircraft are made from composite laminates with thickness exceeding 40 mm.

As a consequence of this development composite structures are expected to be exposed to higher interlaminar loads (bending, transverse shear etc.). Furthermore there is a strive to, in a larger extend, permit operation in the post-buckled regime, which also contributes to the out of plane loads. Cut-outs and holes are commonly used in the structure to facilitate placement of cables, as lightening holes, for inspection of inner structure etc. Such cut-outs result in notch stresses that are known to cause significant reduction in both tensile and compressive strength of a composite structure.

S. Nilsson (✉) · A. André
Composite Structures, Swerea SICOMP, 431 22 Mölndal, Sweden
e-mail: soren.nilsson@swerea.se

A. Bredberg
Saab Aeronautics, Linköping, Sweden

Traditionally composite structures are designed to minimize out of plane loading, due to the low interlaminar strength of the material. Because of this there is a lack of design tools and data that handles these loads. To facilitate the modern requirements on design mentioned above and to increase the potential and reduce conservatism during design there is a need to increase the knowledge regarding strength of out of plane loaded composite structures. The experimental study presented in this work is one step in this direction. Here laminates with two different thicknesses and widths as well as notch sizes are tested in bending. For comparison, also impacted laminates have been tested in bending and compression. Accompanying tests in compression are performed and reported to allow the evaluation of the full effects of bending.

10.2 Mechanical Tests

Saab Aerostructures manufactured laminates from HTA/6376C carbon fibre/epoxy pre-preg, according to the Saab standard and test plan [1]. Two nominal laminate thicknesses were manufactured, 4.16 and 8.32 mm respectively, using the quasi isotropic layups $[(0/90/+45/-45)_4]_S$ and $[(0/90/+45/-45)_8]_S$.

Specimens were machined to a width of 36 and 156 mm with a 6 and a 25 mm drilled hole respectively, giving the same D/W-ratio. The specimens were manufactured to be tested in four point bending or compression.

Specimens to be impacted before mechanical test were machined to a width of 156 mm. The specimens were clamped (150 × 230 mm) and impacted in a drop-weight rig with 35 J using a spherical impactor with a radius of 8 mm.

10.2.1 Bending and Compressions Tests

Bending tests were performed in a Zwick 150 kN electromechanical test rig using a specially manufactured bending rig according to Fig. 10.1. It should be noted that the span length of the specimen with 6 mm hole is only 210 mm compared to specimens with 25 mm hole or with an impact damage that have a span length of 390 mm, see Fig. 10.1. During tests, the load and displacement were measured using the internal load cell and displacement recorder in the test rig.

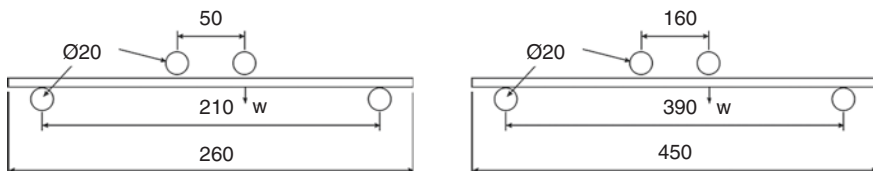
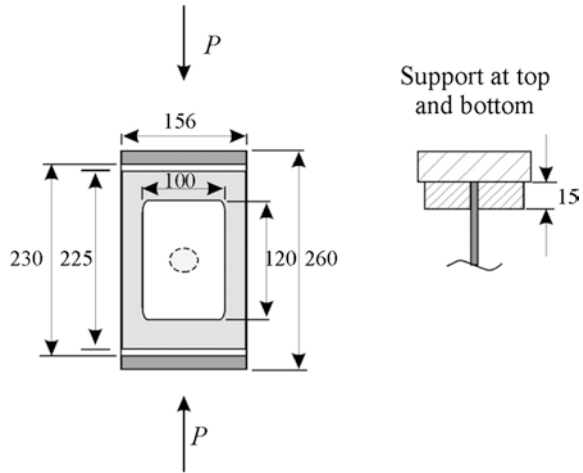


Fig. 10.1 Bending tests of laminate with 6 mm hole (left) and 25 mm hole (right) respectively

Fig. 10.2 Antibuckling device used during compression tests of the 156 mm wide specimens



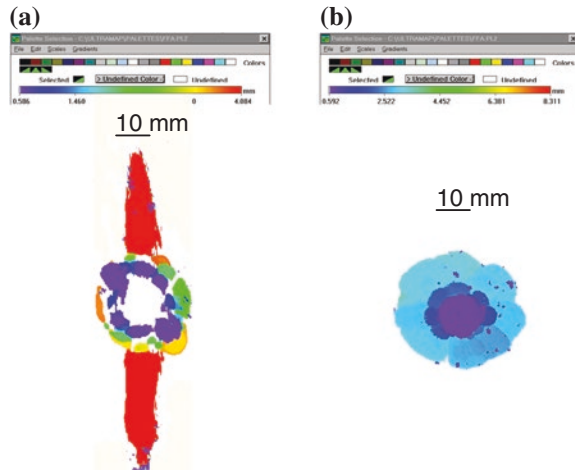
The bending tests were performed with a deformation test speed of 5 mm/min. The procedure during the bending tests was to load the specimens until a significant drop in load was recognized. The specimens were then unloaded and dismounted from the test rig. The failure was photographed using a digital camera. One specimen in each set was also subjected to fractographic analysis to determine failure distribution through the thickness. The fractographic analysis included inspection with ultrasonic C-scan and optical microscopy.

Compression tests on panels with a 25 mm hole or an impact damage were performed on specimens with a width of 156 mm to fit in an existing rig. Antibuckling devices, depicted in Fig. 10.2, were used during the tests, which were performed in a 1,000 kN MTS servohydraulic test rig in load control at a load rate of 2 kN/s. Compressive tests of the 36 mm wide specimens were performed in a 160 kN MTS servohydraulic test rig in load control at a load rate of 2 kN/s, with a sufficiently short free span to prevent global buckling of the specimen. The anti-buckling rig used in these tests is similar to the rig described in ASTM D7137, also known as the Boeing “compression after impact rig”. However, the dimensions of the specimens are approximately 50 % larger. Furthermore the used rig is supplied with antibuckling plates with a window with a square opening of 100×120 mm to prevent global buckling of the specimens. In contrast the ASTM standard uses clamped/simply supported boundary conditions.

10.2.2 Inspection—NDT and Fractography

After impact the residual dent depth was measured using a sliding calliper. The dent depth was found to vary between 0.9–1.1 and 0.1–0.3 mm for the 4 and 8 mm laminates respectively.

Fig. 10.3 Damage caused by a 35 J impact on **a** 4 mm (left) and **b** 8 mm (right) thick laminate



On the backside of the 4 mm laminates splitting of the outermost 0° ply due to the impact was recognised. In connection with the splitting, a very large delamination between the outermost 0° ply and the rest of the specimen was observed as shown in the C-scan picture in Fig. 10.3. As seen in the C-scan pictures the impact damage is distributed through the whole thickness in the 4 mm specimen whereas damage in the 8 mm specimen only is observed in the upper third part of the specimen, as a result of high contact stresses present during impact of the thicker laminate. Fractographic studies of two specimens, one of each thickness, were performed in an optical microscope to verify the C-scan recordings.

The scatter in size of the damage in the 4 mm specimens is small; the width varies from 27–30 mm, whereas the scatter for the 8 mm specimens is large, as the width varies from 10–30 mm. The reason is that for the 8 mm specimens a 35 J impact slightly exceeds the energy threshold level for damage initiation.

10.3 Experimental Results

During bending tests, the impacted side of the laminates was loaded either in compression or tension to determine effect of damage distribution through the thickness on the bending strength. A significant effect on both failure strain and failure mode was recognised depending on damage distribution through the thickness.

The study of different thicknesses of the notched specimens is motivated as several papers have been published [2–5] discussing size effect of damage on both tensile and compressive strength of composite laminates. Conclusions from these papers are that there is a significant reduction of the tensile notch strength with increased thickness and also with increased hole size. The compressive strength however decreased with increasing hole size if laminate thickness were scaled on a sub-laminate level, i.e. ply thickness where kept constant. An impact

Table 10.1 Summary of the results

		Loaded in bending		Loaded in compression	
Hole diameter (mm)	Plate thickness (mm)	Normalized far field failure strain	Failure mode	Normalized far field failure strain	Failure mode
6	4.16	1.00	c+t	0.53	c
6	8.32	0.86	c+t	–	–
25	4.16	0.67	t	0.48	c
25	8.32	0.74	t	–	–
Impact energy (J)		Impacted side loaded in compression			
35	4.16	0.70	c	0.35	db
35	8.32	0.92	c	0.75	c
		Impacted side loaded in tension			
35	4.16	0.64	db	–	–
35	4.16	1.07	t	–	–

c compressive, *t* tensile, *db* delamination buckling

damage subjected to bending loads will result in an even more complicated problem as the laminate is subjected to both compressive and tensile stresses from the mechanical loads in combination with three-dimensional stress concentrations from the damage. Consequently it can be assumed that changes of the geometry can affect both failure load and failure mode. All results are summarized in Table 10.1.

10.3.1 Bending Tests of Impacted Laminates

As seen in Table 10.1, the failure strain is lower when the impacted side of the 4 mm laminate is loaded in tension. This effect can be explained by the fact that the impact damage resulted in larger delaminations on the back side of the thin specimens as well as a residual local geometric deformation of the panel which facilitated delamination buckling of the specimen. On the other hand, specimens with the impacted side loaded in compression typically failed in compression.

In contrast, the thick specimens with the impacted side loaded in compression failed at lower strain than those with the impacted side loaded in tension, see Table 10.1. This result reflects the difference in damage distribution through the thickness observed for the 8 mm laminates compared to the 4 mm laminates. In the 8 mm laminates damage has only been detected close to the impacted surface, i.e. the part loaded in compression when the impacted side is loaded in compression.

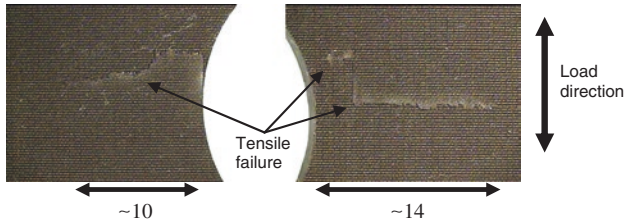


Fig. 10.4 Initiation of tensile failure at the hole boundary

For comparison, compressive tests were performed on impacted specimens with both 4 and 8 mm thickness. The compressively loaded 8 mm specimens show approximately twice the failure strain as the 4 mm specimens.

10.3.2 Bending Test of Notched Laminates

The notched laminates with 25 mm hole were tested in bending and in compression in the same test rigs as the impacted laminates. The procedure during the bending tests were to load the specimens until a significant drop in load was recognized.

As seen in Table 10.1 there is a difference in failure mode between specimens with 6 mm hole and 25 mm hole as the specimens with the larger hole in general failed in tension, whereas specimens with 6 mm hole typically failed in tension and compression.

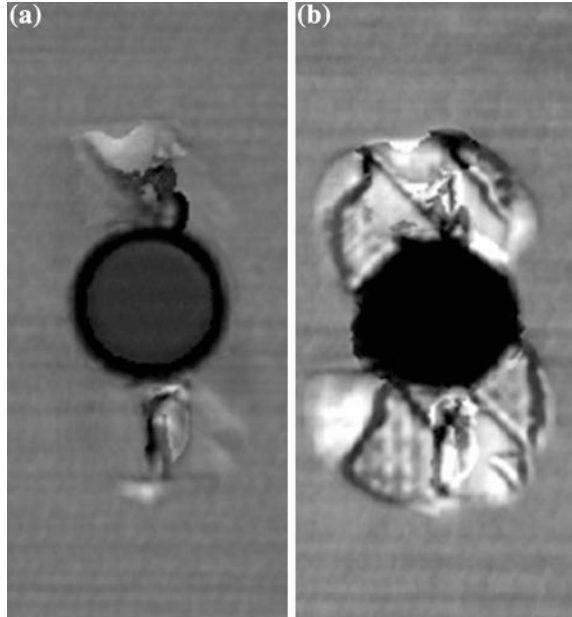
Bending test of the first 4 mm specimen with 25 mm hole was interrupted when clear indications of damage initiation was seen on the load-displacement curve, as well as indications of damage growth could be heard. As seen in Fig. 10.4 tensile failure has started to grow at the hole boundary in the interrupted test.

10.3.3 Fractographic Results

Some results of the fractographic analysis carried out are depicted in Fig. 10.5. Delaminations were observed between multiple layers at the tension loaded side (between layers 1–2, layers 2–3, layers 4–5, layers 7–8 and layers 9–10).

From the ultrasonic C-scan study, the size and the direction in which the damage propagates are clearly identified. Figure 10.5b shows an extensive delamination damage area at the second interface, i.e. between 90° and 45° layers. Delamination have grown in the transverse direction to the load, with a delaminated area extended 20 mm from the hole edges at a maximum load of 3.9 kN of the 4 mm thick and 150 mm wide specimen.

Fig. 10.5 **a** Damage observed by ultrasonic C-Scan microscopy at interface 1 and **b** interface 2



10.4 Conclusions

Four point bending tests on specimens with a 35 J impact damage were performed and, for comparison, the same type of specimens were tested in compression. After impact, the damage were characterised using ultrasonic C-scan, and a couple of specimens were also subjected to fractographic analysis. The impacted specimens were tested with both the impacted side loaded in tension and in compression.

As expected the impact damage were more extensive in the thin laminates than in the thick laminates. The damage in the thin laminates were also distributed through the whole thickness, whereas the damage in the thick laminate only could be detected in the upper third of the laminate.

For the thin laminates a 10 % lower failure load was observed when the impacted side was loaded in tension, i.e. the back side with largest delaminations where loaded in compression. For this loading condition the failure was typically delamination buckling, whereas compressive failure was observed when the impacted side was loaded in compression.

For the thick laminates a 15 % lower failure load was recognised when the impacted side, with delaminations, was loaded in compression.

The failure load is more reduced when the side with the larger damage is loaded in compression. As the damage was more extensive in the thin laminates a 40 % higher far field failure strain was obtained in the thick laminates when impacted side loaded in tension.

As expected the far field strain at failure is considerable higher at bending compared to in-plane compression loading. The calculated failure strain of the compressive loaded impacted thin laminates is approximately 45 % lower than the failure strain of the impacted specimens loaded in bending with the impacted surface loaded in tension. The calculated failure strain of the compressive loaded thick laminates is approximately 19 % lower than the laminates loaded in bending with the impacted side loaded in compression.

An expected effect of hole size on the bending strength has been observed as the failure strain of the thin laminates with 25 mm hole was only 65 % of the failure strain of the laminates with a 6 mm hole. Corresponding number for the thick laminates is that the laminate with 25 mm hole has 85 % of the strength of the laminate with a 6 mm hole.

The effect of laminate thickness is however somewhat contra dictionary as for laminates with 25 mm hole resulted in a 10 % higher failure strain for the thick laminates. Whereas for laminates with 6 mm hole the thinner laminates showed a 15 % higher failure strain. However it should be noted that the specimens with 25 mm hole failed in tension, whereas the specimens with 6 mm hole failed in compression and tension.

The calculated failure strain of the compressive loaded thin laminates with 6 mm hole was only 55 % of the calculated failure strain of the specimens loaded in 4-point bending. For the specimens with 25 mm hole the compressive failure strain was approximately 70 % of the specimens loaded in 4-point bending.

References

1. Nyman, T.: Fatigue and residual strength of composite aircraft structures. Doctoral thesis, Royal Institute of Technology, ISSN 0280-4646 (1999)
2. Green, B.G., Wisnom, M.R., Hallet, S.R.: An experimental investigation into the tensile strength scaling of notched composites. *Compos. A* **38**, 867–878 (2007)
3. Lee, J., Soutis, C.: Measuring the notch compressive strength of composite laminates: specimen size effects. *Compos. Sci. Tech.* (2007). doi:10.1016/j.compscitech.2007.09.003
4. Soutis, C., Lee, J.: Specimen size effect on the notch sensitivity of composite laminates loaded in compression, In: 16th International Conference on Composite Materials ICCM16 (2007)
5. Lee, J., Soutis, C.: Thickness effect on the compressive strength of T800/924C carbon fibre-epoxy laminates. *Compos. A* **36**, 213–227 (2005)

Chapter 11

Buckling and Collapse Tests Using Advanced Measurement Systems

Richard Degenhardt

11.1 Introduction

For the validation of new design methods reliable data from experiments are needed. This chapter focuses on the experimental activities performed at the buckling test facility of the DLR Institute of Composite Structures and Adaptive Systems. It presents the working of the buckling test facility, the advanced measurement systems, which are running in parallel to the tests, and gives exemplarily test results. The test results presented were performed on a stringer stiffened panel, which is understood as a section of a cylinder (e.g. fuselage) and on one unstiffened cylinder which is related to space applications. The load case considered for the investigations presented is axial compression under static loading. However, it must be mentioned that the buckling facility has the capability to test structures also under internal pressure and shear by static loading as well as axial compression under dynamic loading. To get as much as possible results from the experiments advanced measurement systems as ultrasonic inspections, high-speed cameras, thermography or lamb-waves are applied.

The results presented were achieved in different research activities at DLR. More details to test and project results can be found in [1–8]. The measurements on thermography were performed in co-operation with the University of Stuttgart. More details on their publications are given in [9–11].

R. Degenhardt (✉)

DLR (German Aerospace Center), Lilienthalplatz 7, 38116 Braunschweig, Germany
e-mail: Richard.Degenhardt@dlr.de

11.2 Definitions

The terms *buckling*, *postbuckling* and *collapse* used in this chapter are explained in the following based on experimental results of a stiffened panel. Figure 11.1 illustrates a realistic (experimentally measured) load-shortening curve of an axially compressed stiffened CFRP panel tested at the DLR buckling test facility representing a stringer dominant design. It explains the terminology of three remarkable load levels. The lowest one usually provokes the first local buckling where the buckling mode is restricted to local skin buckles between the stringers. The second level causes the first global buckling which is stringer based-buckling. The highest load level is reached at collapse. The other curve is a simplified representation of the real load-shortening curve with knees at these characteristic load levels.

First local buckling: This is the onset of buckling of the skin between the stiffeners. It is represented by several small local buckles and occurs in stiffened aerospace structures usually as the first buckling mode (before first global buckling). At this point there is a slight knee in the load-shortening curve and the axial stiffness is slightly decreased.

First global buckling: This is the onset of buckling of the stiffeners. It is represented by a global buckle of the structure and also a larger knee in the load-shortening curve. Typical aerospace structures are usually stringer dominant and show here a larger decrease of the axial stiffness. For these kinds of structures the first global buckling load is usually beyond the first local buckling load.

Collapse: Collapse is specified by that point of the load-displacement-curve where a sharp load decrease occurs. This is usually the maximum value of the load carrying capacity.

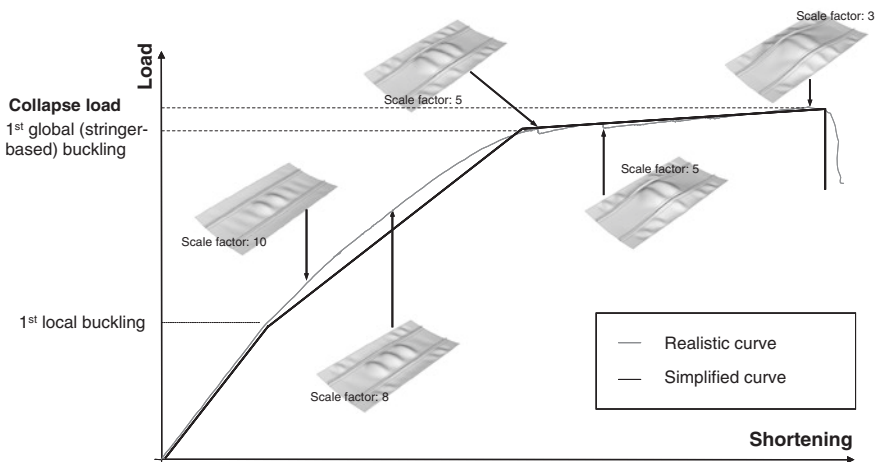


Fig. 11.1 Realistic and simplified load-shortening curve of an axially compressed stiffened CFRP panel

Postbuckling: The area between the first buckling load (usually first local buckling) and the collapse load is called postbuckling area.

For *unstiffened cylinders* the definitions are in principal the same. However, one does not distinguish between local and global first buckling because there are no stiffeners. The *first buckling* can be characterized by some local buckles or by buckles distributed around the cylinder, depending on homogeneity of load introduction and test structure. After first buckling there is usually a significant decrease of the load in the load-shortening curve. *Collapse* is marked by maximum load value of the load-shortening curve, and the *postbuckling* area is that after first buckling.

11.3 DLR Buckling Test Facility

New design methods or new software tools in the engineering have to be validated by test results. In addition, stochastic approaches require comprehensive data bases. In order to achieve suitable results appropriate test facilities and measurement systems, but also experience is needed. In the following, facilities and procedures are listed as currently used at DLR.

The buckling test facility is the main instrument to investigate buckling phenomena and to validate software simulations. Figure 11.2 shows on the left the axial compression configuration and on the right the compression-shear-configuration of the DLR buckling test facility. The test facility can be changed from one configuration to another according to the test requirements.



Fig. 11.2 DLR's buckling test facility, axial compression configuration (*left*), compression-shear-configuration (*right*)

The axial compression configuration is best suited for investigation of imperfection sensitivity on cylindrical structures. All parts of the test device are extremely stiff. The test specimen is located between an axially supporting top plate and a lower drive plate. The top plate can be moved in vertical direction on three spindle columns in order to adapt the test device to various lengths of test specimens. Due to the great sensitivity of stability tests against non-uniform load introduction even the small necessary clearance inside the spindle drives is fixed during the tests by automatically operating hydraulic clamps. The top plate functions as a counter bearing to the axial force that is applied to the movable lower drive plate by a servo-controlled hydraulic cylinder. The drive plate acts against the specimen, which itself acts against a stout cylindrical structure that is meant to distribute the three concentrated forces coming from three load cells at its upper surface, into a smooth force distribution. The test specimen is placed between the load distributor and the drive plate. Although the test device and test specimen are manufactured with particular care one cannot expect, that the fixed upper plate and the load distributor are perfectly plane and parallel to each other, nor can one expect the end plates or clamping boxes of the test specimen to be perfectly plane and parallel. To make sure, that the test specimen will be uniformly loaded, thin layers of a kind of epoxy concrete, i.e. epoxy reinforced with a mixture of sand and quartz powder, are applied between the end plates or clamping boxes of the test specimens and the adjacent parts of the test device. This has the side effect of securing the test specimens against lateral displacement. In order to determine the offset of the load measurement it is required, that at least one side of the specimen may be separated temporarily from the test facility. This is achieved by using a separating foil between the top plate and the upper epoxy layer. Two displacement transducers (LVDT) are used to measure axial shortening of the specimen during the tests. Their signals are recorded and, moreover, used for control purposes as actual values. Hence, the test device is displacement controlled. According to the particular arrangement of the transducers the elastic deformation of the test device does not influence the control by shortening at quasi-static loading. Table 11.1 summarizes the characteristics of the test facility.

Table 11.1 Characteristics of the DLR buckling test facility

<i>Load case</i>	
Axial compression	Max. 1,000 kN
Torsion	Max. 20 kNm
Internal pressure	Max. 800 kPa
External pressure	Max. 80 kPa
Shear	Max. 500 kN
<i>Geometry limits of the test structure</i>	
Length	Max. 2,100 mm
Width (diameter)	Max. 1,000 mm
<i>Load frequency (axial compression only)</i>	Max. 50 Hz

11.4 Preparation of the Test Structures

After the manufacturing process the preparation of the test-structure up to the test plays an important role to ensure reliable and high quality experimental data. In the following the preparation process performed at DLR is described. Some steps using advanced measurement systems (cf. Sect. 11.5) as full scale thickness measurement or imperfection measurement may not be in all cases—from the authors point of view—required if for instance imperfection sensitivity is not expected to play a major role.

- Ultrasonic inspection to examine the quality of the panel (cf. Sect. 11.5)
- Thickness measurement
 - Measurement of single points (simple and fast) or
 - Full scale measurement (cf. Sect. 11.5)
- Casting of the panel into preliminary end boxes, hardening of the end blocks
- Detaching from the boxes
- Milling of the end block edges (to obtain a full loading contact of the circumferential edges of the panel)
- Measuring of the imperfection with ATOS (cf. Sect. 11.5)
- Application of longitudinal edge supports (if foreseen)
- Application of strain gauges
- Stress free casting into final end boxes
- Connection of the strain gauges to cables
- Application of sensors for the Lamb-waves method (cf. Sect. 11.5)
- Assembling to the buckling test facility

Figure 11.3 shows as example some preparation stages of a typical panel similar to the panel P29 for which test results are presented in Sect. 11.7. As shown in Fig. 11.3 (left) the panel was subsequently encased using epoxy resin with filler. The centre picture displays the panel after the application of strain gauges and wiring. The schematic drawing in Fig. 11.3 (right) depicts the exact location of strain gauges and of the actuators for the lamb-waves measurement (cf. Sect. 11.5).

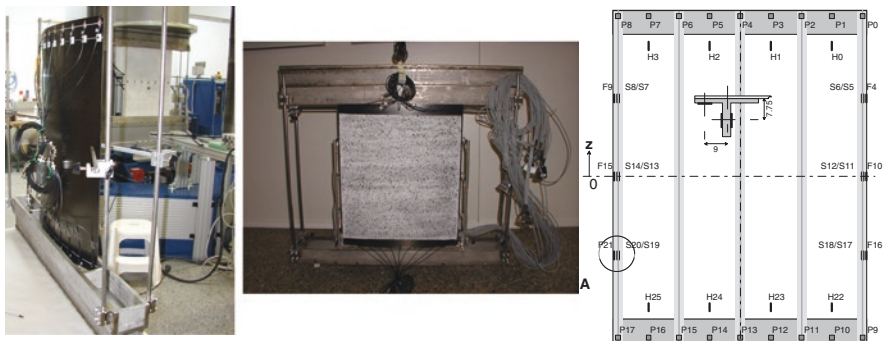


Fig. 11.3 Preparation of the panel and schematic drawing of sensor locations

11.5 Advanced Measurement Systems

Running stability tests is an expensive task. Further, testing the structures until collapse can be performed only once. In order to get as many results as possible (e.g. information about degradation of skin-stringer separation) already during the tests or even to perform a 360° full scale deformation measurement highly advanced measurement systems are applied before and during the tests.

11.5.1 Before the Test

11.5.1.1 Non-destructive Testing and Thickness Measurement

The automatic ultrasonic testing of CFRP structures using water split coupling depicted in Fig. 11.4 is applied to detect any defects in the structure (e.g. delaminations). The left and middle graph of Fig. 11.13 show as an example the flaw echo of the panel P29 (cf. Sect. 11.7) where almost no inhomogeneity in the lamina as well as at the stringer-skin interface can be found. The same test method can be utilized for full field thickness measurement. The test is carried out with a broadband transducer in echo-technique and the results are displayed in a D-scan.

11.5.1.2 ATOS System—Optical Measurement of Imperfections

In order to identify the real shape of the skin of the test-structure, ATOS, an optical 3D digitizing measurement system (based on photogrammetry), is utilized to extract the actual radius of the panel as well as the initial geometric imperfections of the skin utilizing a best-fit procedure. Differences between the nominal and measured structure can for instances be due to snap-back effects during the manufacturing process. As one result the right graph of Fig. 11.3 shows the false colour rendering (in

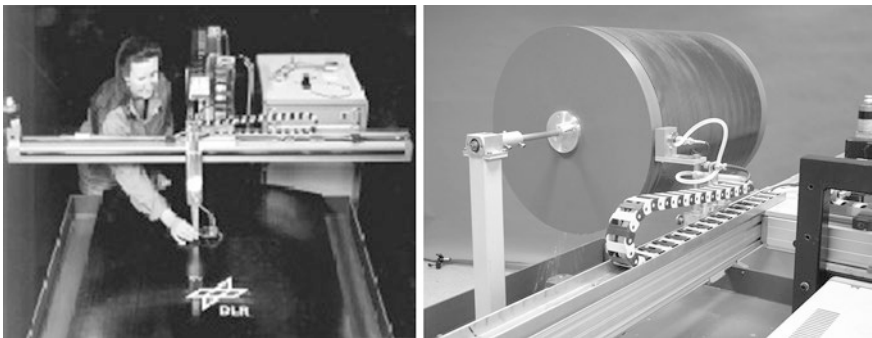


Fig. 11.4 Stationary ultrasonic equipment (*left*) and ultrasonic test setup for cylinders (*right*)

black and white) as aberration with respect to the perfect panel P29 (cf. Sect. 11.7). This deviation can not only be used as a qualitative estimate of the panel geometry, but it also can be introduced as imperfections within the nonlinear analysis.

11.5.2 During the Test

During testing a mixture of conventional (e.g. strain gauges) and advanced (e.g. ARAMIS, thermography) measurement systems are applied. At the beginning, after calibration of the test set-up, the test-structure is loaded by three cycles up to about 50 % of the expected linear buckling load in order to compensate possible settlements, followed by loading until the load level planned (e.g. collapse). The load and the respective shortening, the strains, the displacement field of the skin, single transverse displacements of the stringer blades are measured and video records are taken. The strains are measured by strain gauges at different positions and directions. The displacement field of the skin is gauged by the ARAMIS system, which is based on an optical 3D digitising method [12]. In order to measure the degradation of the skin-stringer connection the following three methods, which are described in the next sections in detail, are applied: Lamb-waves, optical lockin thermography and the High-Speed ARAMIS-system. During testing load and shortening are measured as global values of the structural behaviour. Three load cells are located between drive plate and load distributor, the applied load is calculated as the sum of the three loads. Two displacement pickups are mounted between load distributor and top plate. The shortening is calculated as the average of the measured displacements. The pickups also serve for displacement control of the servo-hydraulic cylinder. So the deformations of the test facility, in particular of the load cells, are settled. In the following the advanced measurement systems are described in more detail.

11.5.2.1 ARAMIS System—Optical Measurement of Deformations

For components to be integrated into structures and assemblies it is necessary to test its deformation behaviour under special load conditions. It can be performed by using optical metrology. In order to obtain precise results on dynamics of buckling deformations a high speed optical grating system ARAMIS was established in the Institute of Composite Structures and Adaptive Systems (available since 2003). Based on a former standard system the new ARAMIS-concept was designed in co-operation with the German company GOM GmbH ('Gesellschaft für Optische Messtechnik'), situated in Braunschweig. The standard ARAMIS system records an object under load using a pair of CCD cameras. Prior to the test the surface of the test object must be prepared by a thin layer of a grey-scale pattern. The object surface is divided in a grid of facets the size of which must be represented by at least 7×7 pixels of the CCD. After the loading process, the 3-dimensional (3-D) coordinates of the centres of these facets are calculated offline on the basis of



Fig. 11.5 Stationary ultrasonic equipment (*left*) and ultrasonic test setup for cylinders (*right*)

digital image processing, additionally delivering the all-over 3-D displacements. The accuracy of the displacement measurement is about a twentieth of the pixel distance of the cameras. A resolution of 500 pixels for a specimen size of 500 mm, e.g., would result in a displacement accuracy of 50 μm . In contrast to most other optical systems for all-over displacement measurement ARAMIS accepts very large displacements, too. With sufficient resolution of the displacement measurement the evaluation of longitudinal and transverse strain distributions is possible. The resolution of smaller object surfaces can be improved by appropriate selection of facet size, facet overlapping, and the grey-scale-pattern.

The new Highspeed-ARAMIS concept includes four fast systems each of which can measure the 3-dimensional deformation field of an object by applying fast digital cameras with a max. speed of 1,000 images/s. Figure 11.5 illustrates the test setup with four individual camera pairs in the buckling test facility. When coupled all with the same part of the specimen surface these systems can enable measurements of up to 4,000 images/s by fast switching through the camera pairs by a special electronic trigger box. For this purpose the frames of the different systems are grabbed and offline attached to a repeated sequence.

As a second opportunity of coupling the four ARAMIS systems the cameras can aim different areas of an object. With adjacent areas the observed area is expanded. By observation from different directions the full field survey of the surface of a 3-D object is possible. This opportunity includes measuring front and back side surface of a panel and all-over circumference survey of a cylinder.

At this point, all measured full field displacements are transferred to a global coordinate system of the cylinder by means of at least three reference points in each area. The reference points are allocated to the global coordinate system by TRITOP, another photogrammetric system. The result of this procedure is a complete 3-D visualisation of the cylinder deformation (cf. Fig. 11.6 left). A 360° survey of a CFRP cylinder (selected deformation patterns of one loading and unloading sequence) is presented in Fig. 11.7. The four camera pairs can also be placed on one part of the structure which allows a quadruplicating of the number of taken pictures per time (Fig. 11.6 right).

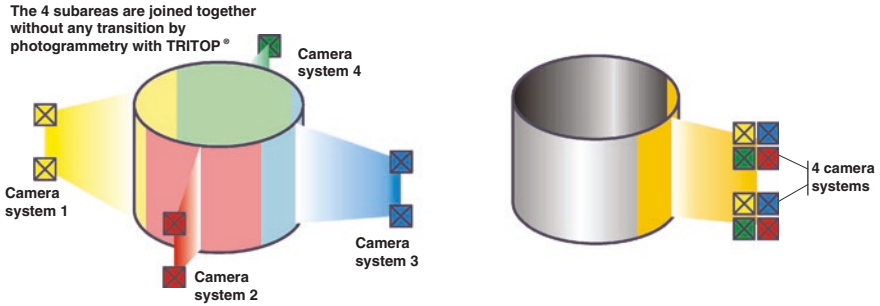


Fig. 11.6 360° measurement on a cylinder (left) and high speed ARAMIS set-up (right)

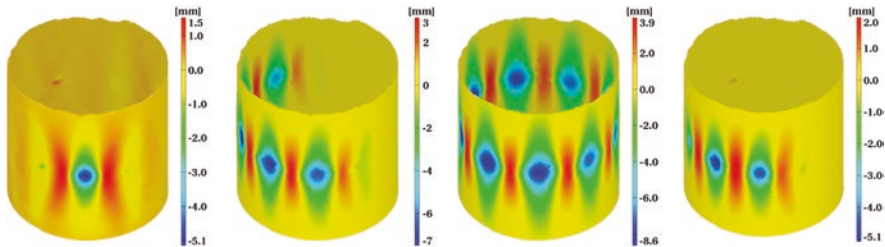
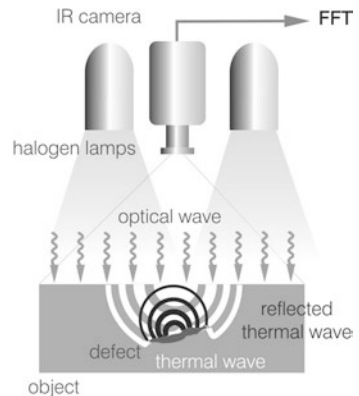


Fig. 11.7 Results of a 360° measurement on a CFRP cylinder (selected deformation patterns of one loading and unloading sequence)

11.5.2.2 Thermography—Measurement of Degradation

The thermography measurements at the DLR are performed by the Institute of Polymer Technology (IKT) of the University of Stuttgart using optically activated lockin thermography (OLT). OLT is being used for several years for remote non-destructive testing. It is based on propagation and reflection of thermal waves which are launched from the surface into the inspected component by absorption of modulated radiation (cf. Fig. 11.8). Phase angle images obtained by superposition

Fig. 11.8 Principle of optical lockin thermography (OLT) in reflection mode [Source institute of polymer technology (IKT), University of Stuttgart]



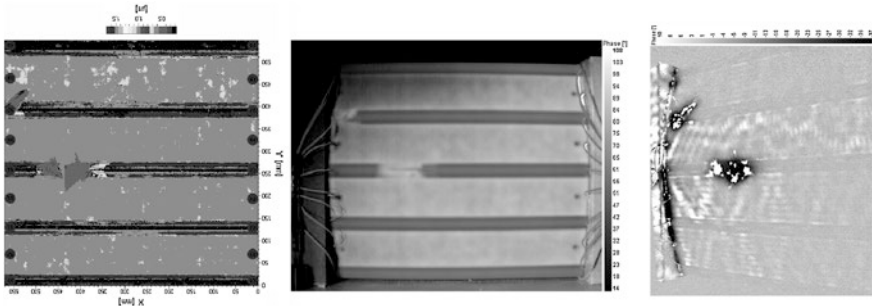


Fig. 11.9 NDT of one stiffened CFRP panel (*left* US inspection, *centre* OLT, *right* ULT)

of the initial thermal wave and its reflection display defects and hidden structures down to a certain depth underneath the surface. The thermal diffusion length μ depends on the lockin frequency f :

$$\mu = \sqrt{\alpha/(\pi f)} \tag{11.1}$$

(α thermal diffusivity of the specimen). For details see [9, 10]. The lockin-frequencies used for these measurements vary from 0.1 to 0.5 Hz. This suffices to get information through the specimen to the rear side, as can be seen in Fig. 11.9 (centre image).

Another technique uses ultrasound for thermal excitation: A defect leads to locally enhanced mechanical losses and consequently selective heating up. A better signal-to-noise ratio is achieved by using the lockin technique. Therefore, this method is called ultrasound activated lockin thermography (ULT). The image in Fig. 11.9 (right) shows a phase image measured after the mechanical test. One substantial difference compared to OLT images is that ULT is defect selective: Only defect areas are displayed, whereas in OLT images the inner structure of the specimen is visible.

Preliminary results are promising. Figure 11.9 shows detected damages of skin-stringer separation of one DLR panel measured after the collapse test. The left figure was obtained from standard ultrasonic inspection. OLT (center image) and ULT (right image) results are in good agreement with the results of conventional ultrasound testing. More details are given in [11].

11.5.2.3 Lamb-Waves—Measurement of Degradation

Acousto Ultrasonics with Lamb-Waves can be utilized to characterize damages in CFRP structures. For this kind of Structural Health Monitoring (SHM) piezo-patches, which are working as senders as well as receivers, are glued at the structures. The main advantages are that lamb waves can penetrate large areas and, in comparison to standard US inspections, no time consuming scanning is necessary. For the measurement one selected piezo-patch excites a Lamb-wave which is received by the others. If a structure is damaged, the response is different.

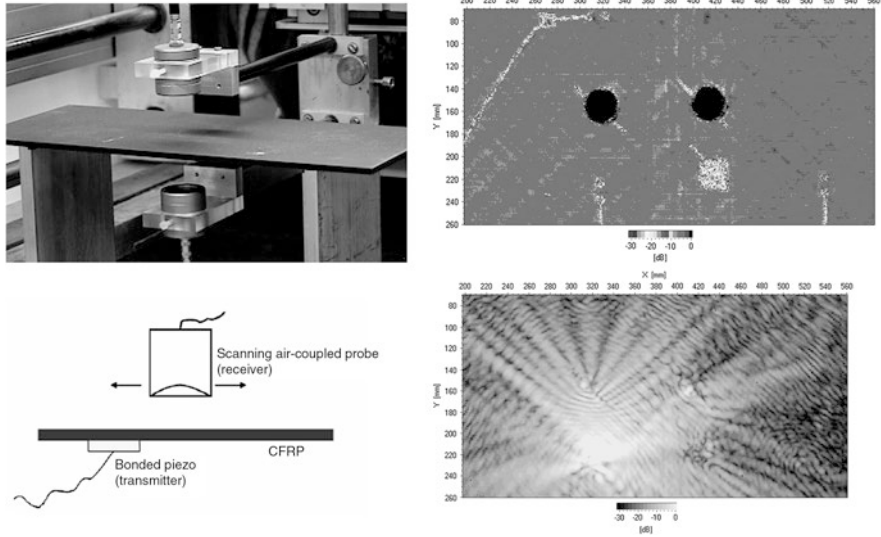


Fig. 11.10 CFRP-specimen

However, it must be mentioned that it is still under research to interpret the results and to conclude to the position and kind of damage.

Figure 11.10 shows air-coupled ultrasonic inspection and the visualisation of the Lamb wave propagation (including interaction with defects) of the same CFRP-specimen. The challenge for the future is to conclude from this different answer to the place and also the kind of damage. In addition, damages can be detected and monitored in complex structures, where the applied patches are used as transmitters and receivers. However, for each frequency at least two different wave modes exist and each mode is dispersive. Therefore, the modes have to be carefully optimised for different types of damage and for the material of the component. Figure 11.11 shows as an example the results of the Lamb-waves measurement of one sensor before and after a collapse panel test. It can be seen that a clear difference was measurement. The next challenge will be to conclude from the result to the kind and position of damage.

11.6 Material Properties

The prepreg material IM7/8552 (Hexcel) was used in several research projects. Although the properties for that kind of material are known from the producer [13], for each project an own test series on small specimens was performed in order to obtain real material properties used in the project and in order to have more information real about the sensitivity and reliability of the material properties for the selected prepreg system. The testing methodology followed the procedure given in the German standard DIN 29971. Table 11.2 gives a summary of the test

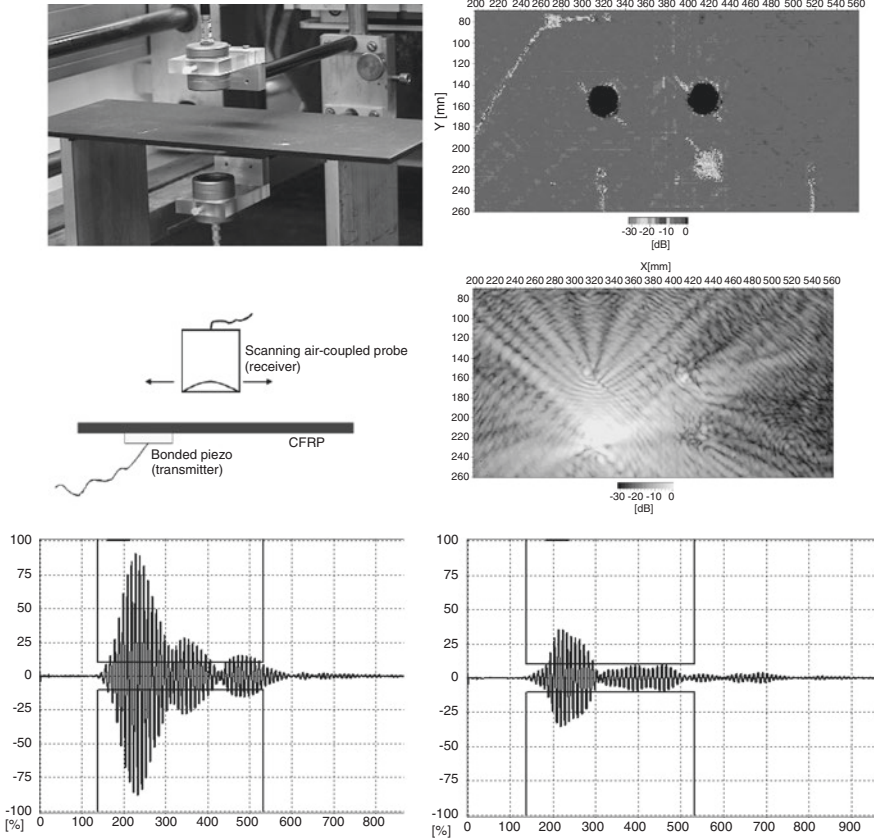


Fig. 11.11 Results before (*left*) and after test (*right*) of one sensor using the lamb-waves method—differences due to damages

results for the stiffnesses and strength values with the corresponding standard deviations. The test procedure was in all cases under the same conditions, however, the material was manufactured by different partners. This is likely the reason for differences between the mean values or standard deviations.

11.7 Test Results

11.7.1 Cyclic Tests and Collapse Test of a Stiffened Panel

The following test results were obtained within the finished COCOMAT project [2] on the panel P29 manufactured by AERONNOVA and tested by DLR. Panel P29 is one validation design which is not pre-damaged and which was loaded first

Table 11.2 Material properties of CFRP prepreg IM7/8552 UD

	POSICOSS		COCOMAT		ESA study		Hexcel
	Mean value/standard deviation						Data-sheet
Stiffness	(GPa)	(%)	(GPa)	(%)	(GPa)	(%)	(GPa)
E_{tL}	192.3	1.17	164.1	3.09	175.3	1.38	163
E_{cL}	146.5	1.84	142.5	1.69	157.4	2.39	150
E_{tT}	10.6	2.36	8.7	3.91	8.6	2.9	12
E_{cT}	9.7	6.77	9.7	4.85	10.1	4.11	–
G_{LT}	6.1	2.28	5.1	13.58	5.3	1.10	–
Poisson’s ratio	–	(%)	–	(%)	–	(%)	–
$\nu_{LT(t)}$	0.31	5.55	0.28	13.49	–	–	–
Strength	(N/mm ²)	(%)	(N/mm ²)	(%)	(N/mm ²)	(%)	(N/mm ²)
R_{tL}	2,715	3.42	1,741	11.92	2,440	3.64	2,724
R_{cL}	1,400	4.93	854.7	9.04	1,332	7.24	1,690
R_{tT}	56	18.56	28.8	18.08	42	26.45	11
R_{cT}	250	6.60	282.5	5.11	269	5.98	–
R_{LT}	101	4.55	98.2	17.54	129	0.84	120

t tension, *c* compression, *L* longitudinal direction, *T* transverse direction

Table 11.3 DLR panel P29: nominal and measured data

Geometry/lay-up	Nominal	Measured
Panel length	$l = 780$ mm	$l = 780.5$ mm
Free length (buckling length)	$l_f = 660$ mm	$l_f = 660$ mm
Radius	$r = 1,000$ mm	$r = 848$ mm
Thickness	$t = 1$ mm	$t = 0.98$ mm
Arc length	$a = 560$ mm	$a = 560.5$ mm
Number of stringers	$n = 5$	$n = 5$
Distance stringer to stringer	$d = 132$ mm	$d = 132$ mm
Distance stringer to longitudinal edge	$e = f/2 = 16$ mm	$e = 16.2$ mm
Laminate set-up of skin	$[90, +45, -45, 0]_s$	
Laminate set-up of stringers blade	$[(+45, -45)_3, 0_6]_s$	
(cf. Fig. 11.14) flange	$[(45, -45)_3, 0_6]$	
Ply thickness	$t = 0.125$ mm	
Stringer thickness	$t = 3$ mm	$t = 2.9$ mm
Stringer height	$h = 14$ mm	$h = 14.3$ mm
Stringer width	$f = 32$ mm	$f = 32$ mm
Panel mass, g		1,238 g

3,700 times by cyclic loading and finally until collapse. Table 11.3 summarises the nominal and measured data of this panel. The geometry of the stringer is illustrated in Fig. 11.12. Material properties are given in Table 11.2.

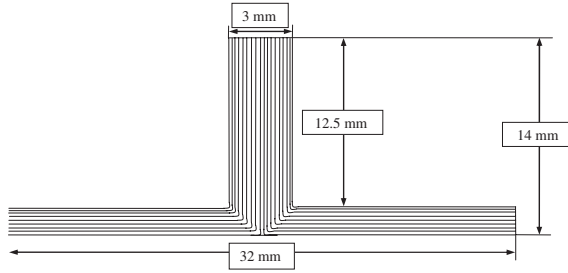


Fig. 11.12 DLR panel P29—stringer type

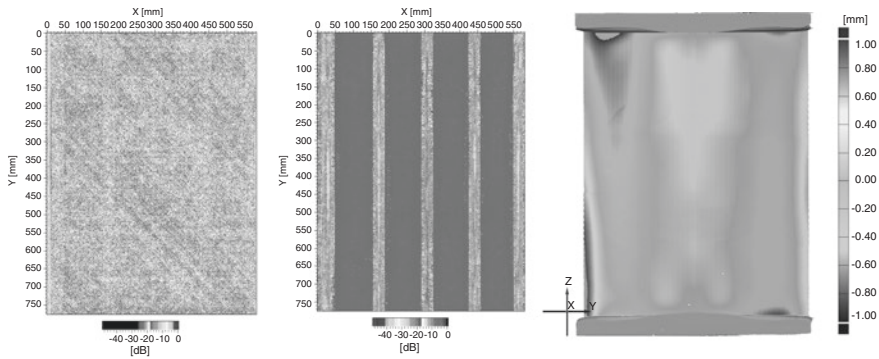


Fig. 11.13 DLR panel P29—ultrasonic flaw echo (*left + middle*), measured imperfections (*right*)

Before the test the panel was investigated by ultrasonic inspection and ATOS—the optical measurement system determining best-fit radius and imperfection. Figure 11.13 (left + middle) shows the flaw echo of the panel where almost no inhomogeneity in the lamina as well as at the stringer-skin interface can be found. Figure 11.13 (right) illustrates by shade rendering the deviation of the real shape from the shape of the perfect panel. During the test the panel was loaded statically and displacement-controlled by axial compression at 3 different load steps:

1. 2,000 load cycles until the shortening of $u = 1.08$ mm (80 % of expected collapse)
2. 1,700 load cycles until the shortening of $u = 1.93$ mm (95 % of expected collapse)
3. 1 step until collapse

During the test the load-shortening curve, strains using strain gauges and full-scale deformations using the ARAMIS systems were monitored. Figure 11.14 shows the load-shortening curve, strain-shortening curve of one selected strain gauge and out-of-plane deformations at 3 different levels. Picture A is just after first local buckling with small skin buckles between the stringers, Picture B is

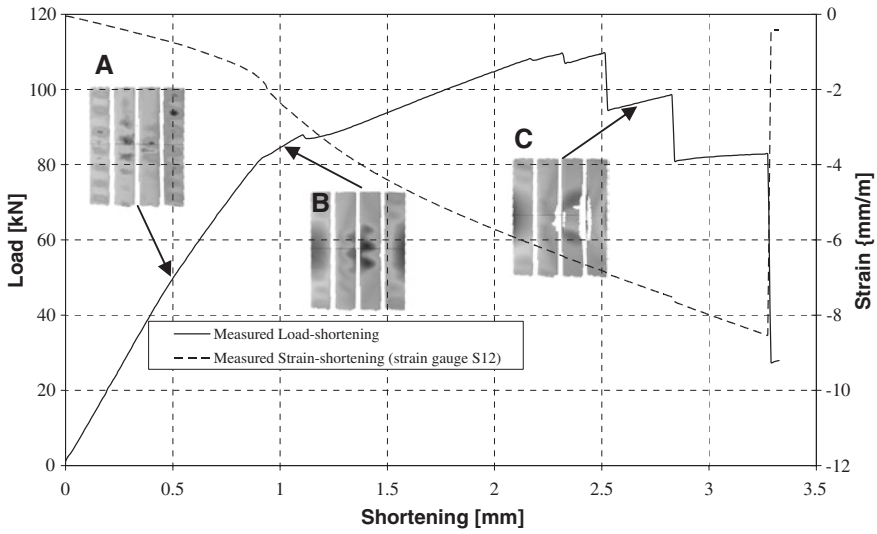


Fig. 11.14 DLR panel P29—test results

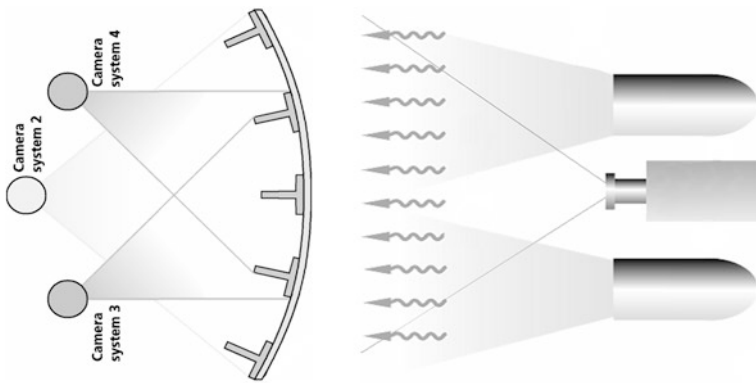


Fig. 11.15 Schematic drawing of the test setup [ARAMIS (left) with and lockin thermography (right)]

just after first global buckling and Picture C after collapse. To get information about the progress of degradation of skin-stringer separation the Lamb-waves method and Optical lockin thermography method were applied every 400 cycles. Figure 11.15 shows the position of the thermography equipment for the measurement from skin-side of the panel and the ARAMIS system for the measurement from stringer-side of the panel. After the first load step of 2,000 cycles no skin-stringer separation was observed. The cyclic loading process was almost elastic. In the second load step after about 400 cycles the stringers began to separate

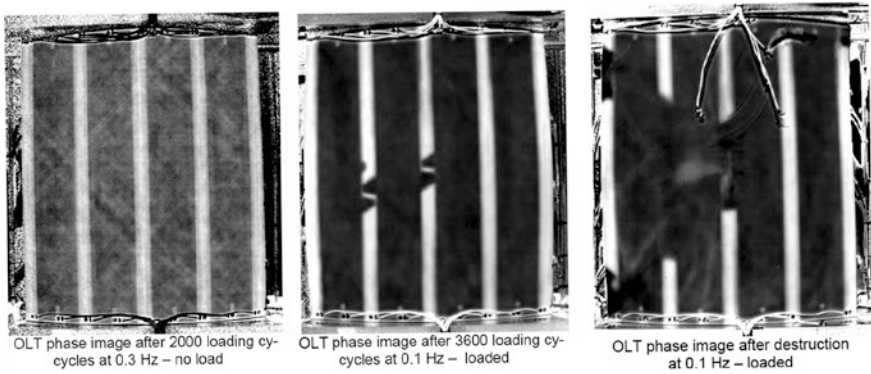


Fig. 11.16 DLR panel P29—thermographic measurements before, during and the after the collapse test

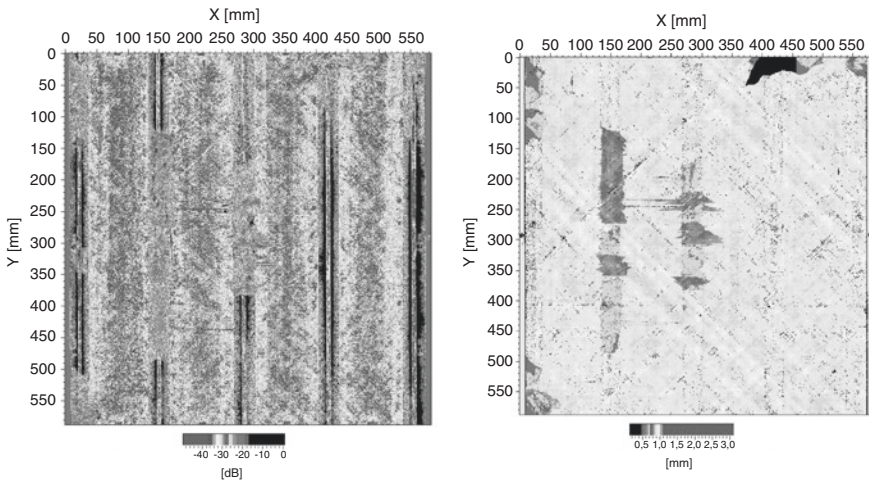


Fig. 11.17 DLR panel P29—ultrasonic inspection measurements after the collapse test

partly from the skin. The area of separation was growing during the cycling process. The optical lockin thermography proved to be excellent for monitoring that kind of degradation already during the loading process. Figure 11.16 shows pictures with measured results after 2,000 cycles (left), where no damages are visible, after 3,600 cycles (middle), where clear areas of separation between skin and stringer are visible, and after collapse (right), where the structure is damaged in larger areas. Figure 11.17 shows echo flows obtained by ultrasonic investigations after the collapse test. The damaged area of the skin-stringer separation is clearly visible and agrees well with the measurement of the lockin thermography of Fig. 11.16 (right).

Table 11.4 DLR Cylinder Z07: nominal and measured data

Geometry/lay-up	Nominal	Measured
Total length	$l = 530 \text{ mm}$	$l = 530 \text{ mm}$
Free length	$l_f = 510 \text{ mm}$	$l_f = 510 \text{ mm}$
Radius	$r = 250 \text{ mm}$	$r = 248.5 \text{ mm}$
Thickness	$t = 0.5 \text{ mm}$	$t = 0.51 \text{ mm}$
Lay-up	+24, -24, +41, -41	
Cylinder mass, g		638 g

11.7.2 Buckling Test of an Unstiffened Cylinder

This section shows test results of the selected unstiffened imperfection sensitive cylinder Z07 to demonstrate the measurement results. With an ESA study 10 additional unstiffened imperfection sensitive cylinders of the same design were tested. The reason for the choice of that design was the high imperfection sensitivity and a large value of slenderness which allows achieving a preferably small knock down factor. This was the first cylinder tested at DLR on which the 360° full scale measurement of deformation by means of ARAMIS was applied. Table 11.4 summarises the nominal and measured data of the cylinder Z07. Material properties are given in Table 11.2.

Before the test the cylinder was investigated by ultrasonic inspection in order to assure that there are no major inhomogeneities in the laminate. Next the cylinder was inspected by the ATOS system to measure the shape imperfections. During the test the cylinder was loaded by axial compression just beyond the buckling load and was then unloaded. In that loading area the structure behaves elastically and will not be damaged. The full scale deformations and buckling shapes were measured using the ARAMIS-system. Figure 11.18 illustrates the measured

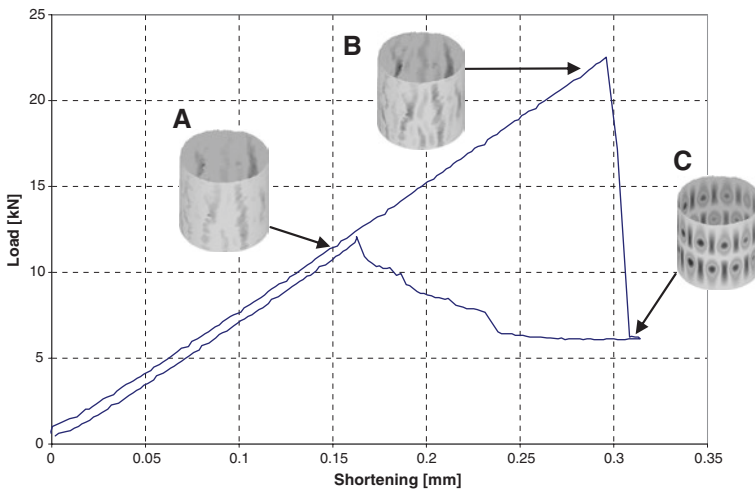


Fig. 11.18 DLR cylinder Z07—test results

load-shortening curve with 3 selected ARAMIS measurement pictures obtained from the 360° measurement. Picture A and B are from the pre-buckling and Picture C from the early postbuckling region. Picture B is just before and Picture C just after the first buckling load.

Additional test results can be found in [7].

Acknowledgments The finished project *COCOMAT* was supported by the European Commission. The finished study *Probabilistic Aspects of Buckling Knock Down Factors* was funded by the European Space Agency (ESA). All support is gratefully acknowledged. The information in this paper is provided as is and no warranty is given that the information is fit for any particular purpose. The reader thereof uses the information at its sole risk and liability.

References

1. Zimmermann, R., Klein, H., Kling, A.: Buckling and postbuckling of stringer stiffened fibre composite curved panels—tests and computations. *Compos. Struct.* **73**, 150–161 (2006)
2. Degenhardt, R., Rolfes, R., Zimmermann, R., Rohwer, K.: COCOMAT—improved material exploitation at safe design of composite airframe structures by accurate simulation of collapse. *J. Compos. Struct.* **73**, 175–178 (2006)
3. Degenhardt, R., Kling, A., Klein, H., Hillger, W., Goetting, Ch., Zimmermann, R., Rohwer, K., Gleiter, A.: Experiments on buckling and postbuckling of thin-walled CFRP structures using advanced measurement systems. *Int. J. Struct. Stab. Dyn.* **7**(2), 337–358 (2007)
4. Degenhardt, R., Kling, A., Rohwer, K., Orifici, A.C., Thomson, R.S.: Design and analysis of stiffened composite panels including postbuckling and collapse. *Comput. Struct.* **86**, 919–929 (2008)
5. Degenhardt, R., Wilckens, D., Klein, H., Kling, A., Hillger, W., Goetting, C.H., Rohwer, K., Gleiter, A.: Experiments to detect the damage progress of axially compressed CFRP panels under cyclic loading. *Key Eng. Mater.* (special volume of) **383**(2008), 1–24 (2009)
6. Wilckens, D., Degenhardt, R., Rohwer, K.R., Zimmermann, R., Kepke, M., Hildebrandt, B., Zipfel, A.: Cyclic buckling tests of pre-damaged CFRP stringer stiffened panels. *Int. J. Struct. Stab. Dyn.* **10**(4), 827–852 (2010)
7. Degenhardt, R., Kling, A., Bethge, A., Orf, J., Kärger, L., Rohwer, K., Zimmermann, R., Calvi, A.: Investigations of imperfection sensitivity of unstiffened CFRP cylindrical shells. *Compos. Struct.* **92**(8), 1939–1946 (2010)
8. Degenhardt, R., Kling, A., Zimmermann, R., Odermann, F., de Araújo, F.C.: Dealing with imperfection sensitivity of composite structures prone to buckling. *Advances in Computational Stability Analysis* (2012). <http://dx.doi.org/10.5772/45810>
9. Busse, G., Wu, D., Karpen, W.: Thermal wave imaging with phase sensitive modulated thermography. *J. Appl. Phys.* **71**(8), S3962–3965 (1992)
10. Wu, D., Busse, G.: Zerstörungsfreie phasempfindliche Modulationsthermographie: Prinzip und Anwendungen, *Materialprüfung* vol. 36, pp. S.393–399. Carl Hanser Verlag, München, (1994)
11. Gleiter, A., Riegert, G., Zweschper, TH., Degenhardt, R., Busse, G.: Advanced ultrasound activated lockin-thermography for defect selective depth resolved imaging. In: 28th Thermosense Conference, Orlando, pp. 17–20 (2006)
12. www.gom.com
13. Hexcel, www.hexcel.com

Chapter 12

Vacuum Infusion Manufacturing of CFRP Panels with Induced Delamination

Vincenza Antonucci and Mauro Zarrelli

12.1 Introduction

Composite materials, used in aerospace and automotive, may be damaged as a result of impacts. These events can occur during the normal service of the structure due to multiple reasons, including contributing factors related to the manufacturing process and material handling. The effect of the damage, though not always welcome, because in most cases generates in inaccessible parts of the structure, can reduce the integrity of the system during its “service life”.

The different types of damage and their effects are the focus of very important research area that involves many aspects of materials science and engineering: the material study, the development of experimental techniques for the damage monitoring and the definition of computational and numerical models for prediction or analysis. The optimal design of composite structures requires the use of numerical tools able to perform accurate stress analysis and predict the mechanical behaviour under specified loading conditions. Therefore, laminated composite plates and shell elements are available in most of commercial finite-element codes in order to simulate the composite mechanical behaviour. In general, several authors focused their attention on the numerical study of the impact behaviour of composites panels by the application of finite element (FE) codes and the development of proper models for delamination or other composite damage mechanisms, such as

V. Antonucci (✉) · M. Zarrelli
National Research Council Italy—CNR, Institute for Polymer,
Composites and Biomedical Materials—IPCB,
p.le Enrico Fermi 1, 80055 Portici, Italy
e-mail: vinanton@unina.it

M. Zarrelli
e-mail: mauro.zarrelli@imcb.cnr.it

matrix cracks, fiber-matrix debond, fiber fractures. However, the proper modelling of laminated composites is a not trivial task and can be still considered an open research problem due to the complex and anisotropic behaviour of composites and due to the presence of complex failure mechanisms. In order to assess the validity of FE models, it is important to perform experimental measurements that can provide useful information to validate the numerical results and can help to develop predictive models for the mechanical behaviour of the composite material.

Hence, it can be understood why one of the main concerns in aerospace and automotive material sciences is the capability to design and realize composite laminates taking into account delamination damages, that are one of most recurrent defect in fiber reinforcement materials. Delamination can be induced both by in-service loads and by incorrect manufacturing procedures. These types of defects are often very difficult to detect through non-destructive inspection and can have a detrimental effect on the structural health of the composite component. Thus, the availability of effective NDE techniques coupled with affordable and effective manufacturing processes can be useful to manage this damage mechanism. Additionally, effective Liquid molding flexible low cost manufacturing techniques together with NDE techniques can be helpful to assess the suitability of numerical tools by realizing and inspecting proper composite panels with artificial delamination defects for validation activities. In this chapter, after an overview on the liquid molding, the experimental manufacturing of different carbon/epoxy composites with artificial defects is described and discussed.

12.2 Liquid Composite Molding Overview

Liquid Composite Molding (LCM) processes, such as Resin Transfer Molding (RTM), Vacuum Assisted Resin Transfer Molding (VARTM), Seemann Composite Resin Infusion Molding Process (SCRIMP), and Fast Remotely Actuated Channeling (FASTRAC), involve the impregnation of a net-shape fiber preform by a polymeric resin to produce a composite structure. The quality of such processes depends on the complete impregnation and consolidation of the dry preforms.

RTM is one of the most efficient and attractive processes of high performance composite materials with low cost manufacturing. The major benefit over other polymer composites manufacturing techniques is the separation of the moulding process and the composite consolidation from the design of the fibre architecture. This allows to the designer to combine different kinds of fibre preform and to produce parts with tailored properties to fit specific mechanical requirements. In fact, liquid moulding enables attainment of high levels of microstructure control and part complexity compared with processes like injection moulding and compression moulding, where the initial fibre distribution changes as consequence of the fibre orientation during the mould filling. Further RTM is a low temperature and pressure process. It is characterized by preforming followed by mould filling and composite consolidation.

It can be schematized into five main steps [1]:

- Preform manufacturing;
- Preform positioning into the mould cavity;
- Resin injection;
- Cure;
- Part removal.

The first phase, preform design and manufacturing, involves the assembly of the fibre reinforcement into a preform that is shaped, oriented and located into the mould cavity. After the mould closing a low viscosity resin is injected. The resin, usually a thermoset polymer, wets the fibres and, ideally after the complete mould filling, polymerises to form the composite part. To activate the cure reaction, the mould and the preform generally are heated. The air is displaced and escapes from vent ports located at the end of the mould. Once the part consolidation is complete, the extraction takes place.

VARTM [2–7] is an attractive composite manufacturing process that requires only one tool side being the other a polymeric flexible bag, as a consequence, it is cheaper than RTM that becomes expensive for the manufacturing of large parts with high fibre volume fraction.

The VARTM process is also appreciated because it eliminates the emission of volatile organic compounds (VOC), which is under increased regulation for the composite industry. The VARTM process consists of stacking a fibrous material, called preform, on a rigid one sided net shaped molding surface and below a bagging film. A vacuum pump extracts the air between the bagging film and the molding surface and compacts the preform. After the fibers compression, the vacuum drives a polymer resin that impregnates the preform. Afterwards the part is cured to form a complete net shaped composite component.

The primary advantage of VARTM is the balance between the low cost and the good quality of the final product. VARTM has several variants, the most known is the “SCRIMP” [8–10] process developed by Seeman Composite’s. In the SCRIMP a permeable distribution medium is placed in direct contact with the dry fiber reinforcement. Thus, the resin flow is eased along the surface and, simultaneously, through the thickness. In general, the ancillaries materials, such as the peel ply, the distribution media and the vacuum bag, are not reusable after the processing cycle. Thus, an high amount of waste is produced. In addition, conversely to RTM, this process exhibit significant through-the-thickness impregnation gradients that may affect the total fiber impregnation, the filling time and, consequently, the dimensions and mechanical properties of the final composite part. Further, due to the use of the flexible vacuum bag and, consequently, due to the variation of compaction pressure, the part thickness and local permeability of the fibre preform change during resin injection as function of time and space [12].

In order to reduce the voids, the thickness variation along the final part and to increase the mechanical properties, new infusion procedures have been investigated and developed [13–15], such as Controlled Atmospheric Pressure Resin Infusion method (CAPRI) and the Double-Bagging techniques [15]. In the CAPRI process, patented by the Boeing Co., the resin feed tank is not exposed to the atmospheric

pressure, but it is connected to an additional vacuum pump, that reduces the pressure in the resin tank. Thus, the reduced pressure differential, combined with a cyclic vacuum debulking of the dry fiber reinforcement, allow to manufacture composites with an higher fiber volume that those produced by SCRIMP. The double vacuum bagging method consists of applying two discrete vacuum bags, an inner bag, next to the laminate, and an outer bag, which is sealed to the tool outside of the sealed inner bag perimeter. In this way, the two main vacuum functions are split, assigning volatiles extraction (removal of entrapped air, ambient moisture and/or solvents) and the resin infusion to the inner bag and, then, using the outer bag for compaction. The resulting composites have a reduced void content beyond that possible with conventional vacuum-bagging regimes [15].

Other infusion techniques have been developed with the objective to reduce the amount of waste material such as Fast Remotely Actuated Channeling (FASTRAC) method [16–18] which adopts a double vacuum bag set-up consisting of a primary vacuum bag sealing the dry preform on a metal plate and a FASTRAC non contacting tool placed over the primary vacuum bag and under a secondary vacuum bag. The FASTRAC non contacting tool has a large number of machined channels that increase the resin flow during infusion.

Before resin injection, the vacuum pressure inside the two bags is kept constant, then the vacuum inside the primary bag is released to the atmospheric pressure determining a drawn up of the bag into the FASTRAC non-contacting tool, thus creating distribution channels (see Fig. 12.1). These distribution channels allow the resin to flow across and through the thickness of the preform once the resin infusion starts. The channels of FASTRAC system under vacuum separate the bag from the fabric reinforcement, by inducing a space between the film and the fabric, that act as the distribution medium of the conventional VARTM.

The non-contacting tool is reusable and, hence, the FASTRAC manufacturing costs are lower than those of VARTM due to the elimination of peel ply and the distribution net.

An evolution of this method is the flow flooding chamber (FFC) process that uses a rigid chamber that is placed on top of the standard VARTM assembly [19, 20]. After the vacuum application to the primary vacuum bag to compact the dry fiber reinforcement, before resin infusion, vacuum is drawn inside the rigid chamber. This higher vacuum pulls the bagging material away from the fabric and creates an empty chamber. As soon as the inlet is opened, the resin flows into the empty space unimpeded. Once the preform is covered with the resin, the vacuum inside the rigid chamber is released and the atmospheric pressure pushes the resin into the fiber stack. The FFC is very similar to FASTRAC method because it utilizes a rigid plate and a vacuum to create chambers to accelerate the flow [21]. However, the cost of implementing the FFC is much less than the FASTRAC method because the FFC method does not require a rigid plate machined with channels. In addition, FFC doesn't require any additional materials such as distribution media as in SCRIMP.

Pulsed Infusion [22] is an alternative vacuum infusion process based on the use of double bag and a silicon membrane in place of the traditional VIP distribution net (Fig. 12.2).

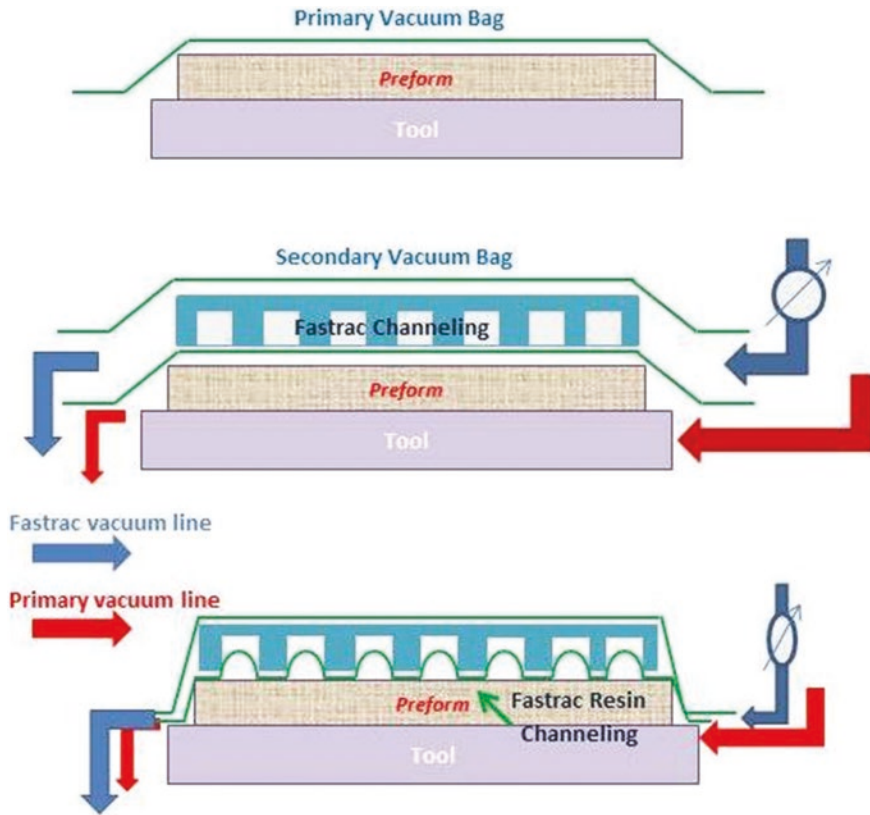


Fig. 12.1 Schematic of fastrac process

It is based on the use of a proper designed reusable pressure distributor (Fig. 12.3), able to better control the vacuum pressure in a pulsed way. Thus, the transverse resin flow through the dry fiber reinforcement is promoted and a better adhesion between the resin and the fibers is achieved.

In particular, the lower vacuum bag determines a lower chamber where the resin infusion occurs almost likely in the VARTM. The lower vacuum bag is stacked on the dry fiber reinforcement without placing the resin distribution net. A proper designed pressure distributor (Fig. 12.3) is positioned on the lower vacuum bag and under the second upper vacuum bag allowing to identify an upper chamber. By applying a different vacuum pressure in the two chambers and controlling timely the pressure difference between the two chambers, the resin flow is pulsed and promoted both in the plane and through the thickness of the reinforcement.

At the beginning in the upper chamber an higher depression is imposed. Thus, the lower bag will move up and, due to the shape of the distributor, some preferential channels for the resin flow will be created. The resin will fill these channels. Once all resin has entered, the vacuum is applied to the lower bag to induce the transverse infiltration.



Fig. 12.2 Pulse infusion

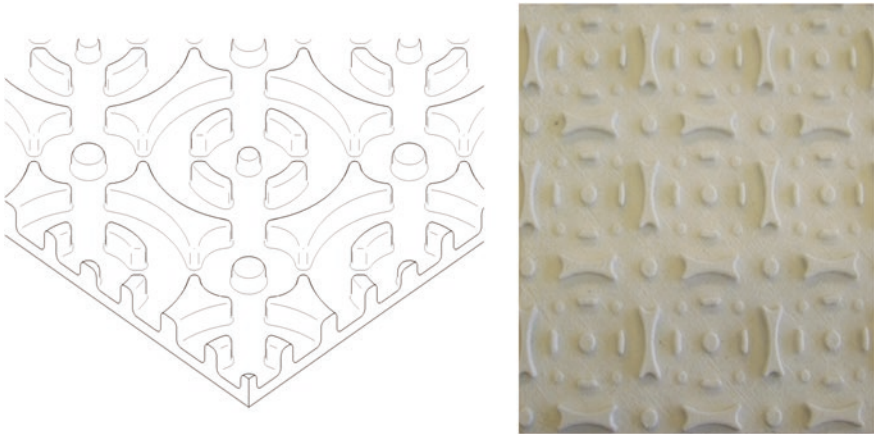


Fig. 12.3 Pressure distributor

The process can be performed in a static or in a dynamic way. In the dynamic way, the pressure difference between the upper and lower bag is controlled by a pressure regulator with a certain frequency.

This process allows to obtain laminates with the same fiber volume fraction and tensile properties of those produced by conventional infusion technologies. Further, due to a minor consumption of resin and the absence of the distribution net, Pulse Infusion provides a material cost saving advantage of about 19 % and a significant waste reduction.

12.3 Experimental Activity

In recent years significant progress has been made in understanding failure mechanisms of composite materials, such as delamination and fiber-matrix breakage.

Delamination refers to situations in which failure occurs between adjacent plies within a laminate. It can arise as a consequence of impacts with foreign objects and is probably the most investigated mode of failure in composite laminates. However, others damages such as matrix cracks, fiber-matrix debonding, fiber fractures can also appear as a consequence of impacts in composite structures under service conditions. These different damage mechanisms can interact each other and can lead to a considerable reduction in stiffness and strength of local critical areas and consequently to the reduction in the load-carrying capability of the entire composite structure.

Several studies on delamination and on other damage mechanisms have been conducted separately.

Composite delamination has been extensively investigated both experimentally and numerically and, when possible, analytical models have been developed.

From an experimental point of view, an important issue is the capability to investigate the dimension and the extent of delamination area by using non-destructive evaluation techniques in order to acquire affordable methods for the damage detection during the real service conditions of the composite structure.

Thus, in the frame of Garteur AG-32 project part of activities has been devoted to the production of fiber reinforced composites with induced delamination.

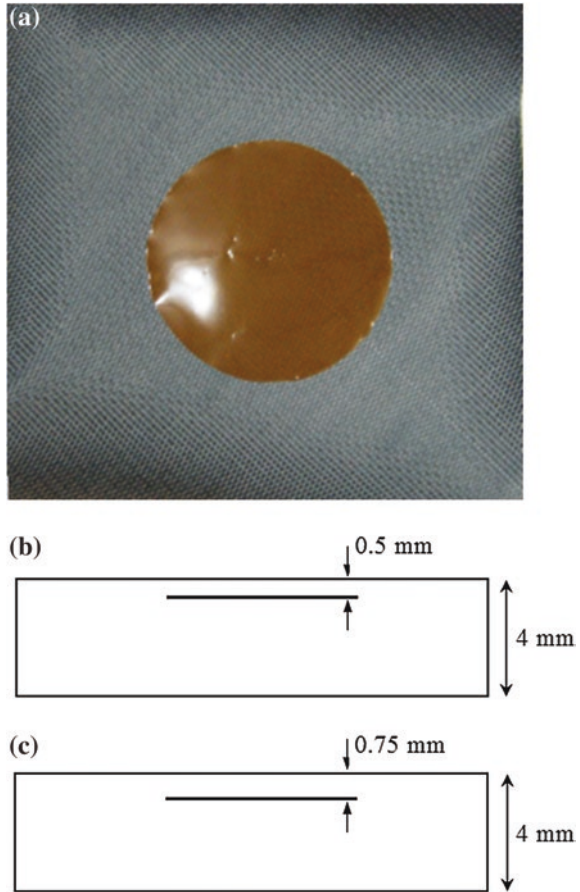
12.3.1 FRCP Manufacturing

The fiber reinforced composite has been manufactured by using unidirectional carbon fibers and an epoxy resin. In particular, the matrix was a commercially thermosetting resin, denominated RTM6; it is a mono-component premixed epoxy-amine system already degassed, specifically designed to implement infusion manufacturing processes. This system, provided by Hexcel Composites (Duxford, UK), is widely used for aerospace composite elements such as Arianna 5 or Airbus A380 [14]. The reinforcement system was a UD carbon fibre plain weave fabric characterized by a standard aerospace grade, 6k, known as G1157.

Specimens were fabricated considering two different stacking sequences: [45/0/90/-45/+45/0/90/-45]S and [0, 90]4S (S stands for symmetrical layout). Specimens involving fibres at the three directions of 0°, 45° and 90° (first stacking sequence) are herein referred to as type I, while specimens with fibres at 0° and 90° (second stacking sequence) are referred to as type II. Delamination was simulated by insertion of thin ($s = 25 \mu\text{m}$) kapton foils. The three specimens, which belong to the type I, are respectively named I-1, I-2 and I-3.

More specifically, I-3 did not include any delamination, while, as sketched in Fig. 12.4, the other two included each a kapton insert 140 mm in diameter (Fig. 12.4a) positioned at 0.5 mm for I-2 (Fig. 12.4b) and at 0.75 mm for I-3 (Fig. 12.4c).

Fig. 12.4 Manufacturing and schematic representation of specimens type I. **a** Frontal cut view. **b** Through thickness at depth of 0.5 mm (specimen I-1). **c** Through thickness at depth of 0.75 mm (specimen I-2)



The three specimens, belonging to the second type, which are named II-1, II-2 and II-3, are characterized by a more complex geometry and then a more detailed drawing (Fig. 12.5) has been provided.

As sketched in Fig. 12.5, each of these specimens was subdivided into four zones (Fig. 12.5a). Owing to a specific zone, the material may be undamaged, or with embedded inserts of different shape (circular, or elliptical), and dimension and located at different depth (Fig. 12.5b). In particular, with reference to Fig. 12.5b, D indicates the insert diameter and T accounts for specimen thickness and insert depth. All details for specimens type II are collected in Table 12.1; more specifically, for each of the four zones (Fig. 12.5a) a combination of D and T values is reported.

Specimens II-1 and II-2 contain only one insert per zone which is circular, or elliptical and located at depth of 0.5 or 0.75 mm. The last specimen II-3 contains overlapped concentric inserts of increasing diameter D from 15 up to 60 mm moving from depth of 0.25 mm up to 0.75 mm. More specifically, the kapton diskettes are positioned over three different layers of carbon fibres as better shown in Fig. 12.6.

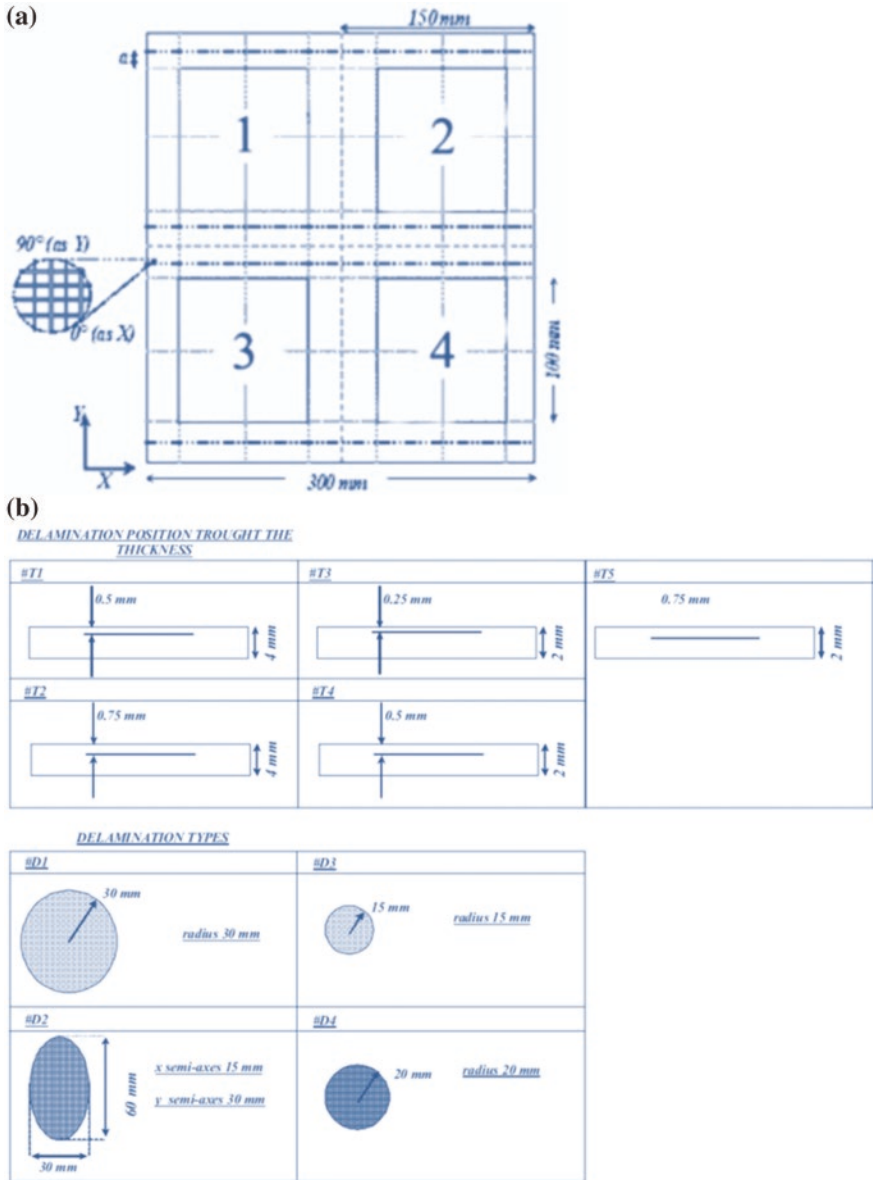


Fig. 12.5 Schematic representation of specimens type II. **a** Frontal view. **b** Details of inserts shape, dimension and position (for more details see Table 12.1)

The composite panels have been manufactured by vacuum infusion technique.

The fibrous reinforcement was laid onto an open-faced heating plate, where a liquid mold release agent had been spread (Loctite Frewax Frekote). Then, a release film (Release Ease 234TFP) was placed on top of the preform up to the

Table 12.1 Details about the location of inserts in specimens type II

		Sectors of specimen			
		1	2	3	4
Specimen	II-1	D1/T1	D1/T1	D2/T1	D1/T2
	II-2	D1/T2	D2/T1	D2/T2	D2/T2
	II-3	Undamaged	D1/T3 D3/T4	D1/T3 D3/T4	D1/T3 D4/T4 D3/T5

D shape and dimension of kapton
T kapton position

vacuum tube followed by the bleeder material (Compoflex 150) that absorbs the resin exceeding during the infusion and assures a good vacuum distribution. Finally, a resin distribution medium (Green Flow) was placed on the top partially in contact with the heating plate, useful for helping the resin to impregnate all the plies. A nylon vacuum bag was finally put on the layers to cover the entire plate and stitched to the plate by means of a high temperature resistance adhesive, the tacky tape (Fig. 12.7).

After the fiber infiltration, the resin curing was performed according to RTM6 data sheet at 160 °C for 1 h 30 s and at 180 °C for 2 h.

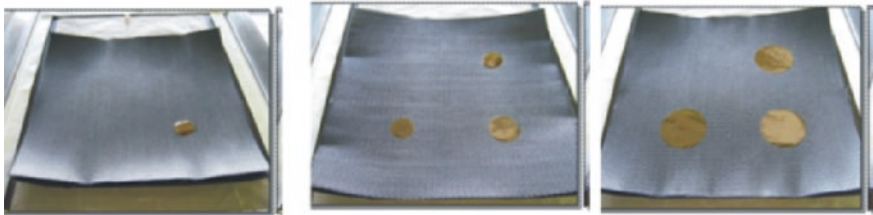


Fig. 12.6 Kapton inserts position in specimen II-3

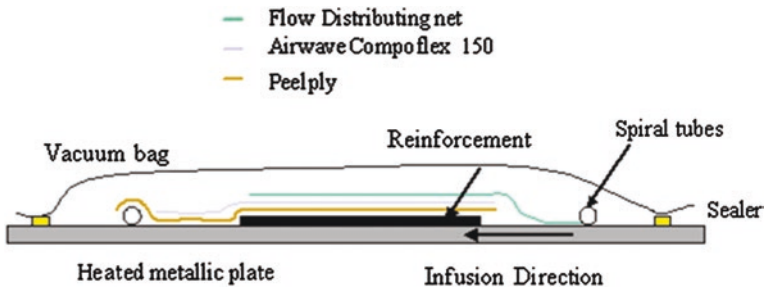
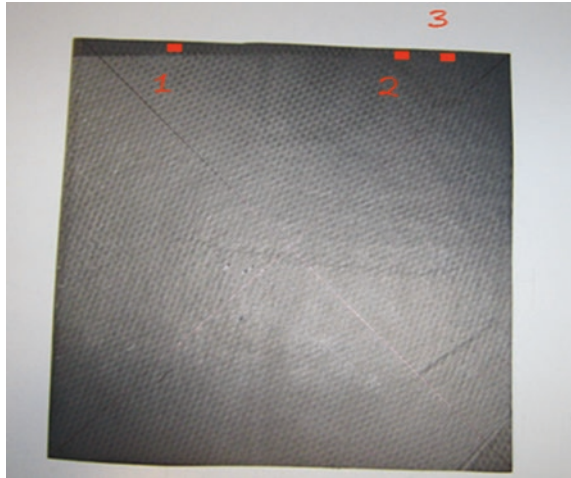


Fig. 12.7 Schematic of vacuum infusion process

Fig. 12.8 Composite panel with the stacking sequences: [45/0/90/-45/+45/0/90/-45]S



12.3.2 Microscopy Analysis

The manufactured composite panels have been analysed by means of optical microscopy by using the polarized light optical Olympus BX51 Instruments. The optical microscope analysis has been useful to evaluate the fiber content and the quality of the panel even if it can lead to discrepancy in the overall percentage due to the difficulty to identify correctly the fiber-resin interface.

In particular, the method of phases has been adopted to evaluate the fiber content in three different areas of 1.4 mm width of the composite with the stacking sequences: [45/0/90/-45/+45/0/90/-45]S. Figure 12.8 shows a picture of the panel by evidencing the three areas with red color, while Fig. 12.9 reports a micrograph of the panel in the area 1 along the thickness.

A good impregnation of the fibers and absence of voids can be noticed.

The analysis of the micrographs allowed to estimate the fiber and the resin content of the composite panel in three areas which are reported in Table 12.2. It can be observed that the fiber and resin fractions attain typical values of the vacuum infusion process. Thus, the introduction of kapton foils didn't affect the resin flow and the fiber infiltration.

12.4 Conclusions

Vacuum Infusion process has been adopted to manufacture carbon/epoxy composites with induced delaminations. In particular, different panel configurations have been realized by embedding kapton foils through the carbon plies at different positions. Microscopy analysis of the final composite panel enabled to observe a good impregnation of the fibers and estimation of the resin/fibers content.

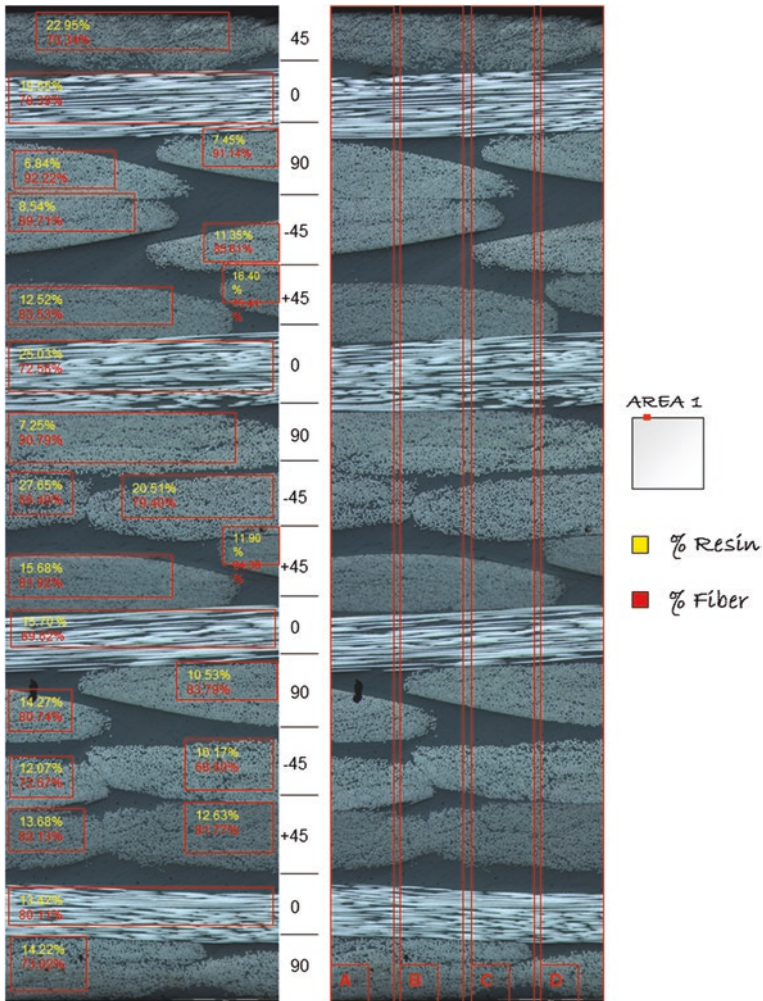


Fig. 12.9 Micrograph of area 1

Table 12.2 Resin and fiber content

	Resin (%)	Fibre (%)
1	42.60	57.05
2	40.60	59
3	41.06	58.55
Average	41.42	58.2

The results evidence that the kapton foils don't affect the resin flow and don't move from their position during the fiber impregnation. Therefore, the liquid molding techniques can be considered as a capable and flexible method to produce proper benchmark composite elements which can be adopted to validate numerical tools prediction their mechanical behaviour.

References

1. Antonucci, V., Giordano, M., Nicolais, L.: Liquid moulding processes. In: Rapra Handbook of Polymer Blends and Composites 2, 53–83 (2002), Rapra Tech.Ltd ISBN 978-1-85957-309-6, electronic ISBN 978-1-60119-666-8
2. Antonucci, V., Giordano, M., Di Vita, G., Nicolais, L.: A simulation of the non-isothermal resin transfer molding process. *Polym. Eng. Sci.* **40**(12), 2471–2481 (2000)
3. Antonucci, V., Giordano, M., Nicolais, L., Calabrò, A., Cusano, A., Cutolo, A., Insera Imparato, S.: Resin flow monitoring in resin film infusion process. *Mater. Process. Technol.* **143–144**, 687–692 (2003)
4. Berenberg, B.: Liquid composite molding achieves aerospace quality. *High Perform Compos.* **11**(6), 18–22 (2003)
5. Brouwer, W.D., van Herpt, E.C.F.C., Labordus, M.: Vacuum injection moulding for large structural applications. *Compos. A.* **34**: 551–558 (2003)
6. Govignon, Q., Bickerton, S., Morris, J., Kelly, P.A.: Full field monitoring of the resin flow and laminate properties during the resin infusion process. *Compos. A.* **35**, 1412–1426 (2008)
7. Mathuw, R., Advani, S.G., Heider, D., Hoffmann, C., Gillespie Jr, J.W., Fink, B.K.: Flow front measurements and model validation in the vacuum assisted resin transfer molding process. *Polym. Compos.* **22**(4), 477–490 (2001)
8. Seeman, B.: Plastic transfer moulding technique for the production of fibre reinforced plastic structures. US Patent 4,902,215 (1990)
9. Li, W., Krehl, J., Gillespie, J.W., Heider, Jr D., Endrulat, M., Hochrein, K., Dunham, M.G., Dubois, C.J.: Process and performance evaluation of the vacuum-assisted process. *J. Compos. Mater.* **38**(20), 1803–1814 (2004)
10. Williams, C., Summerscales, J., Grove, S.: Resin infusion under flexible tooling (RIFT): a review. *Compos. A.* **27**(7), 517–524 (1996)
11. Loos, A.C., Rattazzi, D., Batra, R.C.: A three-dimensional model of the resin film infusion process. *J. Compos. Mater.* **36**(10), 1255–1273 (2002)
12. Yenilmez, B., Senan, M., Murat Sozer, E.: Variation of part thickness and compaction pressure in vacuum infusion process. *Compos. Sci. Technol.* **69**, 1710–1719 (2009)
13. Gardiner, G.: Double bagging through three decades. *Composites Technology*. <http://www.compositesworld.com/articles/archive/6b950fa0-f831-4c08-878f-dd0819c1c71c> (2010)
14. Thagard, J.R., Okoli, O.I., Liang, Z., Wang, H.-P., Zhang, C.: Resin infusion between double flexible tooling: prototype development. *Compos. A.* **34**, 803–811 (2003)
15. Woods, J., Modin, A. E., Hawkins, R. D., Hanks, D. J.: Controlled atmospheric pressure infusion process. International Patent WO 03/101708 A1 (2003)
16. Cornelus, E., Carolus, F., Herpt, V.: Method for the manufacture of a reinforced plastic product. US 2007/0158874 A1 (2007)
17. Allende, M., Mohan, R.V., Walsh, S.M.: Experimental and numerical analysis of flow behavior in the FASTRAC liquid composite manufacturing process. *Polym. Compos.* **25**(4), 384–395 (2004)
18. Walsh, S.M., Fink, B.K.: Achieving low cost composite processes through intelligent design and control. Proc RTO-MP-069(II) (2001)
19. Alms, J., Advani, S.G.: Simulation and experimental validation of flow flooding chamber method of resin delivery in liquid composite molding. *Compos. A.* **38**, 2131–2141(2007)
20. Vernin, N., Chobra, M., Advani, S.G., Alms, J.: Vacuum assisted resin transfer molding techniques with flow flooding chamber. US 2007/0063393 A1 (2007)
21. Markicevic, B., Heider, D., Advani, S.G.: Filling of a system of channels and porous medium: an effectiveness factor based on momentum transfer. *J. Porous Media* **6**, 223–233 (2003)
22. Antonucci, V., Ricciardi, M.R.: Pulsed infusion: a new liquid moulding process. *JEC compos. Mag.* **77**, 42–43 (2012) ISSN:0754-0876

Chapter 13

Lock-in Thermography to Detect Delamination in Carbon Fibres Reinforced Polymers

Carosena Meola and Giovanni Maria Carlomagno

13.1 Introduction

Infrared thermography (IRT) is a methodology which allows for representation of an object surface temperature map due to the electromagnetic energy that is radiated by such an object in the infrared band. This represents a great potentiality to be exploited in a lot of application fields and for many different purposes. IRT is becoming ever more popular in the Material Science field since it is completely non-contact and it may accompany the entire life of a product, from material development and product manufacture (on-line process control), to final product assessment (non-destructive evaluation) and to in-service maintenance. Details can be found in some recent review papers and book chapters by the authors [1–6]; for an up-to-date overview, the reader is also addressed to the Proceedings of three main Conferences concerned with infrared thermography [7–9].

The attention of the present chapter is focused on the use of IRT in Non Destructive Testing (NDT) of composite materials and particularly to Carbon Fibres Reinforced Polymers (CFRP) used for the construction of aircraft.

Composite materials are being ever more extensively used in the aerospace industry since they offer several advantages over metals [10, 11] in terms of low weight and high strength. However, they are susceptible to delamination, which may arise either during manufacturing, or in service.

Delamination is often very light and difficult to be detected in non-destructive way, while its detrimental effects could lead to the component discharge with also

C. Meola (✉) · G.M. Carlomagno
Department of Industrial Engineering, Aerospace Division,
University of Naples Federico II, Via Claudio, 21, 80125 Naples, Italy
e-mail: carmeola@unina.it

catastrophic consequences. Therefore, the availability of effective non-destructive testing techniques, able to detect delamination at an incipient stage, is a primary requirement for the reliable design of aerospace composite structures.

Within this context, infrared thermography is attractive since is non-contact, noninvasive and faster than many other inspection techniques. What is more, infrared thermography has proved its ability to deal with many inspection requirements of composites. In fact, infrared thermography has proved usefulness in non-destructive testing of composites [2, 4, 5], but also for online monitoring of the surface temperature change (thermo-elastic/plastic effects) which is experienced by a body when subjected to volume and shape variations under load [12–16].

In particular, Meola and Carlomagno first [12] tackled with such a task; specifically, by choosing an appropriate image sampling rate, they succeeded in appraising the material temperature changes, which are due to thermo-elastic/plastic effects in composites under low-energy impact. Later, they supplied information on onset and propagation of impact damage in Glass Fibers Reinforced Polymers (GFRP) through the analysis of thermo-plastic effects [13]. Recently, they demonstrated the important role played by manufacturing defects, like porosity and fibers misalignment, in the behavior of GFRP to impact load [14]. Within the behaviour of composites to impact, infrared thermography proved also suitability to establish the impact energy value for onset of material damage in CFRP; in particular, the temperature variation was in agreement with the acoustic emission recorded by piezo-patches [15].

Meola et al. [16] were also able to visualize, with infrared thermography, thermo-elastic effects generated by bending in composites. In particular, they found a general agreement between the temperature changes and the bending moment, while observed deviation from such a distribution when defects, buried in the material, were present.

The attention of the present work is devoted only toward the use of infrared thermography as a non-destructive evaluation technique. Specifically, herein lock-in thermography is used to find and quantify, in terms of size and depth, delaminations in CFRP. This investigation was mainly performed within the involvement in the GARTEUR Action Group 32.

13.2 Non-destructive Testing with IRT

Basically, two thermographic techniques can be used for non-destructive testing of materials: pulse thermography (PT) and lock-in thermography (LT). Actually, it is possible to find in literature mention to other techniques, but these are practically variants of PT and LT because they include either a different heating method, or different processing algorithms.

An example of combination of both PT and LT is the Pulse Phase Thermography (PPT) in which the specimen is pulse heated as in PT. However, the mix of frequencies of the thermal waves launched into the inspected specimen

is unscrambled by performing the Fourier transformation of the temperature evolution over the field of view. In PPT, data can be either presented as amplitude, or phase, images like in LT.

Within the present investigation, lock-in thermography has been considered to be the best choice so, in the following, only this technique will be described and applied.

13.2.1 Basics on Lockin Thermography

The basic concept of lock-in thermography was first introduced by Carlomagno and Berardi [17] and later further investigated by other researchers [18–22], who much later acknowledged their work.

This technique can be accomplished in two different modes: stimulation with an halogen lamp, which is called optical lock-in thermography and abbreviated as LT, or OLT [some authors also call it modulated thermography (MT)], or stimulation with high-frequency elastic waves and is called ultrasound lock-in thermography (ULT).

In the LT, the thermographic system is coherently coupled to a stimulated thermal wave source which is operated in such a way that a continuous temperature modulation on the inspected specimen surface results. The system collects a series of images and compares the modulated heating with the measured temperatures by extracting the sinusoidal wave pattern at each point of the image. By considering photo-thermal methods applied to the lock-in amplifier (which allows filtering the stationary component), the harmonic heat delivered at the surface (i.e. $z = 0$) of a homogeneous and semi-infinite material results in a (time dependent) thermal wave, which propagates inside the material according to the following relationship:

$$\tilde{T}(z, t) = \frac{\eta Q_i}{2e\sqrt{\omega}} \exp\left(-\frac{z}{\mu}\right) \exp i\left(\omega t - \frac{z}{\mu}\right) = A(z) \exp i(\omega t - \phi(z)) \quad (13.1)$$

where $\tilde{T}(z, t)$ is the periodic temperature component at depth z , t is time, η represents the absorbed fraction of the incident heat Q_i , e is the material thermal effusivity, $A(z)$ is the amplitude, $\phi(z)$ is the phase shift of the thermal wave travelling inside the material, μ is the thermal diffusion length which is calculated from the thermal diffusivity α and the wave frequency $f = \omega/2\pi$:

$$\mu = \sqrt{\frac{\alpha}{\pi f}} \quad (13.2)$$

The wave thermal penetration depth p corresponds to 1.8μ [18–20]. The material thickness, which can be inspected, depends on the wave period (the longer the period, the deeper the penetration) and on the material properties (thermal conductivity coefficient, heat capacity and mass density). Generally, tests start at a quite high wave

frequency, at which only surface (or shallow) defects are visible and, later on, to inspect deeper layers, the frequency is decreased until the entire specimen thickness has been examined. Results may be presented as amplitude, or phase, images. The latter are not affected by variations of the surface emissivity and thermal stimulation; so they are generally preferred.

13.3 Experimental Analysis

Different specimens were fabricated with inclusions of different size and at different location and depth. All specimens were inspected with lock-in thermography by heating and viewing with the infrared camera first one side and then the opposite one.

13.3.1 Specimens Preparation

Specimens were fabricated according to two different stacking sequences which were respectively named as type A and type P. The stacking sequence for type A is $[45/0/90/-45/+45/0/90/-45]_S$ while for type P is $[0, 90]_{4S}$. All the specimens were fabricated from RTM6 epoxy resin, reinforced with G1157 UD 6 k carbon fibres by the vacuum infusion process (VIP). In particular, according to this method, dry fibres are laid into the mould; then, vacuum is applied to drive in the resin through the reinforcement mat. More specifically, once complete vacuum is achieved, resin is literally sucked into the laminate via carefully placed tubing; for more information about the specimens fabrication see Ref. [23] or Chap. 12 of this book.

Specimens belonging to the type A include one specimen A1 made of sound material and other two A2 and A3 with embedded delaminations. Each delamination was simulated by inserting a thin ($s = 25 \mu\text{m}$) Kapton® foil; a scheme of the specimens with the enclosed Kapton® foils is given in Fig. 13.1. As it can be seen, Kapton® inserts can be either shallow, or deep, depending on the side A, or B, from which the specimen is thermally stimulated and viewed. In particular, measuring the depth from the side A, the Kapton® disk has been located at 0.75 mm for the specimen A2 and at 0.5 mm for the specimen A3.

The inserts were positioned relatively close to the surface because these specimens were prepared to undergo mechanical tests finalized to investigate the delamination buckling effects.

Three specimens, of type P, were manufactured with enclosed Kapton® inserts of two shapes, at different positions and depths as sketched in Fig. 13.2.

Each specimen of type P can be split in four sub-panels which can be either undamaged, or could enclose Kapton® inserts of different shapes (either circular, or elliptical), dimensions and depth locations.

In particular, specimens P1 and P2 (see Fig. 13.2a, b) are both characterized by an overall thickness of 4 mm and contain only one circular or elliptical insert per sub-panel which can be located at 0.5 mm or 0.75 mm depths.

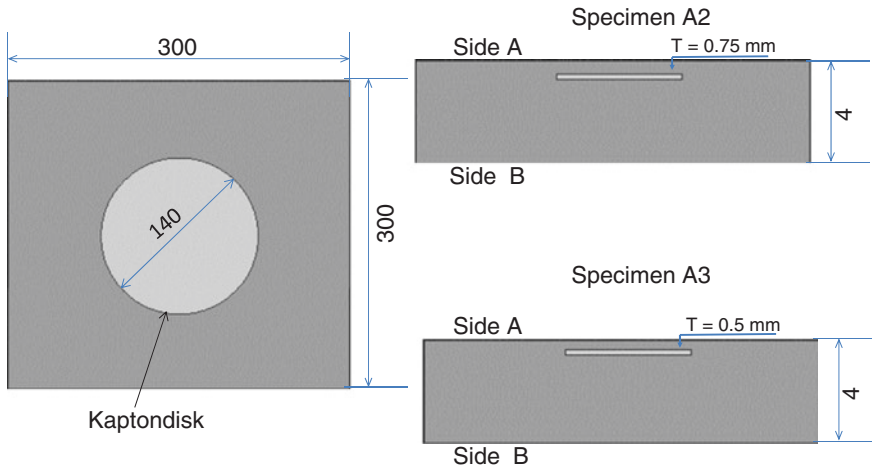


Fig. 13.1 Sketch of specimens type A with buried Kapton® insert

The last specimen P3 (see Fig. 13.2c) is characterized by an overall thickness of 2 mm and contains sub-panels with overlapped concentric inserts of increasing diameter D from 30 mm up to 60 mm positioned at different depth (from 0.75 to 0.25 mm). More details are specified in Table 13.1.

13.3.2 Test Setup

All the specimens described in the previous section were non-destructively evaluated with optical lock-in thermography. The specimen's surface viewed by the IR camera was the same as the heating stimulated one. The test setup is sketched in Fig. 13.3.

The infrared camera is the ThermaCam SC3000 (FLIR Systems), which is equipped with a Stirling cooled Focal Plane Array (FPA) Quantum Well (QWIP) detector of 240×320 pixels working in the Long Wave infrared band 8–9 μm . The sensitivity is 20 mK at ambient temperature, allowing for the detection of small temperature variations over the specimen surface. The standard acquisition rate is 60 Hz full frame, but it can reach up to 900 Hz with a reduced field of view.

For non-destructive test purposes, the infrared camera was equipped with the IRLockIn 4 option and with halogen lamps. With the IRLockIn© software, it is possible to select the several *measure parameters* (heat modulation function, frequency and acquisition rate), as well as the *image processing method* (Fast Fourier, Harmonic Approximation, etc.) and the *analysis parameters* (number of images, first image in the sequence to be analysed, etc.).

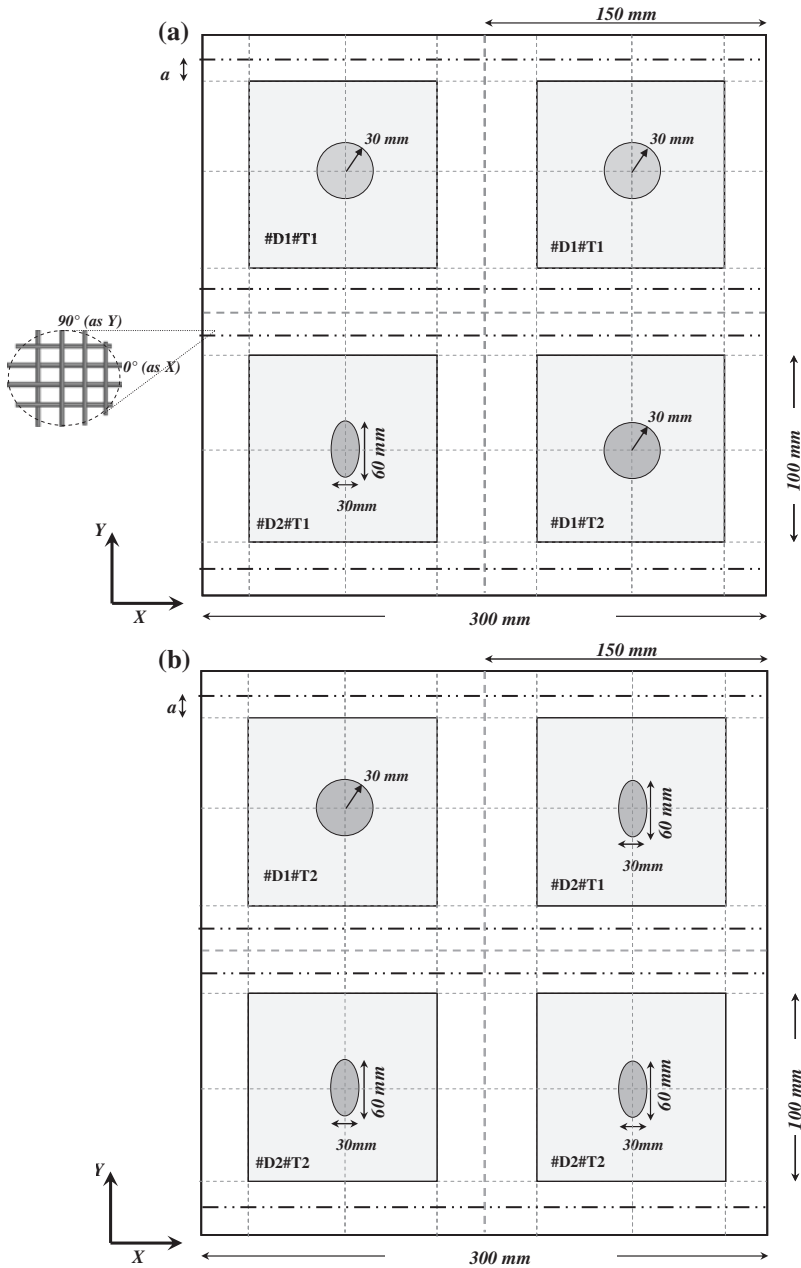


Fig. 13.2 Sketch of type P specimens **a** specimen P1 with Kapton® inserts at depth T1 = 0.5 mm and T2 = 0.75 mm, **b** specimen P2 with Kapton® inserts at depth T1 = 0.5 mm and T2 = 0.75 mm, and **c** specimen P3 with overlapped inserts of different diameter as detailed in Table 13.1

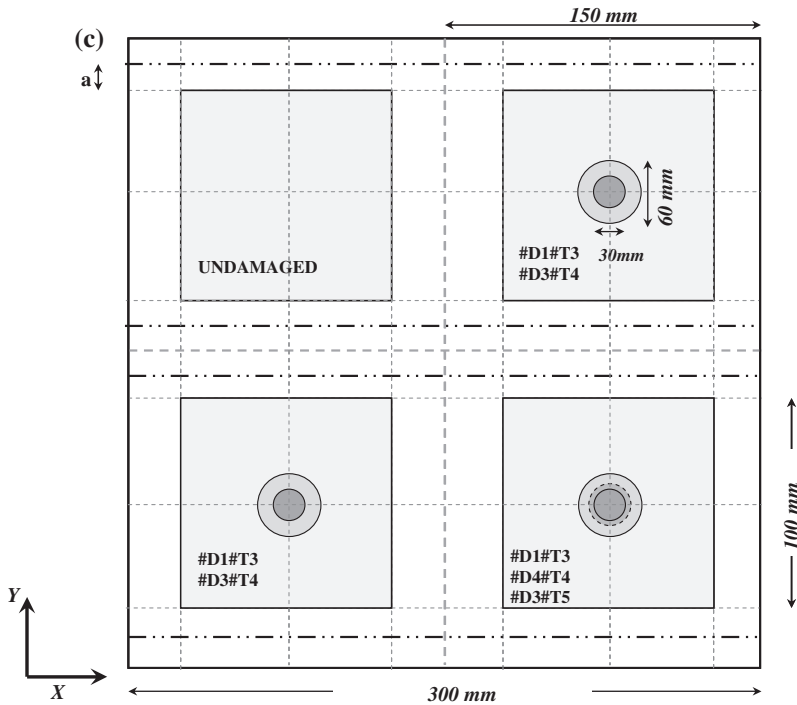


Fig. 13.2 continued

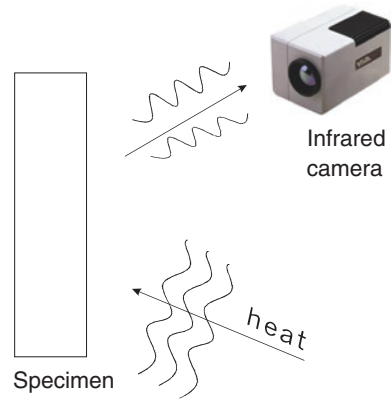
Table 13.1 Insert details for specimen P3

Insert diameter (mm)	Insert depth (mm)
D1 = 60	T3 = 0.25
D3 = 30	T4 = 0.5
D4 = 40	T5 = 0.75

For the tests presented in this chapter, a halogen lamp of 1,000 W was used, which was positioned at a distance such as to illuminate (heat up) the entire surface almost uniformly.

13.4 Results and Discussion

The tests were performed with LT using the test setup sketched in Fig. 13.3 and, in order to analyse the material conditions at different depths from the top surface through the entire specimen thickness, the heating modulation frequency was varied

Fig. 13.3 Test setup

from 1.75 Hz down to 0.05 Hz. Every specimen was viewed by the infrared camera from both sides, each at a time.

Results are presented first as phase images for a qualitative quick analysis. In fact, a local variation of colour indicates a local variation of phase angle, which corresponds to a local variation of material properties [3]. Then, from phase images it is possible to immediately become aware of the presence of any anomaly in the material.

Then, the phase images were subjected to post-processing analysis to acquire quantitative information about the size and the depth of every discovered defect.

13.4.1 Qualitative Analysis

The two phase images (one for the side A and the other for the side B) taken from the sound material specimen A1 are shown in Fig. 13.4a, b. At a first sight, the two images appear completely different.

In fact, the first phase image (side A) displays local variations of colour which correspond to variations in the phase angle distribution. It is worth noting that, even if it is possible to appreciate some variations in the phase angle distribution, this mainly indicates a non-uniform distribution of epoxy resin between the fibres. It is also possible to appraise the fibres orientation which in the external layer is at 45° (North-West to South-East).

Conversely, the second image (Fig. 13.4b), which is relative to the side B, displays an almost uniform colour (uniform phase angle).

Such a difference between the two images is due to the different surface finishing which is accounted for by the phase angle. More specifically, during fabrication, as described in Sect. 13.3.1, one side of the panel remains in contact with the flat mould, resulting in a flat surface finishing. The other side of the panel, being the mould open there, is modelled by the vacuum bag and assumes a quite rough aspect. The external surface may be either covered by an almost uniform

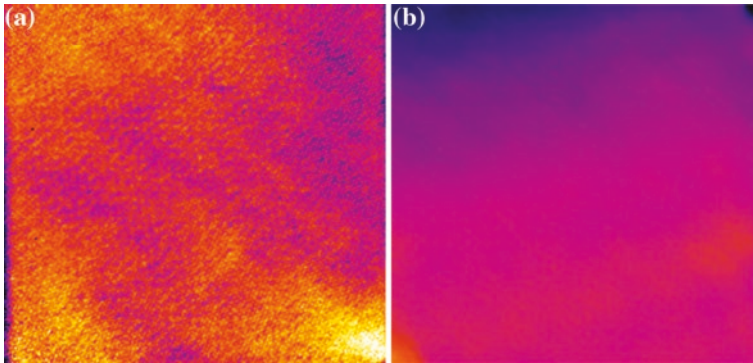


Fig. 13.4 Phase images of the specimen A1: **a** side A, and **b** side B

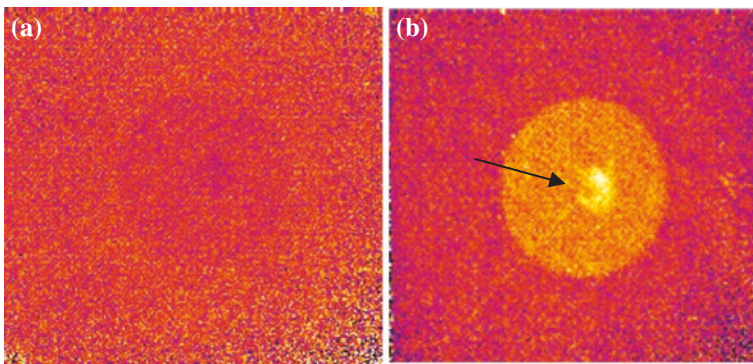


Fig. 13.5 Phase images of the specimen A2 ($T = 0.75$ mm) taken from side A: **a** $f = 0.75$ Hz, and **b** $f = 0.25$ Hz

resin film, or characterized by zones with resin thickening and zones with lack of resin. In addition, any substance, which was likely used, during fabrication, to facilitate detachment of the specimen surfaces from either the mould walls, or the bag, affect the final characteristics of the specimen surfaces.

Phase images of the A2 and A3 specimens, which were taken at different heating frequencies and from both sides A and B, are reported in the following Figs. 13.5, 13.6, and 13.7.

As a main observation, all the images, taken from both A and B sides, display a small central, almost circular shaped, anomaly (indicated by an arrow in Fig. 13.5b) which seems to be present across the entire thickness of each specimen. This is not completely explicable and it may be ascribed to the fixture which was used during the specimen fabrication to help positioning of the Kapton® disk. Such an anomaly, indeed, is the most relevant thing observable on side B for all specimens coupled with a certain non-uniformity of colour (phase angle) to be ascribed to local variations of the amount of resin (see Fig. 13.6).

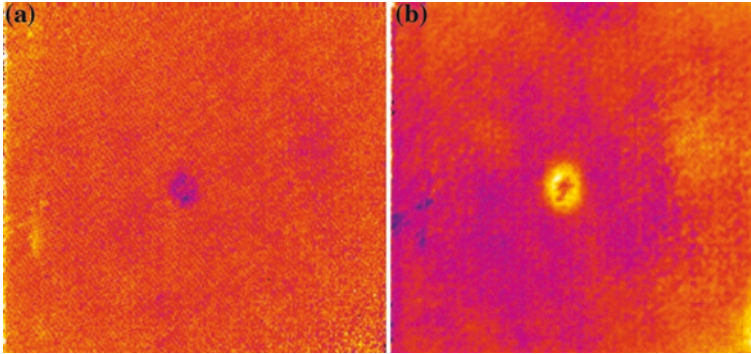


Fig. 13.6 Phase images of the specimen A2 ($T = 0.75$ mm) taken from side B: **a** $f = 0.25$ Hz, and **b** $f = 0.05$ Hz

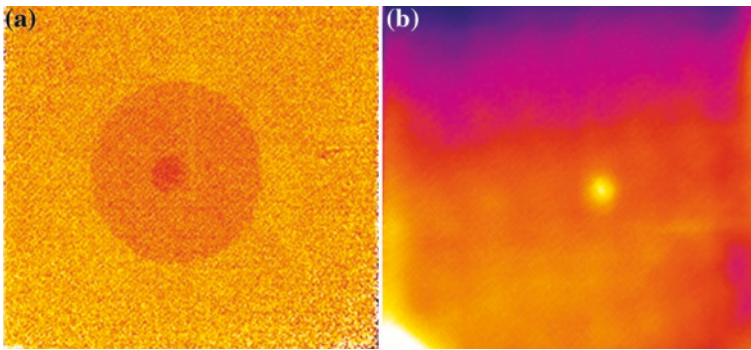


Fig. 13.7 Phase images of the specimen A3 ($T = 0.5$ mm): **a** side A, $f = 0.85$ Hz, and **b** side B, $f = 0.05$ Hz

From side A, in the specimen A2, the Kapton® disk appears just about distinguishable at the heating frequency $f = 0.75$ Hz (Fig. 13.5a) and becomes well outlined for $f = 0.25$ Hz (Fig. 13.5b). Instead, for the specimen A3, the Kapton® disk appears well outlined already at $f = 0.85$ Hz (Fig. 13.7a) due the different depth at which the insert is located. Indeed, the Kapton® disk is positioned at a depth of 0.75 and 0.5 mm, respectively in the A2 and A3 specimen (see Fig. 13.1).

The most significant phase images, taken at different heating frequencies, of specimens type P are reported in the following Figs. 13.8, 13.9, and 13.10.

As shown in Fig. 13.2a, the specimen P1 includes three inserts all located at depth $p = 0.5$ mm and one at $p = 0.75$ mm. They become visible respectively at $f = 1.2$ Hz (Fig. 13.8a) and at $f = 0.5$ Hz (Fig. 13.8b). Decreasing the frequency to 0.05 Hz (Fig. 13.8c) a non uniform distribution of color appears in the central-right side of the specimen accounting for local non uniformity of material characteristics. This is likely to be ascribed to a non-uniform distribution of resin and fibres percentages. Probably, during infusion, a local stagnation of resin occurred, which

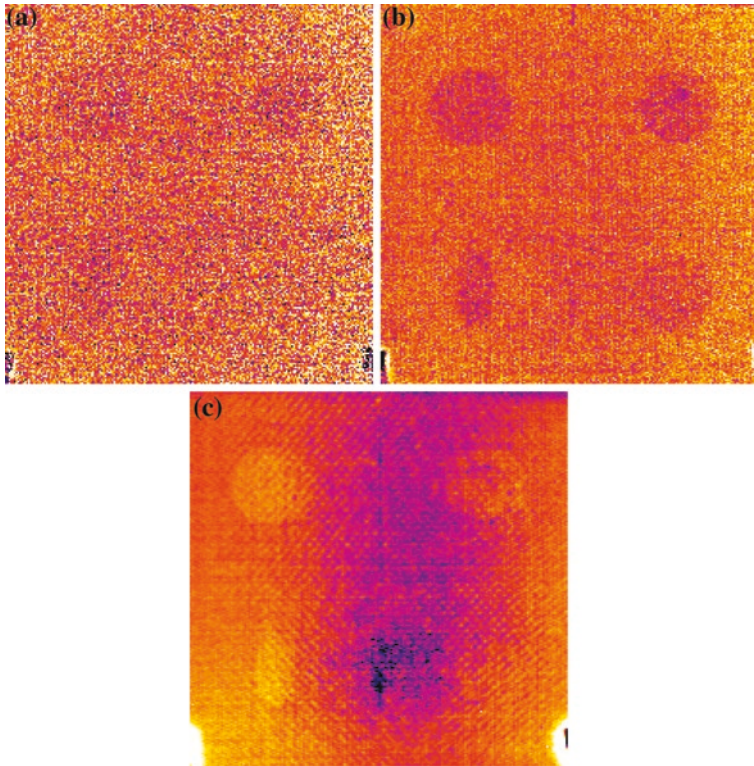


Fig. 13.8 Phase images of specimen P1: **a** $f = 1.2$ Hz, **b** $f = 0.5$ Hz, and **c** $f = 0.05$ Hz

was also favoured by the presence of the Kapton® inserts. More specifically, such a resin stain is located deeper with respect to the Kapton® inserts, as can be stated owing to the values of the heating frequencies at which the inserts and the stain become visible. Then, the presence of the Kapton® disks probably affected the resin flow contribution to create resin reach areas during the infusion process.

The specimen P2 includes one insert at depth $p = 0.5$ mm and three at $p = 0.75$ mm as shown in Fig. 13.2b. The more shallow one, analogously to the three inserts in the P1 specimen, becomes visible at $f = 1.2$ Hz (Fig. 13.9a), while the other three appear at $f = 0.5$ Hz (Fig. 13.9b). In Fig. 13.9b it is possible to see a dark stain on the bottom left close to the elliptic Kapton® insert. This indicates again a non-uniform distribution of resin. However, in general, the specimen P2 is characterized by a more uniform distribution of phase angle with respect to the specimen P1.

The specimen P3 is characterized by a more complex distribution of inserts over two and three layers as sketched in Fig. 13.2c. For this specimen, frequencies of 1.5, 0.5 and 0.25 Hz allow to detect, respectively, the inserts at 0.25 mm (Fig. 13.10a), at 0.5 mm (Fig. 13.10c) and at 0.75 mm (Fig. 13.10d).

The overlapped inserts appear well outlined for $f = 0.05$ Hz (Fig. 13.10e). From all the taken phase images, no significant material variations were observed.

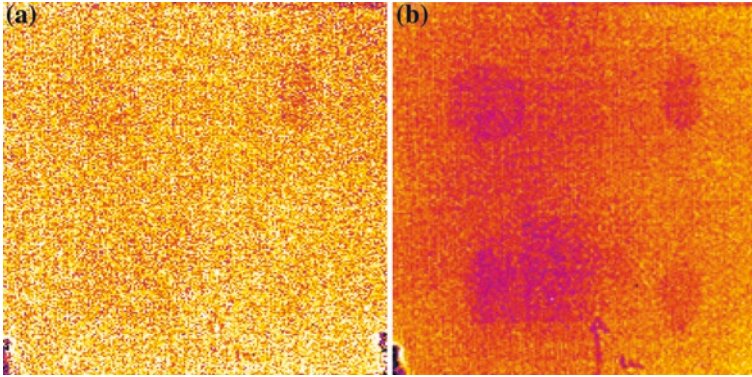


Fig. 13.9 Phase images of specimen P2: **a** $f = 1.2$ Hz, and **b** $f = 0.5$ Hz

To better outline the three overlapped diskettes, some tests were repeated with a close-up view; more specifically, the distance of the infrared camera to the specimen surface was reduced to increase the spatial resolution.

In particular, a close view image of the half bottom of Fig. 13.10e is shown in Fig. 13.11; the different diskettes were contoured with a black circle to facilitate their visibility. It is possible to note that a certain eccentricity of the overlapped foils exists. This is obviously due to difficulties in the alignment of the inserts centres during fabrication. This may suggest the use of a tool, perhaps a pinhead, to maintain the foils aligned during the specimen fabrication.

13.4.2 Quantitative Analysis

From the phase images it is possible to obtain quantitative information in terms of size and depth of the detected defects. The diameter is evaluated by knowing the spatial resolution (i.e. the pixel size) and by choosing a limiting phase angle difference value between sound and defective materials [3]. In particular, the diameter was measured along both horizontal and vertical directions which were then averaged to get the final value D_M . Such measured D_M values were then normalized with respect to the nominal ones D_N . The D_M/D_N ratios were plotted against the nominal values D_N in Fig. 13.12.

As it can be seen, for inserts with smaller diameters, the highest ratios D_M/D_N values was obtained ($D_M/D_N = 1.1$). On the contrary, for all the larger inserts, the ratio D_M/D_N was found to be almost close to unity. Such a deviation is mainly due to difficulties in discriminating (camera spatial resolution) the interface of superimposed disks of the same material, which are characterized by the same phase angle [24].

The depth p of the inserts was calculated from Eq. 13.2 which can be rewritten as:

$$p = 1.8\mu = 1.8\sqrt{\frac{\alpha}{\pi f}} \quad (13.3)$$

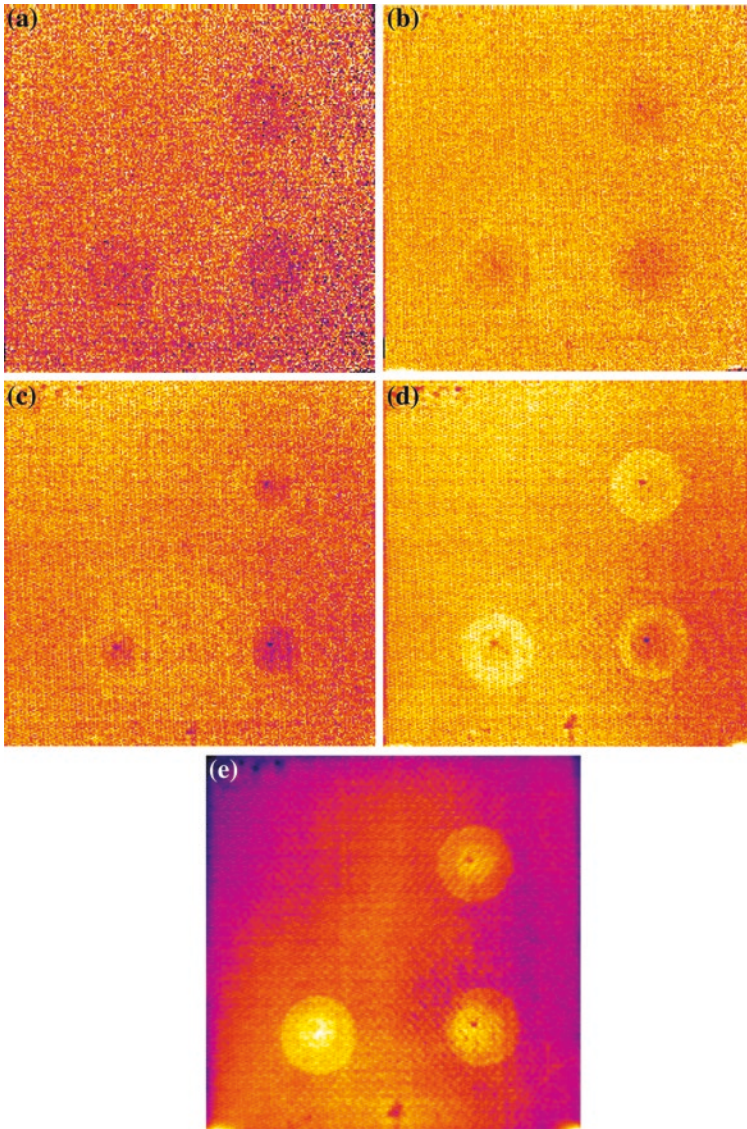


Fig. 13.10 Phase images of specimen P3: **a** $f = 1.5$ Hz, **b** $f = 0.75$ Hz, **c** $f = 0.5$ Hz, **d** $f = 0.25$ Hz, and **e** $f = 0.05$ Hz

From Eq. 13.3, the depth is calculated by considering the value of the heating frequency f for which the defect becomes visible for the first time, or better when the reflection of the heating wave is caused by the defect top surface. Of course, the use of Eq. 13.3 requires the knowledge of the average (through the thickness) thermal diffusivity α . However, α can be evaluated by the lock-in technique itself

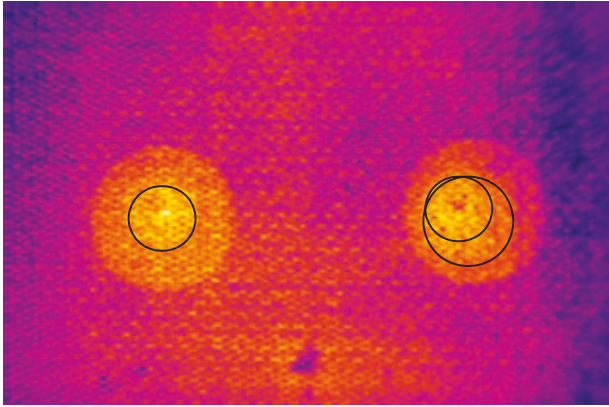
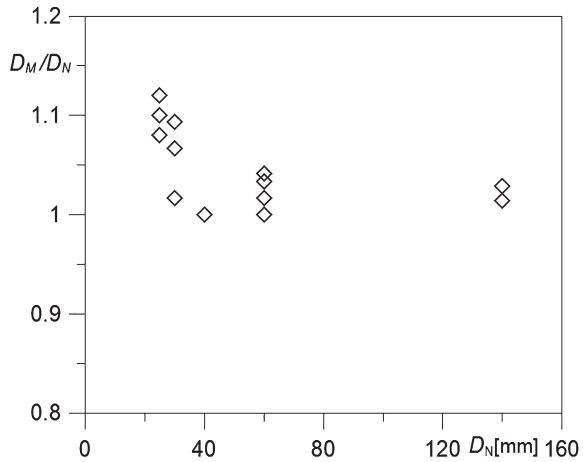


Fig. 13.11 Close up view of the half bottom of Fig. 13.10e

Fig. 13.12 Normalized measured diameter against the nominal one



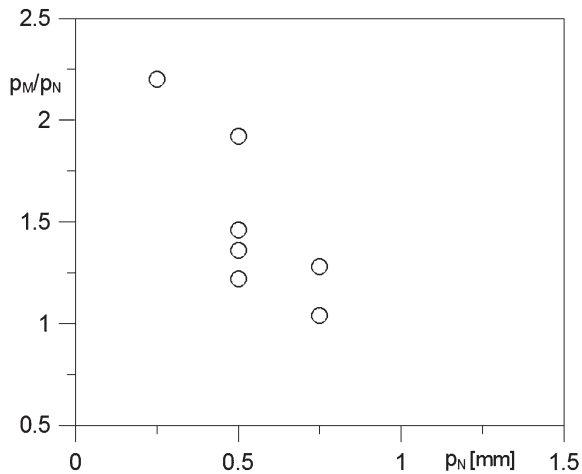
[25], or by flash thermography [26]. Here, α is measured with the lock-in itself and a value of $\alpha = 0.0045 \text{ cm}^2/\text{s}$ has been found for sound material (without inserts). The measured depth is named p_M and is normalized with respect to the nominal one p_N . The ratio p_M/p_N is plotted against the nominal depth p_N in Fig. 13.13.

At a first look p_M appears in general overestimated; to explain this, some considerations should be made.

First, a large deviation of data is observed for low depth values. The reasons for such a deviation are due to the blurring effect at high heating frequencies which prevents from a correct discrimination of the embedded defects. As a consequence, discrimination of a defect is possible at a frequency value which is much lower than the theoretical one (Eq. 13.2).

Secondly, for multiple inserts (i.e., for an insert which is positioned underneath a bigger one) and concentric with it (Fig. 13.2c), the effective thermal diffusivity to be considered for depth calculation in Eq. 13.3 is a function of the thermal

Fig. 13.13 Normalized measured depth against the nominal one



diffusivity of CFRP and that of the Kapton® foil [23]. Being the thermal diffusivity of the Kapton® foil much lower with respect to the one of the basic CFRP material, the observed depth overestimate the nominal ones.

Of course, it should be finally pointed out that the real insert position may differ from the nominal one due to the manufacturing process.

13.5 Conclusions

The use of lock-in thermography to discover the presence of embedded delaminations within CFRP panels has been illustrated in this chapter. Several specimens with very thin Kapton® inserts, enclosed to simulate delamination, has been inspected. As a general observation, by varying the heating frequency, all the embedded inserts were clearly detected and very well outlined also for critical configurations with superimposed inserts. In addition to the induced defects, it was also possible to appreciate imperfections due to manufacturing processes, such as a non uniform distribution of resin within the different material layers as well the eccentricity of some overlapped foils.

Besides the qualitative observations, also a quantitative data analysis was performed involving determination of the inserts size and depth. With regard to the inserts size, a certain data deviation has been observed for the smaller superimposed diskettes due to difficulties in discriminating the disks borders (camera spatial resolution). Whereas, in the measurement of the depth a large data deviation is observed especially for the shallow inserts, due to a blurring effect at the higher heating frequencies and to the higher percentage errors in insert positioning.

The great advantage of lock-in thermography is the possibility to evaluate the conditions of a structure in remotely without any alteration of the part under inspection and without any risk for the personnel.

References

1. Meola, C., Carlomagno, G.M.: Recent advances in the use of infrared thermography. *Meas. Sci. Technol.* **15**, 27–58 (2004)
2. Meola, C. (ed.): *Infrared Thermography: Recent Advances and Future Trends*. Bentham Science Publishers, Sharjah (2012)
3. Meola, C., Carlomagno, G.M.: Application of infrared thermography to adhesion science. *J. Adhes. Sci. Technol.* (review) **20**(7), 589–632 (2006)
4. Meola, C., Carlomagno, G.M.: Infrared thermography in non-destructive inspection: theory and practice. In: Meola, C. (ed.) *Recent Advances in Non Destructive Inspection*. Nova Science Publisher Inc., New York (2010). ISBN 978-1-61668-550-8
5. Meola, C., Toscano, C.: Non-destructive evaluation of carbon fiber reinforced polymers with ultrasonics and infrared thermography: an overview on historical steps and patents (invited review). *Recent Pat. Mater. Sci.* **5**(1), 48–67 (2012)
6. Meola, C., Carlomagno, G.M.: Non-destructive evaluation (NDE) of aerospace composites: detecting impact damage using infrared (IR) thermography (inv. Chap.), Chap. 14. In: *Non-destructive Evaluation (NDE) of Polymer Matrix Composites*. Woodhead Publishing Series in Composites Science and Engineering No. 43, pp. 367–396. Woodhead Publishing, Cambridge (2013). ISBN 0 85709 344 4, ISBN-13: 978 0 85709 344 8
7. Proceedings of Annual SPIE Thermosense Conferences, Bellingham, WA (1978)
8. Proceedings of Biennial Advanced Infrared Technology and Applications (AITA) (1991)
9. Proceedings of Biennial Quantitative Infrared Thermography (QIRT) Conferences (1992)
10. Jones, R.M.: *Mechanics of Composite Materials*. Hemisphere Publishing Corporation, New York (1975)
11. Hull, D., Clyne, T.W.: *An Introduction to Composite Materials*. Cambridge University Press, Cambridge (1996)
12. Meola, C., Carlomagno, G.M.: Infrared thermography to impact-driven thermal effects. *Appl. Phys. A* **96**, 759–762 (2009)
13. Meola, C., Carlomagno, G.M.: Impact damage in GFRP: new insights with infrared thermography. *Compos. A* **41**, 1839–1847 (2010)
14. Meola, C., Carlomagno G.M., Infrared thermography to evaluate impact damage in glass/epoxy with manufacturing defects. *Int. J. Impact Eng.* (2014, in press)
15. Meola, C., Carlomagno G.M., Ricci F.: Monitoring of impact damage in carbon fibre reinforced polymers. In: Proceedings of QIRT 2012, Napoli, paper no. 374, 8 p, 11–14 June 2012
16. Meola C., Carlomagno G.M., Bonavolontà C., Valentino M.: Monitoring composites under bending tests with infrared thermography. *Adv. Opt. Technol.* **2012**, 7 p. (2012) Article ID 720813
17. Carlomagno, G.M., Berardi, P.G.: Unsteady thermotopography in non-destructive testing. In Warren, C. (ed.) Proceedings of III Infrared Information Exchange, pp. 33–40. AGA, St. Louis (1976)
18. Busse, G.: Optoacoustic phase angle measurement for probing a metal. *Appl. Phys. Lett.* **35**, 759–760 (1979)
19. Letho, A., Jaarinen, J., Tiusanen, T., Jokinen, M., Luukkala, M.: Magnitude and phase in thermal wave imaging. *Electron. Lett.* **17**, 364–365 (1981)
20. Bennett, C.A., Patty, R.R.: Thermal wave interferometry: a potential application of the photoacoustic effect. *Appl. Opt.* **21**, 49–54 (1982)
21. Beaudoin, J.L., Merienne, E., Danjoux, R., Egee, M.: Numerical system for infrared scanners and application to the subsurface control of materials by photothermal radiometry. *Infrared Technol. Appl. SPIE* **590**, 287–292 (1985)
22. Kuo P.K., Feng Z.J., Ahmed T., Favro L.D., Thomas R.L., Hartikainen J.: Parallel thermal wave imaging using a vector lock-in video technique. In: Hess, P., Pelzl, J. (Hrsg.) *Photoacoustic and Photothermal Phenomena*, pp. 415–418. Springer, Heidelberg (1987)

23. Meola, C., Carlomagno, G.M., Annicchiarico, D., Giordano, M., Zarrelli, M.: Detection of delamination in CFRP with Lock-in thermography. *Proc. Inst. Mech. Eng. Part G J. Aerosp. Eng.* **224**(11), 1219–1227 (2010)
24. Meola, C., Carlomagno, G.M., Giorleo, L.: The use of infrared thermography for materials characterization. *J. Mater. Process. Technol.* **155**(156), 1132–1137 (2004)
25. Meola, C., Carlomagno, G.M., Squillace, A., Giorleo, G.: Non-destructive control of industrial materials by means of lock-in thermography. *Meas. Sci. Technol.* **13**(10), 1583–1590 (2002)
26. Toscano, C., Meola, C., Carlomagno, G.M.: Porosity distribution in composite structures with infrared thermography. *J. Compos.* **2013**, 1–8 (2013)